COMBINING RADAR AND INFRARED OBSERVATIONS OF NEAR-EARTH ASTEROIDS

A Dissertation

Presented to the Faculty of the Graduate School

of Cornell University

in Partial Fulfillment of the Requirements for the Degree of

Doctor of Philosophy

by

Sean Ernest Marshall

December 2017

COMBINING RADAR AND INFRARED OBSERVATIONS OF NEAR-EARTH ASTEROIDS

Sean Ernest Marshall, Ph.D.

Cornell University 2017

Chapter 1: Near-Earth asteroids are some of Earth's closest neighbors in space. Thousands are known, with dozens of new ones being discovered every week. Yet the physical characterization of near-Earth asteroids lags well behind discovery. Studying some asteroids in detail helps to reveal the properties of the overall population. This work focuses on the detailed characterization of a few specific near-Earth asteroids with high-quality data sets, particularly radar observations that can be used to determine their shapes and rotation states. Incorporating multiple types of observational data enables much better characterization than could be done with any single data set.

Chapter 2: For (162421) 2000 ET70, incorporating lightcurves that had not been used for the modeling of Naidu et al. (2013) allows a better determination of its dimensions and rotation state. Incorporating infrared spectra further refines ET70's rotation state, since thermal modeling shows that some pole directions that provide good fits to the radar and lightcurve data are not compatible with the infrared observations. Thermal modeling also indicates that ET70's surface is heterogeneous, since no thermal model with uniform surface properties could provide an adequate fit to all of the infrared spectra.

Chapter 3: (85989) 1999 JD6 was observed to have a large amplitude in visible and infrared lightcurves, suggesting that it is a highly elongated body. Radar images obtained during JD6's close approach in 2015 confirm this, revealing a

contact binary with a maximum breadth of 3.0 km. Due to fortuitous observing geometry during some of the radar observations, its rotation state can be determined to great accuracy. The direction of JD6's rotation axis is known more accurately than that of any other asteroid for which only Earth-based observations are available.

Chapter 4: One promising way to speed up part of the asteroid shape modeling process is by using Bayesian optimization to test pole directions autonomously. This requires less computational time and less human oversight than a traditional grid search.

BIOGRAPHICAL SKETCH

Sean Ernest Marshall was born and raised in Berks County, Pennsylvania, a rural area with a great view of the night sky (on clear nights). Sean has always been interested in science, particularly astronomy. In middle school and high school, he was actively involved in Science Olympiad, as well as band, student council, and cross country. Sean graduated as valedictorian of Fleetwood Area High School's class of 2006.

Sean did his undergraduate studies at Arizona State University, double-majoring in physics and in the then-new Earth and Space Exploration program. Sean worked in ASU's Mars Space Flight Facility, under the guidance of Phil Christensen, analyzing data from the Thermal Emission Imaging System (THEMIS) instrument on NASA's 2001 Mars Odyssey orbiter. Sean did two Research Experiences for Undergraduates (REU) summer programs, in 2009 at the Maria Mitchell Observatory and in 2010 at the University of California, Los Angeles (UCLA). He graduated with honors in December of 2010, with a BSc in Physics and a BSc in Earth and Space Exploration (astrophysics concentration).

Sean began graduate school at Cornell University in 2011. In the summer of 2012, he traveled to Arecibo Observatory with Don Campbell and Jason Hofgartner to take part in radar observations, and he has been working on radar-related projects ever since then.

While working toward a doctorate, Sean got a Master of Science degree from Cornell in 2015. Also in 2015, he was awarded a NASA Earth and Space Sciences Fellowship (NESSF). Sean managed Cornell's "Ask an Astronomer" website[1] for over four years, and he was awarded the department's Eleanor York Award for community service and academic achievement in 2017.

[1] http://curious.astro.cornell.edu/

Outside of work, Sean enjoys reading, exploring bicycle trails, and cheering for sports teams from Cornell University, Arizona State University, and the city of Philadelphia. Sean currently holds the Cornell astronomy department record for the standing long jump: 2.4 meters.

After completing his PhD work at Cornell, Sean will begin a postdoctoral position in the planetary radar group at Arecibo Observatory.

This dissertation is dedicated to all asteroid enthusiasts of the past, present, and future.

ACKNOWLEDGEMENTS

First and foremost, I thank my family for their love and for their unwavering support of all my endeavors, all the way from early childhood through graduate school.

Don Campbell: First, thank you for that initial trip to Arecibo. Thank you striking a good balance between letting me work independently and steering me toward more productive directions when needed. Thank you for answering my many questions, even when you were on vacation. I am glad I got to be your final graduate student. After I'm finished at Cornell, I hope you will be able to relax and enjoy retirement.

The projects discussed in this dissertation involve observations from many times and locations, by many people. My work would not be possible without them. For observing at all hours and for answering my questions and otherwise providing vital feedback, thank you to my frequent collaborators: Ellen Howell, Mike Nolan, Chris Magri, Jenna Crowell, Yan Fernández, Ron Vervack, and Patrick Taylor.

I also thank my committee members, Joe Burns, Jim Cordes, and Phil Nicholson, for their guidance over the past six years.

Finally, I want to thank everyone else in Cornell's department of astronomy for providing a wonderful work environment. I have been interested in astronomy for my entire life, and I am grateful that my job today is every bit as interesting and exciting as I could have hoped when I was a child. Thank you all for making my dream job possible.

TABLE OF CONTENTS

LIST OF TABLES

LIST OF FIGURES

CHAPTER 1

INTRODUCTION

Some of the text in this chapter is taken from Marshall et al. (2017).

1.1 Planetary radar observations

For most astronomical observations, collecting the photons of interest is done in a passive manner. The observers must make use of whatever light from the target happens to be available. Planetary radar observations are different. With radar, a powerful series of radio waves is transmitted toward the target. Some of the power incident on the target is absorbed, and some is reflected. A small fraction of the power from the reflected echoes is later received, after the round-trip light travel time. With radar, in contrast to other astronomical observations, the observer controls the transmitted signal and therefore can choose its frequency, polarization, and time structure in a manner that maximizes the scientific value of the detected echoes (Ostro, 1993).

The echoes can be analyzed in time (delay) and frequency (Doppler shift) to produce two-dimensional delay-Doppler radar images of the asteroid, a technique that has also been applied to map other planetary bodies (e.g. Ostro, 1993; Campbell et al., 2006). Given that radar observations can be used to spatially resolve the target, radar observations of asteroids are the best way to characterize their physical properties from Earth-based observations. The only way to do better is with a (rare and expensive) spacecraft mission.

At present, there are two active planetary radar facilities: Arecibo Observatory in Puerto Rico and the Goldstone Deep Space Communications Complex

in California (Naidu et al., 2016).

At the time of this writing, over 700 near-Earth asteroids (NEAs) have been detected by radar[1]. There also have been radar observations of the Moon (e.g. Campbell et al., 2006), all inner planets, the four Galilean satellites (Campbell et al., 1978; Ostro, 1993), Saturn's rings (Nicholson et al., 2005) and some of its satellites (e.g. Campbell et al., 2003), over 100 main-belt asteroids, and 20 comets.

1.1.1 Continuous wave spectra

With continuous wave (CW) observations, the transmitted signal is nearly monochromatic, with no modulation. It is not perfectly monochromatic because the tranmitted signal is typically changed continuously so that the echo from the target's center of mass always would be received at the nominal transmitter frequency plus some small offset (e.g. 20 Hz), if the ephemeris were perfect (Magri et al., 2007). (That slight offset helps to clarify the sign of the Doppler shift in case of mistakes in the setup or analysis.) Since the ephemeris has some uncertainty, the echo may not be received at exactly the expected frequency. Any such measured discrepancy can be used to compute a more accurate ephemeris.

The target is rotating, so a monochromatic signal incident on the target is dispersed in frequency. One side of the target is rotating toward the observer, and the other side is rotating away (relative to the center of mass). The Doppler frequency bandwidth, B, of a CW spectrum is

[1] `https://echo.jpl.nasa.gov/asteroids/index.html`

$$B = \frac{4\pi D}{\lambda P} \cos\phi \tag{1.1}$$

where D is the projected breadth (diameter) of the asteroid, λ is the radar wavelength, P is the rotation period of the asteroid, and ϕ is the sub-observer latitude.

If the observing geometry is such that the line of sight is aligned with the target's rotation axis ($\phi \approx \pm 90°$), the observed bandwidth will be very small. In the common case where the period is approximately known from prior lightcurve observations but nothing is known about the orientation of the rotation axis, assuming a sub-radar latitude near the equator ($\cos\phi \approx 1$) gives a lower limit for the target's breadth. Radar observations with a line of sight near the target's equator will look very different from observations in which the line of sight is near its pole, so finding the direction of the asteroid's rotation axis is a key part of the shape modeling process (see Section 1.2).

CW spectra are one-dimensional; the target is resolved in frequency but not in time. These Doppler spectra therefore have a higher signal-to-noise ratio (SNR) in each frequency bin than simultaneous delay-Doppler images would have in each pixel. CW spectra are the observing mode of choice when the target is expected to be relatively faint, due to a large distance from the observer. Figure 1.1 shows a representative CW spectrum.

1.1.2 Delay-Doppler images

One can imagine a transmitted signal that is a delta function in time. In that case, the echoes would be dispersed in time, since the round-trip light travel

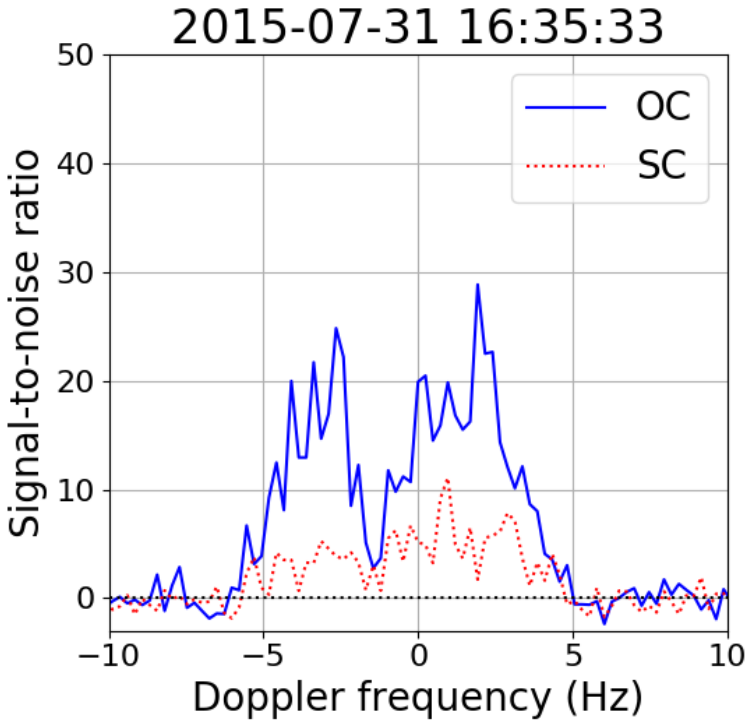

Figure 1.1: A typical continuous-wave (CW) radar spectrum. This shows an observation of 1999 JD6 from Arecibo when I was there in 2015. OC and SC are the two circular polarizations, which are explained in Section 1.1.4. The bifurcated spectrum is indicative of a contact binary NEA; see Section 3.3.2.

time would be slightly less for the regions of the target asteroid that are closest to the observer, and slightly greater for regions near its limb. In practice, one wants to transmit continously, so that more energy reaches the asteroid. Transmitting a signal that is modulated in frequency (chirped) or in phase (with a periodic pseudo-random binary code) allows the received signal to be de-chirped or decoded to provide echo power versus time (delay).

When the transmitted signal is modulated, decoding the measured echoes in both delay and frequency allows one to produce two-dimensional delay-Doppler images of the target. With delay-Doppler images, an asteroid can be spatially resolved with Earth-based observations. However, one of the dimen-

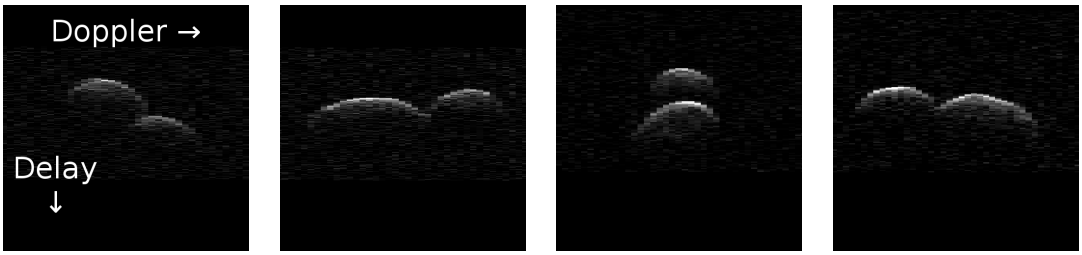

Figure 1.2: Delay-Doppler radar images of 1999 JD6, observed on July 25, 2015. For these images, transmissions from the DSS-14 antenna (at NASA's Goldstone Deep Space Communications Complex in California) were received at the Green Bank Telescope (in West Virginia). For all delay-Doppler images shown in this work, delay is plotted on the vertical axis, increasing from the top down. Doppler frequency is plotted on the horizontal axis, increasing from left to right. These images are stretched along their Doppler axes such that the width of each image corresponds to the same physical distance (3.6 km) for both the delay and Doppler axes; therefore the pixels of the original images appear rectangular here.

sions in delay-Doppler images is in the radial direction, so the images can differ substantially from what one would see in the plane of sky. Figure 1.2 shows some delay-Doppler images.

Each pixel in a delay-Doppler image includes the contributions from all parts of the target's surface that have the same distance and line-of-sight velocity relative to the observer. For a convex object, most delay-Doppler pixels include contributions from two different locations on the surface – leading to the so-called north-south ambiguity – whereas more complicated shapes can have three or more locations contributing to some of the delay-Doppler pixels (Ostro et al., 2002). Careful analysis of radar images acquired over the course of an asteroid's rotation makes it possible to determine the asteroid's three-dimensional shape, size, and rotation state, often with great accuracy (e.g. Magri et al., 2007, 2011; Nolan et al., 2013). Surface resolutions of a few meters are sometimes possible, much better than can be achieved by any other Earth-based technique. However, some regions of the asteroid may not be well constrained by the data. For

instance, if the viewing geometry during the radar observations was such that the sub-radar points always fell near the model's north pole, there would be little information on the asteroid's shape near its south pole.

In most cases, the radar echoes are received at the same station from which they were transmitted. For these monostatic observations, the signal is transmitted for (slightly less than) the round-trip light travel time to the asteroid. Then the telescope is switched from transmission to reception, and the echoes are received. Thus, for Arecibo, the integration time for a CW spectrum or delay-Doppler image is usually the two-way light time minus eight seconds, since normally it takes eight seconds to switch from transmission to reception. If the target's signal is faint, consecutive images can be summed. However, for targets of particular interest, transmissions from one telescope can be received elsewhere. For instance, for some of the observations of (85989) 1999 JD6, transmissions from Goldstone were received at the Green Bank Telescope; see Section 3.3.2. These bistatic observations allow each frame to have a greater integration time than the round-trip light travel time.

1.1.3 Radar equations

The power incident on the target is given by

$$P_{\text{inc}} = \frac{G_{\text{tx}} P_{\text{tx}}}{4\pi\Delta^2}, \tag{1.2}$$

where

$$G_{\text{tx}} = \frac{4\pi A_{\text{tx,eff}}}{\lambda^2} \tag{1.3}$$

is the gain (directionality) of the transmitter ($A_{\text{tx,eff}}$ is the effective area of the transmitter, which is the product of the geometric area of the transmitter and its aperture efficiency), P_{tx} is the transmitted power, and Δ is the distance between the transmitter and the target.

The power received from the target's echoes is

$$P_{\text{rx}} = \frac{G_{\text{tx}} P_{\text{tx}}}{4\pi\Delta^2} \frac{\sigma}{4\pi\Delta^2} A_{\text{rx,eff}}, \tag{1.4}$$

where σ is the radar cross section of the target (the projected area of a perfectly reflecting metal sphere from which the same echo power would be received) and $A_{\text{rx,eff}}$ is the effective area of the receiver.

The mean noise level is subtracted from the data, leaving thermal fluctuations that vary randomly with frequency. The measured root-mean-square noise is given by

$$N_{\text{rms}} = \frac{k_{\text{B}} T_{\text{sys}} B}{\sqrt{B\tau_{\text{int}}}} = k_{\text{B}} T_{\text{sys}} \sqrt{\frac{B}{\tau_{\text{int}}}}, \tag{1.5}$$

where k_{B} is Boltzmann's constant, T_{sys} is the system temperature of the receiver, B is the target's frequency bandwidth (from above), and τ_{int} is the integration time. The term inside the square root comes from there being $B\tau_{\text{int}}$ effectively independent measurements of the noise, which add in quadrature.

Combining these, the observed signal-to-noise ratio is

$$\mathrm{SNR} = \frac{P_{\mathrm{rx}}}{N_{\mathrm{rms}}} = \frac{G_{\mathrm{tx}} P_{\mathrm{tx}}}{(4\pi\Delta^2)^2} \frac{\sigma A_{\mathrm{rx,eff}}}{k_{\mathrm{B}} T_{\mathrm{sys}}} \sqrt{\frac{\tau_{\mathrm{int}}}{B}}, \tag{1.6}$$

assuming that Δ is effectively the same for the transmitter and the receiver. Note that the signal-to-noise ratio is proportional to Δ^{-4}, since there is a factor of Δ^{-2} from the transmitter to the target and the same factor between the target and the receiver. This steep dependence on distance is a major limitation for radar observations. To date, the most distant objects that have been observed with Earth-based radar are Saturn's rings and satellites (e.g. Campbell et al., 2003; Nicholson et al., 2005).

1.1.4 Polarization and related properties

All of the radar transmissions used in this work were circularly polarized. The helicity of a circularly polarized signal is reversed when it reflects off a flat (at wavelength scales) surface at zero incidence angle, so when a circularly polarized transmission reflects off a surface that has a large radius of curvature compared to the wavelength of the radar, almost all of the echo power is in the opposite-sense circular (OC) polarization. Same-sense circular (SC) echoes require a rough surface, multiple scattering, or subsurface refraction (Ostro, 1993; Benner et al., 2008). Therefore the circular polarization ratio,

$$\mu_{\mathrm{C}} = \frac{\sigma_{\mathrm{SC}}}{\sigma_{\mathrm{OC}}}, \tag{1.7}$$

provides information on the roughness of the target's surface on scales comparable to the radar wavelength. A larger circular polarization ratio usually indi-

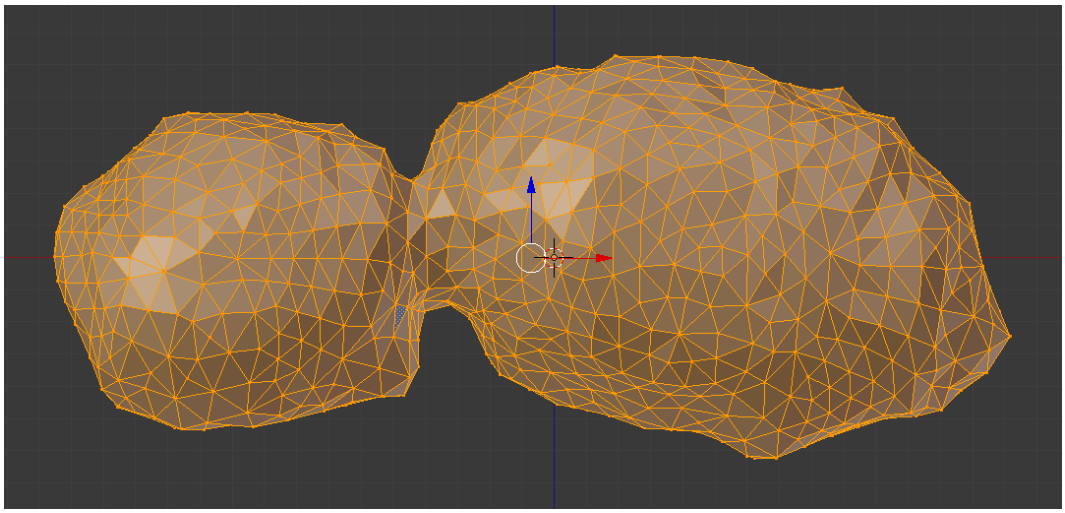

Figure 1.3: A view of the final shape model of (85989) 1999 JD6, showing the individual vertices and triangular facets.

cates a rougher surface; it also can be caused by coherent backscattering from an icy surface (Black et al., 2001).

1.2 Shape modeling

Given a sequence of delay-Doppler images acquired over the course of an asteroid's rotation, it is possible to do the inverse problem, searching for the model that best matches the observations. The general methodology for radar-based shape modeling was first described by Hudson (1993) and is discussed in more detail by Magri et al. (2007, 2011). For the shape modeling process, I have used the code SHAPE, as described in these papers. SHAPE represents the asteroid's surface as a polyhedron with a series of triangular facets. Figure 1.3 shows a view of one such shape model. In addition to delay-Doppler images, SHAPE also can calculate CW spectra and optical lightcurves for a model, comparing those simulated observations to the actual data.

SHAPE iterates through the model parameters that describe the asteroid's shape, photometric properties, and rotation state, finding the optimal value of each parameter by calculating a simulated data set for each possible model and comparing it to the observations, searching for the parameter values that minimize the objective function. The objective function is the weighted sum of squared normalized residuals (of the model values minus the data values, for all delay-Doppler pixels, CW frequency channels, and lightcurve points) plus user-specified penalties. Penalty functions are used to steer SHAPE away from models that are not physically realistic, such as shapes with narrow spikes.

In general, SHAPE can only make incremental changes to the input model, so it cannot make progress if the initial input does not provide at least a modest fit to some of the observations (e.g., if the initial model's size is wrong by a factor of two). Therefore, even in the early stages of shape modeling, the user must be careful to specify an initial model that is at least a fair approximation to the asteroid's shape. In practice, one normally begins by specifying an ellipsoid that is thought to be close to the asteroid's size and elongation. Over time, the model is gradually refined, and additional levels of complexity are added. Intermediate stages of shape modeling often represent that asteroid's surface with low-order spherical harmonics. Finally, if the data show enough fine details, SHAPE can work with models with over 1,000 vertices whose displacements can all be varied independently.

However, describing more complex shapes requires more free parameters. An ellipsoid can be described with three parameters (its extent along each axis), and a spherical harmonic model typically has a few dozen parameters, but models with 1,000 independent vertices have one free parameter for each vertex,

which greatly increases the required computation time.

One can estimate how many vertices are needed for a polyhedral model by approximating the error introduced by using a subdivided icosahedron to represent a spherical asteroid. A regular icosahedron has twelve vertices and a central angle of

$$\beta(12) = \arccos \frac{\sqrt{5}}{5} \approx 63.4^\circ \tag{1.8}$$

between neighboring vertices[2]. For a sphere of radius R, the relative difference between the actual radius and the distance δr from the sphere's center to the midpoint of one of the icosahedron's edges is

$$\frac{\delta r}{R} = 1 - \cos \frac{\beta(12)}{2} \approx 0.15 \tag{1.9}$$

Subdividing each edge at its midpoint quadruples the number of vertices but only cuts the angle between neighboring vertices in half, giving

$$\beta(48) = \frac{\beta(12)}{2} \approx 31.7^\circ \tag{1.10}$$

Thus, the overall pattern that emerges for N vertices, approximately evenly spaced with N sufficiently large, is

$$\beta(N) = \frac{\beta(12)}{\sqrt{N/12}} \approx \frac{220^\circ}{\sqrt{N}} \tag{1.11}$$

[2] http://mathworld.wolfram.com/RegularIcosahedron.html

$$\frac{\delta r}{R} \approx 1 - \cos\frac{\beta(N)}{2} \approx 1 - \cos\frac{110^\circ}{\sqrt{N}} \tag{1.12}$$

Setting δr to the finest range resolution of any delay-Doppler images, and using the best available estimate of the asteroid's size, one can use these relations to estimate the minimum number of required vertices. In practice, shape models often have more vertices than this suggested minimum.

For the asteroid's rotation state, one normally begins by assuming principal-axis rotation about the model's shortest axis. The model's rotation period is often known approximately from previous lightcurve observations. If not, one can use the observed delay depth as an estimate of the asteroid's radius and then figure out what rotation period would be needed to match the observed CW bandwidths, assuming a sub-radar latitude near the equator. If a model with principal-axis rotation does not provide an adequate fit to the observations, SHAPE includes the capability to model non-principal-axis rotation, but that was not necessary for any of the asteroids discussed in this work.

Typically, the radar scattering properties of the asteroid are represented as a cosine law with respect to incidence angle (Mitchell et al., 1996):

$$\frac{d\sigma}{dA} = R(C + 1)(\cos\theta)^{2C} \tag{1.13}$$

where σ is the radar cross section, A is the surface area, R and C are fit parameters, and θ is the incidence angle. $\frac{d\sigma}{dA}$ is the radar cross section per unit surface area at an incidence angle θ. C is typically of order unity, e.g. 0.87 for (136617) 1994 CC Alpha (Brozović et al., 2011) or 1.4 for (162421) 2000 ET70 (Naidu et al., 2013).

1.2.1 My contributions

Unfortunately, it can take a while to go from observations to a publishable shape model. Even for an experienced researcher utilizing PSHAPE (a version of SHAPE that can use multiple processors in parallel) on a capable server, several months of work are typically needed for each asteroid. However, over the past few years I have written a variety of Perl and Python scripts to speed up some parts of the process:

- Normalizing delay-Doppler images
- Converting lightcurves to the format expected by SHAPE
- Finding the optimal distribution of node assignments when running PSHAPE (actually a spreadsheet, not a script)
- Preliminary work on using Bayesian optimization to automatically find the best pole direction (see Section 4.3)
- Quickly plotting SHAPE's modeled data sets next to the corresponding radar or lightcurve observations
- Plotting the dependence of the objective function (or chi-squared) on various model parameters

Additionally, I have written other scripts that added new functionality to some existing scripts used at Arecibo:

- Copying and modifying a template model, to do a grid search over some part of the parameter space
- Analyzing radar data to obtain astrometric measurements
- Calculating radar cross sections from CW data

1.3 Infrared observations and thermal modeling

1.3.1 Infrared observations

Observations of an asteroid's thermal emission at infrared wavelengths can be used to constrain its thermal properties (e.g. Lebofsky et al., 1978; Harris and Lagerros, 2002). Most of the infrared observations considered in this work are from the SpeX instrument (Rayner et al., 2003) of NASA's InfraRed Telescope Facility (IRTF), acquired as part of an ongoing project to obtain infrared spectra of near-Earth asteroids that also have been targeted with radar (Howell et al., 2017).

Our SpeX observations are obtained as relative reflectance, also called scaled spectra, meaning that the asteroid's observed spectrum is divided by the Sun's spectrum (or rather, the spectrum of a Sun-like star in a nearby part of the sky) and then normalized to unity at some reference wavelength. Scaled spectra are more robust to observing conditions than absolute spectra, since most atmospheric variations should cancel when dividing by the spectrum of the comparison star. However, scaled spectra are relative photometry – they quantity the target's color ratios but not the absolute fluxes, so they cannot (by themselves) be used to estimate the size of an asteroid. Note that a scaled spectrum includes contributions from both reflected sunlight and thermal emission. For the near-Earth asteroids considered in this work, reflected sunlight typically dominates at wavelengths less than about 2.5 microns; thermal emission typically dominates at wavelengths above about 3.5 microns. Figure 1.4 shows a few scaled spectra.

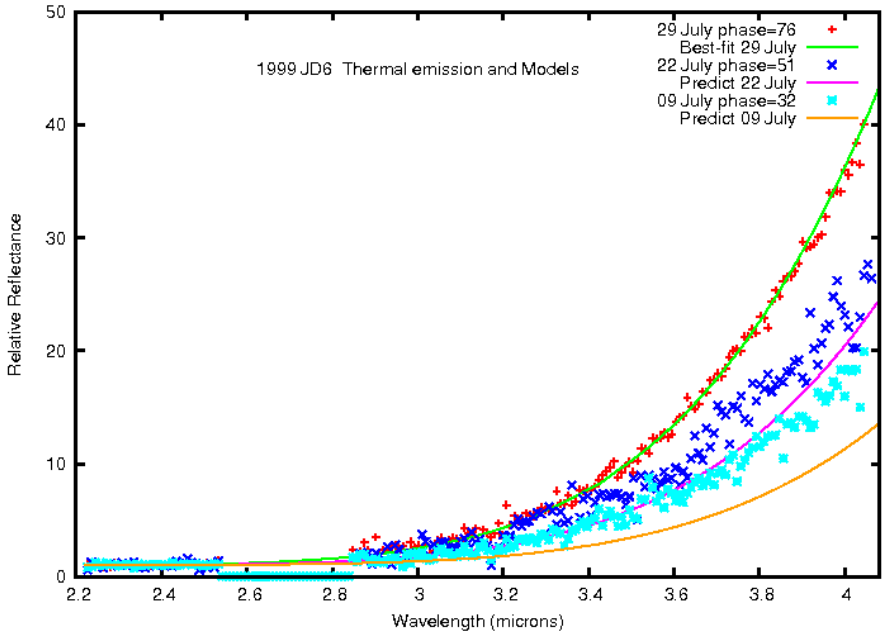

Figure 1.4: Scaled spectra of 1999 JD6 (crosses), from SpeX observations in 2010. The curves show model spectra; see Section 1.3.3. Image courtesy of Ellen Howell.

SpeX observations cover wavelengths from 0.8 to 4.1 microns (before 2015) or 0.8 to 5.1 microns (since 2015), a wavelength range which includes a combination of reflected sunlight and thermal emission. Typically, thermal emission is too weak to be measured at wavelengths shorter than about 2.5 microns. When possible, these near-infrared observations from SpeX are supplemented by published observations at mid-infrared wavelengths from NASA's Spitzer Space Telescope and/or Wide-field Infrared Survey Explorer (WISE).

1.3.2 Thermal properties

Albedo is the fraction of incident light that is reflected by the object. In this work, I am using models that represent optical scattering with a Hapke law (Hapke, 1984), so the relevant parameter is the Hapke single-scattering albedo (w). The single-scattering albedo is for individual particles or grains, so the albedo of the asteroid as a whole cannot be greater than the single-scattering albedo (e.g., Section 2.7).

Surface roughness is parameterized as a fraction of each model facet's surface that is partially covered by spherical-section craters, a representation which Lagerros (1998) found to be computationally efficient while giving similar results to other (more complicated) parameterizations of surface roughness.

Thermal inertia quantifies the body's resistance to changes in temperature, much like how inertia (mass) quantifies a body's resistance to changes in its motion. A body with low thermal inertia is subject to strong diurnal temperature variations, as in a desert. A body with high thermal inertia has a relatively constant temperature over the course of its rotation, like a region near an ocean.

1.3.3 Thermal modeling

In order to make the connection between the asteroid's thermal properties and the observed infrared spectra, one must use a thermal model. The thermal model specifies how to calculate the temperatures across the asteroid's surface, based on the actual solar illumination and the asteroid's properties (Morrison, 1973; Spencer et al., 1989; Lagerros, 1996; Harris and Lagerros, 2002). The mod-

eled thermal spectra of the regions visible to the observer at a given time are then summed to find the disk-integrated spectrum that would be observed, which can be compared to the measured spectrum.

Thermal models often assume the target is spherical if there is no other information available (e.g. Campins et al., 2009; Trilling et al., 2010; Mainzer et al., 2014). However, I am working with asteroids for which we have detailed shape models. I can use their known shapes and rotation states to find a more accurate representation of the thermal emission.

I am using a thermophysical modeling code called SHERMAN (Magri et al., 2017). SHERMAN calculates the asteroid's temperature distribution based on how the various parts of the asteroid's surface are illuminated by the Sun, solving the heat equation at closely spaced time steps to represent vertical heat transport (conduction and radiation) into and out of the subsurface layers beneath each facet (horizontal heat transport is ignored). Calculations of the asteroid's thermal state begin several rotations before the observation times, in order to ensure that the model's thermal state has stabilized by the observation times.

With SHERMAN, the user can specify the asteroid's physical properties, including its size, shape, and rotation state. For the asteroids discussed in this work, I am using the shapes and spin states that were found from my own prior shape modeling. Then one can run a set of models with a range of thermal parameter values, to find the thermal properties that best match the data (Howell et al., 2017; Marshall et al., 2017).

Surface roughness on scales smaller than the facet size (i.e., ten-meter scales and smaller) is modeled by having some fraction of the asteroid's surface cov-

ered by a set of spherical-section craters. This parameterization of roughness follows the method of Lagerros (1998), who found that such craters give similar results to more complicated representations of surface roughness (for disk-integrated spectra), while requiring far less computational effort. SHERMAN allows sunlight to scatter multiple times within the crater, as per the assumed Hapke law. It then uses the absorbed fluxes to calculate the surface temperatures in the crater, following Lagerros (1998), with mutual heating (infrared emission and absorption) taken into account but assuming zero thermal inertia. The temperatures within the crater are then corrected for finite thermal inertia.

Modifying the notation of Lagerros (1998), I will denote the crater coverage fraction as f_c and the RMS slope as ρ. (Note that ρ is a dimensionless slope; $\rho = \tan\theta_{\rm rms}$.) I use γ to denote the craters' opening angle. An opening angle of $\gamma = 180^\circ$ would indicate craters that are hemispheres, and $\gamma < 180^\circ$ indicates shallower craters. ρ, f_c, and γ are related by

$$\rho^2 = f_c \frac{\ln(1-2S) - 2S(S-1)}{4S(S-1)} \tag{1.14}$$

where

$$S = \frac{1-\cos(\gamma/2)}{2} = \sin^2(\gamma/4) \tag{1.15}$$

is the ratio of the crater's depth to the diameter of its defining sphere.

1.3.4 My contributions

For simple convex shapes (such as spheres), the computation of a disk-integrated infrared spectrum can be done in less than a second. However, for shapes with concavities, some model facets can cover (shadow) other facets or scatter light onto other facets, and accurately accounting for these effects greatly increases the complexity of the computations. When running thermal models for concave shapes with multiple scattering, SHERMAN can take an hour or more for each model – sometimes many hours. However, since each model only uses one processor, it is possible to run many models in parallel.

As with shape modeling, I have written numerous scripts to automate some of the process:

- Running the preliminary optical scattering calculations for batches of models
- Running batches of thermal models
- Plotting SHERMAN's simulated observations next to the corresponding data, to enable quick visual inspection of a model
- Calculating chi-squared for sets of thermal models and plotting its dependence on the thermal parameters, to enable easy determination of which models are best

1.4 Summary

Chapter 2, from Marshall et al. (2017), discusses near-Earth asteroid (162421) 2000 ET70, for which Naidu et al. (2013) originally found a shape model using only radar data. After finding that thermal models using their their published shape model and rotation state were unable to provide adequate fits to our infrared observations, my coauthors and I revisited the shape modeling, incorporating previously unused lightcurves. We ultimately found that the infrared spectra help to constrain ET70's pole position, and that ET70 is significantly shorter along its z-axis.

Chapter 3, soon to be submitted as Marshall et al. (2018), describes shape modeling of another NEA, (85989) 1999 JD6. Lightcurve observations of JD6 had suggested that it is a very elongated body. A high-quality series of radar observations from Goldstone and Arecibo in 2015 confirm this, revealing a contact binary with a maximum extent of 3.0 kilometers. During the first set of Goldstone observations, the lines of sight happened to pass within two degrees of JD6's pole direction. These fortunate circumstances provided very strong constraints on JD6's rotation state. The uncertainty in its pole direction is just 0.25°; this is the most accurately known pole position of any asteroid for which there are only Earth-based observations.

Chapter 4 summarizes three other not-yet-published projects that I have worked on as a graduate student: thermal modeling of 1999 JD6 using infrared spectra from Spitzer and the IRTF, shape modeling of 1998 UO1 from radar and lightcurve data, and applying Bayesian optimization to automate NEA pole searches.

CHAPTER 2

THERMAL PROPERTIES AND AN IMPROVED SHAPE MODEL FOR NEAR-EARTH ASTEROID (162421) 2000 ET70

The contents of this chapter originally were published in: S. E. Marshall, E. S. Howell, C. Magri, R. J. Vervack, D. B. Campbell, Y. R. Fernández, M. C. Nolan, J. L. Crowell, M. D. Hicks, K. J. Lawrence, and P. A. Taylor. Thermal properties and an improved shape model for near-Earth asteroid (162421) 2000 ET70. *Icarus*, 292:22-35, August 2017.

2.1 Abstract

We (Marshall et al., 2017) present thermal properties and an improved shape model for potentially hazardous asteroid (162421) 2000 ET70. In addition to the radar data from 2000 ET70's apparition in 2012, our model incorporates optical lightcurves and infrared spectra that were not included in the analysis of Naidu et al. (2013, *Icarus* 226, 323-335). We confirm the general "clenched fist" appearance of the Naidu et al. model, but compared to their model, our best-fit model is about 10% longer along its long principal axis, nearly identical along the intermediate axis, and about 25% shorter along the short axis. We find the asteroid's dimensions to be 2.9 km × 2.2 km × 1.5 km (with relative uncertainties of about 10%, 15%, and 25%, respectively). With the available data, 2000 ET70's period and pole position are degenerate with each other. The radar and lightcurve data together constrain the pole direction to fall along an arc that is about twenty-three degrees long and eight degrees wide.

Infrared spectra from the NASA InfraRed Telescope Facility (IRTF) provide

an additional constraint on the pole. Thermophysical modeling, using our SHERMAN software, shows that only a subset of the pole directions, about twelve degrees of that arc, are compatible with the infrared data. Using all of the available data, we find that 2000 ET70 has a sidereal rotation period of 8.944 hours (± 0.009 h) and a north pole direction of ecliptic coordinates $(52°, -60°) \pm 6°$. The infrared data, acquired over several dates, require that the thermal properties (albedo, thermal inertia, surface roughness) must change across the asteroid's surface. By incorporating the detailed shape model and spin state into our thermal modeling, the multiple ground-based observations at different viewing geometries have allowed us to constrain the levels of the variations in the surface properties of this asteroid.

2.2 Introduction to 2000 ET70

Near-Earth asteroid (162421) 2000 ET70 (hereafter ET70) was discovered on March 8, 2000, by the Lincoln Near-Earth Asteroid Research (LINEAR) program in Socorro, New Mexico. It is an Aten asteroid (a = 0.947 au). Williams (2000) and Whiteley (2001) reported an absolute visible magnitude of 18.2, but that value was based on observations at a phase angle of 70 degrees.

ET70 passed near Earth in February of 2012, with a closest approach distance of 0.0454 au (18 lunar distances) on February 19. A series of radar observations with the 305-meter William E. Gordon Telescope at the Arecibo Observatory and with the 70-meter DSS-14 antenna at NASA's Goldstone Deep Space Communications Complex provided continuous-wave spectra and delay-Doppler images that yielded a shape model (Naidu et al., 2013), somewhat reminiscent of

a clenched fist – roughly ellipsoidal with ridges and valleys near its north pole. Naidu et al. found ET70's dimensions to be 2.61 km × 2.22 km × 2.04 km (with uncertainties of 5%). ET70's size and its Minimum Orbit Intersection Distance (MOID) with respect to Earth of 0.03 au make it a potentially hazardous asteroid (PHA).

Using the Naidu et al. (2013) shape, we attempted to model the thermal emission from ET70 as constrained by spectra we obtained at NASA's InfraRed Telescope Facility (IRTF). Our early thermal modeling runs suggested that the pole might be further south than the position at ecliptic coordinates $(\lambda, \beta) = (80°, -50°) \pm 10°$ obtained by Naidu et al. This motivated a reassessment of their shape model, which was based solely upon the radar observations.

Lightcurve observations of ET70 that were also obtained in February 2012 can provide additional constraints for the shape modeling process, particularly the determination of the pole location. We have therefore revisited the Naidu et al. model using both the radar and lightcurve data in concert with thermal modeling of our IR observations in order to improve the shape model for ET70, with a focus on the pole position, and to determine the best estimates of its thermal parameters based on its revised shape. This study demonstrates the power of multiple data sets in the investigation of near-Earth asteroids (NEAs).

2.3 Observations

2.3.1 Radar observations

All of the radar observations of ET70 took place in 2012. We have delay-Doppler images and CW spectra from ten days between February 12 and February 23, 2012, around the time of ET70's closest approach (0.05 au). ET70 was observed with Arecibo planetary radar system (S-band, 2380 MHz frequency, 12.6 cm wavelength) on all six days from February 12 through 17, and with the Goldstone Solar System Radar (X-band, 8560 MHz, 3.5 cm) on seven days from February 15 through 23. There were additional Arecibo observations on two days in August 2012 but, due to ET70's greater distance (0.16 au) at that time, only CW spectra could be acquired. The August CW spectra were used in shape modeling, but they were not particularly helpful in constraining ET70's properties. The details of the radar observations are given in Table 2.1 and Table 2.2. We are using all of the radar data that were used by Naidu et al. (2013), but we have summed some of the images differently. We also have incorporated some lower-quality radar data sets that were not used for the final shape model of Naidu et al.: a few coarse-resolution delay-Doppler images from Goldstone and some additional CW spectra from Arecibo.

UT date	UT times	Tel	Mode	δr (m)	δf (Hz)	Runs	RTT (s)	P_{tx} (kW)
02-12	08:27:51–08:37:55	A	CW		0.167	5	67	828
	08:42:47–10:29:47		DD	15	0.075	48		
	10:53:18–11:07:41		DD	15	0.075	7		
02-13	08:11:06–08:25:56	A	CW		0.182	7	62	860
	08:30:34–10:53:26		DD	15	0.075	50		
02-14	07:59:56–08:04:43	A	CW		0.196	3	58	811
	08:06:40–10:19:45		DD	15	0.075	59		
02-15	07:53:54–08:00:11	A	CW		0.213	4	54	785
	08:03:01–08:14:46		DD	15	0.075	5		
	08:18:28–10:09:46		DD	15	0.075	58		
02-15	09:17:49–09:33:20	G	DD	75	1.532	9	54	420
	09:46:26–12:24:09		DD	37	1.021	77†		

Table 2.1: Radar observations used in this work (part one; continued in Table 2.2). All observations are from 2012. UT times specify when data reception began and ended. The third column specifies which telescope was used: A for Arecibo or G for Goldstone. The fourth column (mode) specifies whether the observations were continuous-wave spectra (CW) or delay-Doppler images (DD). For images, δr, the range resolution, specifies the equivalent distance from the time delay resolution of the data. For instance, delay resolution of 0.1 µs (100 ns) is equivalent to a range resolution of 15 m. δf specifies the frequency resolution of the data that were used in the shape fitting. The numbers of runs listed here are the numbers of usable scans (the numbers of round-trip times for which data was acquired) for each data set. A dagger (†) indicates that subsets of these data were summed before being input to the shape fitting software, in order to increase SNR. For instance, the 77 Goldstone imaging scans on February 15 were summed, with (most) sums having three scans, so that the shape modeling software used 26 sums. RTT is the round-trip time to the asteroid for those observations. A round-trip time of 60 seconds corresponds to a distance of 0.060 au. P_{tx} is the transmitter power.

UT date	UT times	Tel	Mode	δr (m)	δf (Hz)	Runs	RTT (s)	P_{tx} (kW)
02-16	07:34:18–07:38:30	A	CW		0.227	3	51	760
	07:48:38–07:51:06		CW		0.227	2		
	07:53:28–09:36:34		DD	15	0.075	61		
02-16	12:15:56–13:28:09	G	DD	15	1.000	29†	51	420
	13:29:06–15:29:31		DD	15	1.000	70†		
02-17	07:38:00–07:41:57	A	CW		0.244	3	48	775
	07:46:14–08:48:59		DD	15	0.075	39		
02-17	07:42:56–08:00:01	G	DD	75	1.532	11†	48	420
	08:16:58–12:24:19		DD	37	0.977	152†		
02-18	07:36:05–07:50:52	G	DD	75	1.532	10†	47	420
	08:01:16–08:45:24		DD	37	0.977	26		
02-19	07:21:56–07:36:25	G	DD	75	1.532	10†	46	420
	07:46:13–13:07:48		DD	37	0.977	188†		
02-20	08:12:15–11:26:19	G	DD	37	0.977	80†	46	420
02-23	09:20:47–10:55:20	G	DD	75	0.977	55†	51	420
08-24	15:46:51–16:31:17	A	CW		0.342	9	153	721
08-26	15:04:24–16:15:22	A	CW		0.333	14	157	722

Table 2.2: Radar observations used in this work (part two; continued from Table 2.1). All observations are from 2012. UT times specify when data reception began and ended. The third column specifies which telescope was used: A for Arecibo or G for Goldstone. The fourth column (mode) specifies whether the observations were continuous-wave spectra (CW) or delay-Doppler images (DD). For images, δr, the range resolution, specifies the equivalent distance from the time delay resolution of the data. For instance, delay resolution of 0.1 µs (100 ns) is equivalent to a range resolution of 15 m. δf specifies the frequency resolution of the data that were used in the shape fitting. The numbers of runs listed here are the numbers of usable scans (the numbers of round-trip times for which data was acquired) for each data set. A dagger (†) indicates that subsets of these data were summed before being input to the shape fitting software, in order to increase SNR. RTT is the round-trip time to the asteroid for those observations. A round-trip time of 60 seconds corresponds to a distance of 0.060 au. P_{tx} is the transmitter power.

2.3.2 Lightcurve observations

Alvarez et al. (2012) obtained lightcurve observations of ET70 from February 19 through 24, 2012, from four different locations (see Table 2.3), and submitted them to the Minor Planet Center's Asteroid Light Curve Database (Warner et al., 2011). Alvarez et al. (2012) found an apparent rotation period for ET70 of 8.947 ± 0.001 hours. Naidu et al. (2013) noted that without information on ET70's pole position, this observed period allows for sidereal rotation periods from 8.902 to 8.992 hours.

Because the asteroid was moving fairly quickly across the sky (about 7° per day during the lightcurve observations), each night's observations had to be divided into multiple sessions, with each session having a different set of comparison stars. (See Figure A.1 for a plot of ET70's sky positions during all measurements.) Guided by the composite lightcurve in Alvarez et al. (2012), we joined the segments from the different sessions, and combined them into a single consistent lightcurve for each night, an example of which is shown in Figure 2.1. In order to speed up the computations, all lightcurves were decimated in time before being input to the shape modeling software.

The lightcurves provide valuable information on ET70's shape and spin state. In particular, the times of their minima and maxima helped us refine ET70's rotation period, and their amplitudes constrained ET70's dimensions and pole position. There are two brightness maxima per rotation period. The maxima of several of the lightcurves are noticeably asymmetric – that is, one of the maxima is clearly and consistently brighter than the other, as shown in Figure 2.2. This was a useful constraint for shape modeling, because some models could not reproduce the asymmetric maxima.

UT date	UT times	$\Delta\phi$	r (au)	Δ (au)	α	Observatory (and MPC code)	Observer	Data points Raw	Dec.
02-19	03:31–08:54	217°	1.020	0.046	45°	OLASU (I38)	Alvarez	487	21
02-21	05:53–13:05	290°	1.024	0.047	41°	Kitt Peak (695)	Han	1027	42
02-22	01:37–07:10	224°	1.025	0.048	41°	OLASU	Alvarez	531	18
02-22	09:45–14:24	187°	1.025	0.049	41°	Kingsgrove (E19)	Oey	235	24
02-23*	23:59–05:47	234°	1.026	0.050	42°	OLASU	Alvarez	582	18
02-23	09:35–18:20	352°	1.027	0.052	43°	Kingsgrove	Oey	377	35
02-24	00:15–01:30	50°	1.028	0.053	43°	Cerro Tololo	Han	120	9
02-24	09:36–18:38	364°	1.028	0.055	44°	Kingsgrove	Oey	264	33

Table 2.3: Lightcurve observations used in this work. All of these observations were taken within a few days of the New Moon of February 21, 2012. Note that the February 21 lightcurve from Kitt Peak was not listed in Table 1 of Alvarez et al. (2012), though it was uploaded to the Minor Planet Center. $\Delta\phi$ is the range of asteroid rotation phases covered by that night's lightcurves, assuming the best-fit sidereal rotation period of 8.944 hours. A value greater than 360° indicates that the lightcurves encompassed more than a full rotation of ET70. r is the distance from the asteroid to the Sun; Δ is the distance from the asteroid to the Earth; α is the solar phase angle. The final two columns list the numbers of data points in the raw and decimated versions of each lightcurve.

* First observation was at 23:59 UT on February 22; last observation was at 05:47 UT on February 23

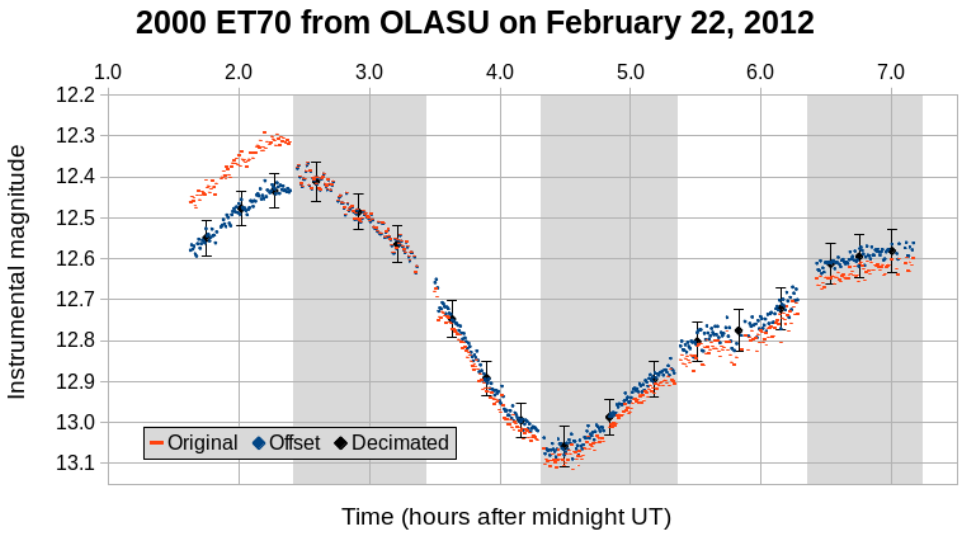

Figure 2.1: Example of lightcurve data at different stages of processing. The alternating white and gray backgrounds indicate the different sessions. Because each session had a different set of comparison stars, there are offsets between the magnitudes from different sessions. The magnitudes from each session had to be shifted vertically, so that the combined lightcurve's amplitude would be consistent with the amplitude of the composite lightcurve in Alvarez et al. (2012). The orange points show the original data (with magnitude offsets not corrected), the blue points show the combined lightcurve (with appropriate magnitude offsets for the different sessions), and the black points with error bars show the final combined and decimated lightcurve that was used for shape modeling. Typically, the decimated lightcurves had three points from each session. There were two contributions to the error bars of the decimated lightcurves: uncertainty in the offsets between the different sessions (0.03 to 0.05 magnitudes) and uncertainty from the scatter in the original (undecimated) lightcurves' data points (usually 0.01 to 0.03 mag).

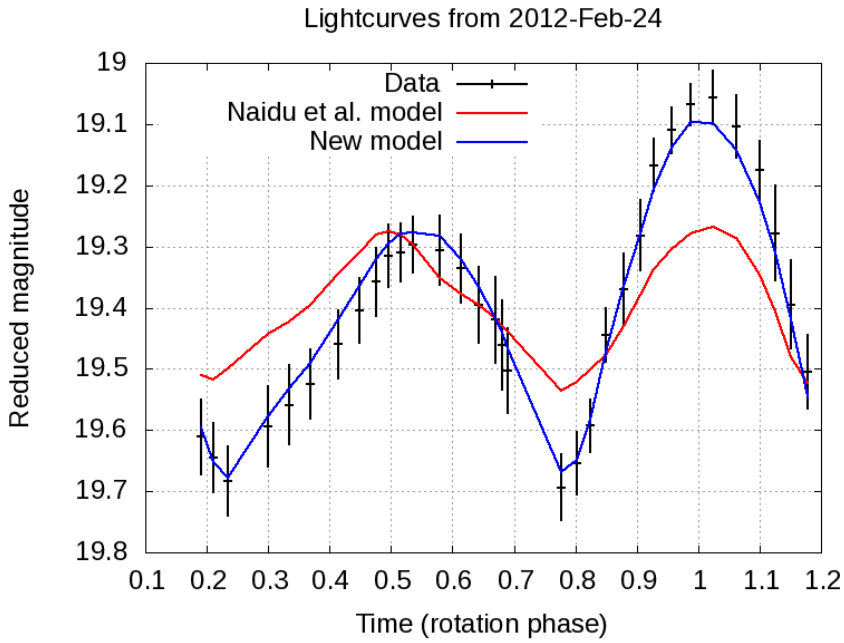

Figure 2.2: Lightcurve observations from Kingsgrove on February 24, 2012 (black points with error bars; decimated). Note the asymmetric maxima, which were a key feature of multiple lightcurves. The blue curve shows the model lightcurve from our best shape model, with a pole at ecliptic coordinates $(\lambda, \beta) = (52^\circ, -60^\circ)$. Also shown, in red, is the lightcurve predicted by the model of Naidu et al. (2013). Their nominal pole direction $(80^\circ, -50^\circ)$ and shape model are incompatible with the lightcurve data. Plots of the Naidu et al. model and our model for the other lightcurves can be found in Figure A.2 through Figure A.9 in the Appendix.

2.4 Shape modeling

We began with the published shape model of Naidu et al. (2013), which has 2000 vertices and 3996 triangular facets. The average edge length of the triangles is about 100 meters. In the early stages of shape modeling, we used floating scale factors for the model's three principal axis lengths – that is, we kept the general "clenched fist" shape of ET70 but allowed it to be stretched or compressed along each axis. This greatly reduced the required computational time, because it meant that SHAPE only had to find optimal values of the three axes' scale factors, instead of optimal displacements for each of the two thousand vertices. In the later stages of shape modeling, we did allow the individual vertices' displacements to vary.

There were far more radar data points (hundreds of thousands of image pixels and spectral channels) than lightcurve data points (two hundred after decimation), so in order to ensure that each type of observation had significant leverage on the modeling results, we had to apply different weights to the various data sets. The final weights were set such that the delay-Doppler images contributed about half of total chi-squared, the CW spectra contributed about one third, and the lightcurves contributed about one sixth.

The Doppler bandwidth, B, of a continuous wave (CW) spectrum is given by $B = \frac{4\pi D}{\lambda P} \cos\phi$ where D is the projected breadth (diameter) of the asteroid, λ is the wavelength of the radar, P is the asteroid's rotation period, and ϕ is the sub-observer latitude. The key constraint from the CW spectra was on the sub-observer latitude at the times of the observations. Therefore our CW spectra, most of which are from a relatively narrow range of observation times, required

ET70's pole to fall along a certain arc across the sky, but they did not allow the specific position on that arc to be determined.

We focused our efforts on examining pole positions near the nominal Naidu et al. (2013) retrograde solution at (80°, −50°). Testing showed that prograde solutions – i.e., those near the conjugate pole (260°, +50°) – are not compatible with the full set of radar and lightcurve data. All prograde models showed clear mismatches between the rotation phases of the model and the data. Most notably, the prograde model's rotation phase lags behind the data in later delay-Doppler images, but the model's rotation phase is ahead of the data in lightcurves from about the same observation times. Some of the delay-Doppler images were particularly helpful in constraining ET70's pole direction because they have two or more bright edges (see Figure A.12 through Figure A.34), and a model with a misaligned pole would have those edges separated by the wrong number of delay cells.

We also found that slight changes to the model's sidereal rotation period (of order 0.1% ≈ 0.009 h ≈ 30 s), combined with a compensating change in ET70's pole position, of order 5°, produced simulated data sets that were practically indistinguishable from each other, and from the actual data (see Figure 2.3). In other words, with the available radar and lightcurve data, ET70's sidereal rotation period and pole direction are degenerate.

In the final stages of shape modeling, we ran over 300 models, for which each model's pole position was held constant but the rotation period was allowed to vary. We found that the pole could fall within a region encompassing ecliptic longitudes 21° to 61° and latitudes −71° to −53°, as shown in Figure 2.4. Different pole positions require slightly different sidereal rotation periods, rang-

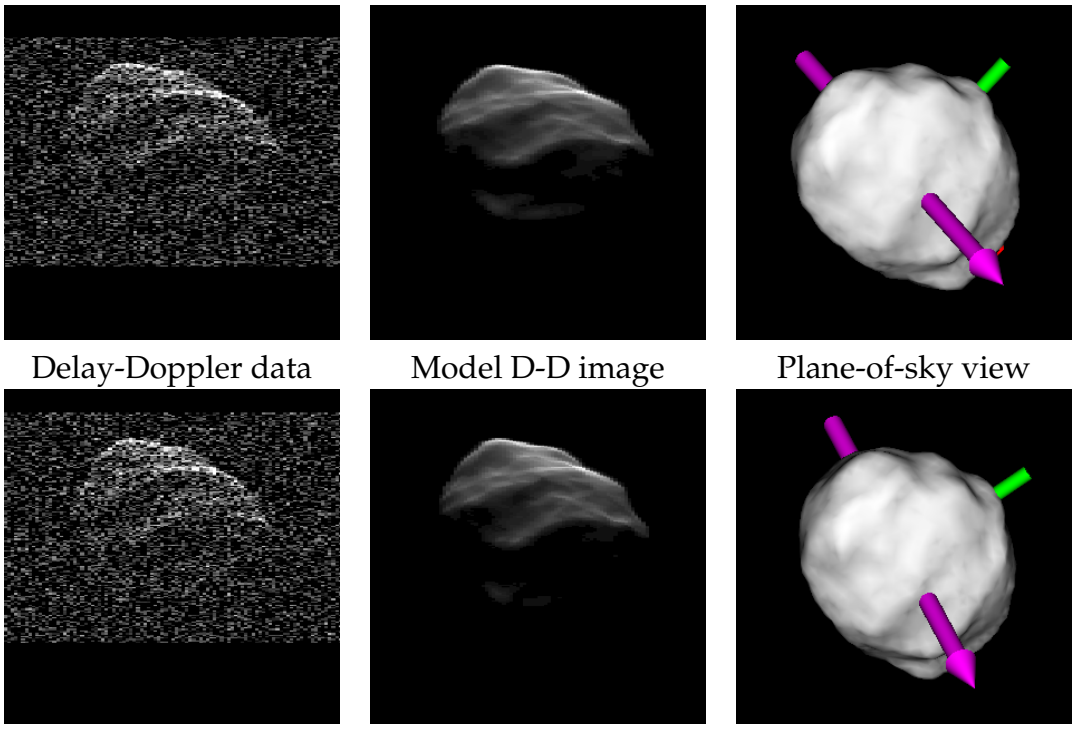

Figure 2.3: An example of delay-Doppler frames for two models with different rotation periods and pole positions but nearly indistinguishable simulated images. The first row shows a model with a sidereal rotation period of 8.944 hours and a pole direction of $(52°, -60°)$. The second row shows a model with a sidereal rotation period of 8.934 hours and a pole direction of $(40°, -68°)$, which is 10° from the first model's pole position. The left column shows the data (same for both models, but with slightly different brightness scaling in the two frames). The center column shows the simulated (noise-free) delay-Doppler images derived from the shape models. In the delay-Doppler images, delay is plotted on the vertical axis (increasing from the top down), and Doppler frequency is plotted on the horizontal axis (increasing from left to right). The right column shows the simulated plane-of-sky views (as seen from Earth), with the sidereal spin vector (the model's shortest principal axis) shown as a magenta arrow and the long and intermediate principal axes shown as red (barely visible) and green shafts, respectively. For all plane-of-sky views, north is upward and east is leftward. The radar images are stretched so that their spatial scale is the same as that of the plane-of-sky image (square frames with a side length of 3.5 kilometers), but the radar images' vertical axis, range, is perpendicular to the plane of the sky. Based on this work, the ET70 model's maximum extent is 2.9 km, and its minimum extent is 1.5 km. Note that the same region of the asteroid is closest to the observer for both models, so the model images are nearly identical. The main difference between these two models is a rotation in the plane of the sky, which does not affect delay-Doppler images. However, the models also differ by a slight rotation (about five degrees) out of the plane.

ing from 8.926 to 8.957 hours. The nominal shape model of this work provides slightly better fits to the radar data than that of Naidu et al. (2013), but the main improvement is how it fits the lightcurves. The nominal pole position of Naidu et al., $(80°, -50°)$ with an uncertainty of $10°$, can be ruled out because it is incompatible with the lightcurve data (see Figure 2.2, and also Figure A.2 through Figure A.9). Our infrared observations provide additional constraints on the pole position, because thermal modeling shows that some poles and periods allowed by the radar and lightcurve data are ruled out by the infrared data (see Section 2.6).

The final best-fit shape model has somewhat different dimensions from the Naidu et al. model, and there are also some small features that are slightly different (see Figure 2.5). The radar and lightcurve data favor a shape that is considerably shorter along its z-axis (rotation axis) than the radar-only model of Naidu et al. (2013). This supports the suggestion of Rozitis and Green (2014) that shape models derived only from radar data may overestimate models' z-lengths, based on their analysis of 1620 Geographos (using infrared data to constrain the shape model). Possibly this is because if the data do not strongly constrain the z-length, SHAPE will leave the z-length close to its initial value. Shape models are often initialized with similar lengths along the y and z axes, whereas in reality an asteroid usually rotates about its shortest principal axis (the one with the greatest moment of inertia), so the z-length is less than the y-length.

However, we note that the region near ET70's southern pole was not seen clearly in the delay-Doppler images, and that ET70's z-length is not well constrained. The relative uncertainty in ET70's z-length is 25%. The best-fit lengths

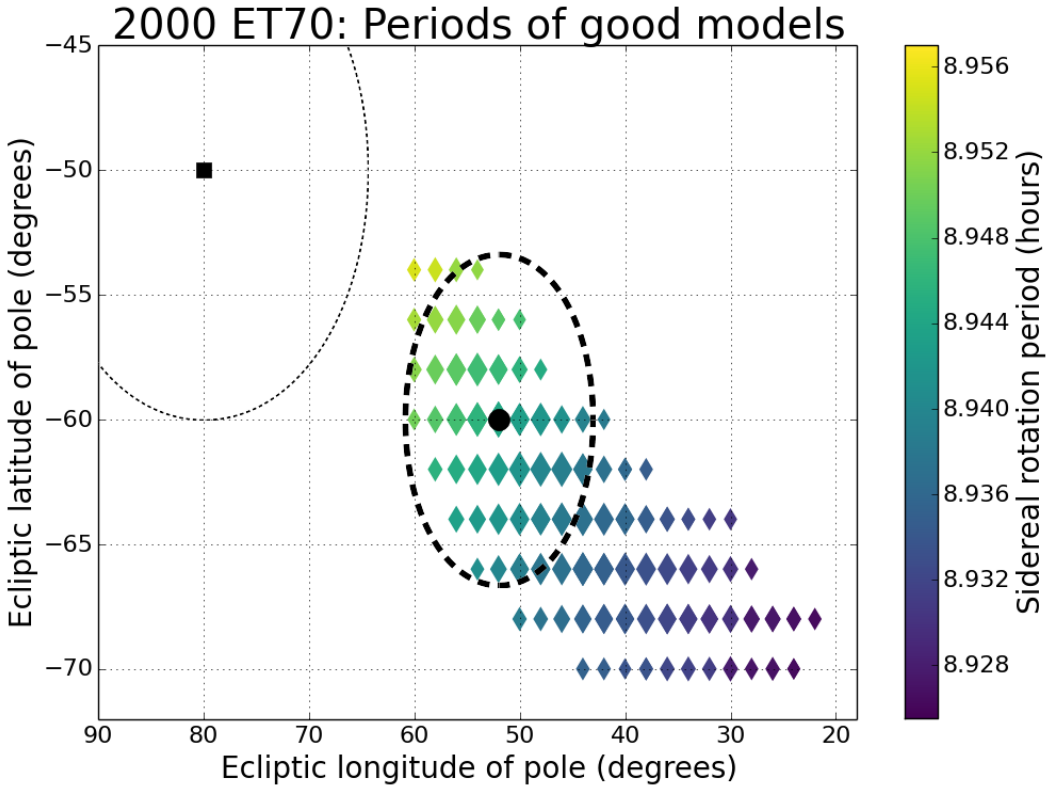

Figure 2.4: The "arc" of good shape models' pole positions. Note that different pole positions require slightly different sidereal rotation periods. The nominal pole solution (80°, −50°) of Naidu et al. (2013), from using only the radar data, is indicated with a black square. The thin dashed ellipse shows their 10° one-sigma uncertainty. This pole is ruled out by the lightcurves. The colored diamonds show models which are compatible at the one-sigma level with the radar and lightcurve data (but not necessarily with the infrared spectra). Larger markers correspond to better shape models (that is, models with lower values of chi-squared). Thermal modeling allows us to place additional constraints on the pole position, because some of the poles along the arc are ruled out by our infrared spectra (see Section 2.6). The points within the thick dashed ellipse are compatible at the one-sigma level with all available data (radar, lightcurve, and infrared). Pole positions on this ellipse are at the outer edges of acceptable thermal models. The black circle shows the pole solution (52°, −60°), which provides the best fits to the radar, lightcurve, and infrared data. Our preferred pole (52°, −60°) is 19° from the pole of Naidu et al., which is about double their stated one-sigma uncertainty.

along each axis vary with pole position (see Figure A.37 through Figure A.39).

Figure A.37 through Figure A.39 show that models with a greater extent along the principal x-axis tend to be longer along the y-axis and shorter along the z-axis. The uncertainties for those three lengths are correlated, which affects the uncertainties in derived parameters (e.g. Bevington and Robinson, 2003, equation 3.13). For the set of 72 good shape models which had pole positions that were compatible with thermal modeling results (that is, poles inside the thick dashed ellipse in Figure 2.4), covariances were calculated according to their definition, i.e.

$$\sigma_{xy} = \frac{1}{n-1} \sum_{i=1}^{n} (x_i - \overline{x})(y_i - \overline{y}) \tag{2.1}$$

(Hartlap et al., 2007, equation 3 and related discussion), and converted to correlation coefficients by

$$\rho_{xy} = \frac{\sigma_{xy}}{\sigma_x \sigma_y}. \tag{2.2}$$

The correlation coefficient between x and y is +0.9, the correlation between x and z is -0.9, and the correlation between y and z is -0.9. These correlations affect the derived uncertainties in ET70's surface area, volume, moment of inertia ratios, and mean diameter; see Table 2.4.

Our improved shape model's parameters and their uncertainties are given in Table 2.4. The reported uncertainties in the model's parameters are conservative estimates based on combining changes in chi-squared with visual inspection of the models. As in Magri et al. (2007, 2011) and Nolan et al. (2013), we ultimately

had to make subjective decisions about what could be considered a good model, based on which models did or did not reproduce the key features of the data. The preferred pole position is indicated in Figure 2.4. Principal axis views of the updated shape model are shown in Figure 2.5. The complete set of delay-Doppler frames and sums used in shape modeling are shown in Figure A.10 through Figure A.36.

Parameter		Naidu et al. (2013)		This work			
		Value	Unc.	Value	Uncertainties		Rel. unc.
Extents along principal axes *	x	2.61 km	5%	2.90 km	-0.24 km	+0.34 km	10%
	y	2.22 km	5%	2.24 km	-0.23 km	+0.36 km	13%
	z	2.04 km	5%	1.50 km	-0.29 km	+0.47 km	25%
Surface area *	A	16.7 km^2	10%	15.3 km^2	1.0 km^2		7%
Volume *	V	6.07 km^3	15%	4.82 km^3	0.50 km^3		10%
Moment of inertia ratios *	I_x/I_z	0.80	10%	0.53	0.11		20%
	I_y/I_z	0.96	10%	0.80	0.13		17%
Volumetric mean diameter *	D	2.26 km	5%	2.10 km	0.07 km		3%
DEEVE extents	$2a$	2.56 km	5%	2.88 km	0.29 km		10%
	$2b$	2.19 km	5%	2.18 km	0.29 km		13%
	$2c$	2.07 km	5%	1.47 km	0.37 km		25%
Radar albedo (2380 MHz, OC)	$\hat{\sigma}_{\mathrm{OC}}$	0.063	0.017	0.062	0.018		30%
Sidereal rotation period	P	8.96 h	0.01 h	8.9444 h	-0.0081 h	+0.0100 h	0.1%
Pole ecliptic longitude	λ	80°	10°	52°	9°		
Pole ecliptic latitude	β	−50°		−60°	6°		

Table 2.4: Parameters and one-sigma uncertainties for the shape model of ET70, utilizing radar, lightcurve, and infrared data. The ranges of values given here are those for which both shape models and thermal models provide good fits to the data. For many parameters, the uncertainties are asymmetric, so we include the values for both the negative and positive error bars. For instance, the model's extent along its principal x-axis has a best-fit value of 2.90 km, with a one-sigma range of 2.66 to 3.24 km. Length uncertainties have contributions from two sources: there is uncertainty in the best-fit length (along each axis) for a fixed pole position, and the best-fit lengths vary with pole position (see Figure A.37 through Figure A.39). Relative uncertainties come from the mean of the positive and negative uncertainties. The moment of inertia ratios were derived with the assumption that the model's density is homogeneous. The dynamically equivalent equal volume ellipsoid (DEEVE) is the uniform-density ellipsoid that has the same volume and moment of inertia ratios as the shape model.

* Our analysis showed that the uncertainties for the three lengths along the principal axes are correlated; see the text.

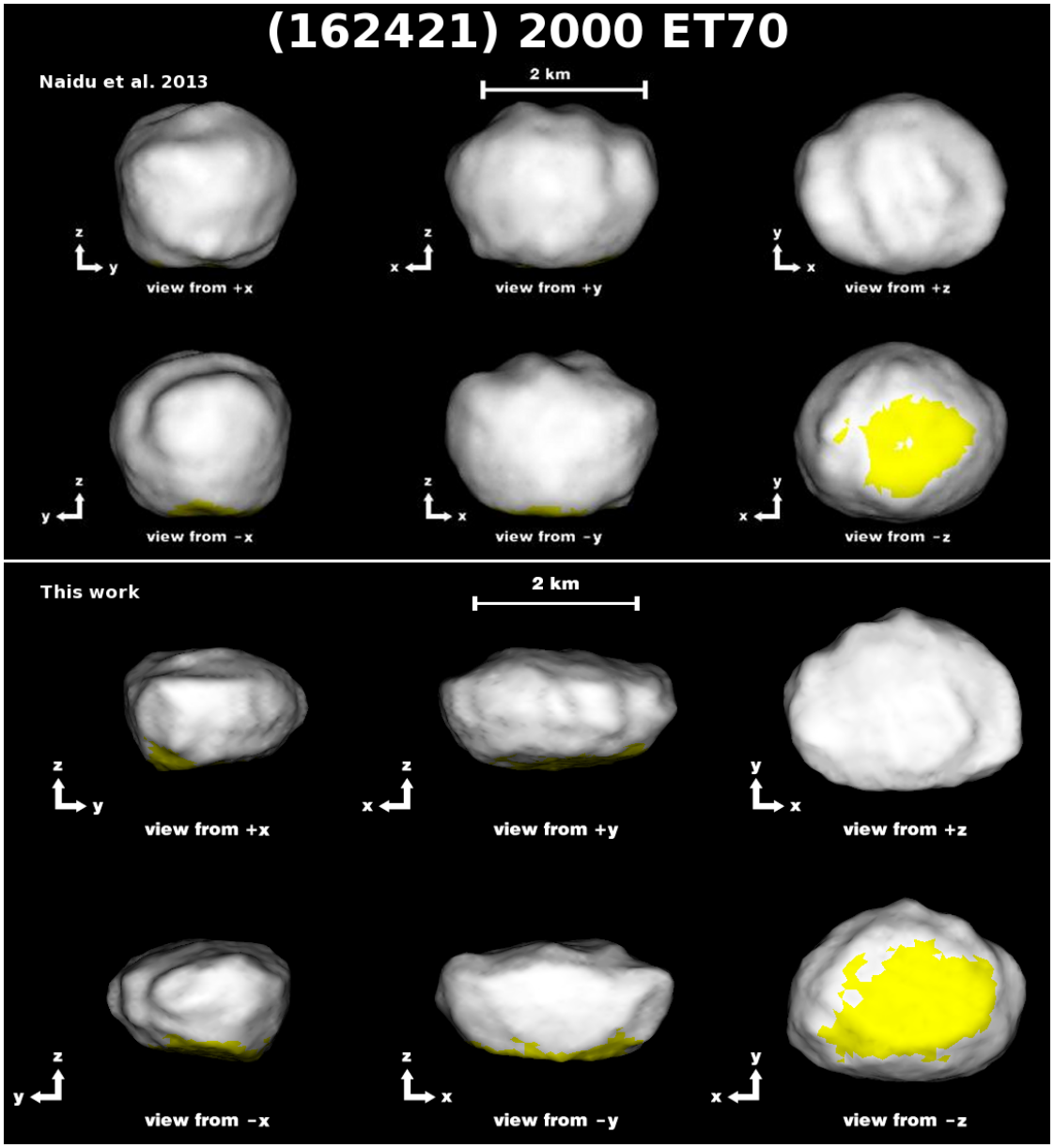

Figure 2.5: The top frame shows views of the shape model of Naidu et al. (2013) from along its three principal axes (their Figure 7). The bottom frame shows the corresponding views of the best shape model from this work. The model rotates about the z-axis, and its maximum diameter is 2.9 kilometers. The facets marked in yellow, near the south pole, were seen at incidence angles greater than sixty degrees in all delay-Doppler images (or not seen at all) and therefore are not well constrained.

2.5 Spectral observations

2.5.1 Infrared observations from IRTF

Infrared observations of an asteroid's thermal emission make it possible to determine the asteroid's albedo, surface roughness, and thermal inertia (e.g. Lebofsky et al., 1978; Harris and Lagerros, 2002). As part of our ongoing program to characterize near-Earth asteroids with both radar and infrared observations, we observed ET70 on three nights in February 2012 from NASA's InfraRed Telescope Facility (IRTF) on Mauna Kea, Hawai'i (see Table 2.5). All of our infrared observations used the SpeX instrument (Rayner et al., 2003) in two modes, PRISM and LXD, giving coverage from 0.8 to 4.1 microns.

Our observations were taken using the standard method of A-B pairs, where the telescope moved fifteen arcseconds along the slit between exposures, so that the target alternated between two positions within the slit. This allowed for a clean sky subtraction while still integrating on the asteroid. In addition to observing the asteroid, we observed solar-type comparison stars within five degrees of the target to match airmass as accurately as possible, as well as known solar analog stars (normally not as close to the target). We used the solar analog star's spectrum to modify the colors of the solar-type comparison star, in order to make the comparison star's spectrum closer to the solar spectrum. We processed our SpeX data using the Spextool software (Cushing et al., 2004), along with Bus's method of correcting for telluric water vapor in PRISM spectra (described in Rivkin et al., 2004) with some minor modifications. Similarly, we correct for telluric features in the LXD spectra as described by Volquardsen et al. (2007). Our procedures for infrared observation and data reduction are dis-

Date	UT times	Instrument mode	Exposure time (s)	Exposures	Standard stars	r (au)	Δ (au)	α
2012-02-11	14:13–14:53	LXD	15	72	SAO 65083, SAO 82194, SAO 83619, SAO 98710	1.008	0.071	71°
	15:00–15:06	PRISM	30	8				
2012-02-18	13:39–13:45	PRISM (A)	30	8	SAO 98710, SAO 120107	1.019	0.046	47°
	13:51–14:01	LXD (A)	15	18				
	14:05–14:29	LXD (B)	15	40				
	14:29–14:47	LXD (C)	15	32				
	14:54–15:00	PRISM (B)	30	8				
	15:11–15:33	LXD (D)	15	40				
2012-02-21	13:12–13:25	LXD (A)	15	24	SAO 98710, SAO 120107, SAO 180396	1.024	0.047	41°
	13:28–13:33	PRISM (A)	30	8				
	13:43–13:49	LXD (B)	15	12				

Table 2.5: Infrared observations of 2000 ET70 that were used in thermal modeling. All of these observations used the SpeX instrument on NASA's InfraRed Telescope Facility (IRTF). The two modes of observations, PRISM and LXD, cover different ranges of wavelengths. PRISM covers 0.8 to 2.5 microns, and LXD (cross-dispersed) covers 2.2 to 4.1 microns. The observations are grouped in terms of which sum each set of exposures went into, which is why there may be consecutive sets with the same mode. For instance, the LXD observations from 13:51 to 14:47 on February 18 were divided into three sums (called A, B, and C). r is the distance from the asteroid to the Sun; Δ is the distance from the asteroid to Earth; α is the solar phase angle. The model's orientations at the times of the LXD observations are shown in Figure 2.9.

cussed in further detail in Howell et al. (2017). Example spectra are shown in Section 2.6 (and also in Section A.1.4). Note that our infrared observations are obtained as relative reflectance as this is more robust to observing conditions than absolute photometry.

2.5.2 Spectral classification

Whiteley (2001) classified ET70 as an X-type asteroid in the Tholen (1984) taxonomy, based on ECAS photometry (0.3 to 1.0 microns, shown in Figure 2.6) that is flat or slightly red with respect to the Sun. The Tholen X-types are separated by albedo into the E, M, and P classes, and the low albedo that we find for ET70 (in Section 2.7) is only consistent with the P class.

ET70 was observed by two of the authors (Hicks and Lawrence) at the Palomar 5.1-meter telescope on February 2, 2012, using the Double Spectrograph (DBSP). The blue and red portions of the spectrum were measured simultaneously, giving coverage from 0.4 to 1.0 microns, and the two portions were scaled to match in the region of overlap.

Using more extended spectral coverage (0.4 to 2.5 microns), with the thermal contribution removed, we have classified ET70 as Xk, in the Bus-DeMeo system (DeMeo et al., 2009) (see Figure 2.6). Depending on whether we scale the spectra to the Palomar spectrum or to the photometry of Whiteley (2004), the relative reflectance in the near-infrared region can vary by about 8%. Measurements of the 0.8-2.5 micron region on the three different IRTF nights in February 2012 are consistent with each other to ±0.015.

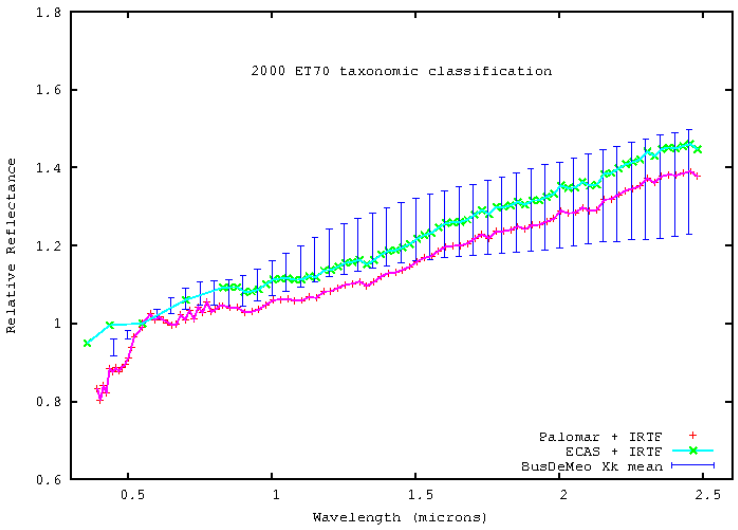

Figure 2.6: Reflectance spectrum of 2000 ET70, combined from Palomar DBSP and IRTF SpeX PRISM observations. For wavelengths of less than 1.0 micron, the green X's (connected by cyan lines) use the data points from the ECAS spectrum obtained by Whiteley (2004).

The photometry by Whiteley (2004) and the visible spectrum from Palomar diverge at short wavelengths, but they were obtained twelve years apart, and the relative orientation of the object is not known. The range of values for other Xk asteroids falls between the two. If the spectra are normalized (matched) at 1.0-1.5 microns, the visible spectra are more consistent with each other, outside of the value at 0.55 microns. We do not have any reason at this time to consider one or the other to be more reliable. Inhomogeneity in surface composition could result in both variable thermal properties and in variable spectral colors, and additional future observations could explore this possibility.

2.6 Thermal modeling

For our thermophysical modeling code, SHERMAN, we specify the asteroid's physical properties, including its size, shape, and rotation state, and fit for its optical scattering law, thermal inertia, and surface roughness; see Magri et al. (2017) and Howell et al. (2017) for more details. The model's infrared emissivity

is assumed to be 0.9, a typical value for silicate minerals (Brown et al., 1982; Spencer et al., 1989; Mueller, 2007).

The asteroid's shape is represented as a polyhedron with triangular facets (the output from SHAPE). Using the asteroid's actual shape instead of a sphere lets the modeling account for large-scale roughness, such as the ridges and valleys near the ET70 model's north pole. However, these valleys (the model's largest concavities) were mostly out of the sunlight during the times of our infrared observations, so they did not make a large contribution to the observed disk-integrated spectra.

For the thermal models of ET70 that had rough surfaces (parameterized with spherical-section craters), we used a crater opening angle of $\gamma = 150°$, similar to angles used for the 'default roughness' and 'high roughness' cases of Mueller (2007). We varied the crater fraction f_c but kept the opening angle fixed, because Lagerros (1998) and Emery et al. (1998) found that combinations of γ and f_c that equate to the same average roughness produce nearly indistinguishable model spectra. Because we used ET70's actual shape and explicitly allowed the model's sub-facet surface roughness to vary, we did not need to separately incorporate a beaming parameter (η), which has been used by many previous studies to incorporate effects of anisotropic scattering, non-spherical shape, thermal inertia, surface roughness, and other inhomogeneous surface properties (e.g. Lebofsky et al., 1986).

Optical scattering was represented with a Hapke law (Hapke, 1984). In order to reduce the dimensionality of the parameter space, we used two free parameters, visual albedo (p_V) and phase slope parameter (G). We converted p_V and G to Hapke parameters using the formulas from Verbiscer and Veverka (1995). A

lower value of G corresponds to a stronger opposition surge, but since all observations of ET70 were taken at phase angles greater than 40 degrees, the data do not constrain ET70's opposition surge. Testing showed that changing the value of G and the corresponding Hapke parameters did not significantly change the thermal modeling results, so we allowed the single-scattering albedo (w) to vary but kept the other Hapke parameters fixed at the values derived from $G = 0.17$, which is the average value for Xk-type asteroids (Warner et al., 2009).

2.6.1 Reflectance spectrum

Careful analysis of our infrared data allowed us to generate the asteroid's reflectance spectrum. At PRISM wavelengths (0.8 to 2.5 microns), most of the observed flux is from reflected sunlight, rather than thermal emission. However, the thermal contribution becomes significant (larger than the data's error bars) above wavelengths of about 2.2 microns. Therefore we had to remove the thermal component from the observed PRISM spectra in order to produce the reflectance spectrum that was used for SHERMAN. Our first estimate of the thermal contribution at the various PRISM wavelengths was based on the results from some early thermal models. However, this resulted in thermal models in which the model spectra consistently had higher values than what we observed at wavelengths near 2.4 microns, so further corrections were needed.

We assumed that the reflectance spectrum is flat above a certain wavelength. This cutoff wavelength was determined iteratively, by testing thermal models with different versions of the reflectance spectrum to see which cutoff wavelength would yield model PRISM spectra (with reflected and thermal contribu-

tions) that best matched the data. Other representations of the reflectance spectrum are possible – for instance, assuming a constant slope out to some point – but these would require additional parameters. Since less than 5% of the power in the solar spectrum comes from wavelengths above 2.2 microns, the details of the parameterization are not critical, so we opted for simplicity. We found that a cutoff wavelength of 2.25 microns is optimal. For comparison, the initial version of the reflectance spectrum had its cutoff at 2.48 microns. Different versions of the reflectance spectrum are shown in Figure A.40. Note that, once a good reflectance spectrum is used, the PRISM spectra are not very sensitive to changes in the thermal parameters, so most of the leverage for the thermal models comes from the LXD spectra.

2.6.2 Parameter search

For thermal modeling, our three primary free parameters were the models' values of Hapke single-scattering albedo (w), crater coverage fraction (f_c), and thermal inertia (Γ). One can consider chi-squared to be a function of the thermal parameters; thermal modeling is effectively a minimization of this function $\chi^2(w, f_c, \Gamma)$. Given that ET70's pole position was uncertain, we also had to vary the pole position. This effectively added two more dimensions to search: the longitude and latitude within that arc of allowed pole directions (see Figure 2.4). We ran thermal models for seven different pole positions. For each pole, we used the lengths and the sidereal rotation period that provided the best fit (from shape modeling) to that pole position. For one pole, we also tested thermal models for a shape with a greater length along its z-axis to see whether that would give better fits; it did not make a significant difference.

For each tested pole position, we typically ran several dozen thermal models, to find the optimal values of w, f_c, and Γ, along with their allowed ranges. Ultimately, thermal modeling provided useful constraints on ET70's pole direction, because some pole directions that are allowed by the radar and lightcurve data had no thermal models that gave an acceptable fit to our IRTF spectra (see Figure 2.7). The radar and lightcurve data allow for pole positions along an arc that is about 23° long; thermal modeling showed that only about 12° of that arc are compatible with the infrared spectra (see Figure 2.4).

The region of pole directions that is compatible with the thermal models is centered on a pole position of $(52°, -60°)$. The corresponding sidereal rotation period for that nominal pole is 8.944 hours. Assuming a surface with homogeneous properties, some of the best thermal models had a crater fraction of 0.0 – that is, no sub-facet surface roughness. This seems physically unlikely, although Naidu et al. (2013) noted that ET70's radar circular polarization ratio is lower than that of most NEAs, indicating a relatively smooth surface at scales of about 10 cm. However, this could be just a coincidence, because the roughness that affects thermal emission could be at spatial scales anywhere between the diurnal thermal skin depth (millimeters) and the size of the facets (tens of meters) (Lagerros, 1998; Mueller, 2007).

No single homogeneous thermal model could provide an acceptable fit to the infrared spectra from all three nights simultaneously; models that fit well for one night were poor for the other nights. For February 18, the situation broke down even further in that fits to data from earlier in the night (LXD sets A, B, and C) required models that were different from the models that fit data from later in the night (LXD set D).

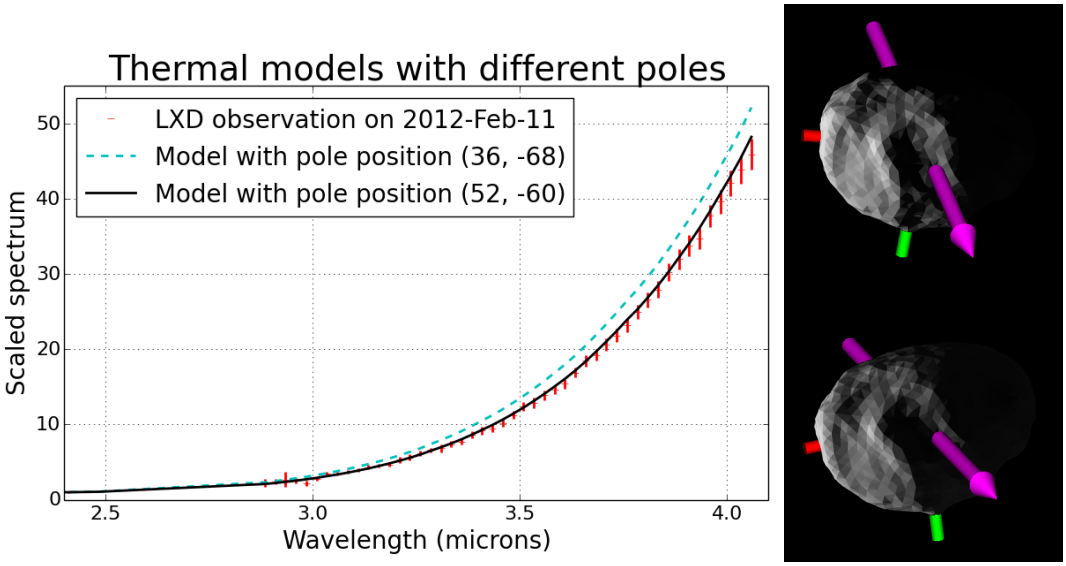

Figure 2.7: Thermal models of 2000 ET70 with different pole positions. Because the models' pole positions differ, the latitude of the subsolar point changes, and different facets near the north pole are in shadow. These changes affect the disk-integrated spectra seen by the observer. The data points and their uncertainties are plotted in red. The first model, plotted in cyan, has a pole position of (36°, −68°), a sidereal rotation period of 8.932 hours, a single-scattering albedo of 0.13, a crater coverage fraction of 10%, and a thermal inertia of 15 J m^{-2} K^{-1} $s^{-1/2}$. The second model, plotted in black, has the nominal pole position (52°, −60°), a sidereal rotation period of 8.944 hours, a Hapke single-scattering albedo of 0.10, a crater coverage fraction of 10%, and a thermal inertia of 65 J m^{-2} K^{-1} $s^{-1/2}$. Both pole positions are within the region shown in Figure 2.4 that is compatible with the radar and lightcurve data. The first model is the best thermal model (lowest overall chi-squared) for its pole position, but it yields a poor fit, and therefore its pole can be ruled out because of thermal modeling. The frames on the right show simulated plane-of-sky views of the two models (as seen from Earth), respectively, where each facet's brightness is proportional to its thermal emission. The magenta arrows are the models' rotation axes (their shortest principal axis). The red and green shafts are the long and intermediate principal axes, respectively. In the plane-of-sky views, north is upward and east is leftward.

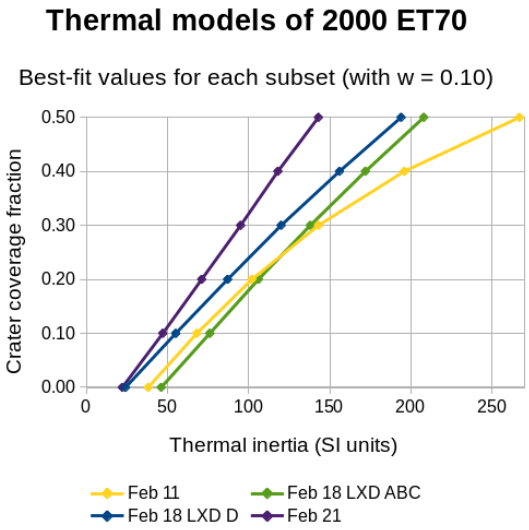

Figure 2.8: The best-fit values of crater fraction and thermal inertia for each subset of the data, for $w = 0.10$ and $G = 0.17$, with the pole at the nominal $(52°, -60°)$. Models whose parameters fall along a single subset's line are nearly indistinguishable for that particular subset, illustrating that a family of solutions exists for each thermal spectrum.

Focusing on four individual subsets of the infrared data (Feb-11, Feb-18 LXD ABC, Feb-18 LXD D, and Feb-21), we found that within a given subset there is a range of thermal parameters that fit the spectrum from that subset reasonably well, indicating that we do not have a single "best fit" in the classical sense but rather a family of solutions in each case. This is illustrated in Figure 2.8 for a single value of the single-scattering albedo w: once w is set, there are curves of crater fraction and thermal inertia that result in nearly indistinguishable model spectra for each subset. To either side of a curve, the chi-squared value falls off rapidly, indicating that the models along a given curve are well constrained, even if the particular choice of curve is not. However, the more important point is that the families of solutions do not all intersect at any one point, indicating that the thermal parameters are changing across the surface of the asteroid.

This is made clearer in Figure 2.9 through Figure 2.13. Figure 2.9 shows the plane-of-sky views of the asteroid shape model during each of the seven individual LXD infrared data sets. Although the subsolar latitude was within five degrees of the model's equator during all of our IRTF observations, the sub-

observer latitude decreased substantially. Initially, we viewed ET70 from the "top" near the northern pole on February 11, but as time progressed, the view changed until we saw primarily the equator by February 21. That difference in viewing geometry is reflected in the thermal models and IR spectra from each subset as shown in Figure 2.10 through Figure 2.13. The left panels in each figure show the range of thermal models for the given subset, illustrating that there is a family of curves in single-scattering albedo and thermal inertia for a given choice of crater fraction, i.e., as we eliminate the beaming parameter and use the actual shape and spin state to investigate the thermal emission, there are multiple solutions that are equally good. As time progresses from Figure 2.10 to Figure 2.13, the allowed family of curves shifts smoothly (downward and to the left) and grows smaller. This clearly demonstrates that the allowed models for the four subsets are not the same and that something is changing across the surface.

The right panels in Figure 2.10 through Figure 2.13 compare the measured thermal spectra for each subset to spectra from three models chosen to span the arcs of solutions. Moving from Figure 2.10 to Figure 2.13, the thermal model parameters that provide good fits to the spectra from one date do not fit well for other dates. This is evidence of a smooth variation in the surface parameters between the northern latitudes and more equatorial ones. Whether it is a change in albedo, thermal inertia, surface roughness, or some combination, we cannot specifically say, but we can quantify the levels of the variations that are needed through comparisons such as these.

For instance, a model with $w = 0.10$, $f_c = 0.2$, and $\Gamma = 70$ J m^{-2} K^{-1} s$^{-1/2}$ provided a good fit to the February 21 data, but its model LXD spectra (2.2 to 4.1 mi-

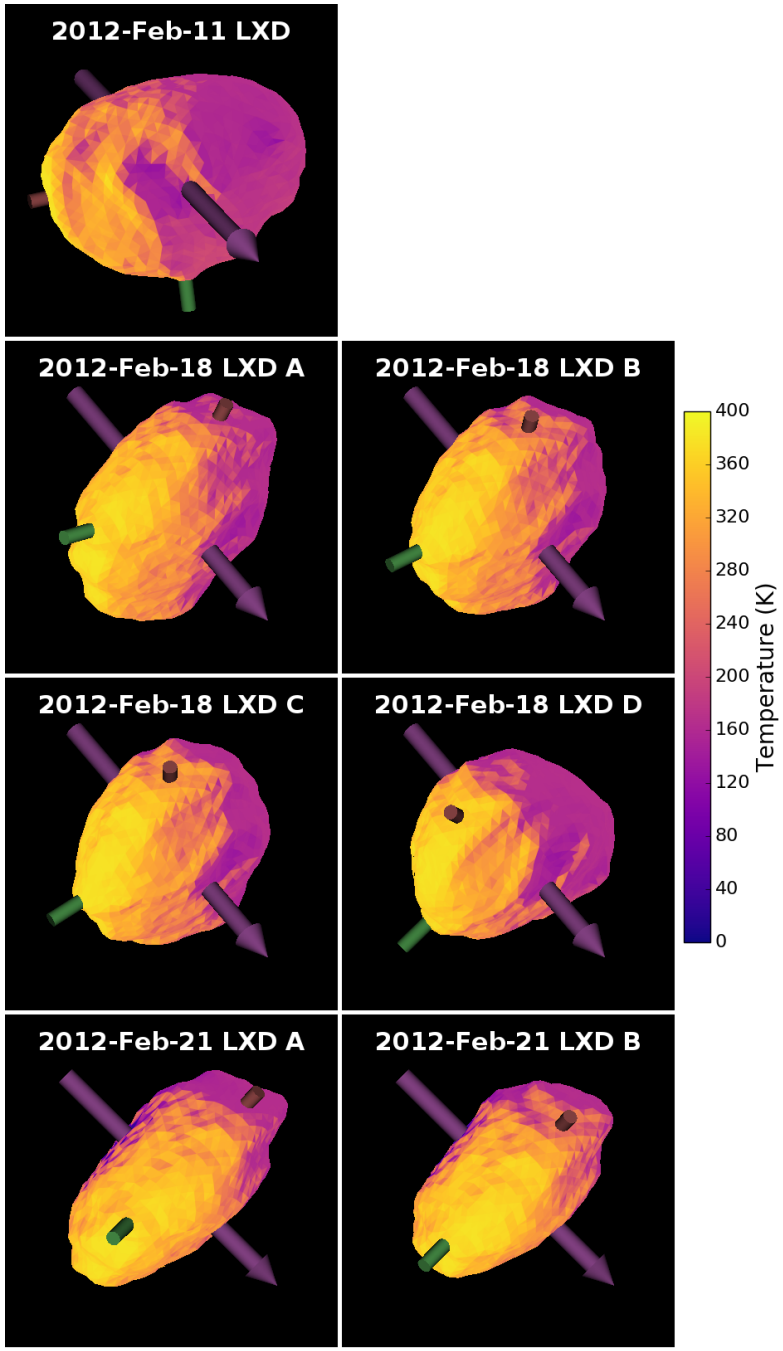

Figure 2.9: Plane-of-sky views (as seen from Earth) for the seven individual LXD time periods using the final shape model and spin state. North is upward and east is leftward. Colors indicate surface temperatures based on a thermal model with $w = 0.108$, $f_c = 0.2$, and $\Gamma = 70\ \mathrm{J\ m^{-2}\ K^{-1}\ s^{-1/2}}$, an arbitrary choice with parameter values that are in the middle of the allowed regions for all dates (see Figure 2.10 through Figure 2.13). Note that most of the observed thermal emission at any given time comes from a small region on the surface, so observations at different times are dominated by the thermal properties of that region.

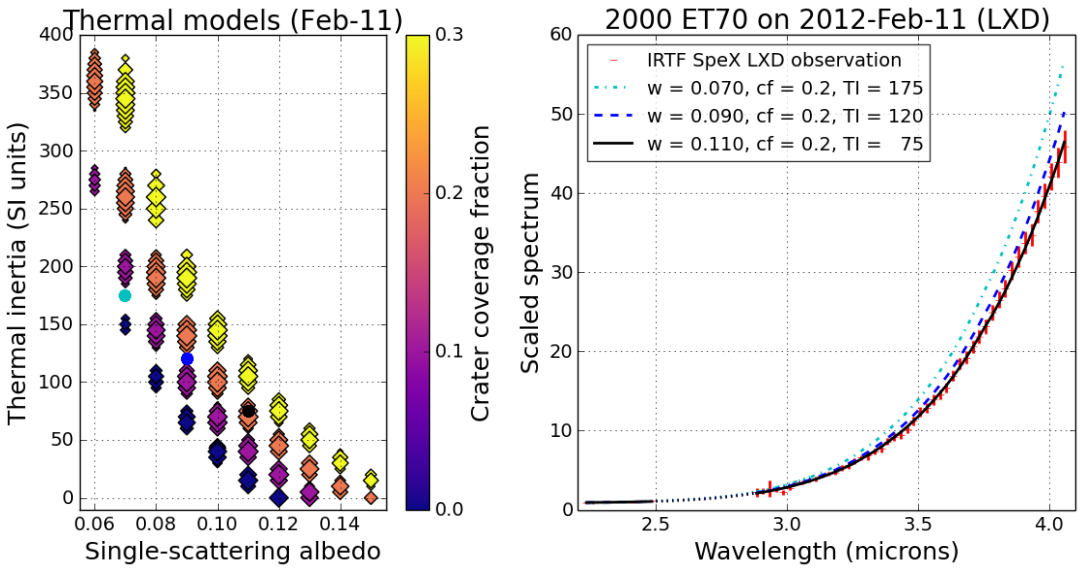

Figure 2.10: Thermal models of ET70 for February 11, 2012.
(Left) Illustration of the range of acceptable thermal models for this subset of data. Each point corresponds to a different model. The markers' colors indicate their values of crater coverage fraction. Larger markers correspond to better thermal models (i.e., those with lower chi-squared for the February 11 spectra). For a given crater fraction, there is a "curve" of models in which thermal inertia and albedo are traded off to be compatible with the infrared spectra. Note that models are only shown for crater fractions of 0.3 or less. Models with greater values of crater fraction may be compatible with certain subsets of spectra, but they are much worse overall. That is, for higher crater fractions, it takes a much wider range of other parameter values to match the observations. For similar reasons, these plots only show thermal inertia values up to 400 J m^{-2} K^{-1} $s^{-1/2}$ and single-scattering albedo values from 0.06 to 0.15. The three dots (cyan, blue, and black) correspond to the models plotted in the right frame.
(Right) Comparison of infrared observations to model LXD spectra. The model shown with the solid black curve fits well for Feb-11 and for Feb-18 LXD ABC, but not for Feb-18 LXD D or for Feb-21.

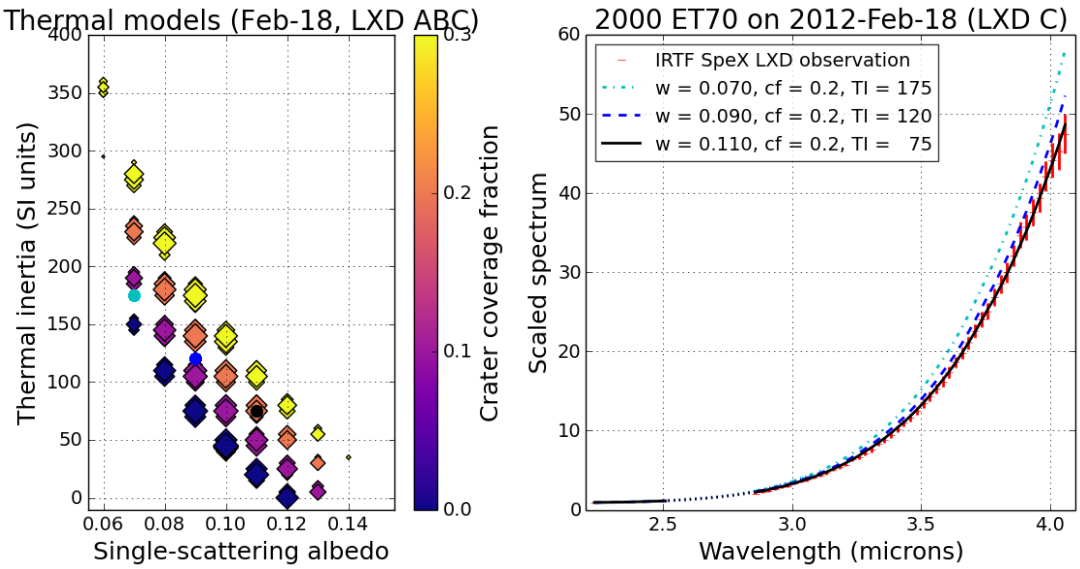

Figure 2.11: Same as Figure 2.10, but for the first three LXD observations from February 18, 2012. On the right, the model shown with the solid black curve fits well for Feb-11 and for Feb-18 LXD ABC, but not for Feb-18 LXD D or for Feb-21.

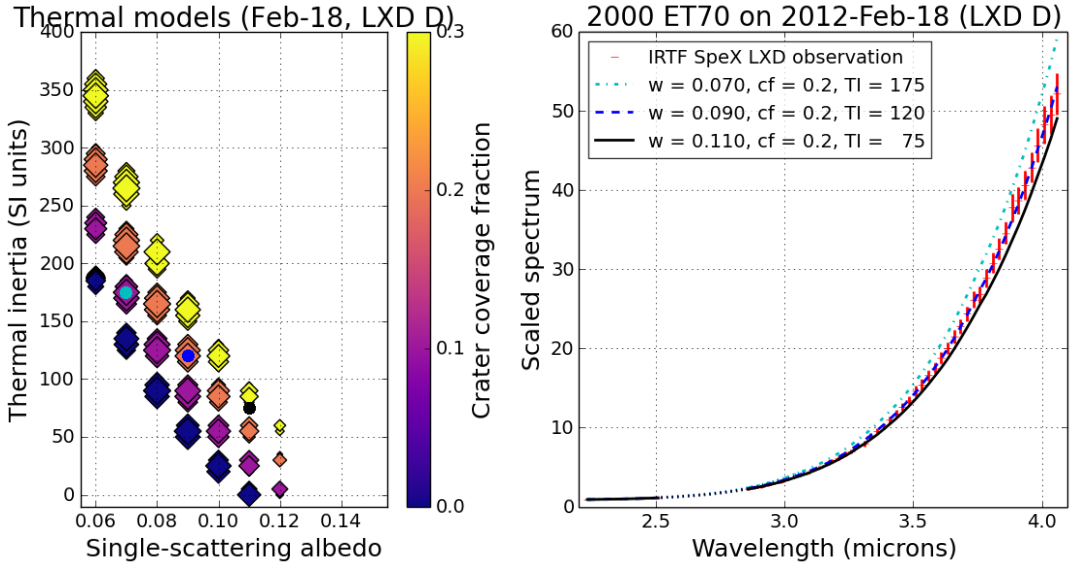

Figure 2.12: Same as Figure 2.10, but for the last LXD observation from February 18, 2012. On the right, the model shown with the dashed blue curve only fits well for Feb-18 LXD D.

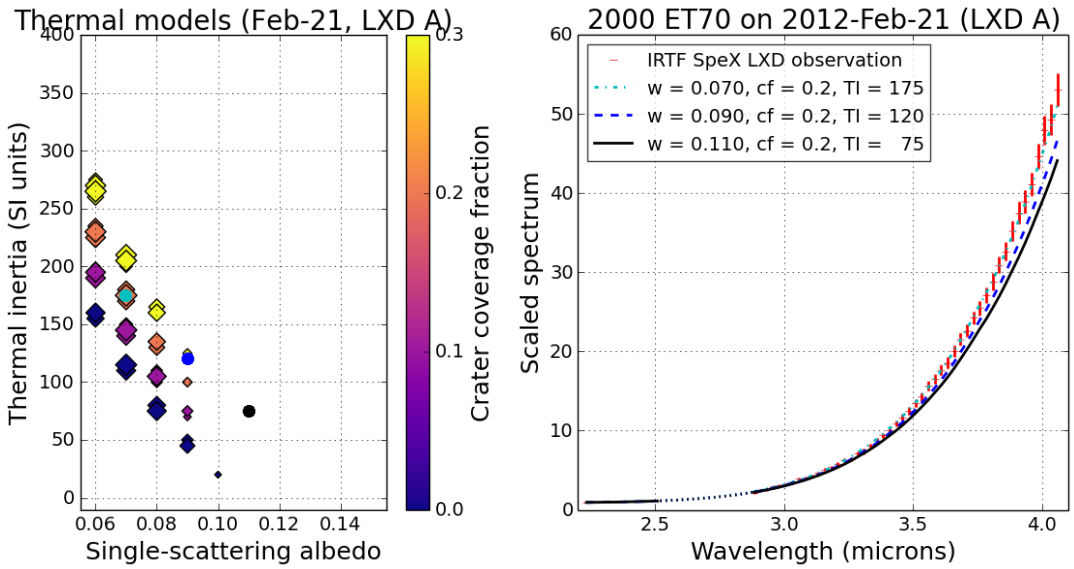

Figure 2.13: Same as Figure 2.10, but for the first LXD observation from February 21, 2012. On the right, the model shown with the dot-dashed cyan curve only fits well for Feb-21.

crons) were too hot (too bright at long wavelengths) for the other two nights. We examined the level of inhomogeneity that would be needed to match our observations by searching for the thermal parameters that would provide the best fits to each individual night's data. Based on allowing one parameter to vary while keeping the others fixed, we found that the first two nights' LXD spectra could be fit by decreasing the crater fraction from 0.2 to 0.1, or by increasing the thermal inertia from 70 to 100 J m^{-2} K^{-1} s$^{-1/2}$, as illustrated in Figure 2.8. The first two nights' LXD spectra could also be fit by increasing w from 0.100 to 0.112.

The thermal model shown in Figure 2.9 (w = 0.108, f_c = 0.2, and Γ = 70 J m^{-2} K^{-1} s$^{-1/2}$) is slightly too hot at some observation times and too cold (too faint at long wavelengths) at other times. Specifically, the first three model LXD spectra for February 18 are slightly too hot, and the model LXD spectra for February 21 are too cold. In order to get good fits to the spectra from

each night, the model's single-scattering albedo must be allowed to vary from 0.100 to 0.112. Figure A.41 through Figure A.51 show spectra of three models with $f_c = 0.2$ and $\Gamma = 70$ J m^{-2} K^{-1} s$^{-1/2}$ that span that range of w.

2.6.3 Comparisons with NEATM

To determine whether simpler thermal models could provide an acceptable fit to our IRTF spectra, we compared our shape-based thermophysical models to thermal models using a sphere with negligible thermal inertia. We used a model that is similar to the widely used near-Earth asteroid thermal model (NEATM) described by Harris (1998), in which the albedo and beaming parameter are varied to match the observations. Howell et al. (2017) describe our NEATM-like modeling program in more detail.

A limitation of this simpler model is that the input reflectance curve cannot be as easily specified as it can for SHERMAN. An object with a strongly red-sloped reflectance spectrum like ET70 is thus more difficult to fit with a model that assumes a flatter input curve. To compare with the NEATM-like model spectra, we chose to normalize the spectra at 1.6 microns where the thermal contribution is negligible. The best-fit model was chosen based on the chi-squared value of the observed-model relative reflectance values in the 0.8-4.05 micron spectral region, but weighted more heavily towards the 3-4 micron region where the thermal contribution is greatest.

We ran over two thousand models covering a wide range of geometric albedo and beaming parameter values. Similar to our results using the more complicated thermophysical models with the ET70 shape, we found that no sin-

Spectrum	α	Assumed $\eta(\alpha)$	Best-fit albedo
Feb-11 LXD	71°	1.58	0.070
Feb-18 LXD B	47°	1.34	0.070
Feb-18 LXD D	47°	1.34	0.060
Feb-21 LXD A	41°	1.28	0.065

Table 2.6: Best-fit albedo values for NEATM-like models with beaming parameters fixed at the values expected from the phase relation of Trilling et al. (2016). Although these models are the best fits for their specific values of the beaming parameter, some of the fits are quite poor. For instance, the Feb-11 LXD model is 3σ below the data (too cold) at 3 microns and 2.5σ above the data (too hot) at 4 microns. Smaller values of the beaming parameter would give better fits for the earlier dates.

gle set of NEATM parameters could provide an adequate fit to the IRTF spectra from all three nights. Furthermore, the LXD spectra from February 18 differ by enough that no single set of model parameters can fit all LXD spectra from that night. We note that although similar results are found here, the advantage of using our more detailed model over these NEATM-like models is that by explicitly taking the shape and illumination into account, the resulting thermal parameters are more physically based and the relationships among the parameters can be meaningfully explored (see Figure 2.10 through Figure 2.13).

For NEATM-like thermal models, the best-fit beaming parameter (η) tends to increase as phase angle (α) increases. For instance, Trilling et al. (2016) found a relation $\eta = 0.87 + (0.01\ \mathrm{deg}^{-1})\alpha$. Using assumed beaming parameters from that relation for each night's thermal models, we found that no single albedo value could fit all of the IRTF observations. The albedo would have to vary from 0.060 to 0.070, as shown in Table 2.6.

2.7 Conclusions

We present an improved shape model and spin state for (162421) 2000 ET70 compared to that of Naidu et al. (2013). Using both radar and lightcurve data, we found that the period-pole degeneracy allows for a sidereal rotation period of $8.944^{+0.013}_{-0.018}$ hours and a twenty-three degree long arc of pole positions (Figure 2.4), a range that already excludes the pole of Naidu et al., which was based solely on radar data. Using our infrared observations, we limited the arc further to an angular length of about twelve degrees, and we determined a best-fit pole at $(52^\circ, -60^\circ) \pm 6^\circ$ with a rotation period of $8.9444^{+0.0100}_{-0.0081}$ hours. There will be opportunities to obtain photometry of ET70 in March of 2023 (expected $m_V \approx 18$) and in February of 2024 ($m_V \approx 17$), and additional observations could provide tighter constraints in the future. However, the next time that ET70 comes within 0.1 au of Earth will be in 2047, so no additional high-SNR radar observations of ET70 will be possible until then.

After extensive thermal modeling using our improved shape model and spin state, we found that our three nights of infrared observations could not be fit with a single homogeneous model. Instead, different thermal models were required for four different subsets of the data, and for any given subset there is a family of models, all of which points to variations in the thermal parameters across the surface of ET70. Similarly, Crowell et al. (2016) observed 1627 Ivar from the IRTF on multiple nights and found that no single set of thermal parameters could fit all of the observations; Ivar's surface properties also seem to be heterogeneous.

The ET70 data are not sufficient to allow a detailed determination of the

thermal parameter values, but they do constrain the levels of inhomogeneity and suggest that it changes smoothly from northern latitudes down to equatorial latitudes. The later LXD spectra require thermal models whose parameters make the visible regions hotter, either with lower albedo, lower thermal inertia, greater roughness, or some combination.

The thermal models favor a surface that is smooth at sub-facet scales (i.e., lower values of crater fraction). Naidu et al. (2013) noted that ET70's relatively low radar circular polarization ratio, $\mu_C = 0.21 \pm 0.02$, implies a surface that is smoother than most NEAs at 10 cm scales. ET70's circular polarization ratio is less than the Benner et al. (2008) mean of 0.34 for all NEAs and consistent with the mean of 0.19 for P- and D-type asteroids. Based on the results from the thermal models, ET70's crater coverage fraction is probably less than 0.4 (assuming an opening angle $\gamma = 150°$). This means that ET70's RMS slope ρ is likely less than about 0.6 (which gives $\theta_{rms} = \arctan\rho \lesssim 30°$). Both the radar observations and the infrared spectra suggest that ET70 has a fairly smooth surface, but those two types of observations are not necessarily probing the surface roughness at the same spatial scales.

Only small variations in the thermal properties are needed to match the spectra in each infrared spectral subset: a change of about 0.01 in albedo, a difference of about 0.1 in crater coverage fraction, or a change in the thermal inertia on the level of 50 J m^{-2} K^{-1} $s^{-1/2}$. Such variations are physically reasonable; for example, the albedo variations needed for ET70 are similar to the relative contrasts of ~6% seen by NEAR on C-type asteroid 253 Mathilde (Clark et al., 1999). Models at the lower end of our possible albedos (Figure 2.10 through Figure 2.13) allow for a thermal inertia that is compatible with the Delbó et al. (2007) average for

kilometer-sized near-Earth asteroids, 200 ± 40 J m^{-2} K^{-1} s$^{-1/2}$. However, there are also possible models with considerably lower thermal inertias – perhaps closer to the Capria et al. (2014) average thermal inertia of Vesta, 30 ± 10 J m^{-2} K^{-1} s$^{-1/2}$.

Based on ET70's size and its absolute magnitude, Naidu et al. (2013) noted that ET70 must have either a very low albedo or a strange phase function. However, the previously reported values for ET70's absolute visual magnitude were extrapolated from high phase angles or had large uncertainties. For ET70, the Minor Planet Center assumes a phase slope of $G = 0.15$ and gives an absolute visual magnitude of $H_V = 18.0$ (Spahr et al., 2014). However, that absolute magnitude is based on observations that were all taken at phase angles of over 40 degrees, with large uncertainties in the observed magnitudes. Using $H_V = 18.0$ with our value $D = 2.10$ km (from shape modeling), the standard relation $D\sqrt{p_V} = K \times 10^{-H_V/5}$, where $K = 1329$ km (Pravec and Harris, 2007), yields a geometric albedo of $p_V = 0.025$, which is not consistent with the thermal models. With $G = 0.17$, $p_V = 0.025$ corresponds to $w = 0.03$ (Verbiscer and Veverka, 1995).

We do not have absolute photometry that can provide an independent estimate of ET70's absolute magnitude, but we can calculate its absolute magnitude from our values of the radar-derived size and the thermal model's albedo. A conservative estimate of the allowed range for the thermal models' single-scattering albedo is 0.06 to 0.15. With $G = 0.17$, that range of single-scattering albedo converts to geometric albedo $p_V \approx 0.09 \pm 0.04$ (Verbiscer and Veverka, 1995). Taking $D = 2.10 \pm 0.07$ km and $p_V = 0.09 \pm 0.04$, ET70's absolute magnitude is $H_V = 16.6 \pm 0.5$, with the uncertainty in ET70's albedo having the greatest contribution to the uncertainty in H_V.

$H_V \approx 16.6$, combined with the Minor Planet Center's tabulated magnitudes, would imply a fairly strong opposition effect, with a phase slope $G \lesssim 0$. However, given that the MPC magnitudes have large uncertainties, and that our thermal models are not very sensitive to the value of G, the available data are not sufficient to determine G.

Our results imply that even small NEAs are complex geologic objects with inhomogeneous surface properties. The thermal parameters derived from observations on a single night may depend more on the local surface properties than generally assumed, and thus may not be representative of the asteroid surface as a whole. Although we cannot uniquely determine the thermal parameters for ET70 from our dataset as the number of observations is too sparse, by using a realistic representation of the shape and the actual spin state, we have been able to investigate the surface of ET70 in terms of physically meaningful thermal parameters. This approach opens the door to treating NEAs as truly physical objects, complete with variations in surface thermal parameters that we can constrain and explore from ground-based observations at multiple viewing geometries.

2.8 Acknowledgments

This project was partially supported by NASA grants NNX10AP87G, NNX12AF24G, and NNX13AQ46G; and by NSF grant AST-1109855. The first author was supported by a NASA Earth and Space Science Fellowship (NASA grant NNX15AR14H). Several co-authors were Visiting Astronomers at the InfraRed Telescope Facility, which is operated by the University of Hawaii under

contract NNH14CK55B with the National Aeronautics and Space Administration. The authors thank the staff members at Arecibo Observatory, at the InfraRed Telescope Facility, and at Palomar Observatory for assistance with the observations. The Arecibo Observatory is operated by SRI International in partnership with Ana G. Méndez – Universidad Metropolitana and the Universities Space Research Association, under a cooperative agreement with the National Science Foundation (AST-1100968). The Arecibo Planetary Radar program is supported by NASA's Near Earth Object Observation program. Part of this research was conducted at the Jet Propulsion Laboratory, California Institute of Technology, under contract with the National Aeronautics and Space Administration (NASA). The material presented represents work supported by NASA under the Science Mission Directorate Research and Analysis Programs. The authors also thank the two reviewers for their constructive feedback. Taxonomic type results presented in this work were determined using a Bus-DeMeo Taxonomy Classification Web tool by Stephen M. Slivan, developed at MIT with the support of National Science Foundation Grant 0506716 and NASA Grant NAG5-12355. This research has made use of NASA's Astrophysics Data System Bibliographic Services. The authors gratefully acknowledge the teams that produce the following free software packages, which were used for this work: Gnuplot[1], ImageMagick[2], Kile[3], LibreOffice[4], Perl[5], Python[6], IPython (Pérez and Granger, 2007), Matplotlib (Hunter, 2007), NumPy (van der Walt et al., 2011), Pillow[7], and SciPy[8].

[1] http://www.gnuplot.info/
[2] https://imagemagick.org/
[3] http://kile.sourceforge.net/
[4] https://www.libreoffice.org/
[5] https://www.perl.org/
[6] https://www.python.org/
[7] https://python-pillow.org/
[8] http://www.scipy.org/

2.9 Supplementary material

Supplementary figures associated with this article can be found in Section A.1.

CHAPTER 3

SHAPE MODELING OF CONTACT BINARY NEAR-EARTH ASTEROID (85989) 1999 JD6 FROM RADAR AND LIGHTCURVE DATA

The contents of this chapter soon will be submitted to *Icarus* as: S. E. Marshall, Brozović, L. A. M. Benner, E. S. Howell, D. B. Campbell, R. J. Vervack, C. Magri, J. L. Crowell, Y. R. Fernández, P. A. Taylor, M. C. Nolan, M. W. Busch, S. P. Naidu, J. D. Giorgini, J. S. Jao, C. G. Lee, J. E. Richardson, L. A. Rodriguez-Ford, F. D. Ghigo, A. R. Kobelski, P. Pravec, B. N. L. Sharkey, M. D. Hicks, B. Bozek, A. Aznar, B.-O. Demory, and R. Behrend. Shape modeling of contact binary near-Earth asteroid (85989) 1999 JD6 from radar and lightcurve data.

3.1 Abstract

We (Marshall et al., 2018) observed potentially hazardous near-Earth asteroid (85989) 1999 JD6 during its 2015 close approach with the Goldstone Solar System Radar and with Arecibo Observatory's planetary radar system, on eleven days between July 15 and August 4. By combining the 2015 radar images and spectra with Arecibo observations from 2010 and with lightcurves from six different apparitions, we were able to determine JD6's size, shape, and rotation state. JD6 is a contact binary, with two connected lobes, such that its shape resembles a peanut. JD6's dimensions are $3.0 \times 1.2 \times 1.0$ km. Due to fortuitous observing geometry during some of the Goldstone observations, when the lines of sight happened to pass within two degrees of JD6's rotation axis, we are able to find its pole position very accurately: $(\lambda, \beta) = (220.3°, -73.43°)$, with an uncertainty of just 0.25°. This pole position is the most accurately known for any asteroid for which there are only Earth-based observations. We are able to link the rotation

phases from all of the lightcurves, from 1999 through 2015, with no ambiguity. We find that JD6's sidereal rotation period is 7.6643464 ± 0.0000056 h.

3.2 Introduction to 1999 JD6

Near-Earth asteroid (85989) 1999 JD6 was discovered on May 12, 1999, by the Lowell Observatory Near-Earth Object Survey (LONEOS) (Williams, 1999). It is an Aten group asteroid with an orbital semi-major axis of 0.883 au, an eccentricity of 0.633, and an inclination of 17.1 degrees[1]. 1999 JD6 (hereafter JD6) has a minimum orbit intersection distance (MOID) with respect to Earth of 0.0478 au, and its absolute magnitude is $H = 17.1$, so it is a potentially hazardous asteroid (PHA). JD6 also can come close to other inner planets, having MOID values with respect to Mercury and Venus of 0.064 au and 0.010 au, respectively[2].

There have been many observations of JD6 since its discovery, yielding a rich data set that has allowed us to place strong constraints on JD6's shape and rotation state. Lightcurve observations of JD6 have been obtained during six apparitions: 1999, 2000, 2004, 2005, 2014, and 2015. JD6 was observed by radar in 2010 and in 2015.

JD6 also has been observed at infrared wavelengths by NASA's Spitzer Space Telescope and Wide-field Infrared Survey Explorer (WISE). Thermal modeling based on those observations of JD6 has led to differing estimates of its size; see Table 3.1. A possible explanation for these discrepancies is that the different observations happened to see it at different rotation phases. Indeed, the NE-

[1] ssd.jpl.nasa.gov/sbdb.cgi?sstr=85989;orb=0;cov=0;log=0;cad=1

[2] http://minorplanetcenter.net/db_search/show_object?utf8=%E2%9C%93&object_id=85989

OWISE team, noting JD6's large infrared lightcurve amplitude, flagged it as a potential binary or contact binary (A. Mainzer, personal communication).

3.3 Observations

3.3.1 Lightcurve observations

Several authors have previously published lightcurves and derived rotation periods for JD6 (Warner et al., 2011); see Table 3.2. Szabó et al. (2001) and Polishook and Brosch (2008), noting JD6's large lightcurve amplitude, suggested that it must be very elongated, likely more than twice as long along its *a* (long) axis as its *b* (intermediate) axis. Given that the JD6 lightcurves have peak-to-peak amplitudes of 1.0 mag or more (see Figure 3.1), it can only realistically have two brightness maxima per rotation period. As discussed in Harris et al. (2014), harmonics with more than two brightness maxima per rotation period would have amplitudes of less than about 0.4 mag (at low phase angles), since no plausible shape that can yield more than two extrema per rotation has a projected area that varies enough to yield larger amplitudes.

We have incorporated all of the previously published lightcurves into our analysis (see Table 3.3 through Table 3.5). We also present lightcurves of JD6 that had not previously been published: from Ondřejov Observatory in 1999, from Table Mountain Observatory in 2000, and from Couvaloup de St-Cergue in 2005.

Spacecraft	Instrument or bands	Observation date(s) †	Estimated diameter	Reference
Spitzer	IRS	June 4, 2008	1.82 km	Campins et al. (2009)
Spitzer	IRAC	August 31, 2009	2.39 km	Trilling et al. (2010)
WISE	W2, W3, W4	2010	1.462 ± 0.021 km	Mainzer et al. (2011)
WISE	W1, W2, W3, W4	April 24 to July 29, 2010	1.839 ± 0.024 km	Mainzer et al. (2014)
WISE	W1, W2, W3, W4	April 24 to July 29, 2010	1.610 ± 0.030 km	Mainzer et al. (2014)

Table 3.1: Previously published estimates of JD6's size, based on infrared observations and thermal modeling.
†Mainzer et al. (2011) did not specify the dates of the individual observations that were used. Mainzer et al. (2014) observed JD6 with WISE a total of 25 times in 2010, during the fully cryogenic phase of the mission: twenty times on April 24 through April 26, once on May 6, and four times on July 29. For some of those observations, JD6 was only detected in two or three of WISE's four bands.

Apparition(s)	Rotation period (h)		Amplitude (mag)		Reference
	Value	Uncertainty	Value	Uncertainty	
2000	7.68	0.03	1.2	0.1	Szabó et al. (2001)
2004, 2005	7.6638	0.0001	1.16	0.05	Polishook and Brosch (2008)
2014	7.667	0.006			Warner (2014)
2015	7.673	0.002	1.13		Warner (2015)
2015	7.65	0.01	0.609		Aznar Macías et al. (2016)

Table 3.2: Previously published rotation periods for JD6, based on lightcurve observations.

Some of the lightcurves were absolutely calibrated. However, for shape modeling, we treated all of them as relative photometry. Kaasalainen and Torppa (2001) noted that doing so generally leads to a cleaner separation of the model's photometric properties from its shape and rotation state.

Note that the periods observed in lightcurves (Table 3.2) include contributions from JD6's motion across the sky. This leads to uncertainty in the rotation period as the direction of JD6's rotation vector was unknown, and this combines with the apparent rotation due to JD6's motion across the sky. With the radar data, we are able to put much more stringent constraints on JD6's rotation state.

3.3.2 Radar observations

JD6 was observed with the 305-meter William E. Gordon Telescope at Arecibo Observatory (S-band radar; 2380 MHz) on three nights in July of 2010, when it was 0.139 au from Earth. During those observations, JD6 was relatively far from Earth (compared to its later close approach), and the main Arecibo Observatory power generator was unavailable. Therefore the radar transmitter had to be run at reduced power, and JD6 was detected in one-dimensional CW spectra but not in two-dimensional delay-Doppler images.

In 2015, JD6 made its closest approach to Earth since its discovery, with a minimum distance of 0.048 au (19 times the Earth-Moon distance) on July 25. During the 2015 apparition, JD6 was observed on six days with Arecibo and on five days with the 70-meter DSS-14 antenna at NASA's Goldstone Deep Space Communications Complex (X-band radar; 8560 MHz). When JD6 was closest to Earth, it was too far north to be observable with Arecibo, because Arecibo can

UT date	UT times	Band*	Data pts.	$\Delta\phi$	r (au)	Δ (au)	α	Observatory	MPC code	Ref†
May 21-22, 1999	23:35–01:18	R	22	81°	1.289	0.426	42°	Ondřejov	557	
May 23-24, 1999	20:33–01:43	R	71	243°	1.299	0.434	41°	Ondřejov	557	
May 24, 1999	20:59–23:07	R	25	101°	1.304	0.438	41°	Ondřejov	557	
June 12-13, 1999	21:54–00:45	R	22	134°	1.384	0.557	39°	Ondřejov	557	
July 2, 2000	21:19–23:56		58	123°	1.337	0.378	28°	Calar Alto	G36	S01
July 5-6, 2000	20:51–02:02		73	243°	1.323	0.371	29°	Calar Alto	G36	S01
July 6, 2000	08:46–10:29	R	13	81°	1.321	0.370	30°	Table Mountain	673	
July 7, 2000	09:02–09:36	R	4	27°	1.316	0.368	31°	Table Mountain	673	
July 9, 2000	06:40–10:07	R	8	162°	1.307	0.365	32°	Table Mountain	673	
July 10, 2000	04:53–09:52	R	13	234°	1.302	0.364	33°	Table Mountain	673	
April 30-	23:35–02:02	B	3	115°	1.221	0.452	52°	Wise	097	P08
May 1, 2004	01:54–01:58	V	2	4°				Observatory		
	22:34–01:49	B	11	153°				Wise		
May 14-15, 2004	22:31–01:53	V	19	158°	1.303	0.448	41°	Observatory	097	P08
	22:40–01:56	R	8	153°						

Table 3.3: Lightcurve observations used in this work (part one; continued in Table 3.4).
* The photometric band (Johnson B, Johnson V, or Cousins R) is only specified for lightcurves which are absolutely calibrated.
The fourth column lists the numbers of data points in each lightcurve.
$\Delta\phi$ is the range of asteroid rotation phases covered by that night's lightcurves, assuming the best-fit sidereal rotation period of 7.664 hours. A value of 360° would indicate that the lightcurve encompassed one full rotation of JD6.
r is the distance from the asteroid to the Sun; Δ is the distance from the asteroid to the Earth; α is the solar phase angle.
† The last column indicates the reference for lightcurves which were previously published: S01 is Szabó et al. (2001), and P08 is Polishook and Brosch (2008).

UT date	UT times	Band*	Data pts.	$\Delta\phi$	r (au)	Δ (au)	α	Observatory	MPC code	Ref†
May 15-16, 2004	22:23–01:45	B	11	158°	1.308	0.449	41°	Wise Observatory	097	P08
	22:16–01:55	V	23	171°						
	22:46–01:51	R	6	145°						
May 16-17, 2004	22:12–01:33	B	12	157°	1.313	0.450	40°	Wise Observatory	097	P08
	22:09–01:45	V	21	169°						
	23:52–01:41	R	6	86°						
May 22-23, 2004	22:21–01:40	B	23	156°	1.341	0.459	37°	Wise Observatory	097	P08
	22:19–01:51	V	49	166°						
	22:26–01:45	R	24	156°						
May 27, 2004	20:30–23:10	B	24	125°	1.361	0.472	35°	Wise Observatory	097	P08
	20:23–23:21	V	42	139°						
June 12-13, 2005	20:02–01:31	B	17	257°	1.381	0.486	34°	Wise Observatory	097	P08
	19:45–01:34	V	28	273°						
	20:09–01:38	R	14	257°						
July 8-9, 2005	18:28–01:39	B	31	337°	1.261	0.293	30°	Wise Observatory	097	P08
	18:25–01:42	V	64	342°						
	18:33–01:44	R	33	338°						

Table 3.4: Lightcurve observations used in this work (part two; continued from Table 3.3).
* The photometric band (Johnson B, Johnson V, or Cousins R) is only specified for lightcurves which are absolutely calibrated.
The fourth column lists the numbers of data points in each lightcurve.
$\Delta\phi$ is the range of asteroid rotation phases covered by that night's lightcurves, assuming the best-fit sidereal rotation period of 7.664 hours. A value of 360° would indicate that the lightcurve encompassed one full rotation of JD6.
r is the distance from the asteroid to the Sun; Δ is the distance from the asteroid to the Earth; α is the solar phase angle.
† The last column indicates the reference for lightcurves which were previously published: P08 is Polishook and Brosch (2008).

UT date	UT times	Band*	Data pts.	$\Delta\phi$	r (au)	Δ (au)	α	Observatory	MPC code	Ref†
July 9, 2005	22:35–23:54	B	10	62°	1.255	0.289	31°	Wise Observatory	097	P08
	22:32–23:51	V	10	62°						
	22:48–23:57	R	9	54°						
July 14, 2005	22:22–22:59		27	30°	1.223	0.272	36°	Couvaloup de St-Cergue	A64	
May 20, 2014	06:05–11:33		38	257°	1.394	0.533	36°	CS3-Palmer Divide	U82	W14
May 21, 2014	05:57–11:31		36	261°	1.397	0.530	35°	CS3-Palmer Divide	U82	W14
May 22, 2014	05:45–08:48		35	143°	1.399	0.528	35°	CS3-Palmer Divide	U82	W14
June 7, 2015	08:17–11:29		19	150°	1.336	0.575	45°	CS3-Palmer Divide	U82	W15
June 8, 2015	08:42–09:31		7	39°	1.332	0.563	45°	CS3-Palmer Divide	U82	W15
June 11, 2015	08:02–11:25		32	159°	1.317	0.526	45°	CS3-Palmer Divide	U82	W15
June 12, 2015	07:58–11:26		33	163°	1.312	0.514	45°	CS3-Palmer Divide	U82	W15
June 14, 2015	07:54 -11:17		18	159°	1.302	0.489	45°	CS3-Palmer Divide	U82	W15
June 15, 2015	07:57–11:01		24	145°	1.297	0.477	45°	CS3-Palmer Divide	U82	W15
July 5-6, 2015	22:28–01:53		91	161°	1.165	0.231	45°	Isaac Aznar Obs.	Z45	A16
July 6, 2015	21:53–22:11		8	14°	1.158	0.220	46°	Isaac Aznar Obs.	Z45	A16
July 7-8, 2015	21:46–02:54		89	241°	1.150	0.207	46°	Isaac Aznar Obs.	Z45	A16

Table 3.5: Lightcurve observations used in this work (part three; continued from Table 3.4).
* The photometric band (Johnson B, Johnson V, or Cousins R) is only specified for lightcurves which are absolutely calibrated.
The fourth column lists the numbers of data points in each lightcurve.
$\Delta\phi$ is the range of asteroid rotation phases covered by that night's lightcurves, assuming the best-fit sidereal rotation period of 7.664 hours. A value of 360° would indicate that the lightcurve encompassed one full rotation of JD6.
r is the distance from the asteroid to the Sun; Δ is the distance from the asteroid to the Earth; α is the solar phase angle.
† The last column indicates the reference for lightcurves which were previously published: P08 is Polishook and Brosch (2008), W14 is Warner (2014), W15 is Warner (2015), and A16 is Aznar Macías et al. (2016).

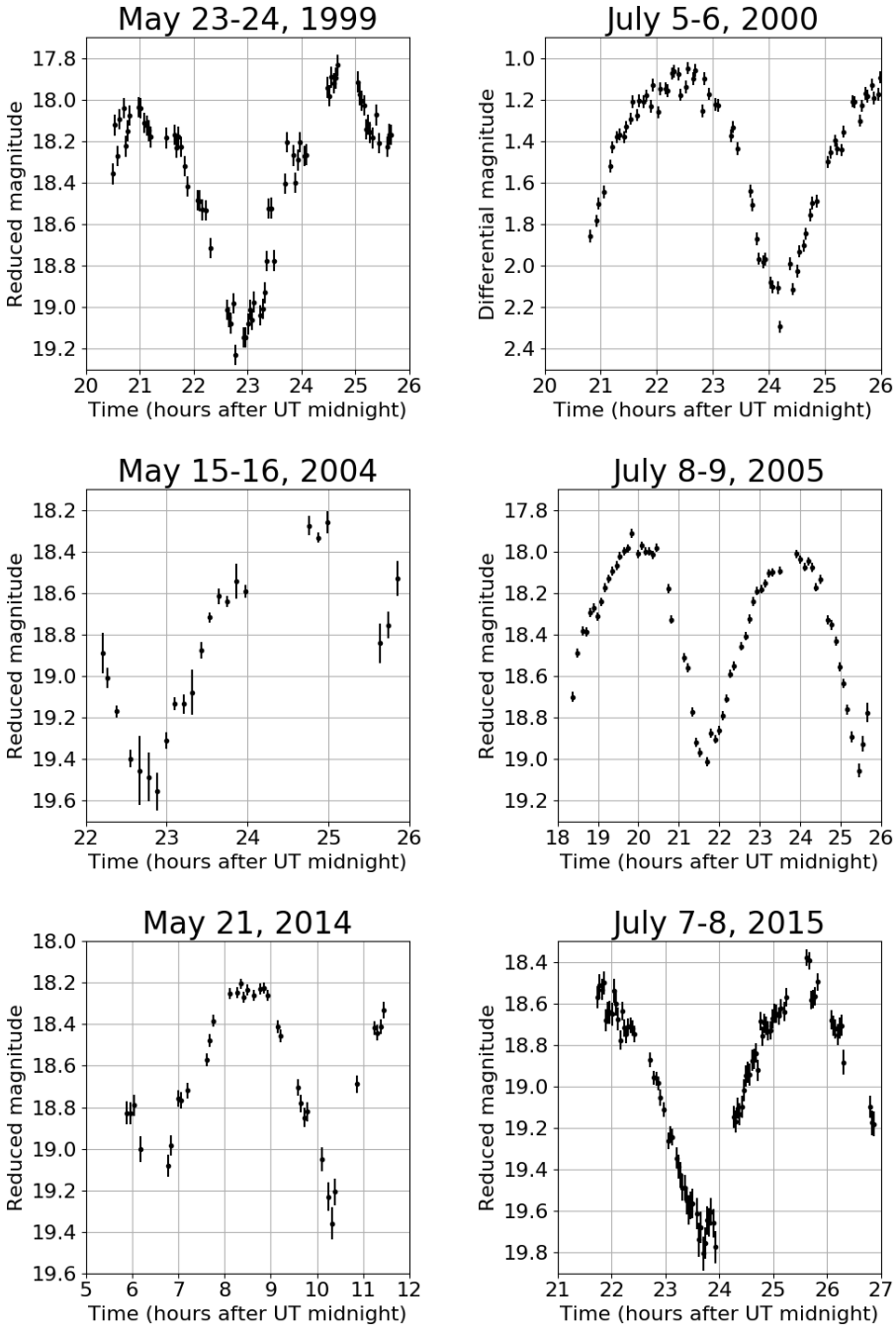

Figure 3.1: Some of the lightcurve observations used in this work. Other lightcurves are shown in the appendix, in Figure B.1 through Figure B.4, and Figure B.7 through Figure B.9.

only observe objects in the declination range −1° to +38°.

On two days (July 25 and 26, 2015), transmissions from Goldstone were received at the 100-meter Green Bank Telescope (GBT). The signal-to-noise ratio from these bistatic observations was considerably higher than it would have been with monostatic DSS-14 observations, for two reasons. First, the GBT is more sensitive, with a greater collecting area and slightly higher aperture efficiency than DSS-14 (Naidu et al., 2016). Second, bistatic observations made it possible for DSS-14 to transmit continuously, with continuous reception at GBT, so that individual images can have longer integration times than the two-way light travel time (which was less than one minute during the dates of the bistatic observations). With monostatic observations, half of the time is spent transmitting and half is spent receiving, and the integration time for a single frame cannot be greater than the round-trip light travel time. For the bistatic observations, the data were processed so that most images used an integration time of 300 seconds (five minutes), rather than the two-way light time. With these two effects combined, the sensitivity for the bistatic images is about five times greater than it would have been for monostatic DSS-14 observations on those dates.

For both Goldstone and Arecibo, the best imaging data had a delay resolution of 0.05 microseconds, which corresponds to a spatial resolution in the radial direction of 7.5 meters. Delay-Doppler images from each day are shown in Figure 3.4. The details of the radar observations are given in Table 3.6 and Table 3.7. The radar observations covered a wide range of sky positions (see Figure 3.5), thus providing good constraints on the direction of JD6's rotation axis (its pole).

In the Arecibo observations from July 15, 2015 (ten days before closest ap-

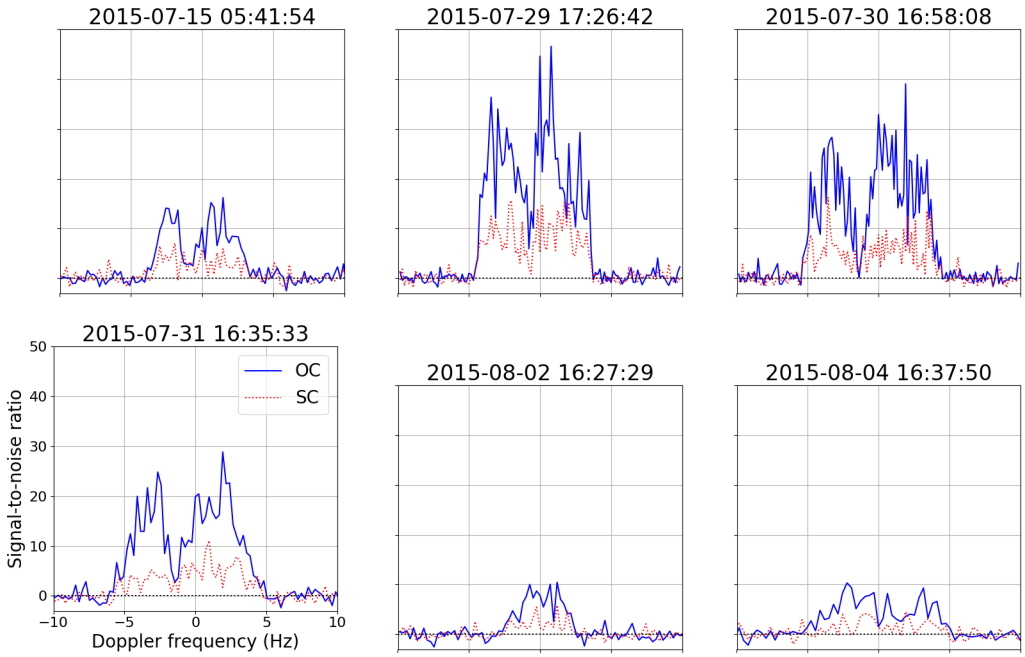

Figure 3.2: Continuous-wave (CW) radar observations of 1999 JD6 from Arecibo in 2015. The scaling along the x- and y-axes is the same for all six frames. The title of each frame specifies its mid-receive time (UT). Frequency resolutions are as given in Table 3.6 and Table 3.7. OC and SC refer to the opposite-sense and same-sense (as transmitted) circular polarizations, respectively.

proach), the CW spectra are bifurcated (see Figure 3.2), and the delay-Doppler images from that morning, despite their coarse resolution, show two separated clusters of relatively bright pixels (see Figure 3.4). These features suggest that JD6 is a contact binary: an asteroid with two components that are connected, but with a clear bifurcation. Contact binaries make up about 14% of NEAs that are larger than about 200 m (Taylor et al., 2012; Benner et al., 2015).

It was known from previously published observations that JD6 has $D \approx 2$ km and $P \approx 7.66$ h, so for observations by Goldstone DSS-14 ($\lambda = 3.5$ cm) with a sub-radar latitude near JD6's equator, one would expect a CW bandwidth of approximately 25 Hz. However, the Goldstone CW spectra from July 23, 2015 showed very narrow bandwidths – less than 2 Hz (see Figure 3.3). These narrow

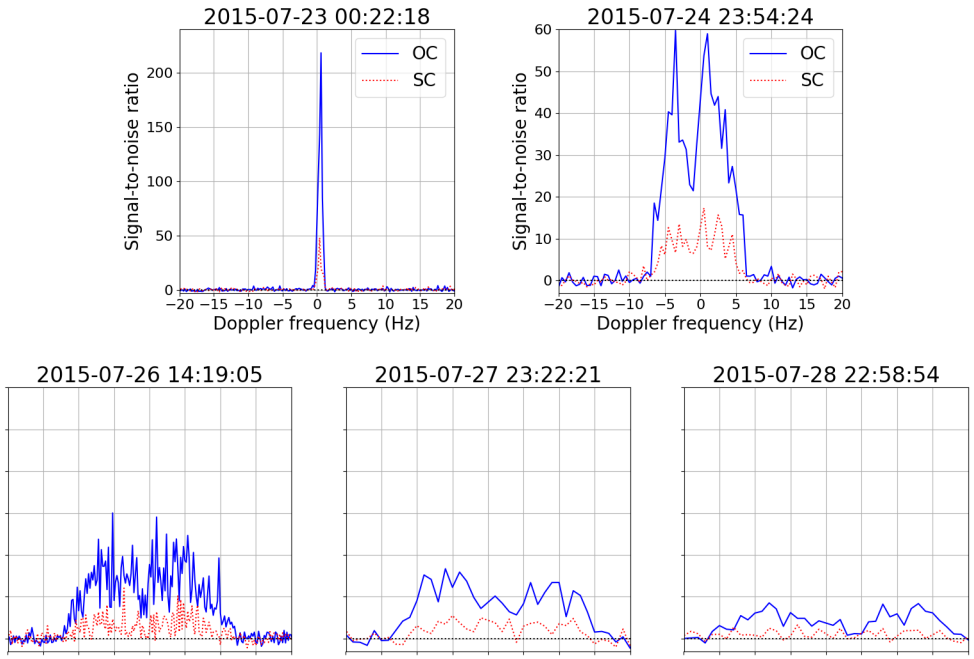

Figure 3.3: Continuous-wave (CW) radar observations of 1999 JD6 from Goldstone in 2015. The plotted range of frequencies is the same for all five frames (-20 to +20 Hz). However, note that the scaling of the first frame's y-axis is different from the scaling for the other four frames. The title of each frame specifies its mid-receive time. Frequency resolutions are as given in Table 3.6 and Table 3.7.

bandwidths meant that the line(s) of sight that night happened to be within just a few degrees of JD6's pole direction. These extremely fortuitous circumstances provide a very strong constraint on JD6's rotation state.

The Goldstone-GBT images from the day of closest approach (July 25; see Figure 3.4) show that it is clearly a contact binary, with two lobes of unequal sizes and a sharp concavity between them. The neck is apparently very sharp, but a faint signal is visible from within it in some frames.

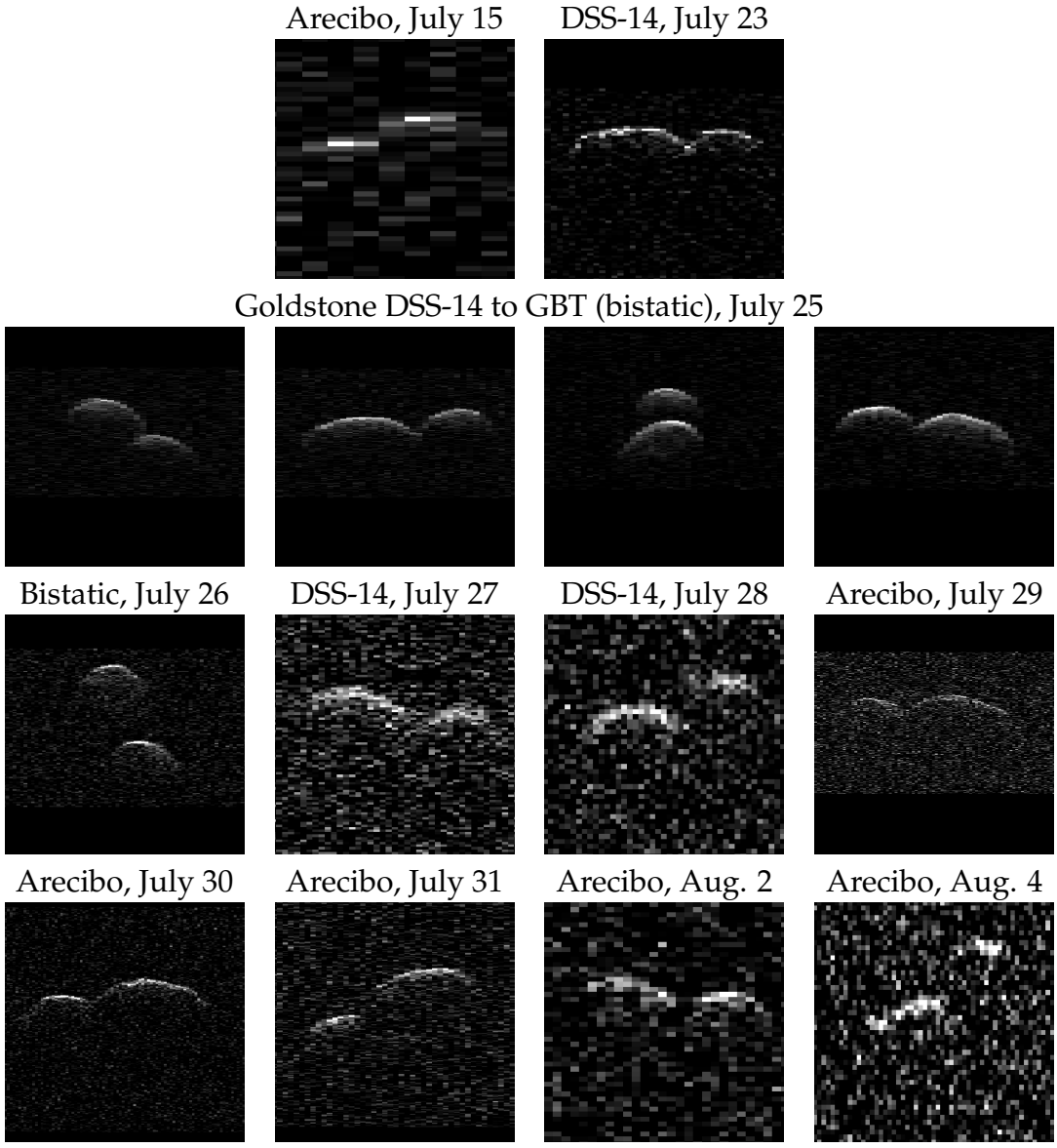

Figure 3.4: Delay-Doppler radar images of 1999 JD6 from 2015. The second row shows images from within a few hours of its closest approach on July 25. For these delay-Doppler images, transmissions from the DSS-14 antenna (at NASA's Goldstone Deep Space Communications Complex) were received at the Green Bank Telescope. For all delay-Doppler images shown in this work, delay is plotted on the vertical axis, increasing from the top down. Doppler frequency is plotted on the horizontal axis, increasing from left to right. These images are stretched along their Doppler axes such that the width of each image corresponds to the same physical distance (3.6 km) for both the delay and Doppler axes; therefore the pixels of the original images appear rectangular here. Some of these frames have regions with no signal (just noise) masked out.

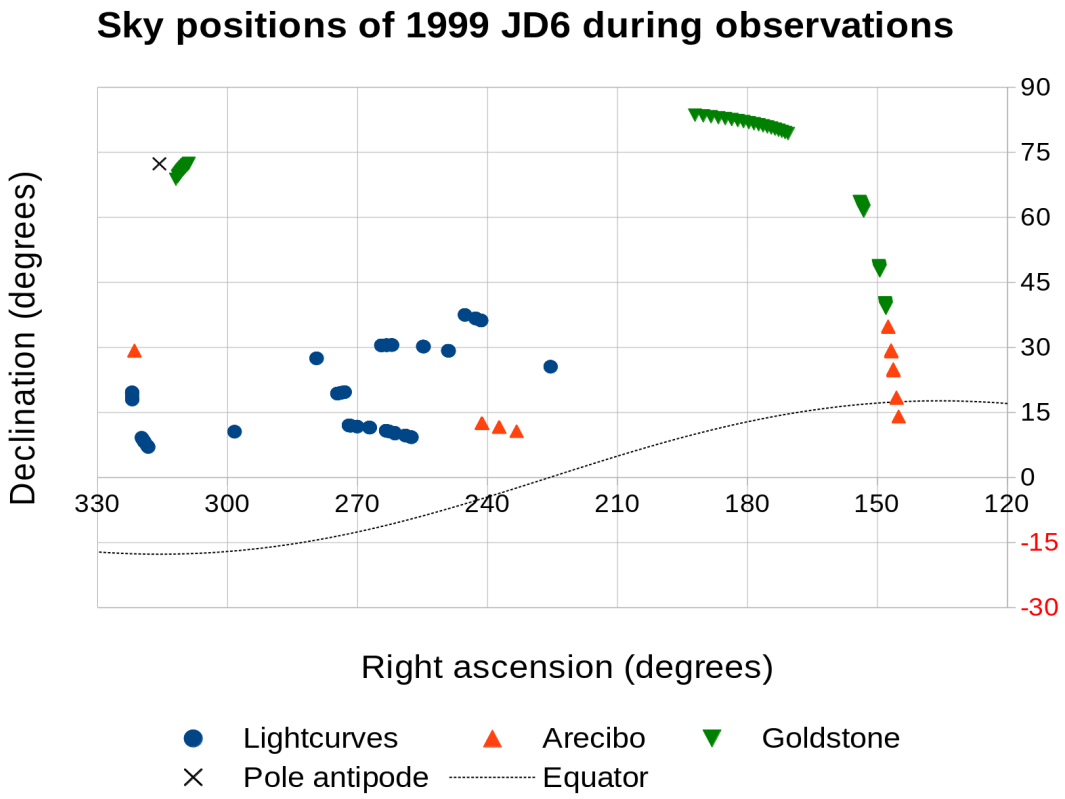

Figure 3.5: Sky positions of 1999 JD6 during the various observations. Note that Arecibo can only observe objects in the declination range −1° to +38°. The black X shows the antipode of JD6's derived pole position, which happened to be very close to the lines of sight during the observations from Goldstone on July 23, 2015. The black dashed curve shows lines of sight for which the sub-observer point would fall on JD6's equator.

UT date	UT times	Tel	Mode	Baud (μs)	spb	δf (Hz)	Runs	RTT (s)	RA	Dec	P_{tx} (kW)
July 25-26, 2010	23:37:32–00:58:46	A	CW			0.382	18†	139	241°	+13°	63
July 26-27, 2010	23:20:07–00:18:06	A	CW			0.382	13†	138	237°	+12°	79
July 27-28, 2010	23:54:15–00:15:02	A	CW			0.379	5†	138	233°	+11°	77
July 15, 2015	05:24:04–05:42:53	A	CW			0.212	5	126	321°	+29°	611
	05:51:02–07:29:36		DD	0.50	1	0.954	24	126	321°	+29°	639
July 23, 2015	00:20:02–00:28:14	Gm	CW			0.200	5	55	312°	+69°	406
	02:08:46–04:34:28		DD	0.25	1	0.058	79	54	311°	+70°	394
	04:41:37–08:20:22		DD	0.125	1	0.060	122	53	310°	+71°	388

Table 3.6: Radar observations used in this work (part one; continued in Table 3.7). UT times specify when data reception began and ended. The third column specifies which telescope was used for the observations. The Arecibo planetary radar (A) uses S-band (2380 MHz frequency, 12.6 cm wavelength), and the Goldstone Solar System Radar (G) uses X-band (8560 MHz, 3.5 cm). Gb indicates bistatic observations with transmission from Goldstone and reception at the Green Bank Telescope; Gm indicates monostatic Goldstone observations. All Arecibo observations of JD6 were monostatic. Note that when JD6 was closest to Earth (July 25, 2015), it was too far north to be observable with Arecibo. The fourth column (mode) specifies whether the observations were continuous-wave spectra (CW) or delay-Doppler images (DD). For delay-Doppler images, the baud length specifies the time delay resolution of the data; spb is the number of samples per baud. For instance, delay resolution of 0.20 microseconds (200 nanoseconds) is equivalent to a range resolution of 30 meters. A baud of 0.20 μs with 4 samples per baud means that the data were processed to have a pixel spacing of 7.5 m, but neighboring delay rows are correlated. δf specifies the frequency resolution of the data that were used in the shape fitting.The numbers of runs listed here are the numbers of usable scans (the numbers of round-trip times for which data was acquired) for each data set. A dagger (†) indicates that subsets of these data were summed before being input to the shape fitting software, in order to increase SNR. For instance, the 18 Arecibo CW scans on July 25-26, 2010, were summed, with each sum having nine scans, so that the shape modeling software used two sums. RTT is the round-trip time to the asteroid for that set of observations. A round-trip time of 60 seconds corresponds to a distance of 0.060 au. P_{tx} is the transmitter power.

UT date	UT times	Tel	Mode	Baud (μs)	spb	δf (Hz)	Runs	RTT (s)	RA	Dec	P_{tx} (kW)
July 24-25, 2015	23:52:25–00:01:10	Gm	CW			0.500	6	48	192°	+84°	395
July 25, 2015	00:11:38–00:18:47		DD	1.00	1	3.830	5	48	191°	+83°	385
	00:33:26–00:43:47		DD	0.125	1	0.447	7	48	190°	+83°	380
	00:56:20–01:03:29		DD	0.05	1	0.500	5	48	188°	+83°	401
July 25, 2015	01:09:57–01:23:21	Gb	CW			0.500	3	48	188°	+83°	
	01:30:03–04:00:03		DD	0.05	1	0.500	30	48	183°	+82°	
	04:12:04–09:13:05		DD	0.125	1	0.502	60	48	174°	+80°	
July 26, 2015	14:16:55–14:22:59	Gb	CW			0.200	7	51	154°	+64°	
	14:27:36–19:02:29		DD	0.125	1	0.500	55	51	154°	+63°	
July 27, 2015	22:46:31–23:22:48	Gm	CW			1.000	2	58	150°	+49°	392
	23:33:09–23:38:04		DD	1.00	1	3.830	3	58	150°	+49°	398
July 27-28, 2015	23:46:56–02:05:23		DD	0.25	1	1.021	54†	59	150°	+48°	393

Table 3.7: Radar observations used in this work (part two; continued from Table 3.6).

UT date	UT times	Tel	Mode	Baud (μs)	spb	δf (Hz)	Runs	RTT (s)	RA	Dec	P_{tx} (kW)
July 28, 2015	22:56:10–23:06:00	Gm	CW			1.000	5	65	148°	+40°	417
July 28-29, 2015	23:10:03–03:14:14		DD	0.50	1	1.021	111†	66	148°	+40°	391
July 29, 2015	17:21:22–17:32:02	A	CW			0.156	5	72	148°	+35°	758
	17:43:57–18:38:23		DD	0.05	1	0.149	23	72	147°	+35°	633
July 30, 2015	16:52:08–16:58:45	A	CW			0.137	3	81	147°	+29°	630
	17:10:02–18:55:45		DD	0.20	4	0.149	20	81	147°	+29°	673
July 31, 2015	16:31:49–16:36:14	A	CW			0.241	2	90	146°	+25°	682
	16:48:35–18:42:42		DD	0.20	4	0.298	33	91	146°	+25°	684
	18:53:49–18:55:13		CW			0.238	1	91	146°	+25°	727
August 2, 2015	16:22:53–16:28:21	A	CW			0.240	2	111	146°	+19°	689
	16:39:16–18:47:45		DD	0.50	1	0.477	31	112	146°	+18°	714
August 4, 2015	16:27:51–16:38:53	A	CW			0.317	3	134	145°	+14°	608
	16:47:21–18:32:51		DD	1.00	2	0.238	24	134	145°	+14°	622

Table 3.8: Radar observations used in this work (part three; continued from Table 3.7).

3.4 Shape modeling

To determine the shape of JD6, we used the SHAPE software, which combines all observations via weighted least squares fitting to produce a shape model. SHAPE was originally written by Hudson (1993); many additional features were introduced by Magri et al. (2007, 2011). SHAPE represents a model's surface as a polyhedron with a set of triangular facets. Other types of models, such as ellipsoids or spherical harmonics, are internally converted to that form (which does not require any additional parameters). SHAPE iterates through the parameters that describe the model's size, shape, rotation state, and photometric properties, finding the optimal value of each parameter by calculating a noise-free simulated set of observations and comparing those to the real observational data. SHAPE searches for the set of parameters that minimize the objective function, which is the weighted sum of squared residuals plus penalty functions that discourage physically unrealistic models.

In the early stages of JD6 shape modeling, we only used a subset of the radar observations from within about one week of the July 25, 2015 close approach. While making the shape models more complex, we also gradually incorporated more of the radar data, and then the 2015 lightcurves. By starting with the most detailed data sets, we found models that showed the main features of JD6's shape early in the modeling process.

We began by representing JD6's shape as an ellipsoid, then as a fifth-order spherical harmonic (see the left frame of Figure 3.6). However, those ellipsoid and harmonic models could not provide a good representation of the concavity that was prominently visible in many of the delay-Doppler images (see Fig-

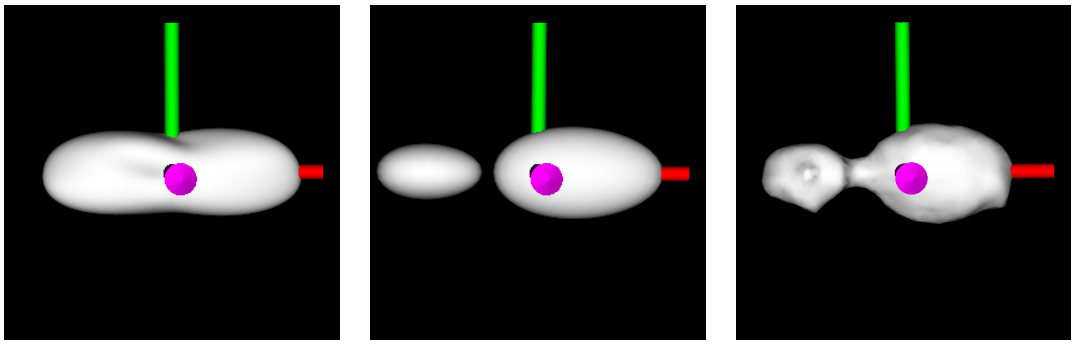

Figure 3.6: Early shape models. The frame on the left shows a spherical harmonic model. The center frame shows a two-ovoid model. The right frame shows an early vertex model for which the "neck" connecting the two lobes was too long. The side length of all three square frames corresponds to 3.6 kilometers. The sidereal spin vector (the model's shortest principal axis) is shown as a magenta arrow, and the long and intermediate principal axes are shown as red and green shafts, respectively.

ure 3.4). For a better approximation of JD6's two-lobe shape, we then used two ellipsoidal (or ovoidal) components that initially were separated in space (Figure 3.6 center). Then we added a small "neck" to connect the two lobes and combined them into a single model with about one thousand vertices whose individual displacements were allowed to vary (Figure 3.6 right).

The final number of radar data points (hundreds of thousands of image pixels and spectral channels) greatly exceeded the number of lightcurve data points (1266 total). Therefore we had to apply different weights to the different data sets, in order to make sure that each type of observation would have a significant influence on the resulting shape model. The final weights were set such that the delay-Doppler images contributed about half of total chi-squared, and the CW spectra and the lightcurves each contributed about one fourth of the total.

3.4.1 Rotation state

The narrow bandwidths of the CW spectra from Goldstone on July 23 greatly simplified the search for JD6's pole direction. We could only have seen those narrow bandwidths if the lines of sight from that night were within a few degrees of JD6's pole. Therefore, when trying to establish JD6's pole direction, we only had to search within two small regions of the sky, rather than the entire celestial sphere. However, it was not immediately obvious whether JD6's north pole or its south pole had been pointed toward Earth, so we had to test both of those cases. We found that models with prograde pole directions – i.e., those with a pole position near $(\lambda, \beta) = (40^\circ, +75^\circ)$ – cannot provide good fits to the full set of radar and lightcurve data.

Based on the July 23 CW bandwidths, modeling showed that the lines of sight that night passed within about two degrees of the antipode of JD6's pole position. Prograde pole solutions could be ruled out, but there was another possible degeneracy: whether JD6's antipode was two degrees east or west of those lines of sight (see Figure 3.7). Tests showed that only one of those two positions – the pole with its antipode to the east of the arc (greater right ascension) – could fit the July 23 data. For the other pole, the modeled images and spectra did not match that day's data.

JD6's pole position is close to the south ecliptic pole, among the most populated cluster of asteroid pole directions that was described by La Spina et al. (2004). JD6 is a retrograde rotator, as are the majority of NEAs with known pole positions (Kryszczyńska et al., 2007); this may be a consequence of the Yarkovsky effect.

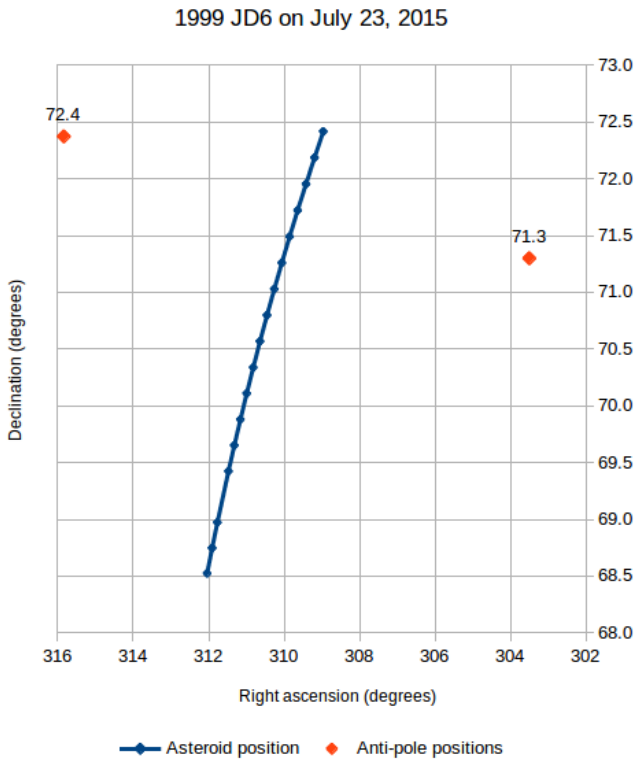

Figure 3.7: Possible pole antipodes $(\alpha, \delta) = (304°, +71.3°)$ and $(316°, +72.4°)$, indicated by orange diamonds. Both are two degrees from the July 23 lines of sight (blue arc), but only one yields model images and spectra whose rotation phases fit the July 23 data.

The final one-sigma uncertainty in JD6's pole position is about 0.25° of great circle distance; a model whose pole direction is half a degree from the best-fit pole has model images whose frequency widths on July 23 are noticeably wrong (see Figure 3.8). The strong constraint on JD6's pole position helps to avoid a potential degeneracy with the rotation period, as was seen for (162421) 2000 ET70 (Marshall et al., 2017, and Chapter 2).

The radar and lightcurve observations from 2015 span about two months, from June 7 to August 4. During that interval, the observations are dense enough in time that there is no ambiguity in how many rotations or half-rotations of JD6 occurred between any pair of observation times. Observations from one night allow JD6's rotation phase (during that time) to be determined to an accuracy of about ten degrees, or possibly somewhat better. An uncertainty of ten degrees over a span of about sixty days equates to an uncertainty in JD6's

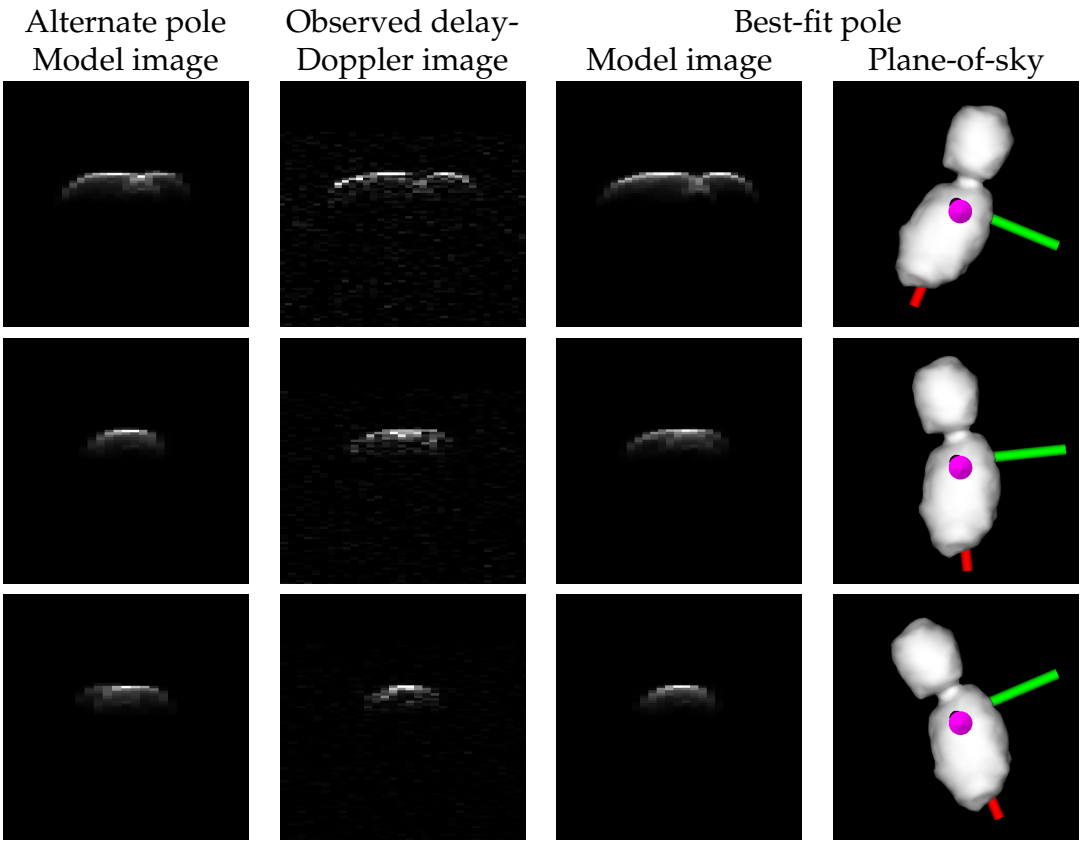

Figure 3.8: Delay-Doppler images from Goldstone (DSS-14) on July 23, 2015. The frequency widths are very narrow, indicating that the line of sight during these observations happened to be within a few degrees of JD6's pole position. However, since the lines of sight never aligned exactly with the pole, the bandwidths are still finite, varying as JD6 rotates. The frames in the first column (from the left) show the noise-free model images, for an alternate model with a pole direction of $(220.3°, -74.00°)$. The frames in the second column show the observations. The frames in the third column show the model images, for our best-fit model with a pole direction of $(\lambda, \beta) = (220.3°, -73.43°)$. The frames in the fourth column show the plane-of-sky views of the best-fit model at those observation times. The sidereal spin vector (the model's shortest principal axis) is shown as a magenta arrow, and the long and intermediate principal axes are shown as red and green shafts, respectively. Despite the alternate model's pole position being only about half of one degree from the best-fit solution, its model frequency widths for these images are noticeably wrong.

spin rate of less than 0.2 deg/day.

Extrapolating that spin rate uncertainty to the lightcurve observations from the previous year means that JD6's rotation phase at those times has an uncertainty of about 70 deg. Half a rotation would be slightly more than double that uncertainty, so it is possible that the true spin rate is actually slightly different, corresponding to half a rotation more or less (over that one-year time span) than the nominal value.

However, separate tests of JD6's spin rate, using the lightcurves from 1999, 2000, 2004, and 2005, showed that none of the alternate periods could fit that set of lightcurves. The single (more accurate) period value that fit those earlier lightcurves, spanning six years, could then be confidently extrapolated to the observations from 2014 and 2015. The final uncertainty in JD6's spin rate is 0.00083 deg/day, which corresponds to about five degrees over the sixteen-year span of lightcurve and radar observations. Converted to more familiar units, JD6's sidereal rotation period is 7.6643464 h, with an uncertainty of just 0.0000056 h = 0.020 s.

We could not detect any change in JD6's rotation period, e.g. due to the YORP effect (Rubincam, 2000). The magnitude of the change in JD6's spin rate is at most 1.6×10^{-6} deg/day^2, and the best-fit value for a change in its spin rate is zero. If the YORP effect is causing any change in JD6's spin state, that change is too small to be detected in the available sixteen years of observations.

3.4.2 Shape improvements with Blender software

In the vertex models, a persistent problem was that the "neck" connecting the model's two lobes was too long (Figure 3.6 right). The delay-Doppler images show that the two lobes nearly overlap, and even when we used a low weight for SHAPE's concavity penalty, the concavity between the lobes appears much sharper in the data than in the early models. In order to produce models that had these features, we used Blender[3], a free and open source program for working with 3D models. Blender was first applied to asteroid shape modeling by Crowell et al. (2017), for 1627 Ivar.

With Blender's graphic interface, one can manually adjust the positions of vertices in regions of interest. We used Blender to make each of the lobes longer (thus making the neck shorter and sharper), and also to remove bumps that appeared in the model but were not clearly visible in any delay-Doppler images (see Figure 3.9). We emphasize that the models we edited in Blender were used to provide better initial conditions for SHAPE, but SHAPE was using the full set of radar and lightcurve data to generate the final models.

Using Blender, we were able to move around some of the vertices near the neck, in order to give SHAPE initial models that were more sharply bifurcated. Blender also provided easy ways to add more vertices to that region, in order to give SHAPE more flexibility in how it changed the model's details near the neck. Our final shape model has 1060 vertices and 2116 triangular facets, with an average edge length of about 100 m. Figure 1.3 shows a view (from Blender) in which the individual facets are clearly visible.

[3] `https://www.blender.org/`

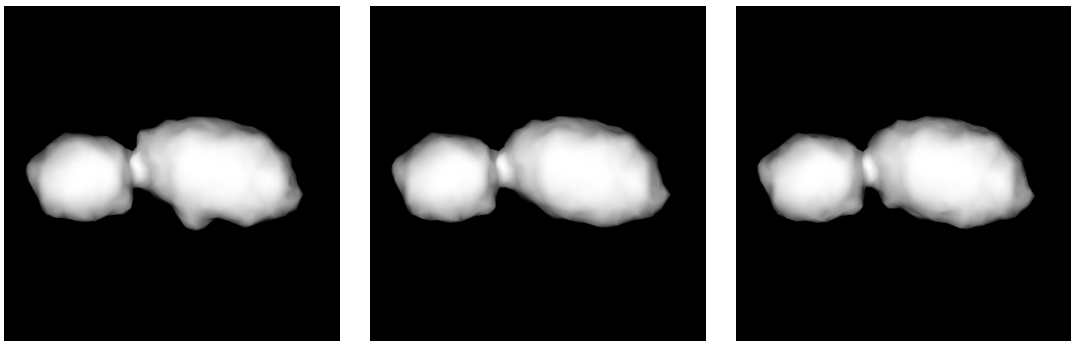

Figure 3.9: Later shape models. The model on the left has a bump (below center) that was not clearly visible in any delay-Doppler images; this bump was then removed with Blender. The center model has that bump removed, but the concavity (below the neck) is not as sharp as it appears in the images. The right model is our near-final model, with a concavity that provides very good fits to the delay-Doppler images. The side length of all three square frames corresponds to 3.6 kilometers.

3.4.3 Shape model parameters

Principal axis views of our final shape model are shown in Figure 3.10. The model's parameters (and their uncertainties) are given in Table 3.9. The tabulated uncertainties are conservative estimates based on considering changes in chi-squared and visual inspection of the models. We could not avoid having to make some subjective decisions about which models could be considered acceptable, as in Magri et al. (2007, 2011) and Nolan et al. (2013).

In order to establish the allowed ranges of JD6's lengths (extents) along its three principal axes, we tested a range of lengths for each of the three axes, searching for the thresholds beyond which there were clear discrepancies between the model images and the observations. In each test, we had SHAPE keep one length constant while allowing the other two to vary, in order to find the widest possible range of acceptable lengths. Through these tests, we found that the three extents are all positively correlated with each other. Stretching the model to make it longer along one axis tends to require compensating changes that make it slightly longer along both other axes. Making the model shorter along one axis also tends to make it shorter along both other axes. The correlation between x and y is +0.8, the correlation between x and z is +0.6, and the correlation between y and z is +0.7. Because of these positive correlations, the uncertainties in JD6's volume, surface area, and other derived quanties are higher than they would be if the three lengths were all independent of each other (Bevington and Robinson, 2003, equation 3.13).

Parameter		Value	Uncertainties		Rel. unc.
Extents along principal axes *	x	2.97 km	-0.17 km	+0.19 km	6%
	y	1.25 km	-0.10 km	+0.12 km	9%
	z	1.03 km	-0.20 km	+0.17 km	18%
Surface area *	A	8.79 km^2	1.71 km^2		19%
Volume *	V	1.60 km^3	0.47 km^3		29%
Moment of inertia ratios *	I_x/I_z	0.17	0.03		16%
	I_y/I_z	0.97	0.02		2%
Volumetric mean diameter *	D	1.45 km	0.14 km		10%
DEEVE extents	$2a$	3.19 km	0.20 km		6%
	$2b$	1.06 km	0.09 km		9%
	$2c$	0.91 km	0.16 km		18%
Sidereal rotation period	P	7.6643464 h	-0.0000058 h	+0.0000054 h	0.7 ppm
Pole ecliptic longitude	λ	220.3°	−0.8°	+0.9°	
Pole ecliptic latitude	β	−73.43°	0.18°		

Table 3.9: Parameters and one-sigma uncertainties for the shape model of 1999 JD6, utilizing radar and lightcurve data. Some uncertainties are asymmetric. For instance, the one-sigma range for JD6's extent along its principal x-axis is 2.80 to 3.16 km.

* Our analysis showed that the uncertainties for JD6's three lengths along its principal axes are all positively correlated with each other. The uncertainties in the model's surface area, volume, moment of inertia ratios, and mean diameter are therefore greater than what they would be if those uncertainties were all uncorrelated.

The moment of inertia ratios were derived with the assumption that the model's density is homogeneous. Volumetric mean diameter is the diameter of a sphere that would have the same volume as this shape model. The dynamically equivalent equal volume ellipsoid (DEEVE) is the uniform-density ellipsoid that has the same volume and moment of inertia ratios as the shape model.

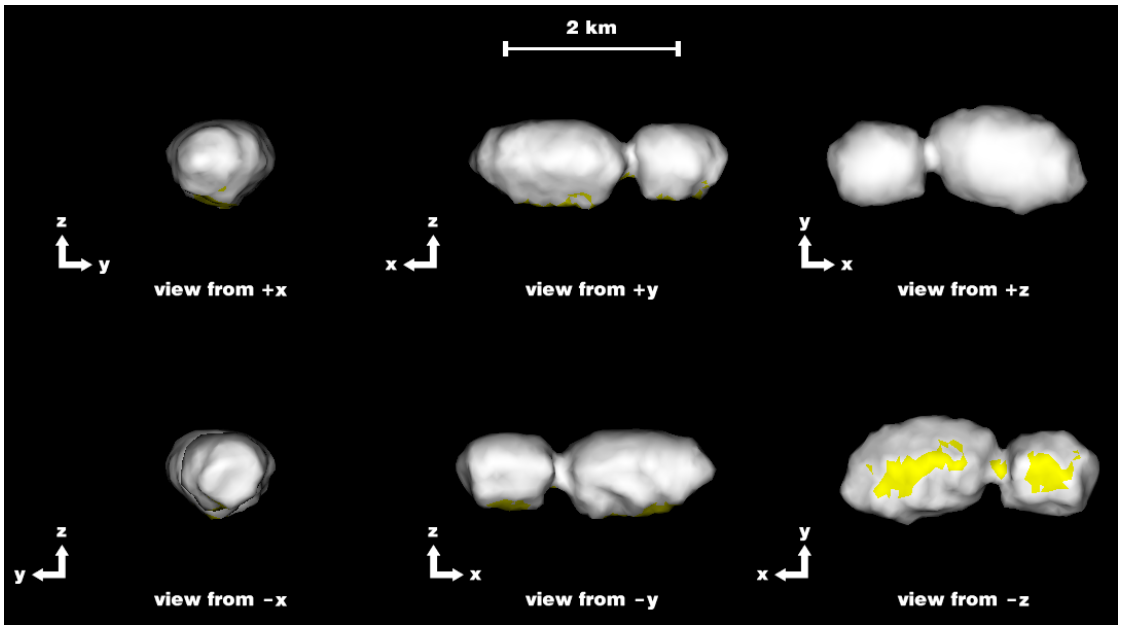

Figure 3.10: These frames show views of the shape model from along its three principal axes. The model rotates about the z-axis, and its maximum diameter is 3.0 kilometers. The facets marked in yellow, in the south, were seen at incidence angles greater than sixty degrees during all delay-Doppler observations (or not seen at all) and therefore are not well constrained.

3.4.4 Radar scattering properties

Radar scattering from JD6's surface is represented as a cosine law of the form

$$\frac{d\sigma}{dA} = R(C+1)(\cos\theta)^{2C} \tag{3.1}$$

(Mitchell et al., 1996), where σ is the radar cross section, A is the surface area, R and C are fit parameters, and θ is the incidence angle. $\frac{d\sigma}{dA}$ is the radar cross section per unit surface area at an incidence angle θ.

Table 3.10 lists the radar cross sections in the same sense (as transmitted) and opposite sense circular polarizations, radar albedos, and circular polarization ratios that were measured from the CW observations of JD6. For some Arecibo

CW scans on some days, there were problems with the telescope's pointing, so the detected echoes were weaker than expected by an unknown amount. In such scans, we cannot measure the cross section. However, problems with the pointing affect both polarization channels equally, so those scans still provide useful measurements of the circular polarization ratio.

There are three sources of error for the cross section measurements: thermal noise from the finite system temperatures, self noise from the statistical properties of observed radar signals, and systematic errors in the radar systems' calibration. When averaging over multiple observations, the errors from thermal noise and self noise add in quadrature (and thus their relative contributions decrease), but the relative uncertainty from calibration remains constant. Therefore the calibration uncertainty is the dominant source of error in the overall radar albedos in both polarizations. Based on past experience (e.g. Brozović et al., 2011; Nolan et al., 2013), we have assigned relative uncertainties of 25% and 35% for cross sections measured from Arecibo and Goldstone data, respectively.

When dividing SC cross section by OC cross section to find the circular polarization ratio, those calibration errors mostly cancel. However, they do not cancel perfectly, because the system temperatures may differ slightly between the OC and SC channels. We therefore add a relative error of 5% in quadrature with the uncertainties from thermal noise and self noise to each cross section before taking their ratio. That 5% uncertainty for each channel means that the circular polarization ratio must have a relative error of at least $\sqrt{2} \times 5\% \approx 7\%$.

Given that JD6 is a very elongated object, its projected area varies considerably as it rotates, and the radar cross sections vary accordingly. However, at

Observing date (UT)	Sub-radar lon	lat	Proj. A (km²)	# σ runs	σ_{OC} (km²)	$\hat{\sigma}_{OC}$	σ_{SC} (km²)	$\hat{\sigma}_{SC}$	# μ_C runs	μ_C
S-band:										
July 15, 2015	94,	+47	2.4	5	0.20	0.08	0.07	0.03	5	0.37
July 29, 2015	129,	+18	2.0	2	0.12	0.06	0.04	0.02	5	0.36
July 30, 2015	106,	+12	2.2	1	0.13	0.06	0.04	0.02	3	0.37
July 31, 2015	77,	+8	2.2	1	0.14	0.06	0.04	0.02	3	0.33
August 2, 2015	350,	+1	1.1	2	0.05	0.05	0.02	0.02	2	0.34
August 4, 2015	248,	-3	2.2	2	0.18	0.08	0.07	0.03	3	0.37
Overall						0.07 ± 0.02		0.03 ± 0.01		0.36 ± 0.03
X-band:										
July 23, 2015	346,	+86	2.6	5	0.30	0.11	0.08	0.03	5	0.27
July 24, 2015	57,	+68	2.5	6	0.39	0.15	0.10	0.04	6	0.26
July 27, 2015	320,	+31	2.0	2	0.29	0.14	0.07	0.04	2	0.26
July 28, 2015	276,	+23	2.3	5	0.29	0.13	0.07	0.03	5	0.25
Overall						0.13 ± 0.05		0.04 ± 0.01		0.26 ± 0.02

Table 3.10: Radar scattering properties of 1999 JD6 at 12.6 cm (from Arecibo S-band observations) and 3.5 cm (from monostatic Goldstone X-band observations).
A sub-radar longitude of zero is within a few degrees of the $+x$ direction shown in Figure 3.10.
Projected area values are derived from the best-fit shape model.
σ_{OC} and σ_{SC} are the measured cross sections for the opposite-sense (OC) and same-sense (SC) circular polarizations.
$\hat{\sigma}_{OC} = \frac{\sigma_{OC}}{A_{proj}}$ and $\hat{\sigma}_{SC} = \frac{\sigma_{SC}}{A_{proj}}$ are the radar albedos for the two polarizations.
$\mu_C = \frac{\sigma_{SC}}{\sigma_{OC}}$ is the circular polarization ratio.
runs is the number of CW scans from which the cross sections or the circular polarization ratio could be measured; see Section 3.4.4.

both 3.5 cm and 12.6 cm, the measured radar albedos and circular polarization ratios are consistent across the observed surface of the asteroid, within their uncertainties. There do not seem to be any radar-bright or radar-dark features on JD6's surface.

Generally one would expect a surface to be rougher on small scales than on large scales, thus having a greater circular polarization ratio at shorter wavelengths. Therefore it is slightly surpising that JD6 has a circular polarization ratio of 0.36 ± 0.03 at 12.6 cm (measured by Arecibo), and a ratio of just 0.26 ± 0.02 at 3.5 cm (measured by Goldstone). Previous targets that were observed at both wavelengths (e.g. Brozović et al., 2011; Nolan et al., 2013) typically had polarization ratios for the two wavelengths that were equal within their uncertainties.

At both wavelengths, JD6's circular polarization ratio is well within one standard deviation of the mean circular polarization ratio for NEAs, 0.34 ± 0.25[4]. However, the mean radar albedo for NEAs is 0.20 ± 0.12[5]. JD6's OC radar albedo values, 0.07 ± 0.02 at 12.6 cm and 0.13 ± 0.05 at 3.5 cm, fall near the lower end of that range.

3.4.5 Astrometric measurements

With the shape model, we know where JD6's center of mass is relative to the leading edges in the various delay-Doppler images, or relative to the boundaries of the signal in the CW spectra. We used the final shape model to obtain astrometric measurements of JD6 that are more accurate than what one can

[4] https://echo.jpl.nasa.gov/~lance/scoc/scoc.html

[5] https://echo.jpl.nasa.gov/~lance/asteroid_radar_properties/nea.radaralbedo.html

Date	Time (UT)	Measurement	Uncertainty
Doppler:			
July 25, 2010	23:57:00	+24,147.17 Hz	0.76 Hz
July 29, 2015	17:29:00	-240,761.69 Hz	0.31 Hz
Delay:			
July 15, 2015	06:38:00	125,503,251.12 µs	0.79 µs
July 29, 2015	18:11:00	72,086,340.95 µs	0.61 µs
July 30, 2015	17:25:00	80,974,186.48 µs	0.64 µs
July 31, 2015	17:26:00	90,816,962.05 µs	0.64 µs
August 2, 2015	17:43:00	111,994,849.79 µs	0.79 µs
August 4, 2015	17:24:00	134,161,018.36 µs	2.00 µs

Table 3.11: Astrometric measurements derived from the Arecibo observations and the final shape model. For Doppler measurements, the uncertainties are equal to two times the frequency resolution of the processed CW spectra that were used for shape modeling. For delay measurements, the uncertainties come from two terms added in quadrature: the baud length of the images and half of the maximum uncertainty in JD6's extent (90 m, which corresponds to 0.6 µs). However, we manually increased the uncertainty for the August 4 range because the images from that day were rather faint.

obtain with quick visual inspection of the data while taking the observations. Our final measurements are given in Table 3.11. The accuracy of the measured ranges is limited by uncertainty in the dimensions of the shape model, rather than uncertainty in where the center of mass is relative to the observed leading or trailing edges.

3.5 Conclusions

Szabó et al. (2001) and Polishook and Brosch (2008), noting the large amplitude in lightcurve observations of JD6, suggested that it is elongated. Radar images of 1999 JD6 confirm this prediction, revealing a peanut-shaped contact binary with two lobes separated by a sharp concavity – a shape that is very similar to that of (8567) 1996 HW1 (Magri et al., 2011). About 50 contact binaries have been

observed by radar[6]; roughly one out of every seven NEAs larger than about 200 m is a contact binary (Taylor et al., 2012; Benner et al., 2015).

JD6 has an elongation of $x/y = 2.4$, which makes it one of the most elongated known near-Earth asteroids[7]. Only 1620 Geographos (Hudson and Ostro, 1999) and 11066 Sigurd (Benner et al., 2004) are more elongated. JD6's overall shape is quite similar to that of (8567) 1996 HW1 (Magri et al., 2011): two lobes (with the smaller lobe being about 60% the length of the larger one) with a sharp concavity. 1996 HW1 has an elongation of 2.3 and a slightly greater effective diameter (2.0 km).

Accurate determination of an asteroid's pole position often can be extremely difficult, owing to unavoidable ambiguities in the interpretation of the data. During radar observations of JD6 on July 23, 2015, we observed very narrow CW bandwidths, meaning that the line of sight was almost parallel to JD6's rotation axis. Shape modeling showed that the line of sight that morning passed within two degrees of JD6's pole position. Those fortunate observing circumstances made it possible to determine JD6's pole position to an accuracy of about 0.25°. This is the most accurately known pole position for any asteroid for which there are only Earth-based observations. However, some spacecraft missions can find pole directions with even finer accuracy; for instance, the uncertainty in the orientation of 1 Ceres, as measured by the Dawn mission, is just 0.00022° (Konopliv et al., 2018).

We have incorporated lightcurves of JD6 from six different apparitions, from 1999 to 2015. Lightcurves from multiple years sometimes allow for a comb of period solutions, with different values of the period corresponding to differ-

[6] https://echo.jpl.nasa.gov/~lance/binary.neas.html
[7] https://echo.jpl.nasa.gov/~lance/nea_elongations.html

ences of an integer or half-integer number of rotations between apparitions (e.g. 101955 Bennu, Nolan et al., 2013). With JD6 there is no such ambiguity. We are able to unambiguously link the rotation phases of the lightcurves from all of the different years. JD6 has a sidereal rotation period of 7.6643464 h, and the uncertainty in its period is just 0.0000056 h = 0.020 s = 20 ms.

JD6's 2015 apparition was the closest that it will come to Earth until 2054, when it will pass within 0.047 au[8]. Before 2054, during more distant apparitions, it will be possible to obtain additional lightcurve observations, or perhaps faint radar observations. In July of 2020, JD6 will be 0.13 au from Earth, which will be slightly closer than it was during the 2010 Arecibo observations. With Arecibo at full power, JD6 will be observable with a signal-to-noise ratio of about 30 per run, or 150 per day, which is enough for coarse images, and for ranging.

Some of the lightcurve observations of JD6 yielded absolute photometry. Those data can be used to constrain JD6's albedo and other photometric properties. As part of our ongoing program to obtain near-infrared spectra of radar-targeted asteroids, we observed JD6 from the NASA InfraRed Telescope Facility (IRTF) on several nights in 2010 and 2015. Additionally, there are published observations of JD6 at mid-infrared wavelengths from Spitzer (Campins et al., 2009; Trilling et al., 2010) and WISE (Mainzer et al., 2014). We will discuss JD6's albedo, phase function, spectral class, and thermal properties in an upcoming paper.

[8] ssd.jpl.nasa.gov/sbdb.cgi?sstr=85989;orb=0;cov=0;log=0;cad=1

3.6 Acknowledgments

This project was partially supported by NASA grants NNX10AP87G, NNX12AF24G, and NNX13AQ46G; and by NSF grant AST-1109855. The first author was supported by a NASA Earth and Space Science Fellowship (NASA grant NNX15AR14H).

The authors thank the staff members at Arecibo Observatory, at the Deep Space Network, and at the Green Bank Telescope for assistance with the observations.

The Arecibo Observatory is operated by SRI International in partnership with Ana G. Méndez – Universidad Metropolitana and the Universities Space Research Association, under a cooperative agreement with the National Science Foundation (AST-1100968). The Arecibo Planetary Radar program is supported by NASA's Near Earth Object Observation program.

Part of this research was conducted at the Jet Propulsion Laboratory, California Institute of Technology, under contract with the National Aeronautics and Space Administration (NASA). The material presented represents work supported by NASA under the Science Mission Directorate Research and Analysis Programs.

The work at Ondřejov was supported by the Grant Agency of the Czech Republic, Grant 17-00774S.

B.-O. D. acknowledges support from the Swiss National Science Foundation (PP00P2-163967).

This research has made use of NASA's Astrophysics Data System Bibliographic Services.

The authors gratefully acknowledge the teams that produce the following free software packages, which were used for this work: Blender[9], Gnuplot[10], ImageMagick[11], Kile[12], LibreOffice[13], Perl[14], Python[15], IPython (Pérez and Granger, 2007), Jupyter[16], Matplotlib (Hunter, 2007), NumPy (van der Walt et al., 2011), Pillow[17], and SciPy[18].

3.7 Supplementary material

Supplementary figures associated with this article can be found in Section B.1.

[9] https://www.blender.org/
[10] http://www.gnuplot.info/
[11] https://imagemagick.org/
[12] http://kile.sourceforge.net/
[13] https://www.libreoffice.org/
[14] https://www.perl.org/
[15] https://www.python.org/
[16] https://jupyter.org/
[17] https://python-pillow.org/
[18] http://www.scipy.org/

CHAPTER 4

OTHER PROJECTS

This chapter discusses several other projects that I have worked on (but not finished) during my time at Cornell. I aim to get them all written up and published within the next year.

4.1 Photometric and thermal properties of (85989) 1999 JD6

In contrast to the lightcurve observations of 2000 ET70, some of the lightcurves for 1999 JD6 were absolutely calibrated, so they can be used to find JD6's absolute magnitude and, since its size is known, its albedo. However, there is the complication that visual geometric albedo is defined at a phase angle of zero, and the minimum phase angle for any of the absolutely calibrated JD6 lightcurves is 30°. Observations at phase angles less than about 10° would be needed for strong constraints on JD6's phase slope, G, so a range of values of G must be tested. A sample of the range of allowed parameters is given in Table 4.1.

4.1.1 Preliminary thermal modeling results

For thermal modeling, I used $G = +0.05$ (which gave marginally better fits to the lightcurves than +0.15), converted to Hapke parameters as in Verbiscer and Veverka (1995). I ran sets of thermal models to see which model parameters are compatible with infrared measurements of JD6 from Spitzer and the IRTF. For thermal modeling, each possible set of allowed (G, w_V, f_c) values must be tested

G	f_c	Best-fit w_V
+0.05	0.0	0.123
+0.05	0.1	0.125
+0.05	0.2	0.127
+0.05	0.3	0.130
+0.05	0.4	0.132
+0.05	0.5	0.135
+0.05	0.7	0.141
+0.05	1.0	0.150
+0.15	0.0	0.136
+0.15	0.5	0.149
+0.15	1.0	0.166

Table 4.1: The single-scattering albedo values that provide the best fits to the V-band lightcurves of 1999 JD6, for various values of phase slope (G) and crater coverage fraction (f_c). This list is representative, not exhaustive.

with numerous possible values of thermal inertia.

Much like what I found with 2000 ET70, there does not seem to be one single set of thermal parameters for which the model spectra fit well for all of the infrared measurements of 1999 JD6. Figure 4.1 through Figure 4.3 show some of the infrared spectra, along with a thermal model having $G = +0.05$, $w = 0.132$, thermal inertia 280 J m^{-2} K^{-1} s$^{-1/2}$, and 40% coverage of spherical-section craters with an opening angle of 150°. That is one of the best overall models (lowest chi-squared), which splits the difference between being too hot (compared to the data) at some times and too cold at other times.

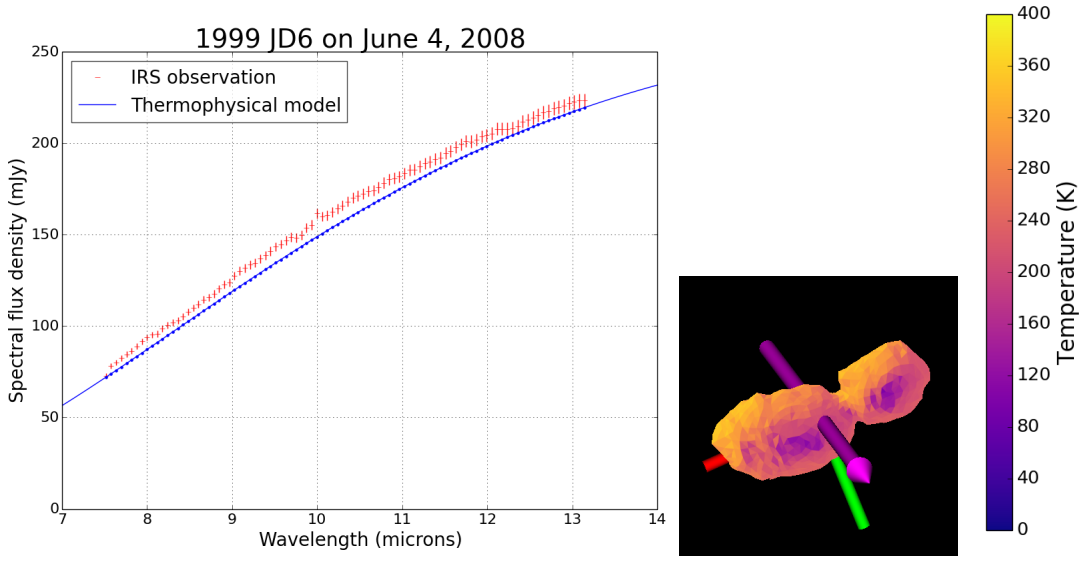

Figure 4.1: Left: The red points show the infrared spectrum of JD6, measured with the Infrared Spectrograph (IRS) on NASA's Spitzer Space Telescope on June 4, 2008 (Campins et al., 2009). The blue curve shows the corresponding spectrum from the (preliminary) best JD6 thermal model, with G = +0.05, w = 0.132, thermal inertia 280 J m^{-2} K^{-1} s$^{-1/2}$, and 40% crater coverage.
Right: A view of the JD6 thermal model, with facets colorized by the modeled surface temperatures.

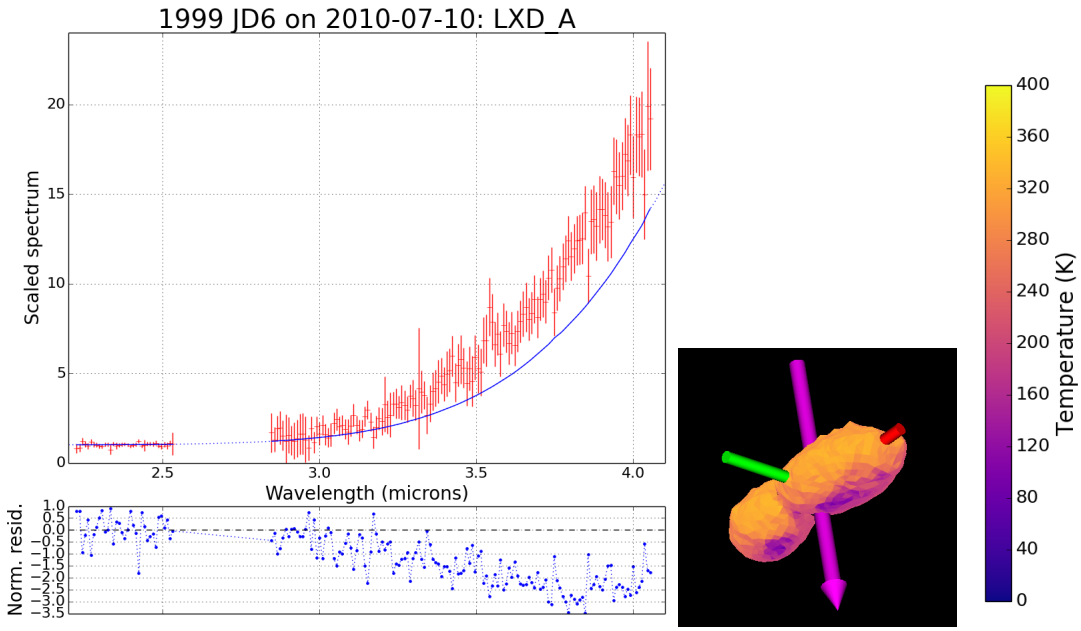

Figure 4.2: Left: The red points show the scaled spectrum of JD6, as measured with SpeX LXD on July 10, 2010. The blue curve shows the corresponding spectrum from the (preliminary) best JD6 thermal model.
Right: A view of the JD6 thermal model, with facets colorized by the modeled surface temperatures.

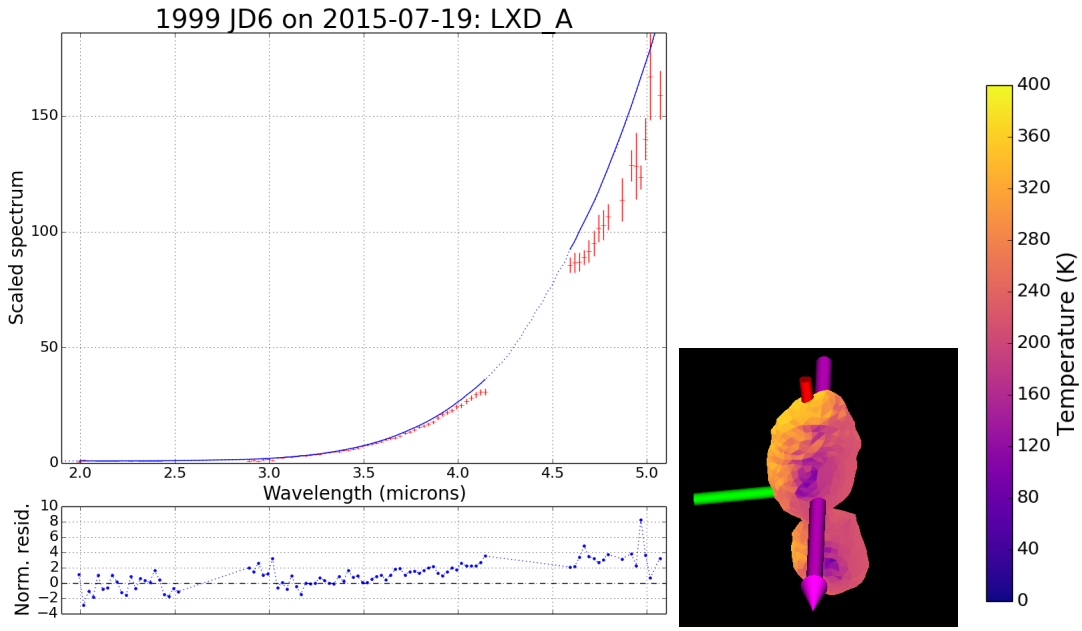

Figure 4.3: Left: The red points show the scaled spectrum of JD6, as measured with SpeX LXD on July 19, 2015. The blue curve shows the corresponding spectrum from the (preliminary) best JD6 thermal model.
Right: A view of the JD6 thermal model, with facets colorized by the modeled surface temperatures.

4.1.2 Future work

In addition to the observations from Spitzer and the IRTF, JD6 was observed by WISE on multiple dates in 2010, in all four bands (Mainzer et al., 2011, 2014). I will compare the thermal models to the WISE observations.

The preliminary results suggest that JD6 has some inhomogeneities, like 1627 Ivar (Crowell et al., 2016) and (162421) 2000 ET70 (Marshall et al., 2017). However, before I can be confident in that conclusion, I will have to test some other possibilities. It is possible that changing JD6's reflectance spectrum (within its uncertainties) will improve the fits. SHERMAN also includes the capability to let a model's thermal properties vary with temperature, as has been measured in some laboratory studies of meteorites (Opeil et al., 2010, 2012; Consolmagno et al., 2013), and to let the asteroid's density vary with depth. Incorporating some or all of these effects will introduce additional model parameters, but the set of infrared observations of JD6 is extensive enough that it still may be possible to find a unique solution.

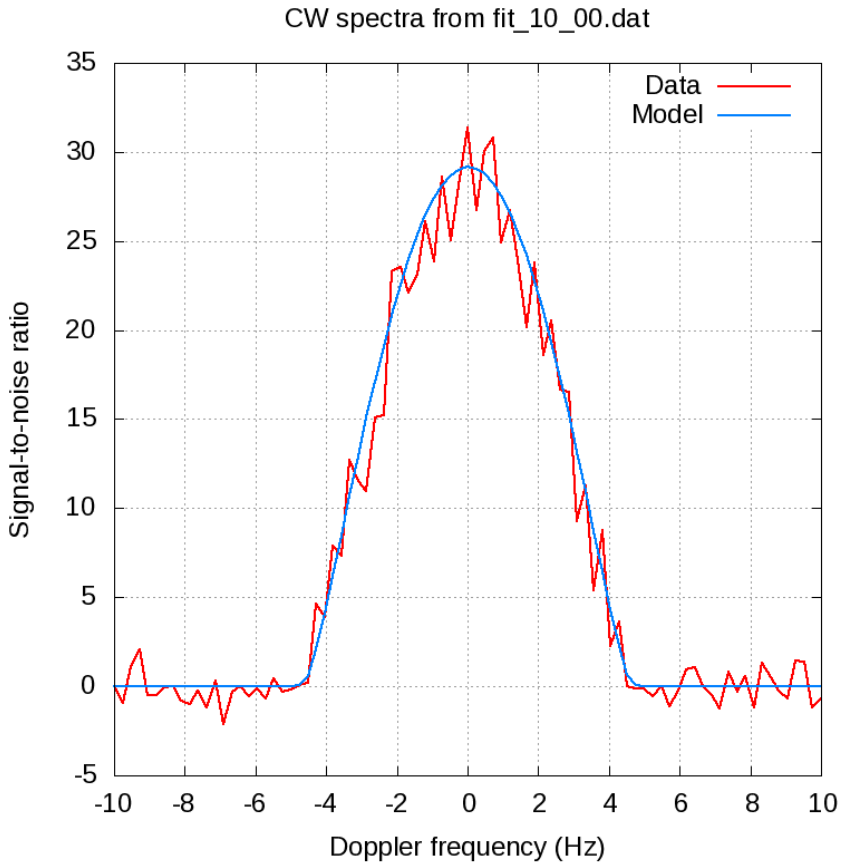

Figure 4.4: Sum of CW spectra of 1998 UO1, observed with Arecibo on September 22, 2008. The mid-receive time was 14:10:53 UT. The blue curve shows the calculated spectrum from one of the best shape models.

4.2 Shape modeling for (137032) 1998 UO1

Near-Earth asteroid (137032) 1998 UO1 was observed by radar during its close approaches in 2008 (0.063 au) and 2010 (0.082 au); one CW spectrum is shown in Figure 4.4. In addition, there are lightcurve observations of UO1 from six different apparitions: 2002, 2004, 2006, 2008, 2010, and 2014; see Figure 4.5.

The delay-Doppler images of UO1 have fairly coarse resolution (at best, 75 m in range), which is not enough to reveal fine details in the shape. This compli-

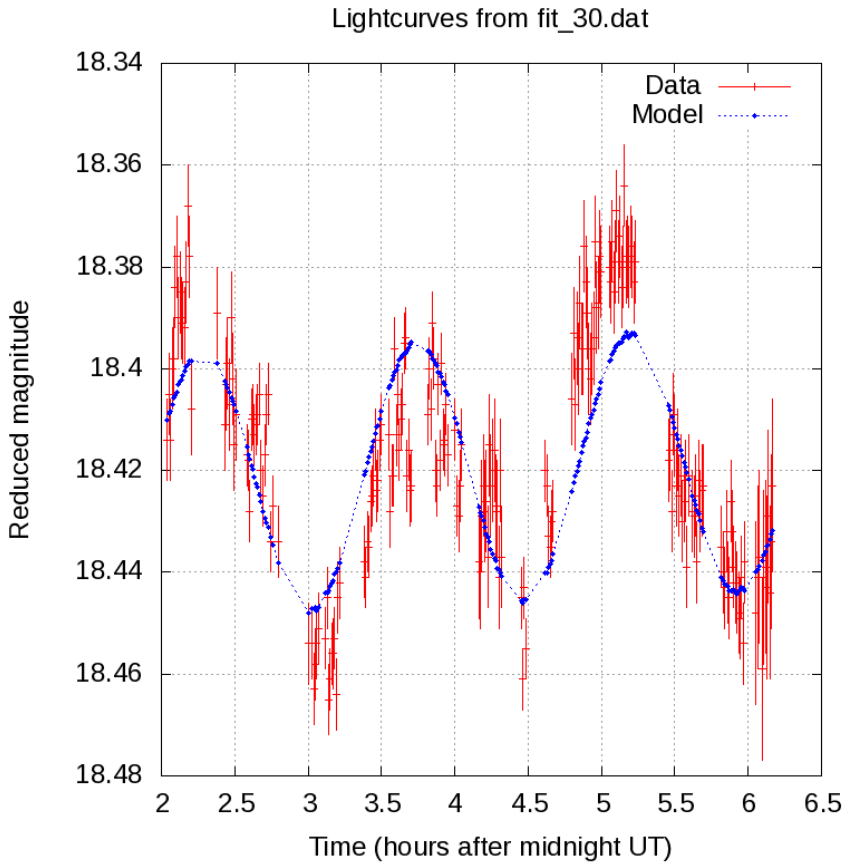

Figure 4.5: Lightcurve of 1998 UO1, from Magdalena Ridge Observatory on October 29, 2014, along with the model lightcurve from one of the best shape models.

cates shape modeling, since there are no features that clearly appear in multiple images. (In contrast, for 1999 JD6 there were distinct bumps and concavities that one could clearly recognize in images from different days.) A summary of UO1's shape is given in Table 4.2.

UO1 is not very elongated, so its lightcurves do not have large amplitudes (0.1 mag or less). Some of the UO1 lightcurves allowed for possible periods of 3.65 or 4.37 hours, but with the full set of data, these alternate periods can be confidently ruled out.

Parameter		Value	Uncertainties	Rel. unc.
Maximum diameter	$2a$	1.32 km	0.09 km	7%
Elongation	a/b	1.12	0.05	5%
Flattening	b/c	1.10	-0.10 +0.16	12%
Sidereal rotation period	P	2.921 h	0.008 h	0.3%

Table 4.2: Parameters and one-sigma uncertainties for the preliminary shape model of 1998 UO1, utilizing radar and lightcurve data.

With the full set of radar and lightcurve data, there are two acceptable solutions for UO1's pole position: near ecliptic coordinates $(\lambda, \beta) = (357°, +36°)$ (prograde) or near $(174°, -36°)$ (retrograde). Delay-Doppler images for both of those poles provide good fits to the data, as shown in Figure 4.6. We have infrared spectra of UO1 which may be sufficient to break this degeneracy.

The available data do not allow a clear determination of whether UO1's shape is closer to an ellipsoid or to the walnut-like shapes with equatorial ridges that are commonly observed among the NEA population, such as the 1999 KW4 primary (Ostro et al., 2006) or 2008 EV5 (Busch et al., 2011). A possible walnut-like model for UO1 is shown in Figure 4.7. Despite UO1 having a fairly short rotation period and a shape that may resemble the primary bodies of some NEA binaries, it does not have a detectable satellite.

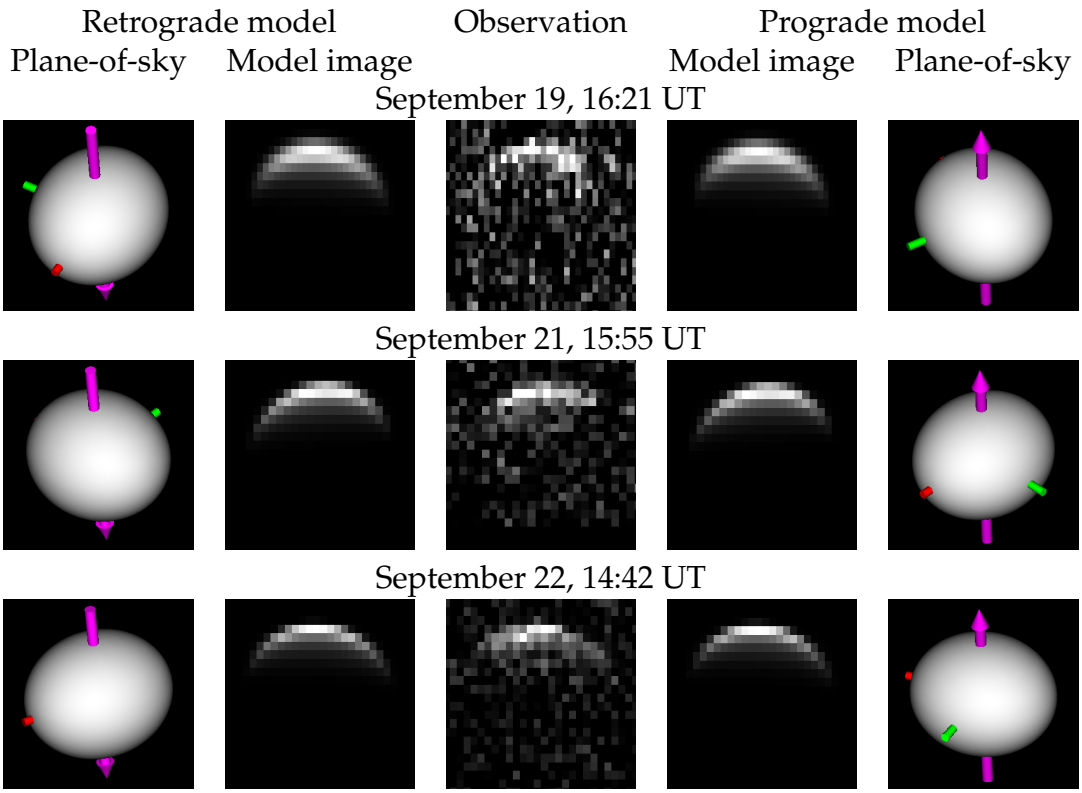

Figure 4.6: Modeled Delay-Doppler frames for two UO1 models with different pole positions. The columns on the left show a model with a pole direction of $(174°, -36°)$. The columns on the right show a model with a pole direction of $(357°, +36°)$, nearly the exact opposite of the first pole. The radar images are stretched so that their spatial scale is the same as that of the plane-of-sky image (square frames with a side length of 1.65 kilometers), but the radar images' vertical axis, range, is perpendicular to the plane of the sky. All of these observations are from September of 2008.

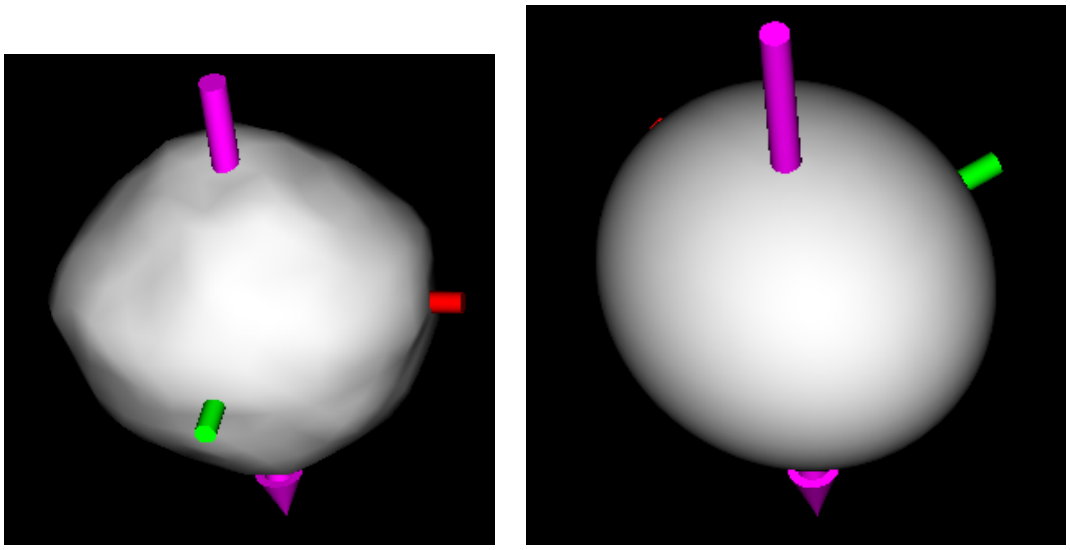

Figure 4.7: Two possible shape models for 1998 UO1. The model on the left has 400 vertices, whose positions all were allowed to vary during the fit. The model on the right is simply an ellipsoid.

4.3 Pole searches with Bayesian optimization

This project was a part of my work at the 2017 NASA Frontier Development Lab (FDL), where we explored several different ways of speeding up asteroid shape modeling. Adam Cobb (Oxford) and I did most of the work on Bayesian optimization. The other team members, who focused on other projects (not described here), were Agata Rożek (Kent) and Grace Young (Oxford). Our mentors were Michael Busch (SETI Institute), Yarin Gal (Cambridge), and Chedy Raïssi (INRIA).

In shape modeling, when doing a pole search, one normally has to specify the various pole positions that should be tested. To sample the entire celestial sphere with test points that are spaced about ten degrees apart requires one to test about 400 pole positions. (Ten degrees is the typical uncertainty in published radar-derived shape models' pole positions, e.g. Busch et al. (2011); Naidu et al. (2013).) Each of those may require over an hour of computational time. After a set of poles has been tested, one then checks the results and decides which pole positions to test next, typically trying finer spacing in the regions of parameter space that provide the best fits. This need for human oversight slows down the process, since someone must be watching the results, and SHAPE can only test the models that a human tells it to try.

Thus, one way to speed up the shape modeling process would be to automate the process of choosing new test points for a pole search. With intelligently chosen test points, one can explore the parameter space more efficiently and find the best pole in less time. One procedure for doing this is to use Bayesian optimization, which provides a means of representing an arbitrary smooth function

and searching for its minimum, as illustrated in Figure 4.8.

We used a software package called Spearmint (Snoek et al., 2012)[1] to do the Bayesian optimization calculations. Spearmint represents the unknown function as a Gaussian process and finds its global minimum automatically, choosing its next test point intelligently based on previous results, rather than just doing a grid search in which all of the test points were chosen before any models had been run. With Bayesian optimization, modeling the function of interest as a Guassian process allows one to estimate its posterior mean and variance over its entire domain, thus enabling systematic estimation of which possible test points are most likely to yield an improvement.

For asteroid shape modeling, we want to minimize the objective function, which can be considered to be a function of the model's pole position (and other parameters). The procedure for doing a pole search with Spearmint is as follows:

1. Set up a template directory and a Python script that can copy and modify it. (In this case, only the template model's pole position will be modified.)
2. Run Spearmint (which is written in Python 2) with that Python script.
3. Spearmint will copy the template directory, modify the pole position, and then run SHAPE (or PSHAPE) on the new model. SHAPE will hold the pole position constant while searching for the best values of other model parameters (e.g. size, photometric properties, rotation period).
4. Once that model has finished, Spearmint will read its value of the objective function from SHAPE's log, compare that value to all previous models, and then run a new model with a different pole position.

[1] `https://github.com/JasperSnoek/Spearmint`

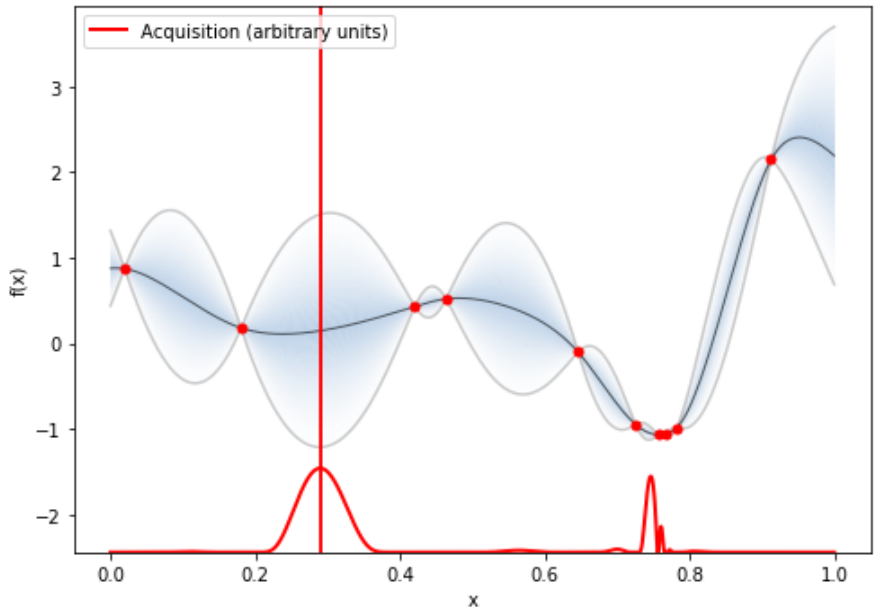

Figure 4.8: One-dimensional example of Bayesian optimization. The red dots are points that have previously been tested. The blue curve shows the current best estimate of the function, modeling it as a Gaussian process, and the blue shading and gray curves indicate the uncertainties. When selecting the next point to test, there is a trade-off between selecting points near the best known minimum vs. points in regions of parameter space that have not been densely sampled. In this case, the next test point will be near $x = 0.3$, in a region that is sparsely sampled. Image courtesy of Adam Cobb, using GPyOpt (GPyOpt team, 2016).

5. Spearmint will repeat this procedure until convergence, or until it is stopped by the user (presumably after a sufficient number of poles have been tested).

Spearmint will gradually search the parameter space (here, the celestial sphere) and find the pole that yields the best fit to the data.

The 2016 FDL team explored the use of Bayesian optimization for pole searches (Raissi et al., 2016). However, their calculations assumed a rectangular coordinate system for pole longitude and latitude. This was inefficient because

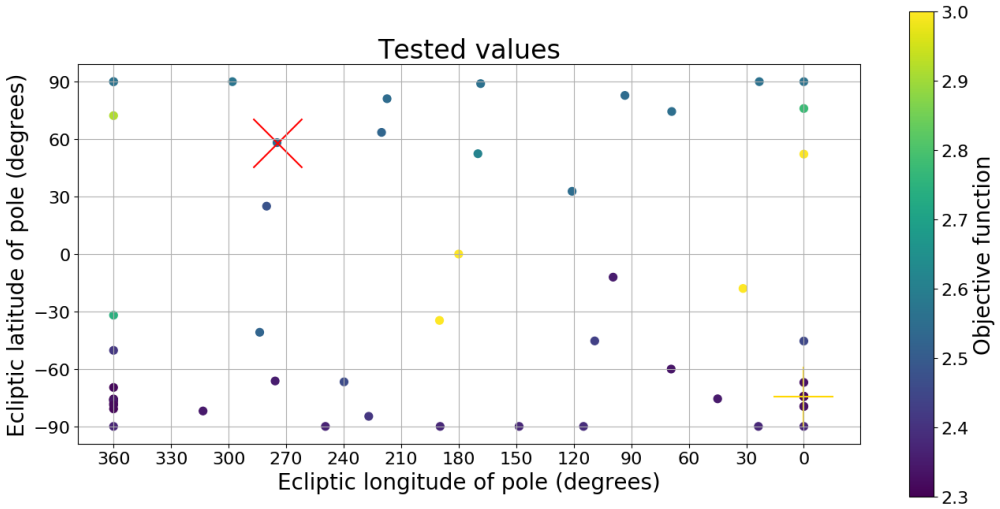

Figure 4.9: A test showing a pole search with Bayesian optimization for 2000 ET70, with a subset of the data. For this test, Spearmint was working in rectangular coordinates, so it unnecessarily spent time exploring redundant points along the "boundaries" of the celestial sphere. The red X shows the latest completed model, and the yellow cross shows the best model that has been found up to this point.

it did not utilize the symmetries of spherical coordinates. For instance, every point at latitude −90° is the same, and every point at latitude +90° is the same, regardless of their longitudes. Similarly, a point at longitude 360° is the same as a point at longitude 0° that has the same latitude. However, assuming a rectangular coordinate system fails to exploit these symmetries, so Spearmint ended up testing many points on the "boundaries" of the coordinates, not recognizing that many of those points were redundant. This is illustrated in Figure 4.9.

For FDL 2017, Adam Cobb added functions to Spearmint to have it evaluate and generate test points in spherical coordinates, following Carr et al. (2016), and I wrote a set of scripts to get Spearmint to work with SHAPE. Figure 4.10 shows a pole search tests for the same asteroid and same data set as Figure 4.9, but using the spherical coordinate system.

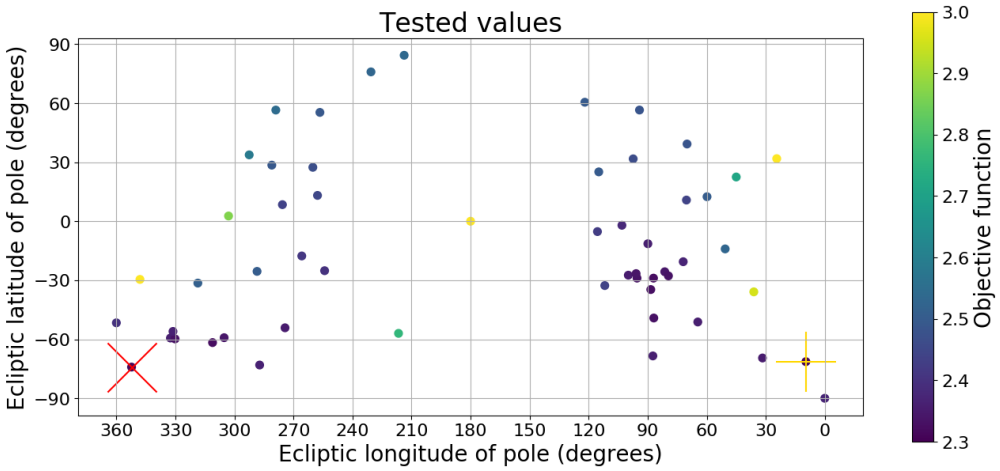

Figure 4.10: Another test showing a pole search with Bayesian optimization for 2000 ET70, with a subset of the data. For this test, Spearmint was working in spherical coordinates, so it recognized the periodic nature of the celestial sphere, and it did not choose redundant test points. The red X shows the latest completed model, and the yellow cross shows the best model that has been found up to this point.

When working in spherical coordinates, Spearmint avoids redundant test points and explores the parameter space more efficiently. The core functionality is working well, but some more testing is needed, in order to determine the fastest configuration for SHAPE and Spearmint. Once that is done, I look forward to getting these automated pole searches into computational pipeline at Arecibo Observatory.

For FDL 2017, we focused on using Bayesian optimization for shape modeling, to find an asteroid's pole position but not any other parameters. However, Bayesian optimization is quite general, and it also could be used to find other parameters of the shape, or used for different tasks. I am particularly interested in using it for thermal modeling, to explore the thermal parameter space in an autonomous fashion.

APPENDIX A

APPENDIX FOR CHAPTER 2

A.1 Supplementary figures for (162421) 2000 ET70

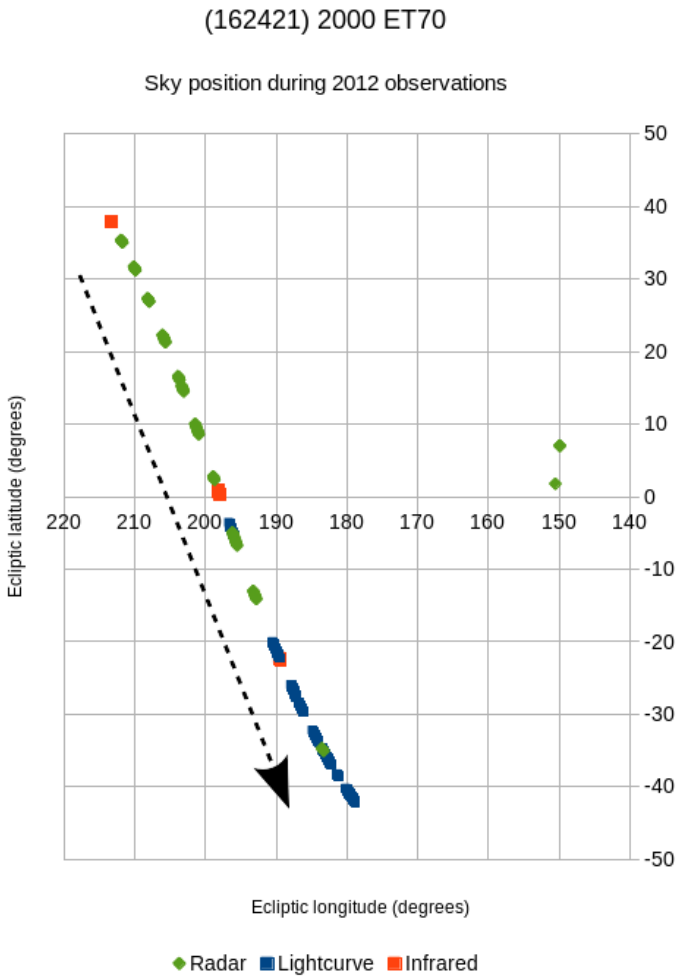

Figure A.1: Sky positions of ET70 during the observations in 2012, color-coded by observation type. This figure illustrates the values given in Table 2.1, Table 2.2, Table 2.3, and Table 2.5. The arrow shows the direction of ET70's apparent motion during the February observations. The points near (150°, +5°) are the Arecibo observations from August.

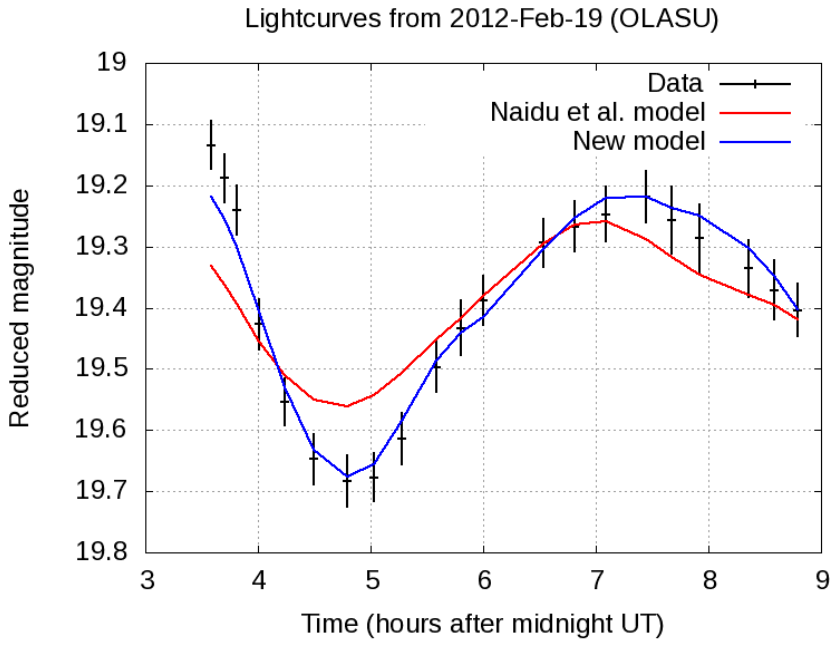

Figure A.2: Lightcurve observations from February 19, 2012 (black points with error bars; decimated). The red curve shows the lightcurve predicted by the model of Naidu et al. (2013), with a pole at ecliptic coordinates $(\lambda, \beta) = (80°, -50°)$. The blue curve shows the model lightcurve from our best shape model, with a pole at $(52°, -60°)$.

A.1.1 Lightcurves

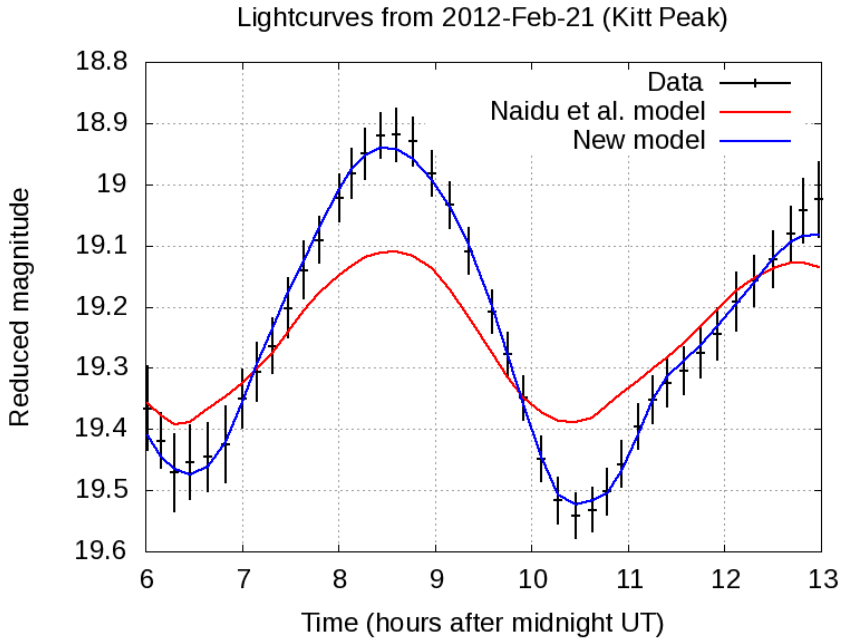

Figure A.3: Same as Figure A.2, for the lightcurve from February 21, 2012.

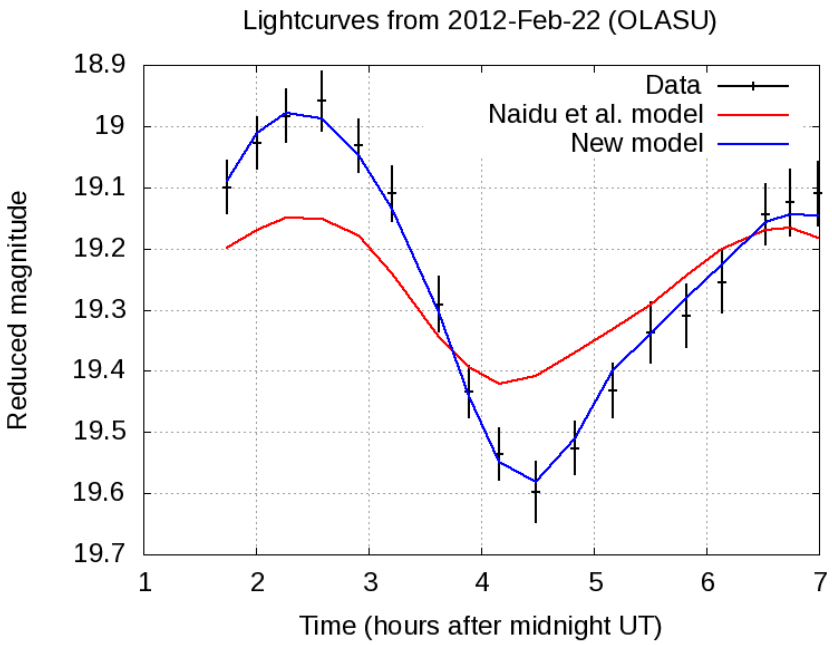

Figure A.4: Same as Figure A.2, for the first lightcurve from February 22, 2012.

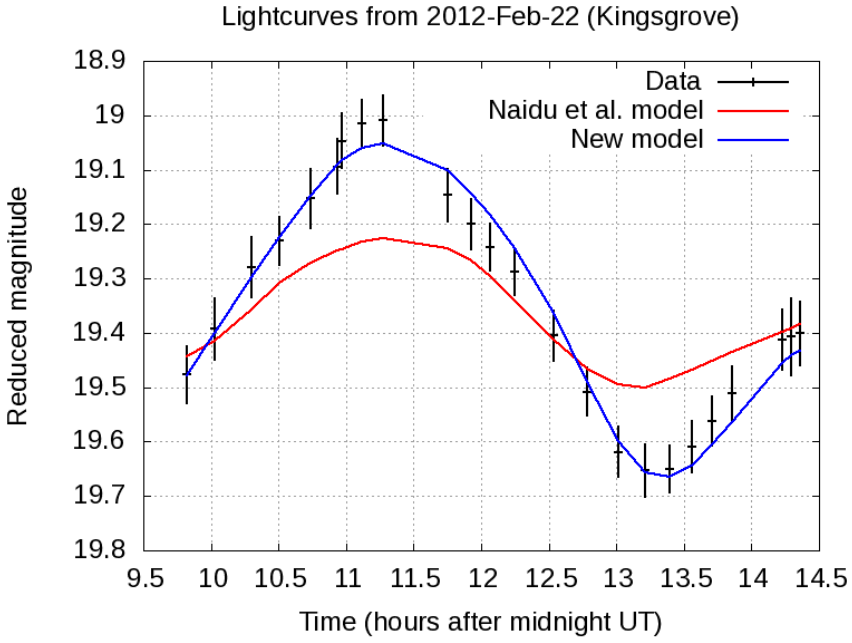

Figure A.5: Same as Figure A.2, for the second lightcurve from February 22, 2012.

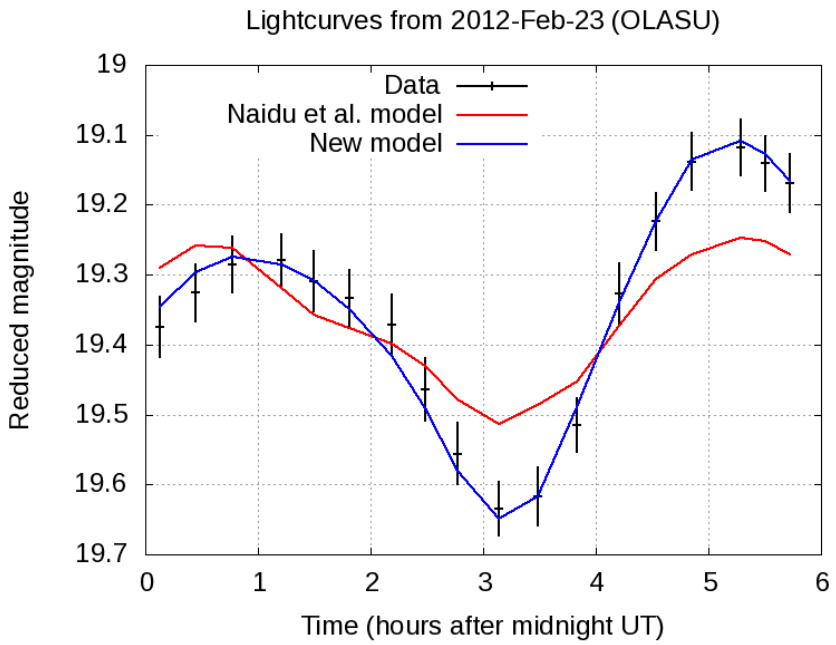

Figure A.6: Same as Figure A.2, for the first lightcurve from February 23, 2012.

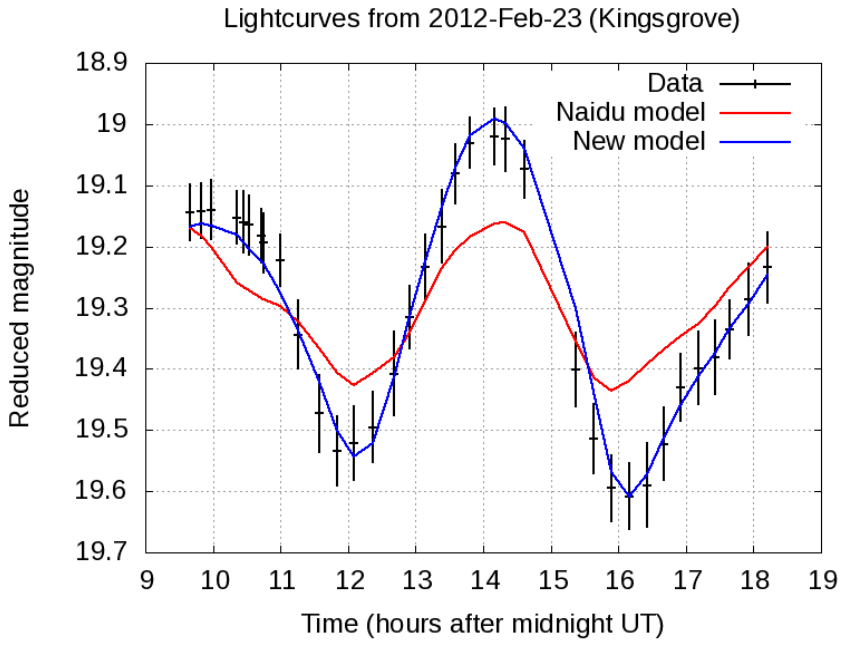

Figure A.7: Same as Figure A.2, for the second lightcurve from February 23, 2012.

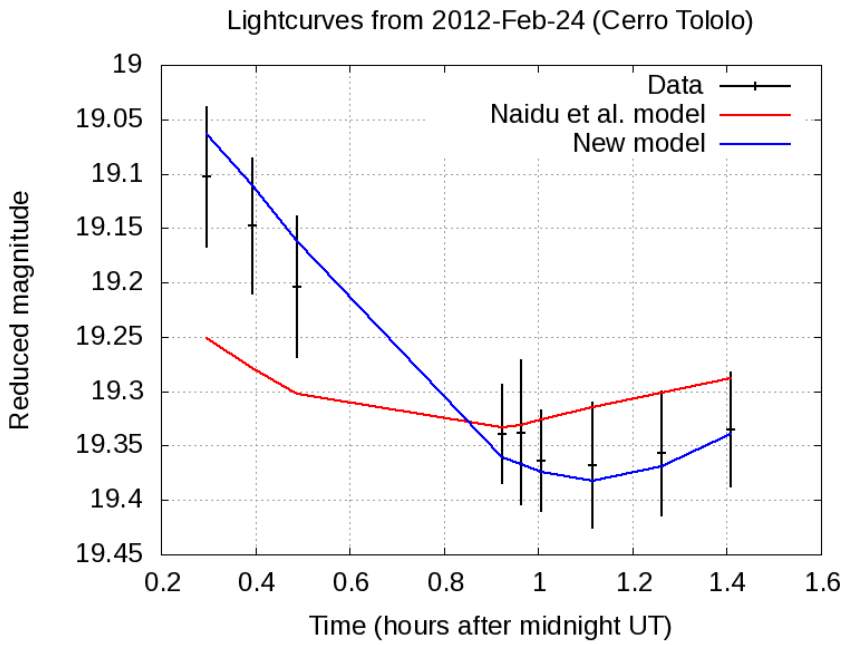

Figure A.8: Same as Figure A.2, for the first lightcurve from February 24, 2012.

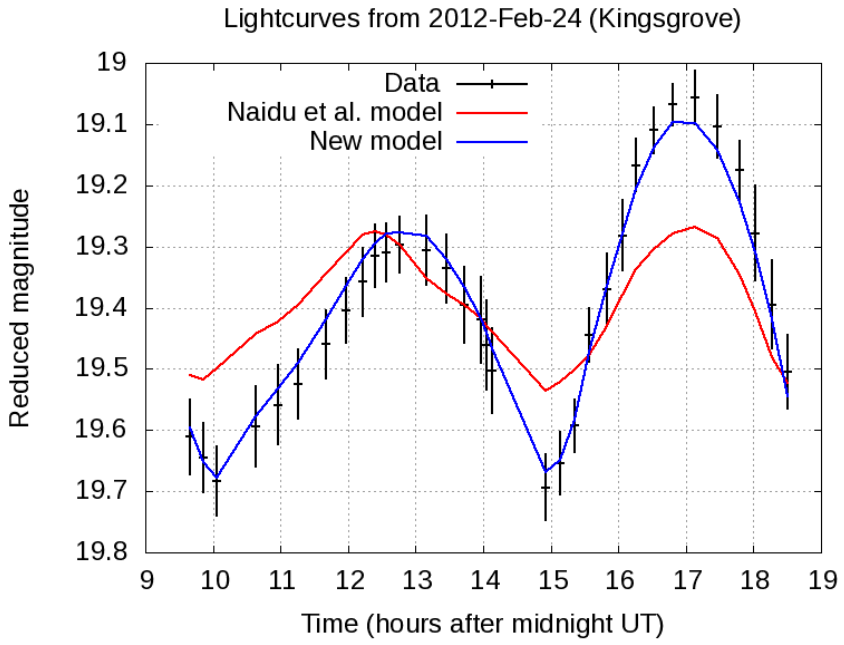

Figure A.9: Same as Figure A.2, for the second lightcurve from February 24, 2012.

A.1.2 Delay-Doppler images

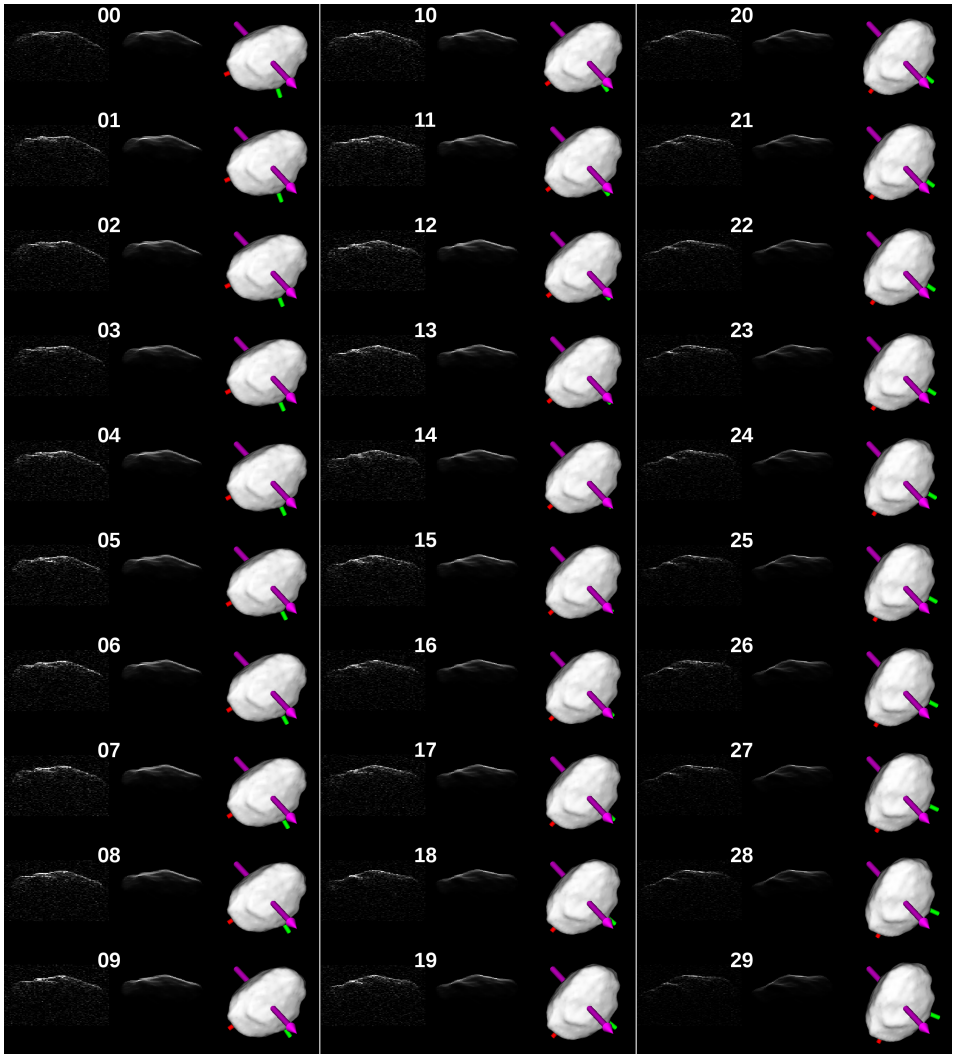

Figure A.10: The first thirty Arecibo delay-Doppler images from February 12, 2012. For each image, the left column shows the radar data, the center column shows the simulated (noise-free) delay-Doppler image derived from the nominal shape model, and the right column shows the simulated plane-of-sky view (as seen from Earth). In the delay-Doppler images, delay is plotted on the vertical axis (increasing from the top down), and Doppler frequency is plotted on the horizontal axis (increasing from left to right). In the plane-of-sky views, the sidereal spin vector (the model's shortest principal axis) is shown as a magenta arrow, and the long and intermediate principal axes are shown as red and green shafts, respectively. In the plane-of-sky views, north is upward and east is leftward. The radar images are stretched so that their spatial scale is the same as that of the plane-of-sky image (square frames with a side length of 3.5 kilometers), but the radar images' vertical axis, range, is perpendicular to the plane of the sky. Based on this work, the ET70 model's maximum diameter is 2.90 km, and its minimum diameter is 1.50 km.

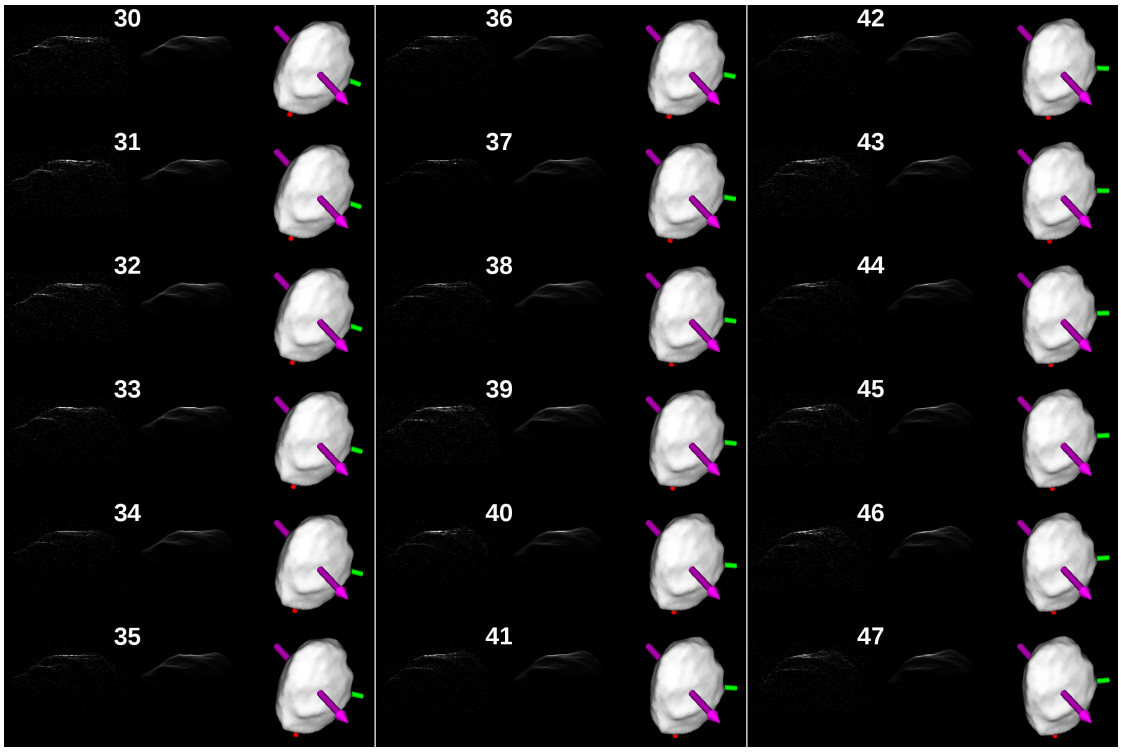

Figure A.11: Same as Figure A.10, for eighteen more Arecibo delay-Doppler images from February 12, 2012.

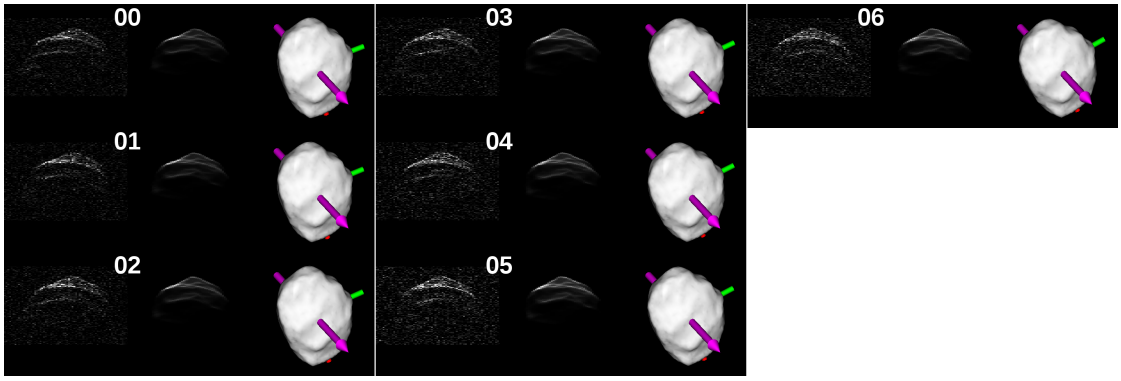

Figure A.12: Same as Figure A.10, for the last seven Arecibo delay-Doppler images from February 12, 2012. Note that these frames each have two or more bright leading edges. This makes them particularly helpful in constraining ET70's pole direction because a model with a misaligned pole would have those edges separated by the wrong number of delay cells.

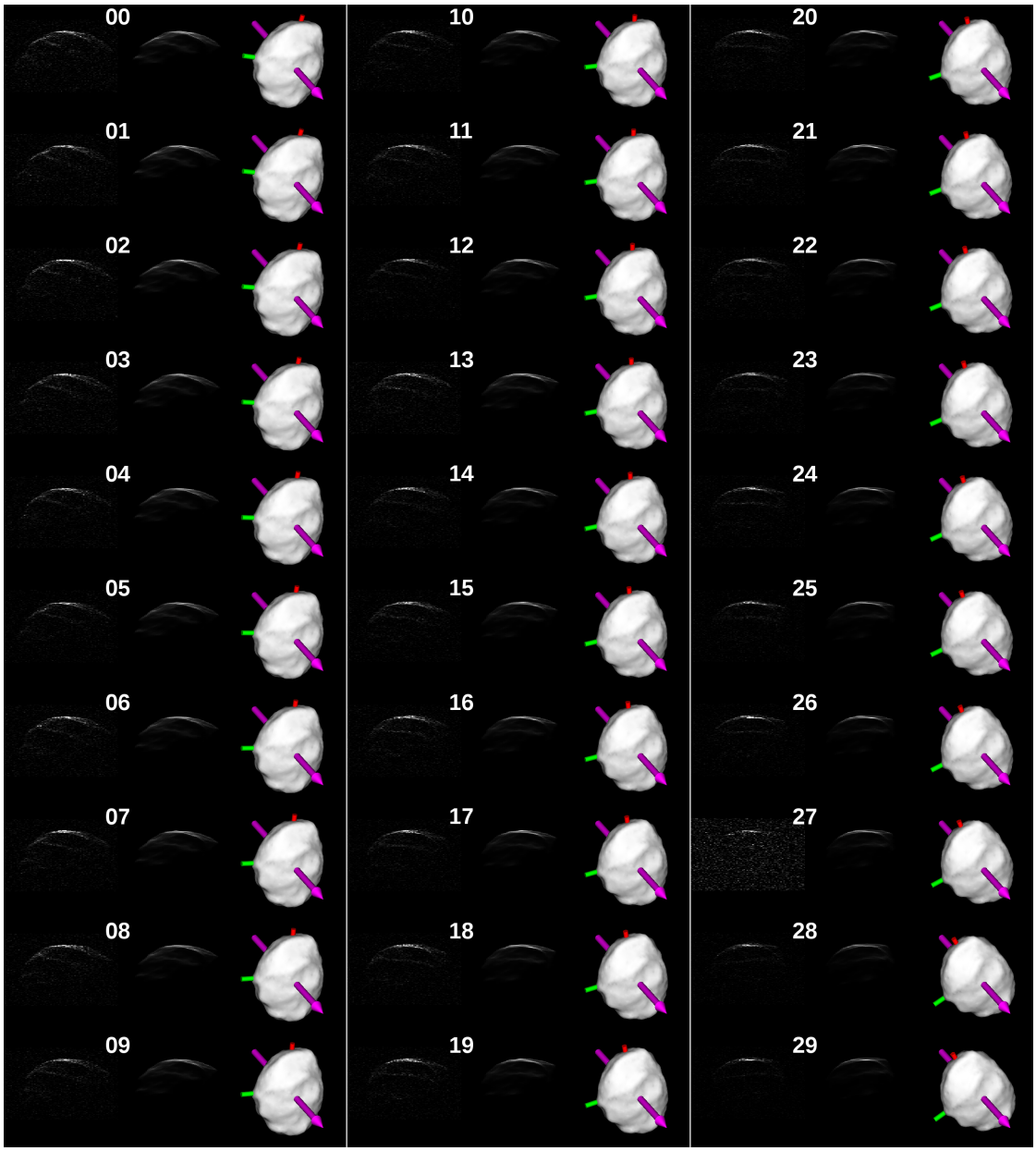

Figure A.13: Same as Figure A.10, for the first thirty Arecibo delay-Doppler images from February 13, 2012.

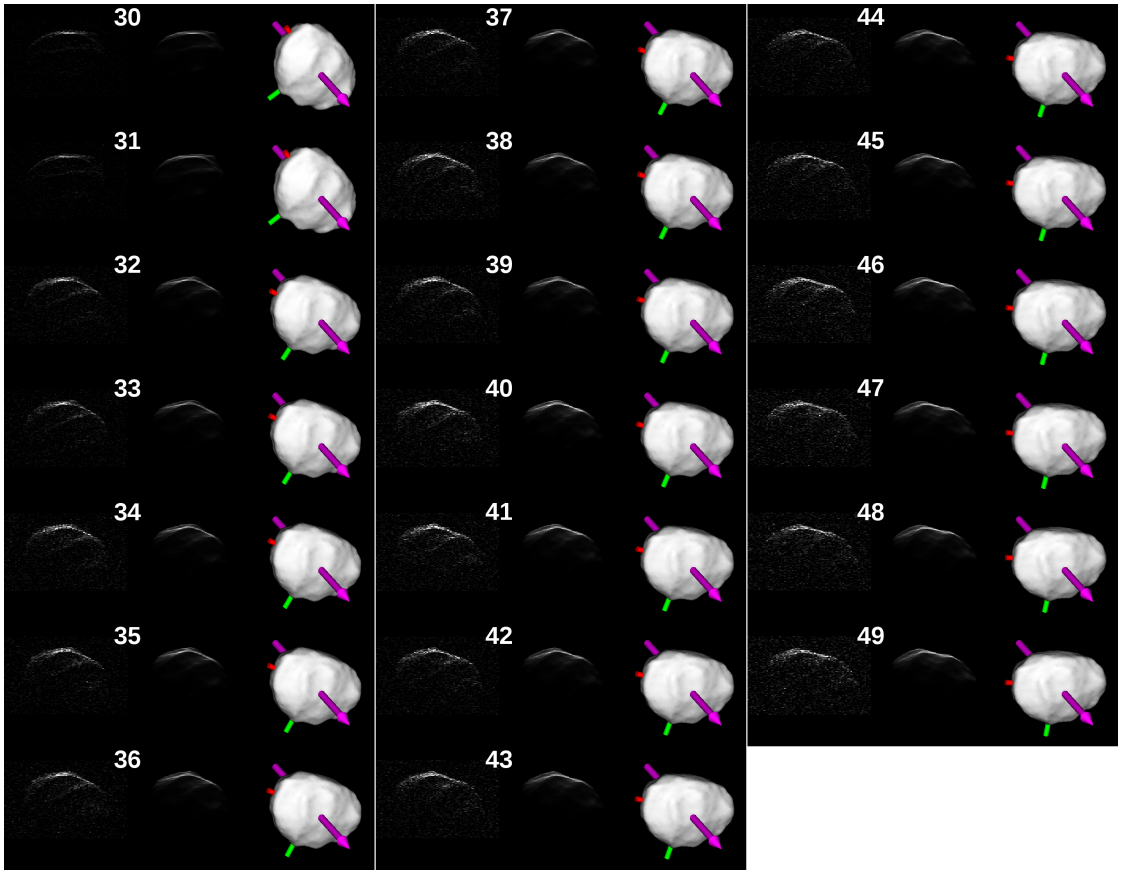

Figure A.14: Same as Figure A.10, for the last twenty Arecibo delay-Doppler images from February 13, 2012.

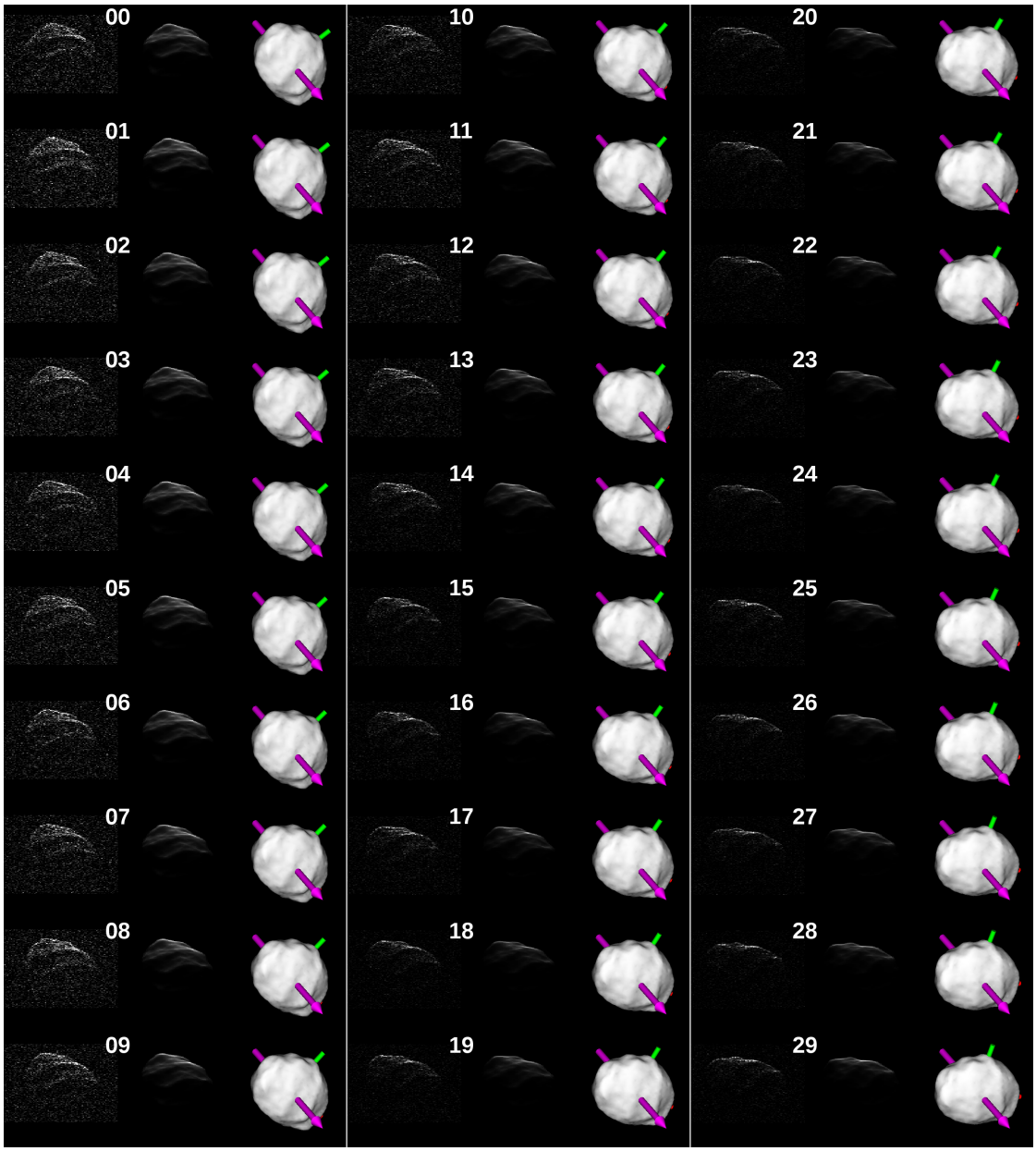

Figure A.15: Same as Figure A.10, for the first thirty Arecibo delay-Doppler images from February 14, 2012.

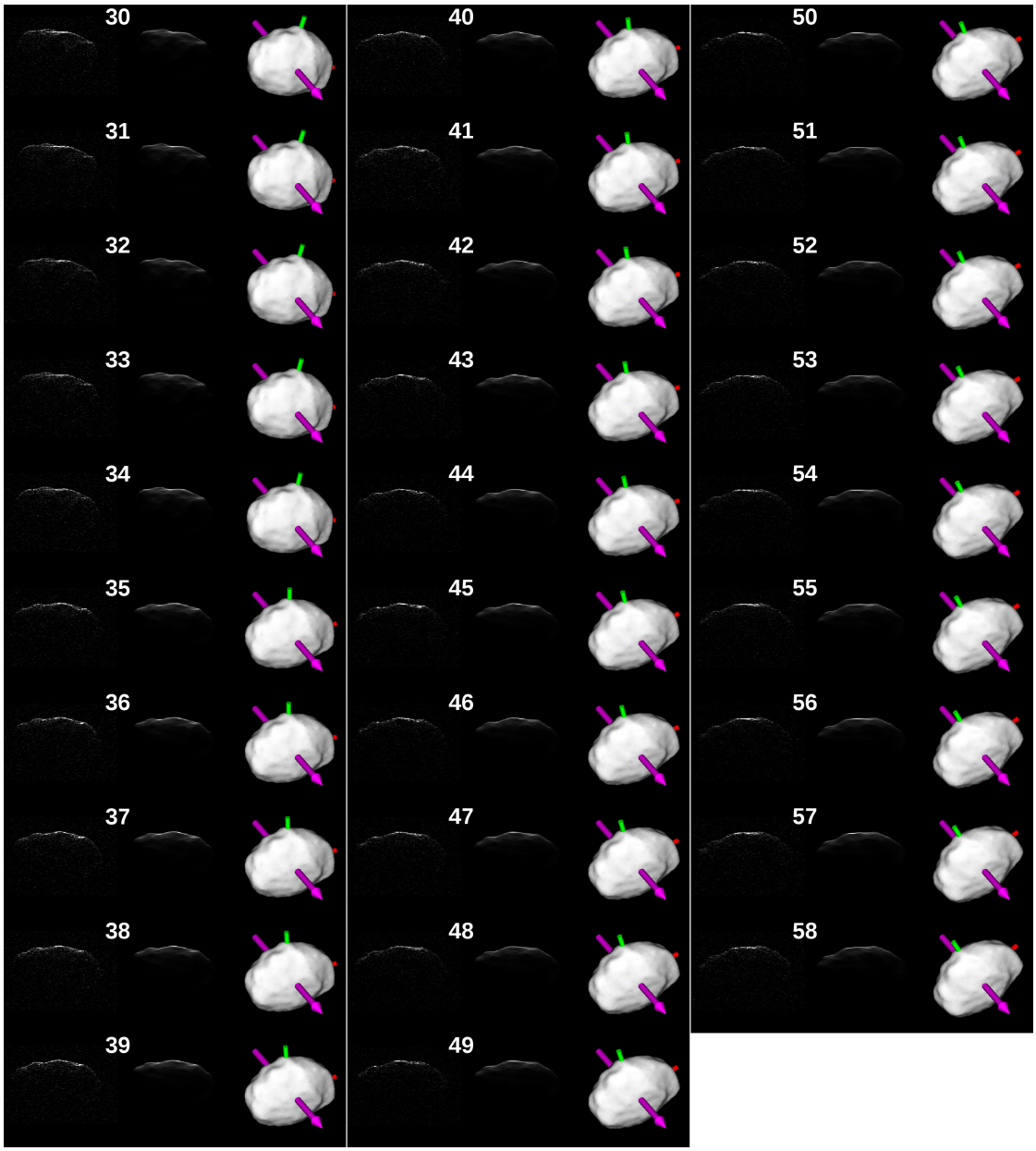

Figure A.16: Same as Figure A.10, for the last twenty-nine Arecibo delay-Doppler images from February 14, 2012.

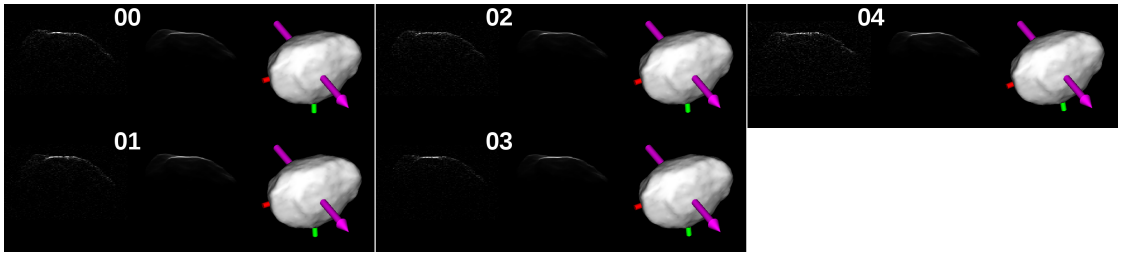

Figure A.17: Same as Figure A.10, for the first five Arecibo delay-Doppler images from February 15, 2012.

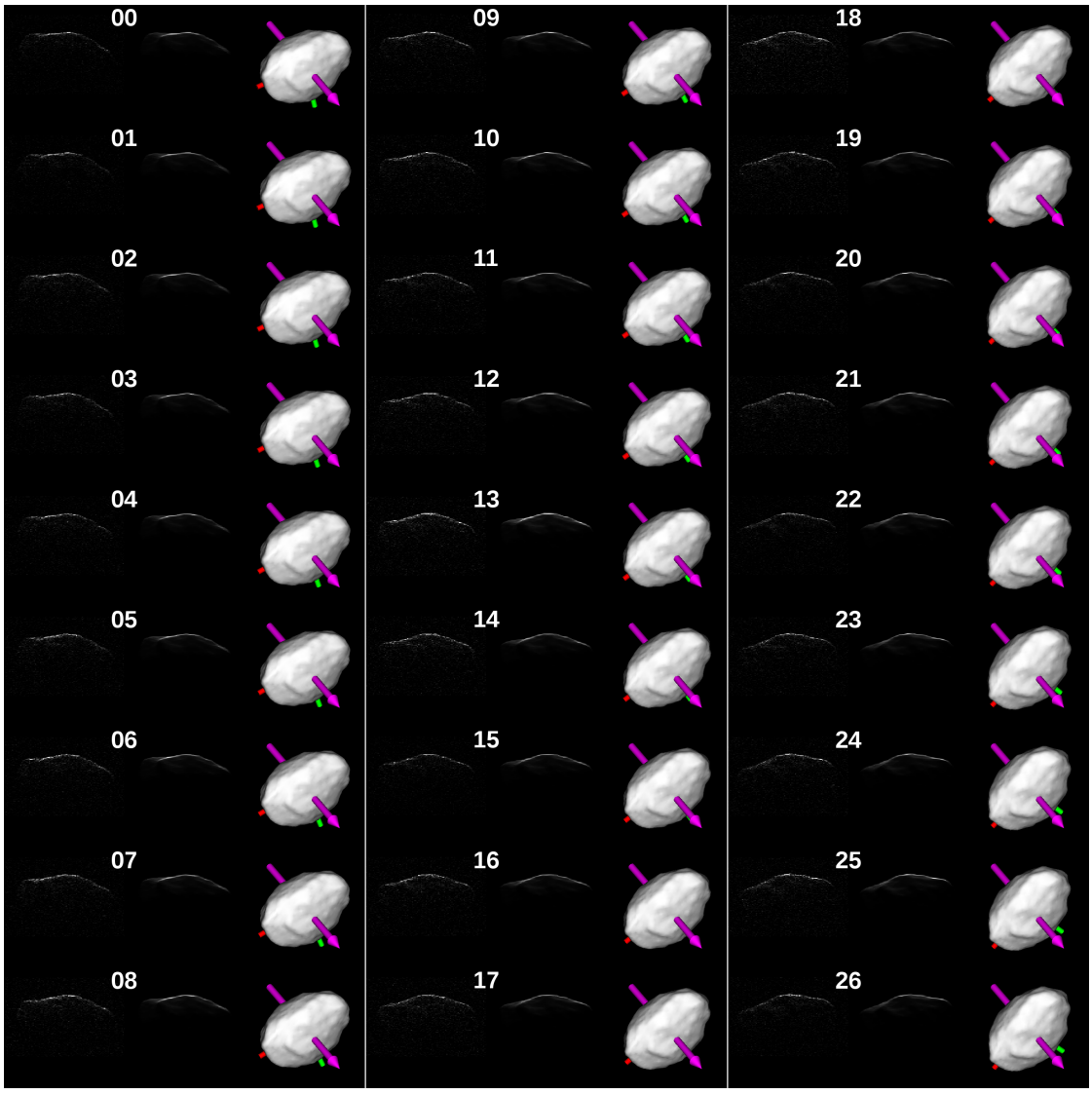

Figure A.18: Same as Figure A.10, for twenty-seven more Arecibo delay-Doppler images from February 15, 2012.

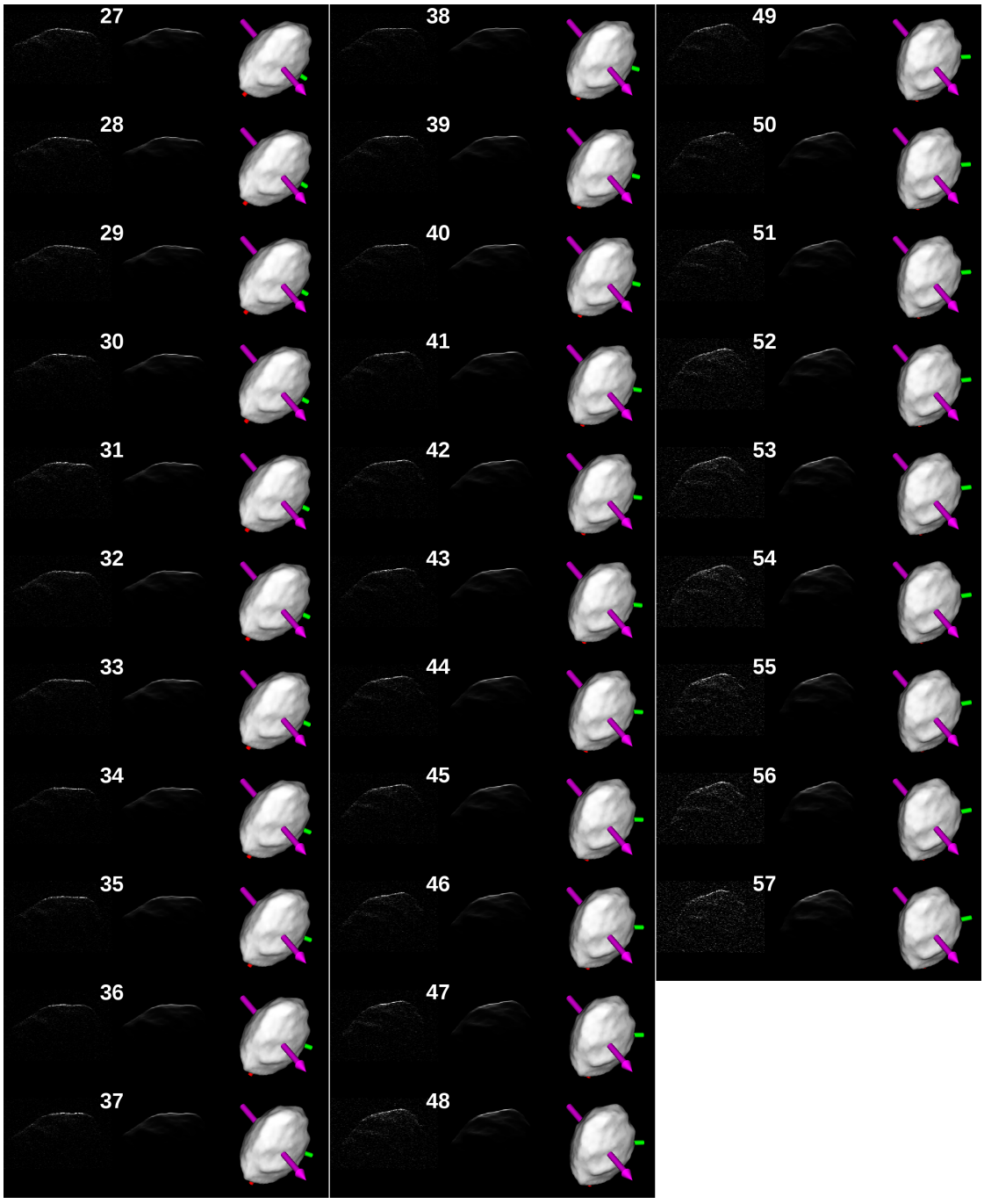

Figure A.19: Same as Figure A.10, for the last thirty-one Arecibo delay-Doppler images from February 15, 2012.

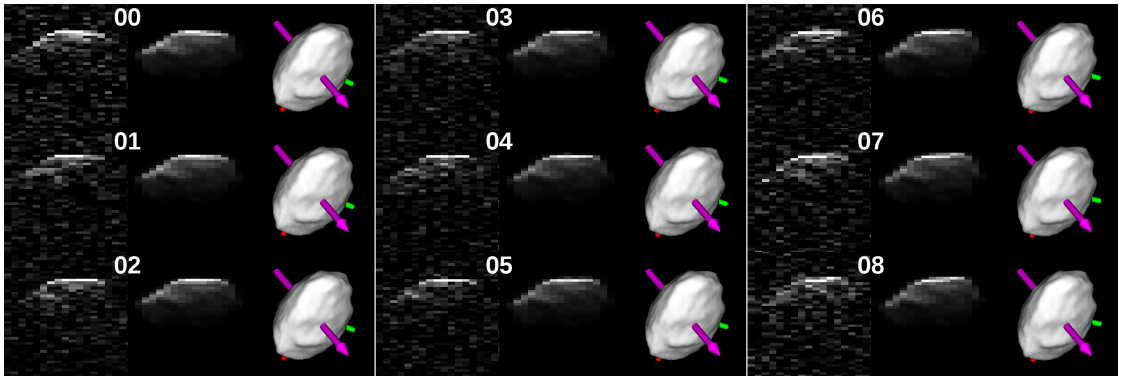

Figure A.20: Same as Figure A.10, for the first nine Goldstone delay-Doppler images from February 15, 2012.

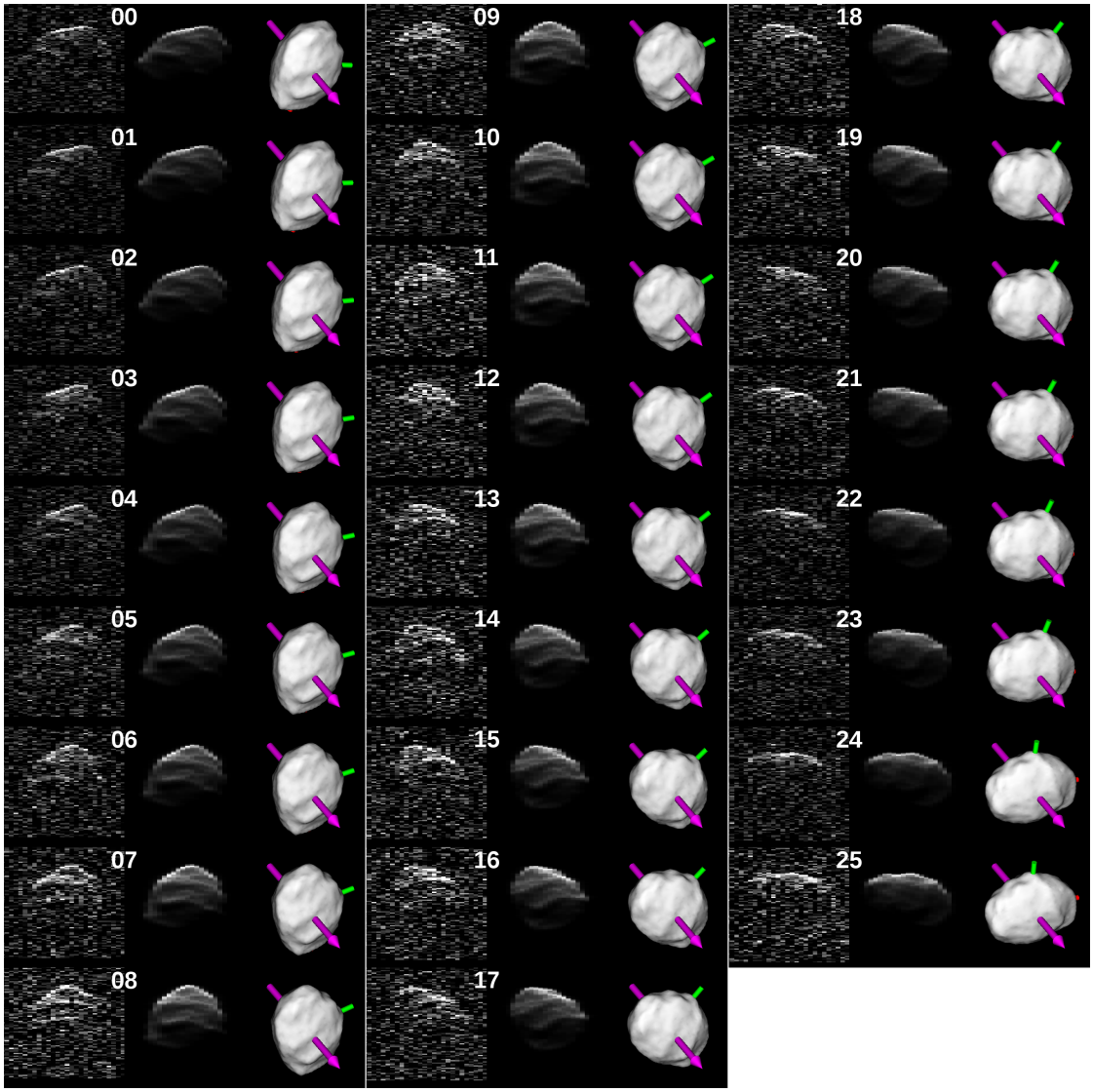

Figure A.21: Same as Figure A.10, for twenty-six sums of the final Goldstone delay-Doppler images from February 15, 2012.

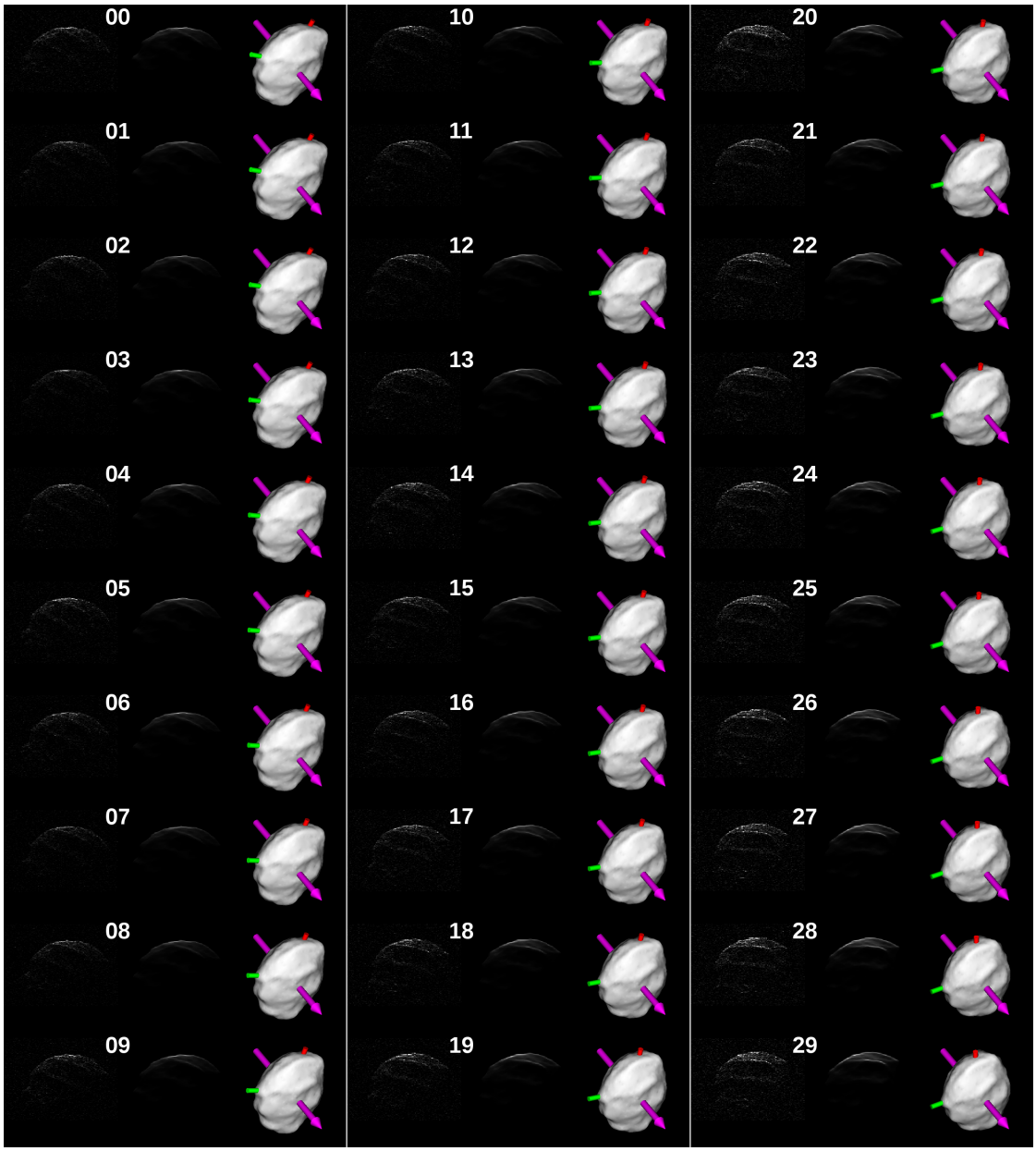

Figure A.22: Same as Figure A.10, for the first thirty Arecibo delay-Doppler images from February 16, 2012.

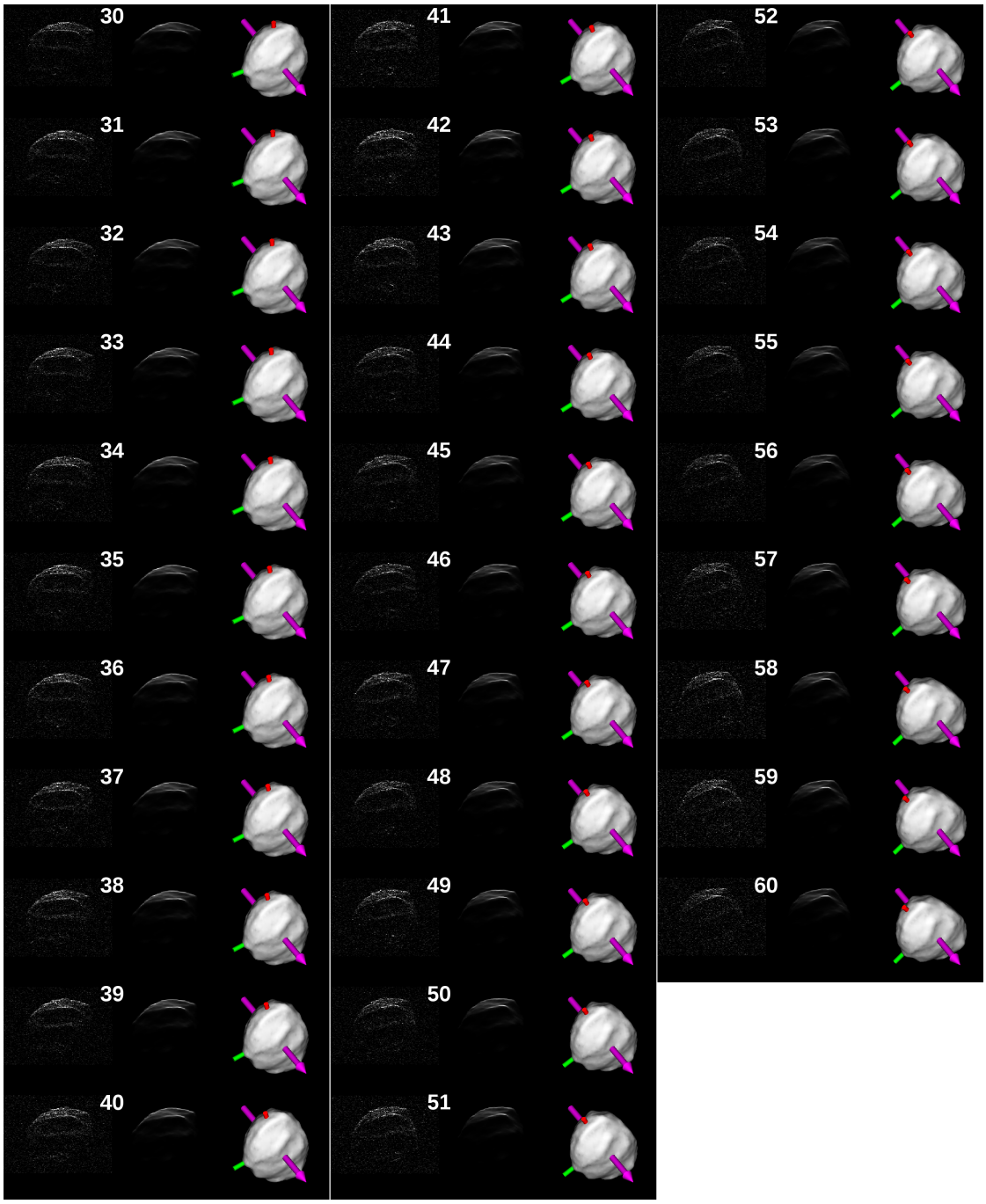

Figure A.23: Same as Figure A.10, for the last thirty-one Arecibo delay-Doppler images from February 16, 2012.

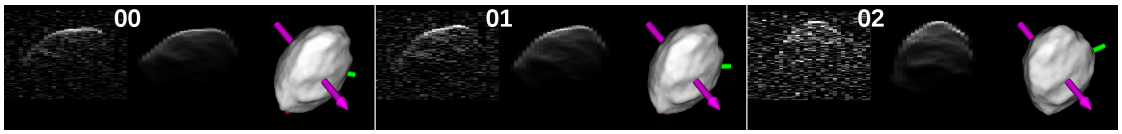

Figure A.24: Same as Figure A.10, for three sums of the first Goldstone delay-Doppler images from February 16, 2012.

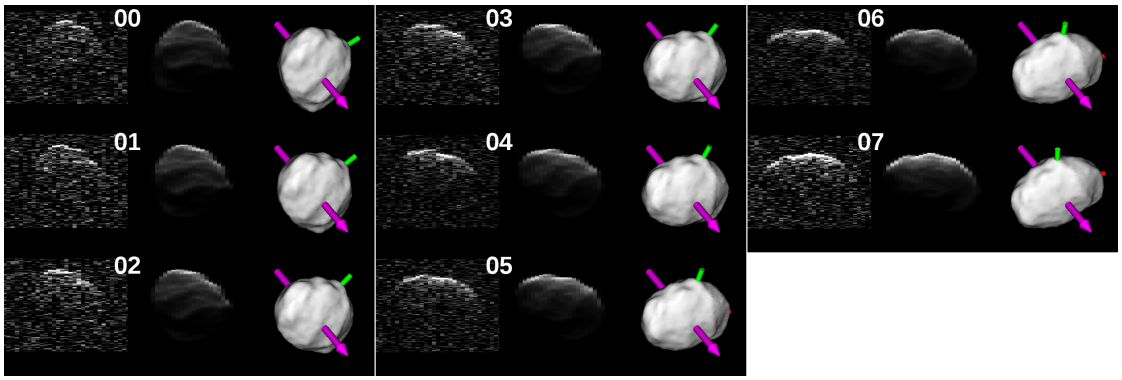

Figure A.25: Same as Figure A.10, for eight sums of the final Goldstone delay-Doppler images from February 16, 2012.

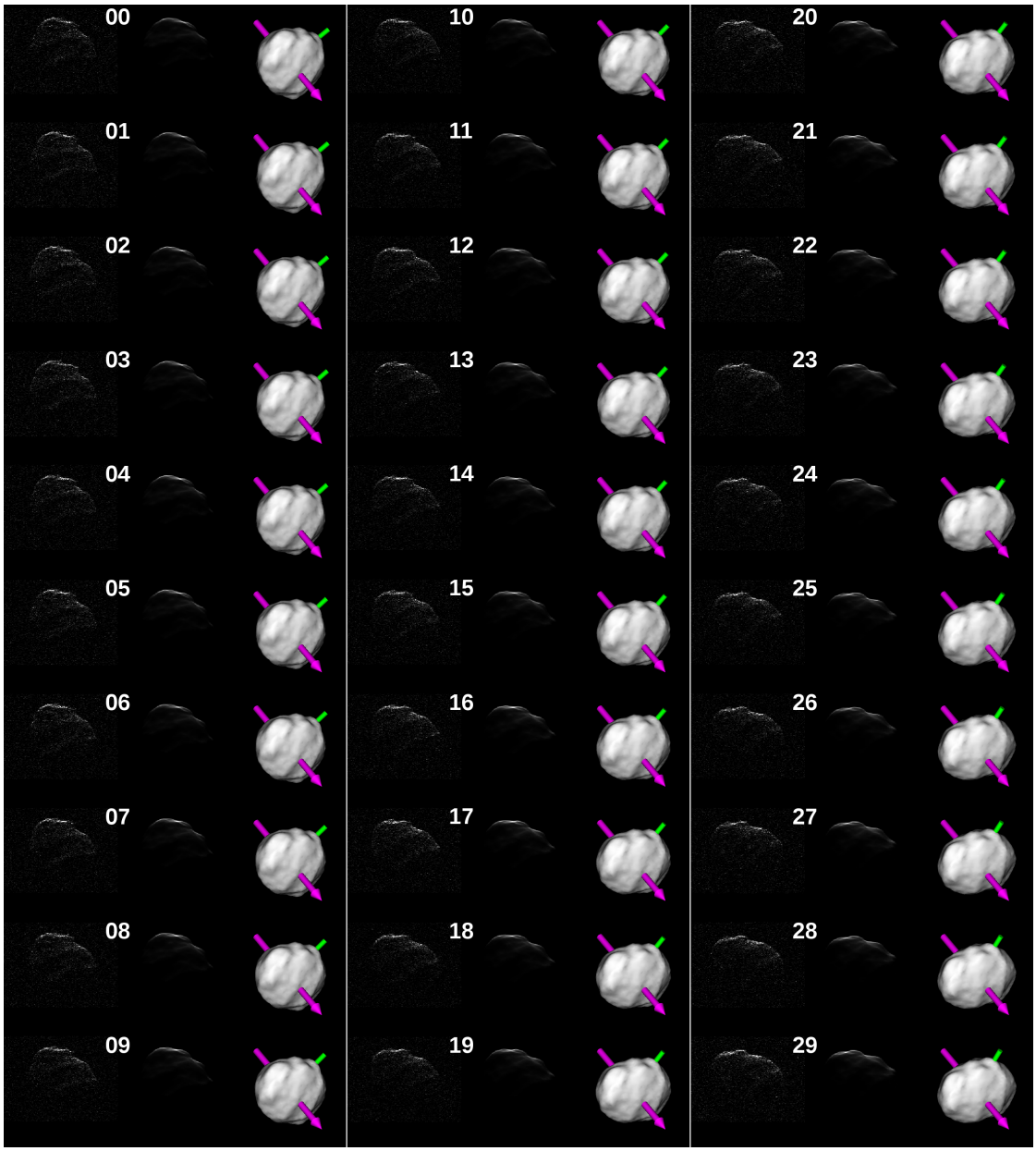

Figure A.26: Same as Figure A.10, for the first thirty Arecibo delay-Doppler images from February 17, 2012.

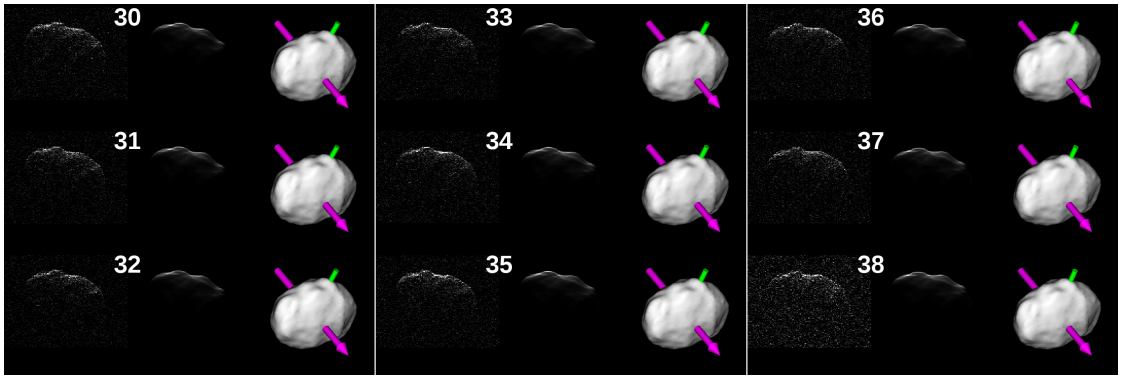

Figure A.27: Same as Figure A.10, for the last nine Arecibo delay-Doppler images from February 17, 2012.

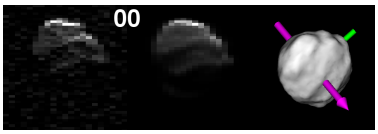

Figure A.28: Same as Figure A.10, for a sum of the first Goldstone delay-Doppler images from February 17, 2012.

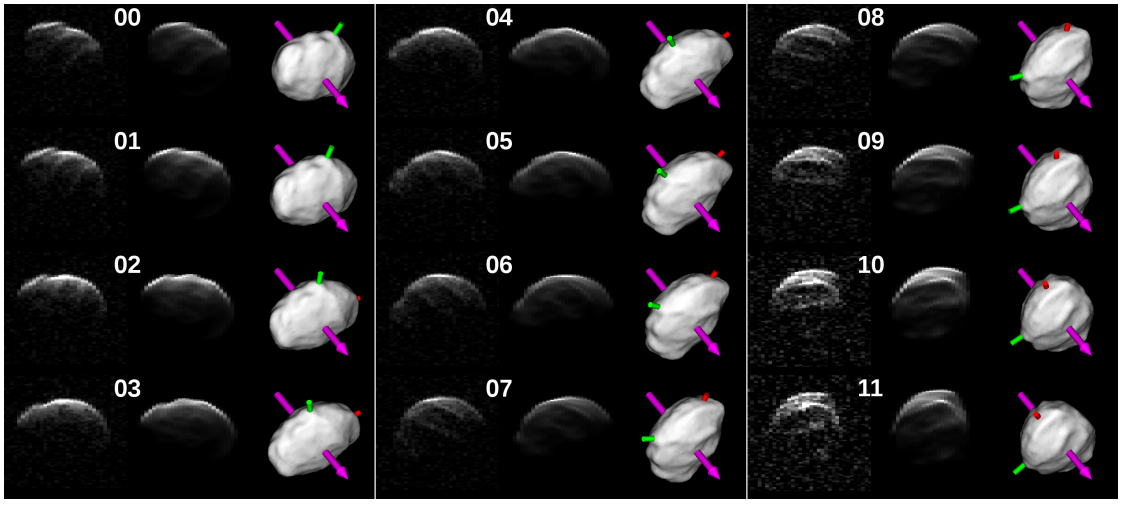

Figure A.29: Same as Figure A.10, for twelve sums of the last Goldstone delay-Doppler images from February 17, 2012.

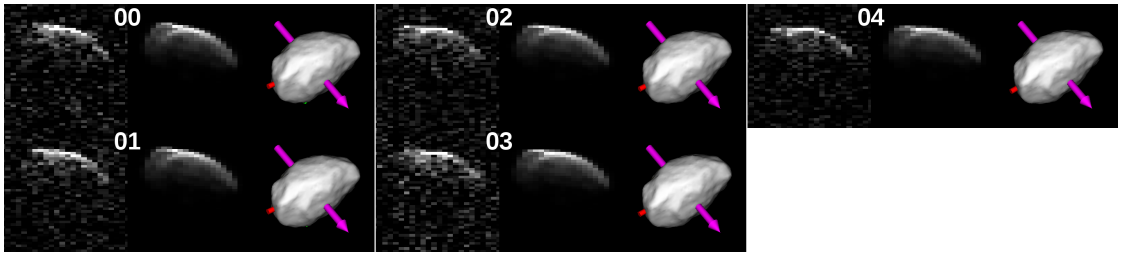

Figure A.30: Same as Figure A.10, for five sums of the first Goldstone delay-Doppler images from February 18, 2012.

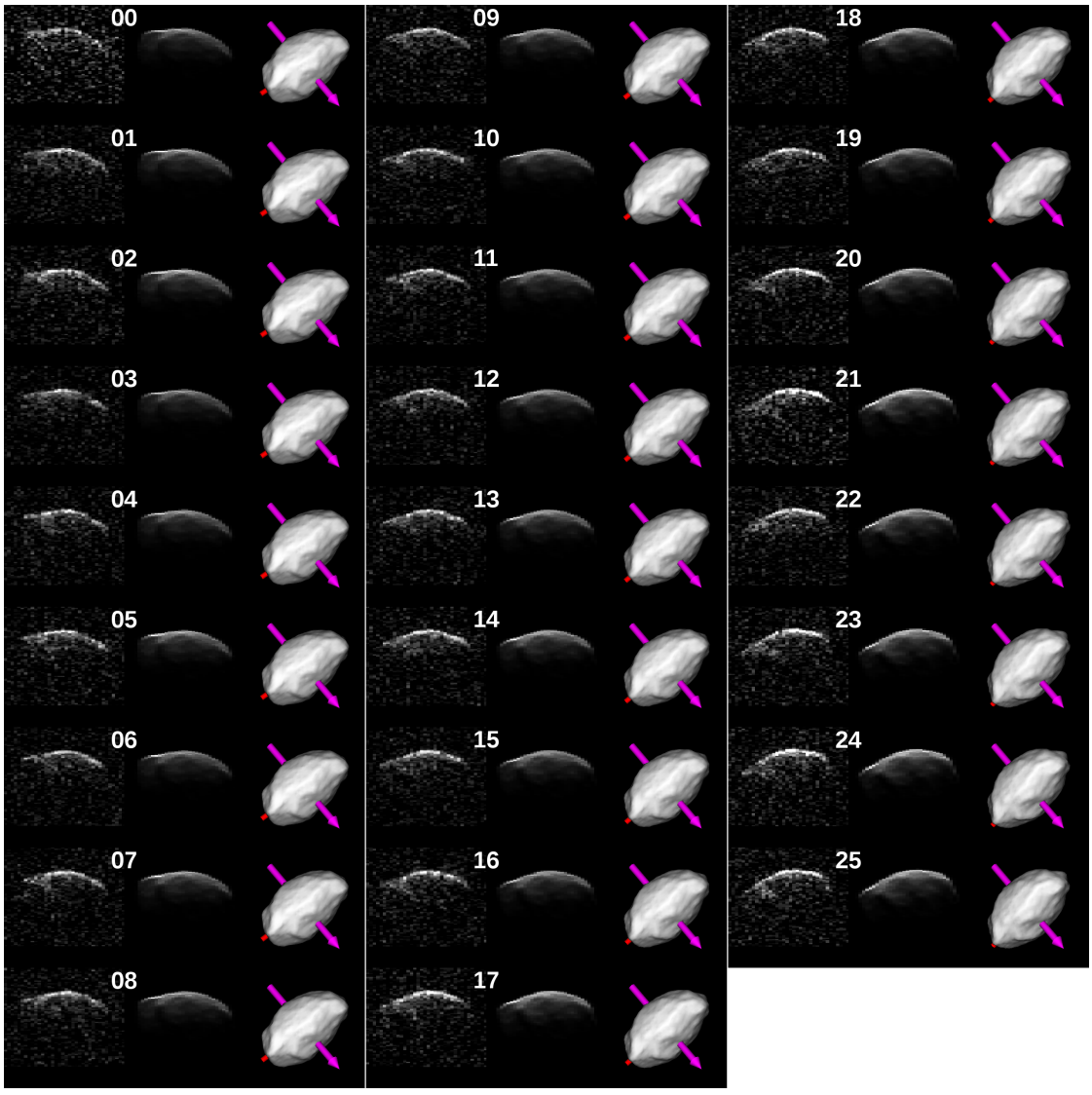

Figure A.31: Same as Figure A.10, for the last twenty-six Goldstone delay-Doppler images from February 18, 2012.

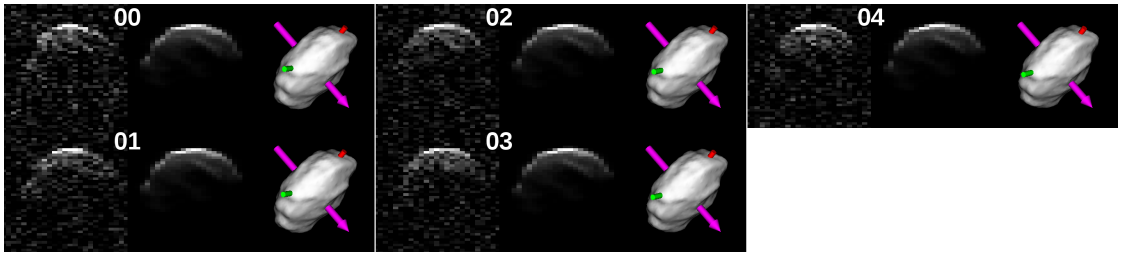

Figure A.32: Same as Figure A.10, for five sums of the first Goldstone delay-Doppler images from February 19, 2012.

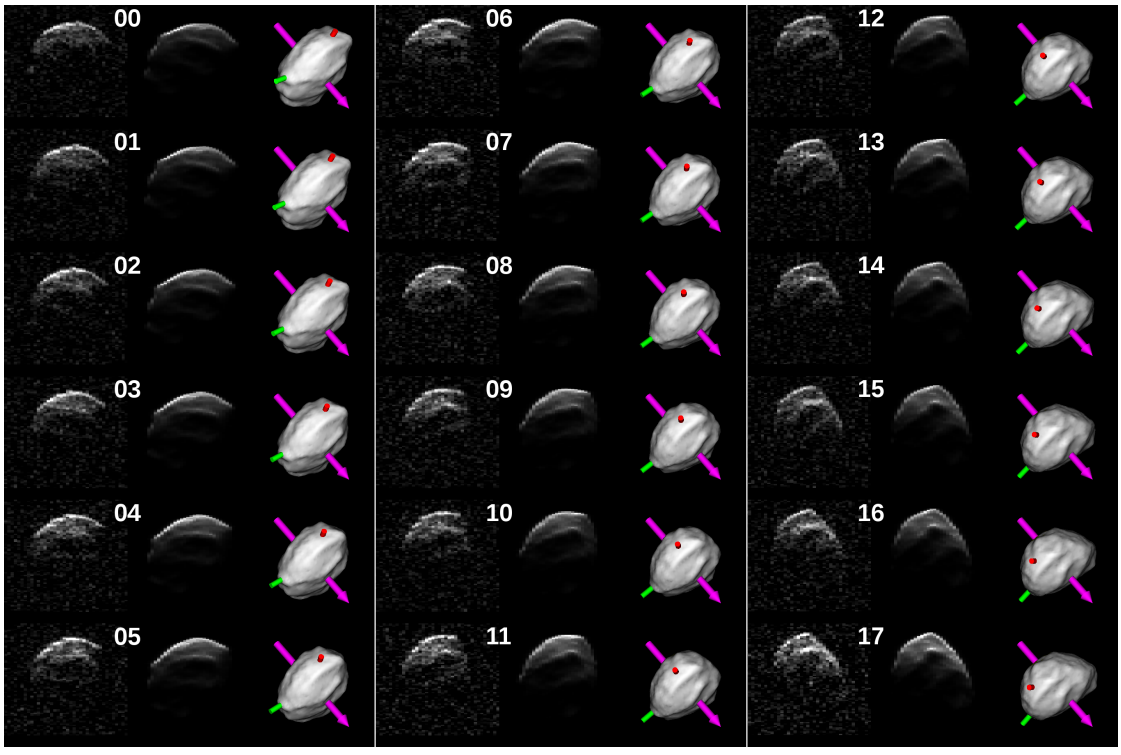

Figure A.33: Same as Figure A.10, for eighteen more sums of Goldstone delay-Doppler images from February 19, 2012.

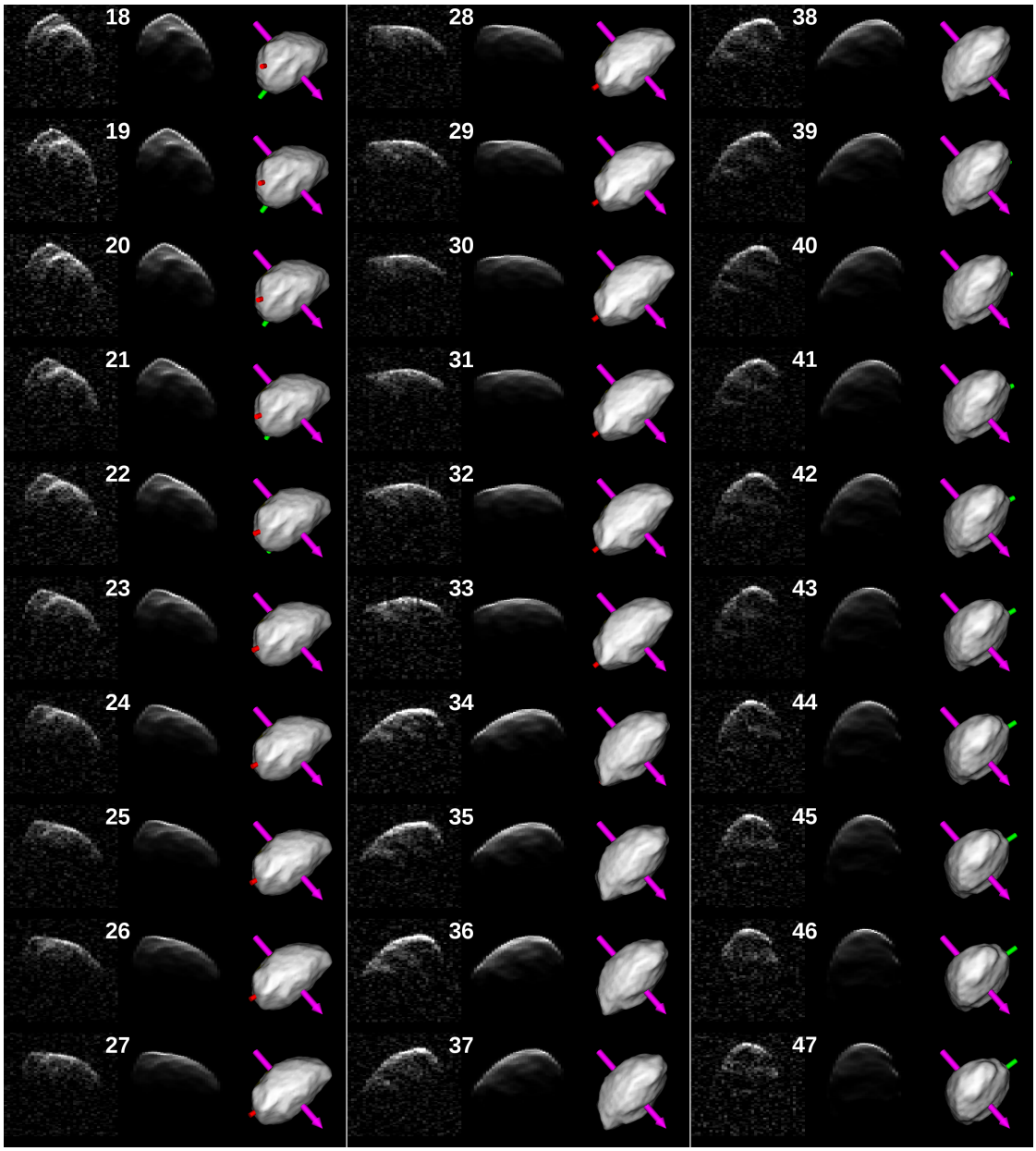

Figure A.34: Same as Figure A.10, for thirty sums of the last Goldstone delay-Doppler images from February 19, 2012.

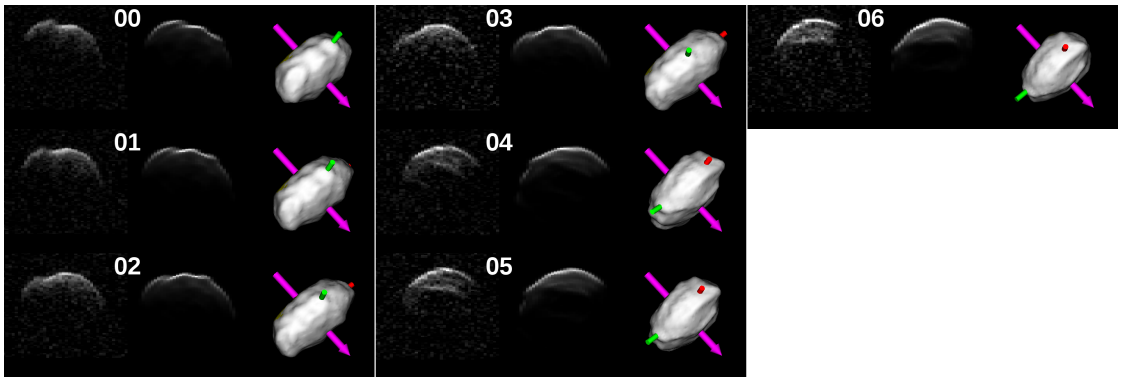

Figure A.35: Same as Figure A.10, for seven sums of the Goldstone delay-Doppler images from February 20, 2012.

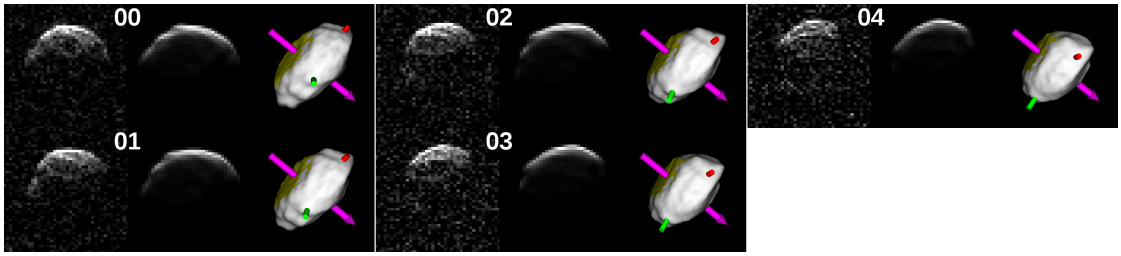

Figure A.36: Same as Figure A.10, for five sums of the Goldstone delay-Doppler images from February 23, 2012.

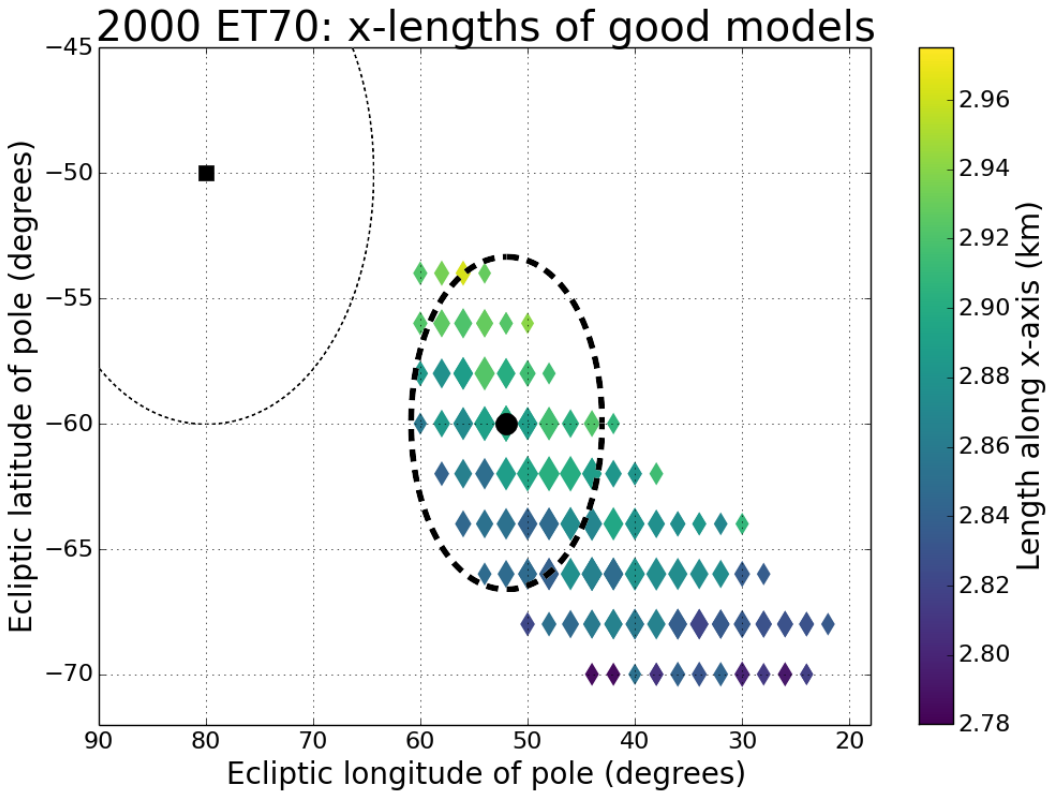

Figure A.37: The "arc" of good shape models' pole positions with their lengths along the x-axis (long principal axis). The nominal pole solution (80°, −50°) of Naidu et al. (2013), from using only the radar data, is indicated with a black square. The thin dashed ellipse shows their 10° one-sigma uncertainty. This pole is ruled out by the lightcurves. The colored diamonds show models which are compatible at the one-sigma level with the radar and lightcurve data (but not necessarily with the infrared spectra). Larger markers correspond to better shape models (that is, models with lower values of chi-squared). Thermal modeling allows us to place additional constraints on the pole position, because some of the poles along the arc are ruled out by our infrared spectra. The points within the thick dashed ellipse are compatible with all available data (radar, lightcurve, and infrared) at the one-sigma level. Pole positions on this ellipse are at the outer edges of acceptable thermal models. The black circle shows the pole solution (52°, −60°), which provides the best fits to the radar, lightcurve, and infrared data.

A.1.3 Shape model parameters

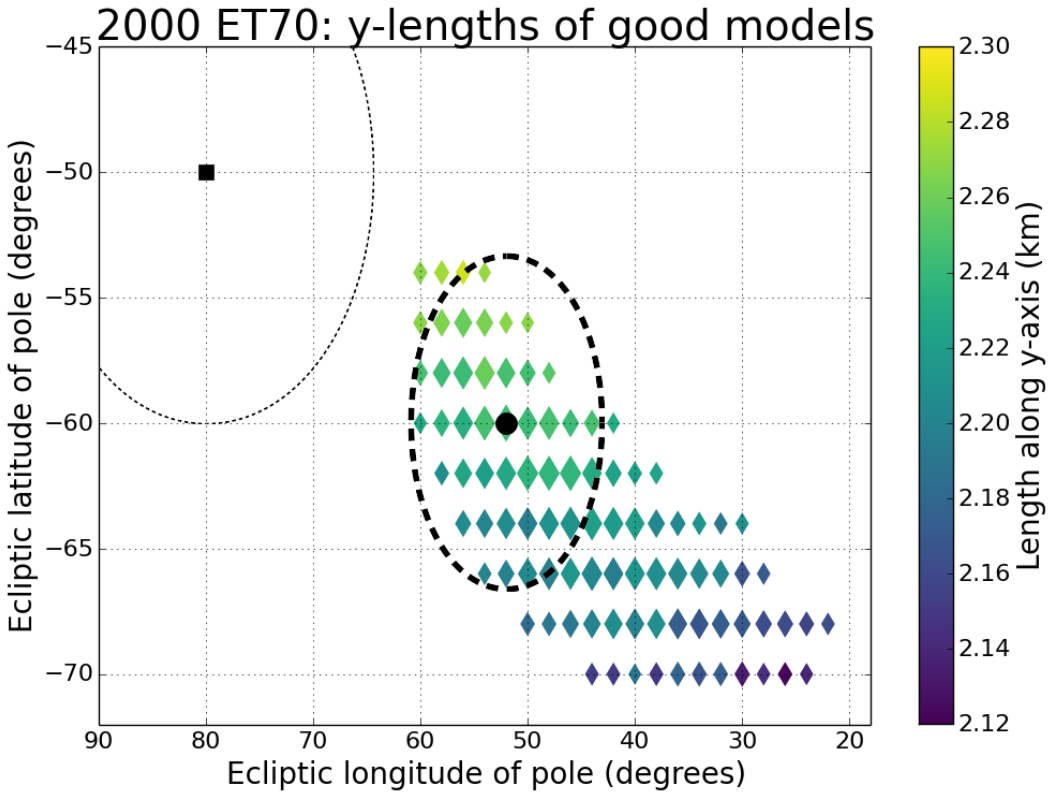

Figure A.38: The "arc" of good shape models' pole positions with their lengths along the *y*-axis (intermediate principal axis). The nominal pole solution $(80°, -50°)$ of Naidu et al. (2013), from using only the radar data, is indicated with a black square. The thin dashed ellipse shows their 10° one-sigma uncertainty. The colored diamonds show models which are compatible at the one-sigma level with the radar and lightcurve data (but not necessarily with the infrared spectra). Larger markers correspond to better shape models (that is, models with lower values of chi-squared). The points within the thick dashed ellipse are compatible with all available data (radar, lightcurve, and infrared) at the one-sigma level. The black circle shows the pole solution $(52°, -60°)$, which provides the best fits to the radar, lightcurve, and infrared data.

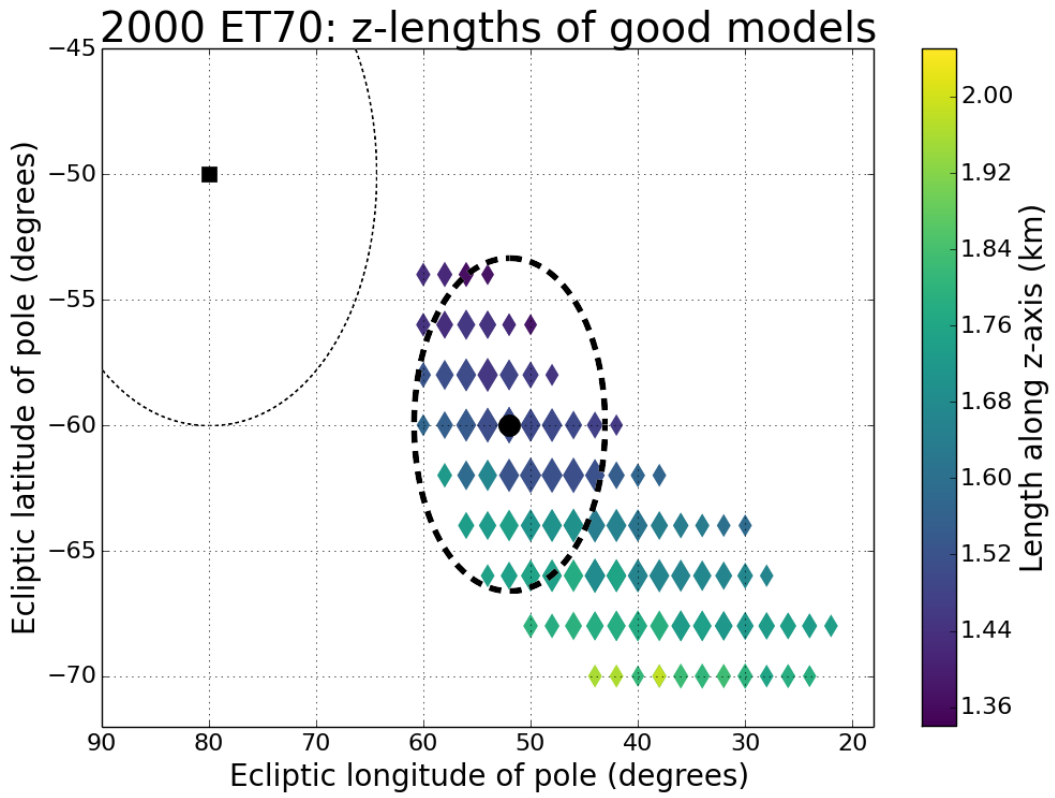

Figure A.39: The "arc" of good shape models' pole positions with their lengths along the principal z-axis (rotation axis). The nominal pole solution $(80°, -50°)$ of Naidu et al. (2013), from using only the radar data, is indicated with a black square. The thin dashed ellipse shows their 10° one-sigma uncertainty. The colored diamonds show models which are compatible at the one-sigma level with the radar and lightcurve data (but not necessarily with the infrared spectra). Larger markers correspond to better shape models (that is, models with lower values of chi-squared). The points within the thick dashed ellipse are compatible with all available data (radar, lightcurve, and infrared) at the one-sigma level. The black circle shows the pole solution $(52°, -60°)$, which provides the best fits to the radar, lightcurve, and infrared data.

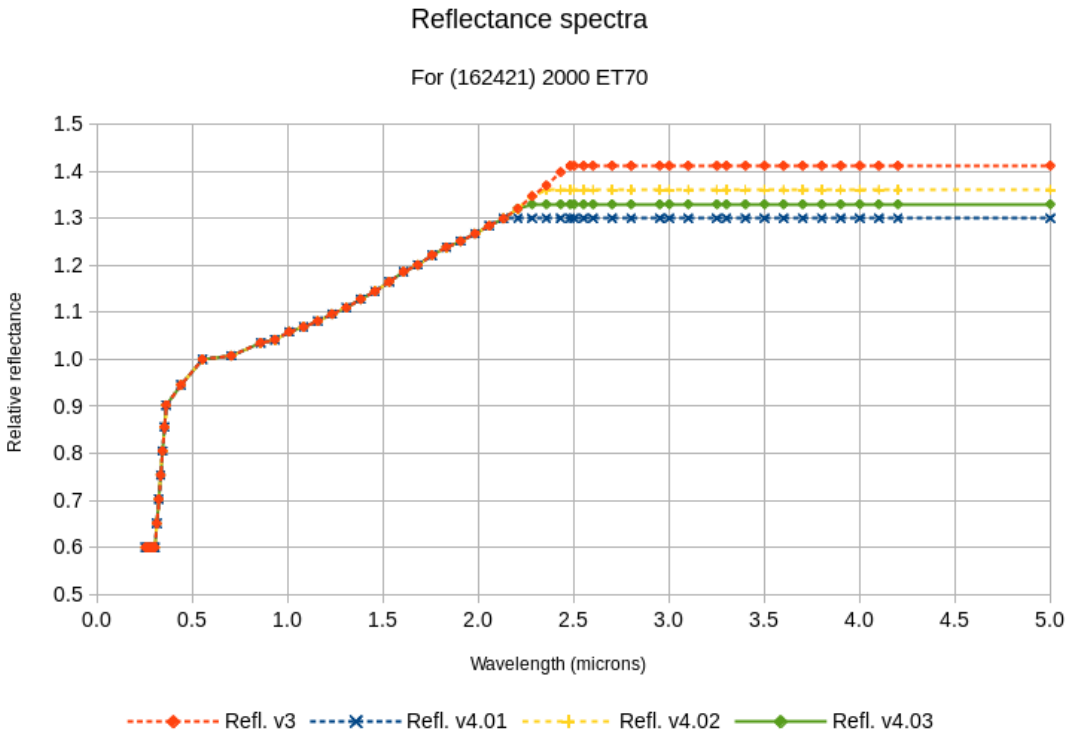

Figure A.40: Different versions of 2000 ET70's reflectance spectrum that were tested in thermal modeling. We found that a cutoff wavelength of 2.25 microns is optimal; that spectrum is shown as v4.03 in the plot. For comparison, the earlier version of the reflectance spectrum (v3) had its cutoff at 2.48 microns.

A.1.4 Infrared observations

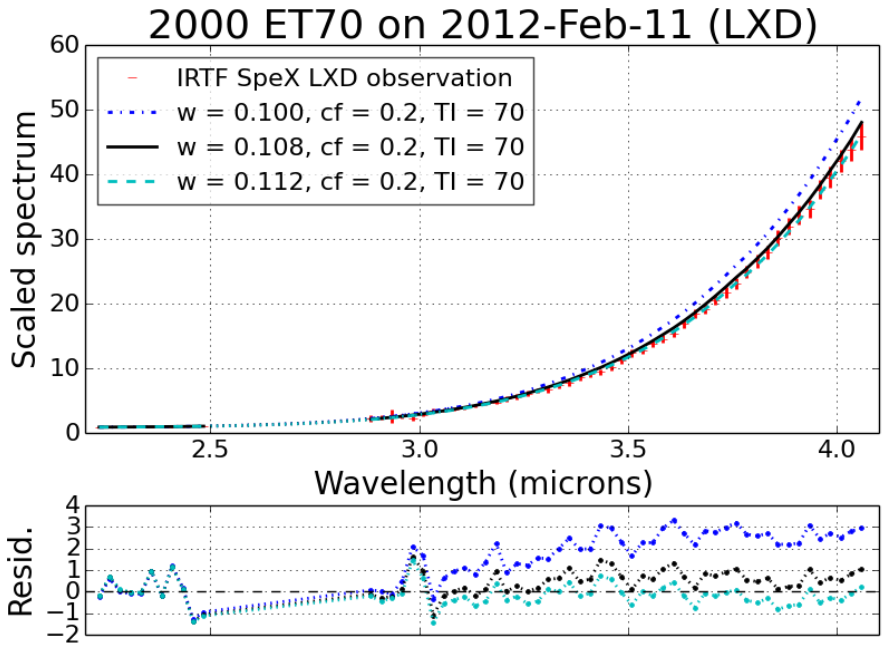

Figure A.41: Spectra of three thermal models, and their normalized residuals, at the time of the first IRTF observation from February 11, 2012. All three of these models have a pole direction of (52°, −60°), 20% crater coverage, and a thermal inertia of 70 J m^{-2} K^{-1} s$^{-1/2}$. Their values of Hapke single-scattering albedo differ: the blue dashed curve shows $w = 0.100$, the black solid curve shows $w = 0.108$, and the cyan dash-dot curve shows $w = 0.112$. These albedo values are the range needed to fit the different spectra from the three nights of infrared observations, assuming that crater coverage fraction and thermal inertia are fixed at the specified values.

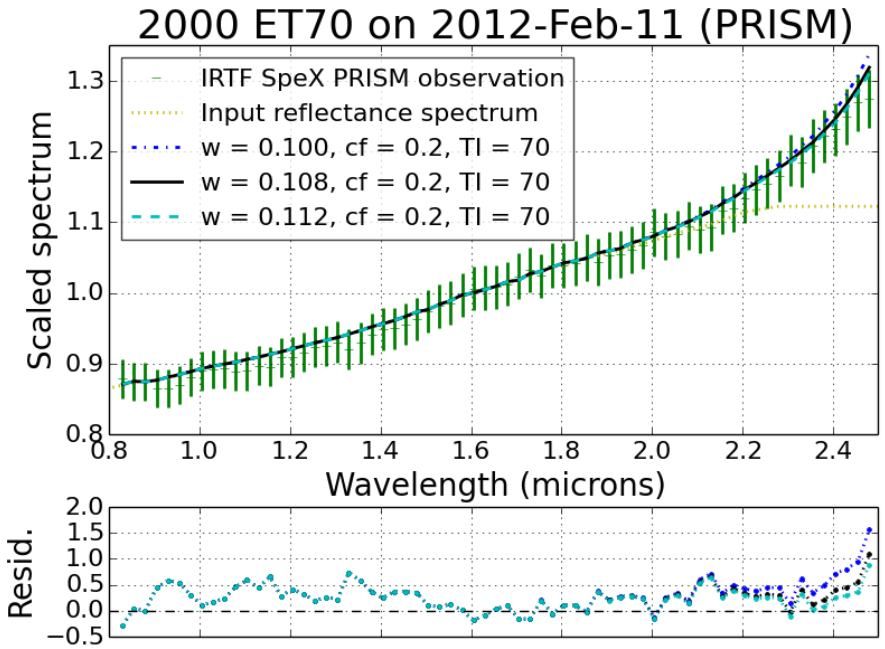

Figure A.42: Same as Figure A.41, for the PRISM observation from February 11, 2012.

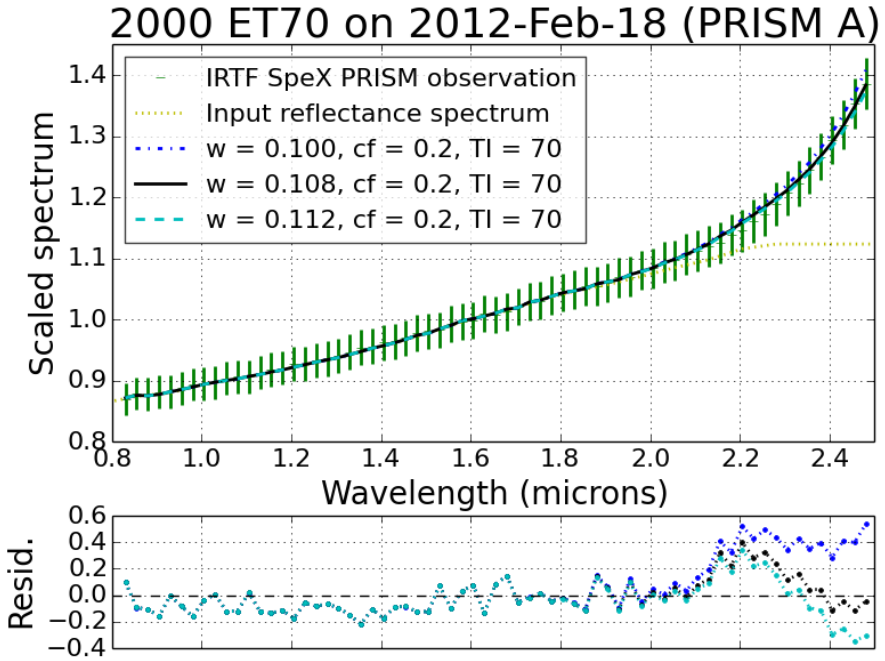

Figure A.43: Same as Figure A.41, for the first PRISM observation from February 18, 2012.

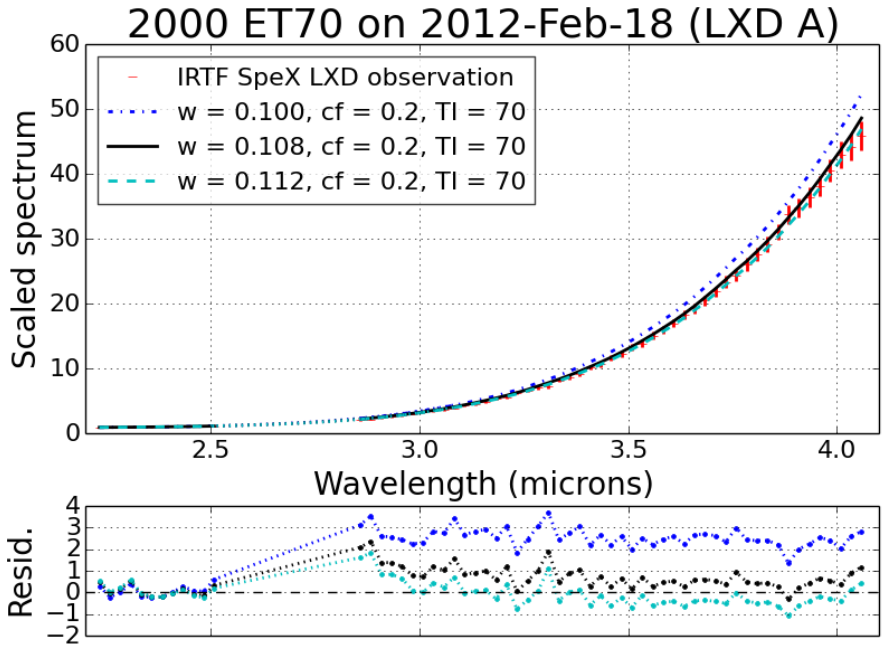

Figure A.44: Same as Figure A.41, for the first LXD observation from February 18, 2012.

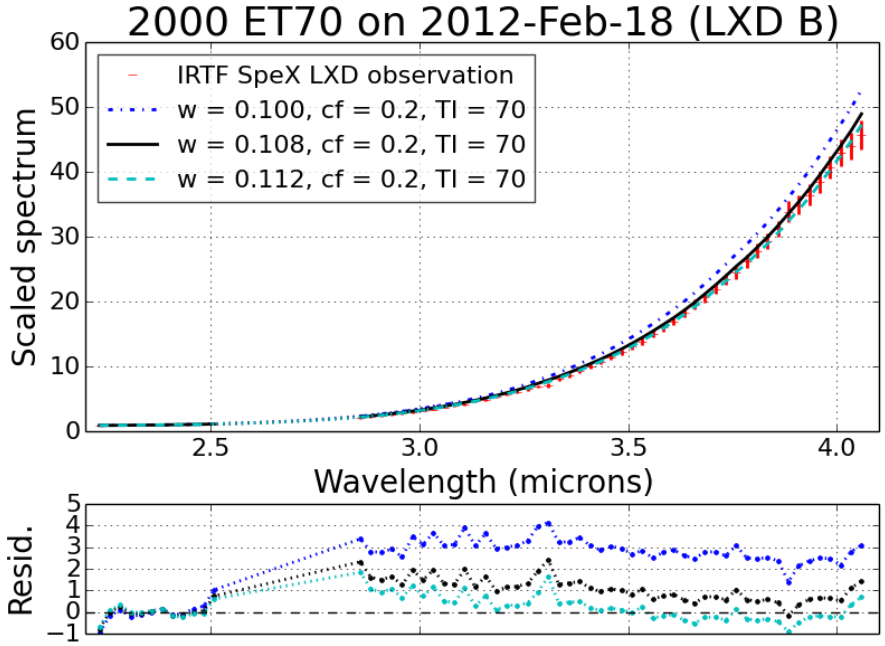

Figure A.45: Same as Figure A.41, for the second LXD observation from February 18, 2012.

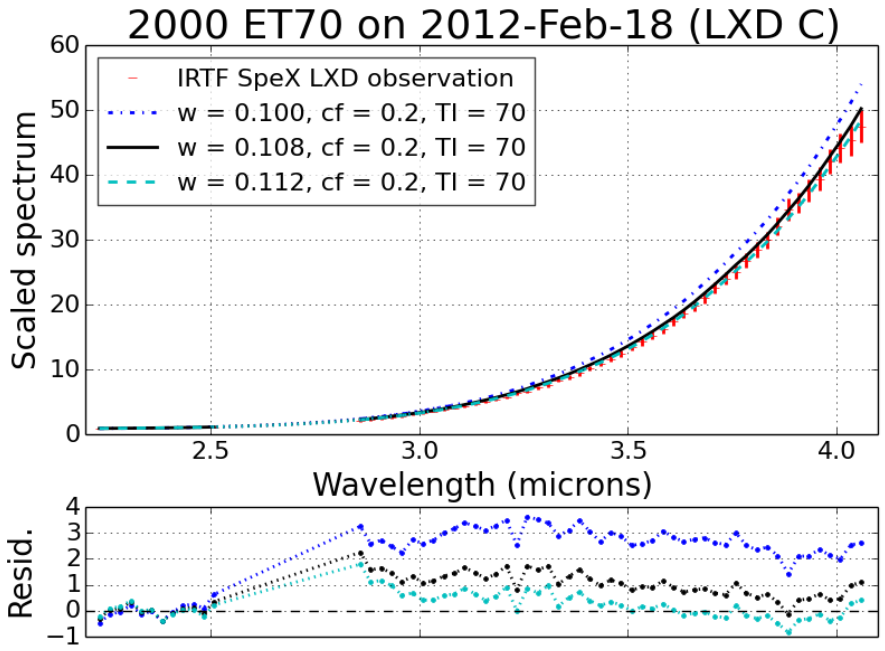

Figure A.46: Same as Figure A.41, for the third LXD observation from February 18, 2012.

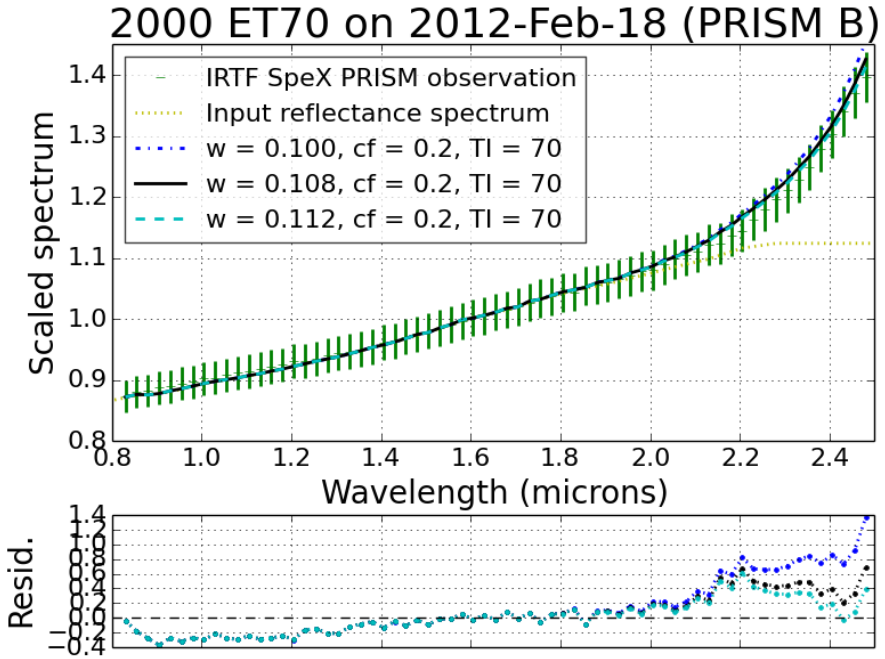

Figure A.47: Same as Figure A.41, for the second PRISM observation from February 18, 2012.

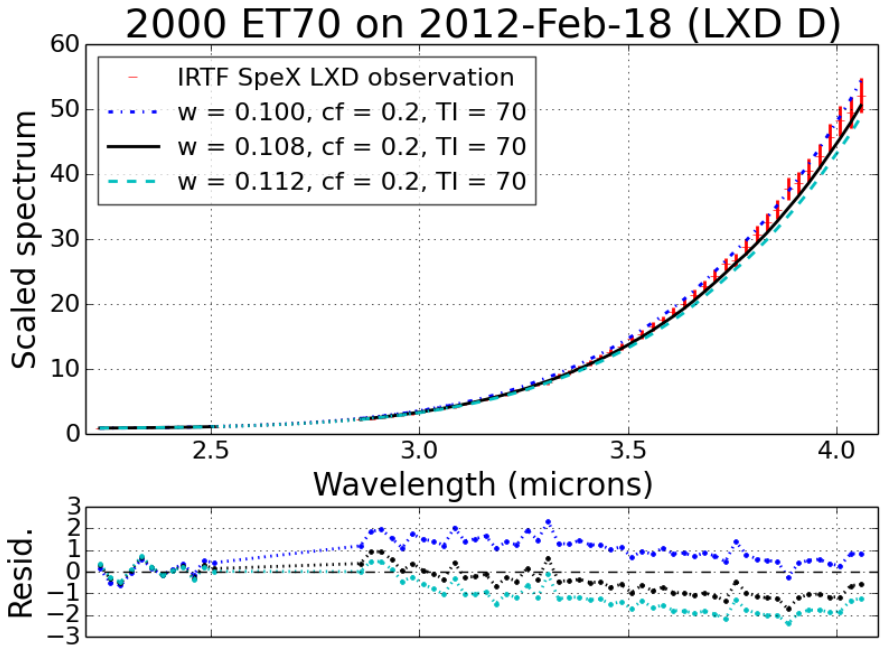

Figure A.48: Same as Figure A.41, for the fourth LXD observation from February 18, 2012.

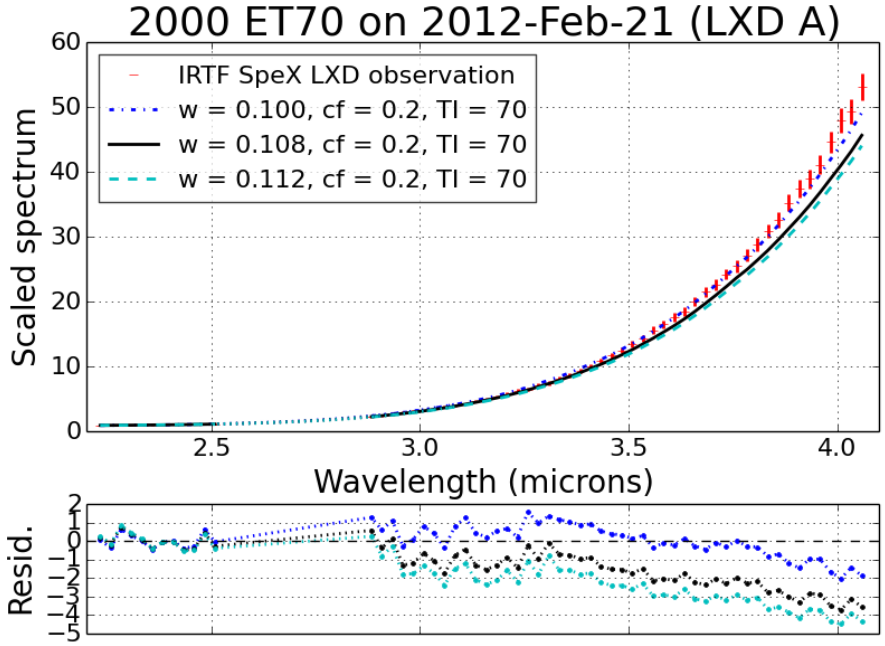

Figure A.49: Same as Figure A.41, for the first LXD observation from February 21, 2012.

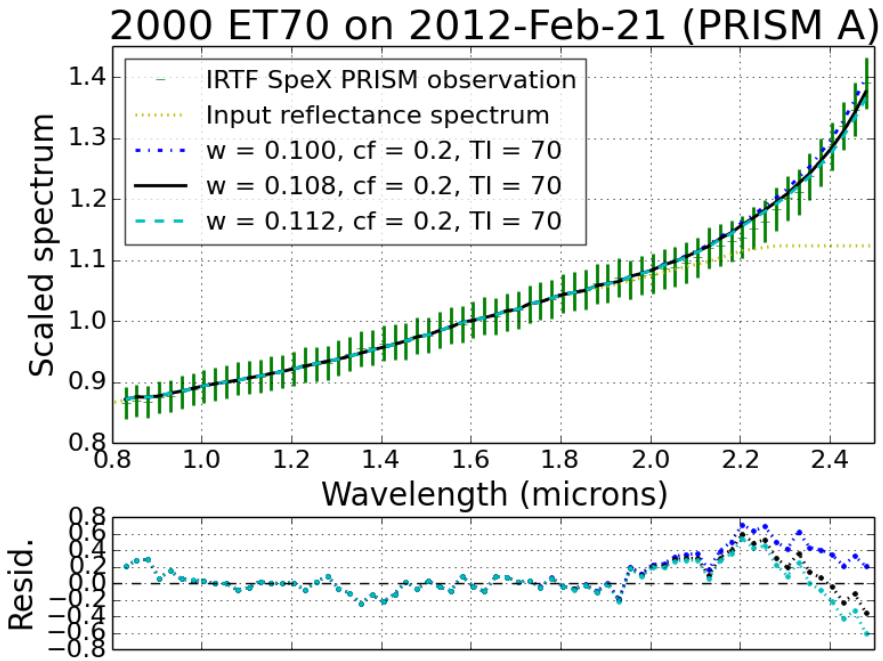

Figure A.50: Same as Figure A.41, for the PRISM observation from February 21, 2012.

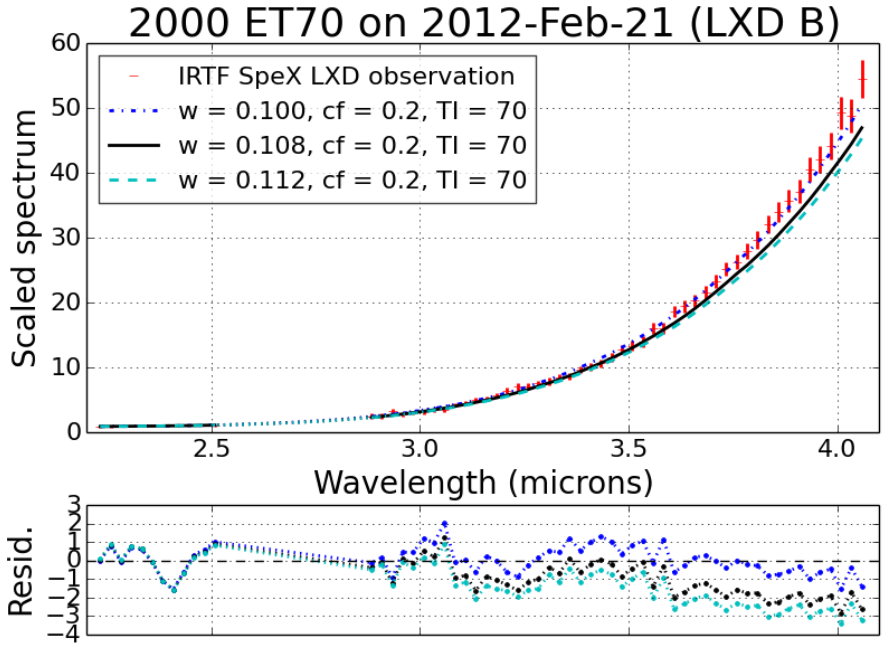

Figure A.51: Same as Figure A.41, for the second LXD observation from February 21, 2012.

APPENDIX B

APPENDIX FOR CHAPTER 3

B.1 Supplementary figures for (85989) 1999 JD6

B.1.1 Lightcurve observations (1999 through 2005)

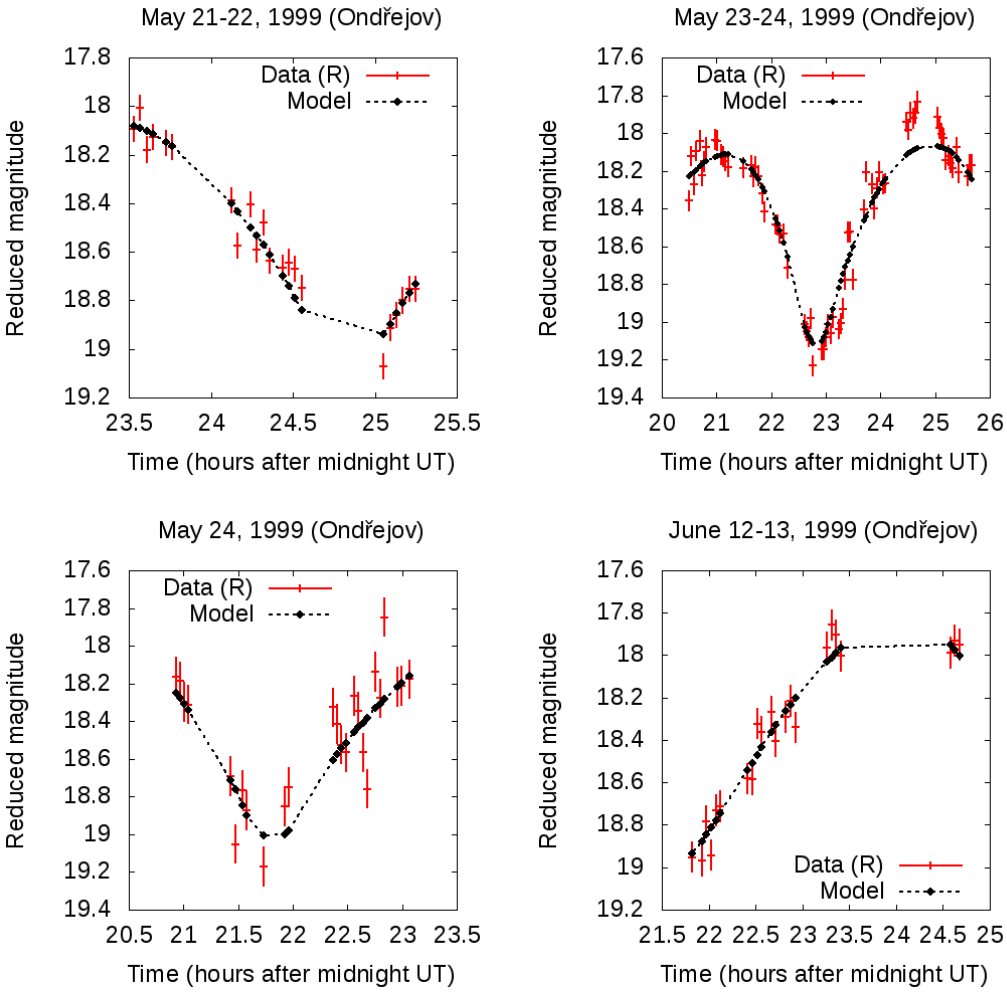

Figure B.1: Lightcurve observations of 1999 JD6, from 1999.

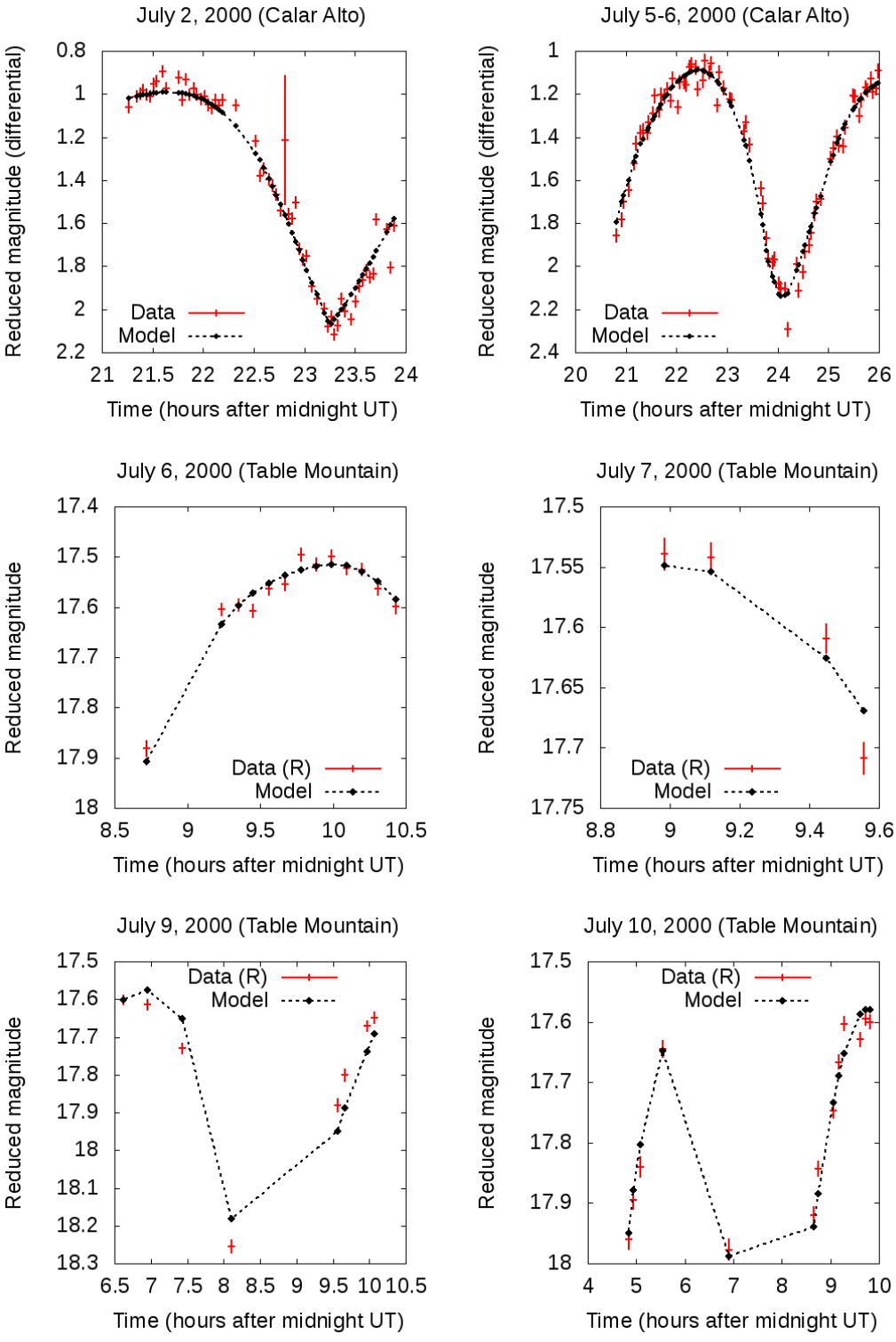

Figure B.2: Lightcurve observations of 1999 JD6, from 2000.

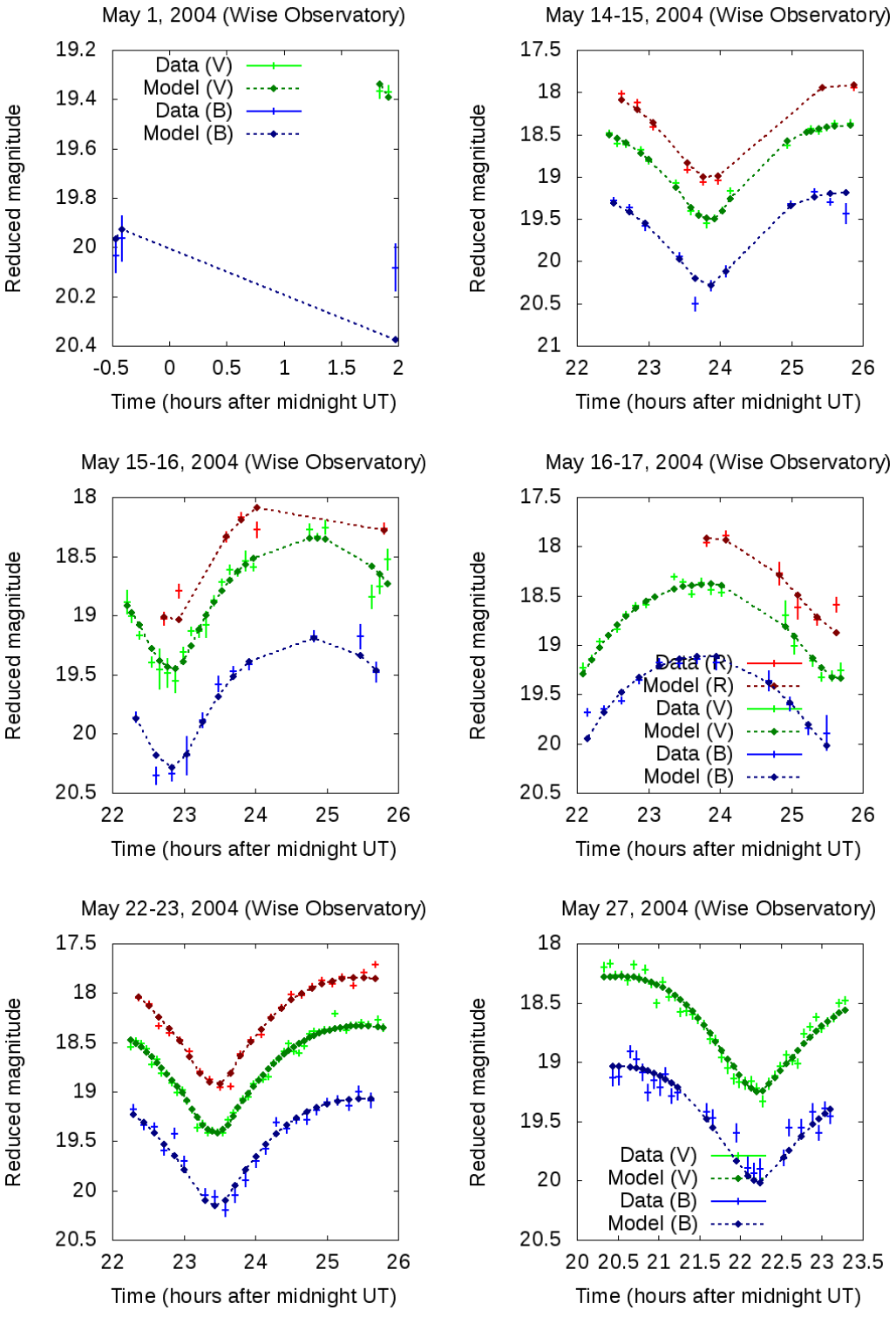

Figure B.3: Lightcurve observations of 1999 JD6, from 2004.

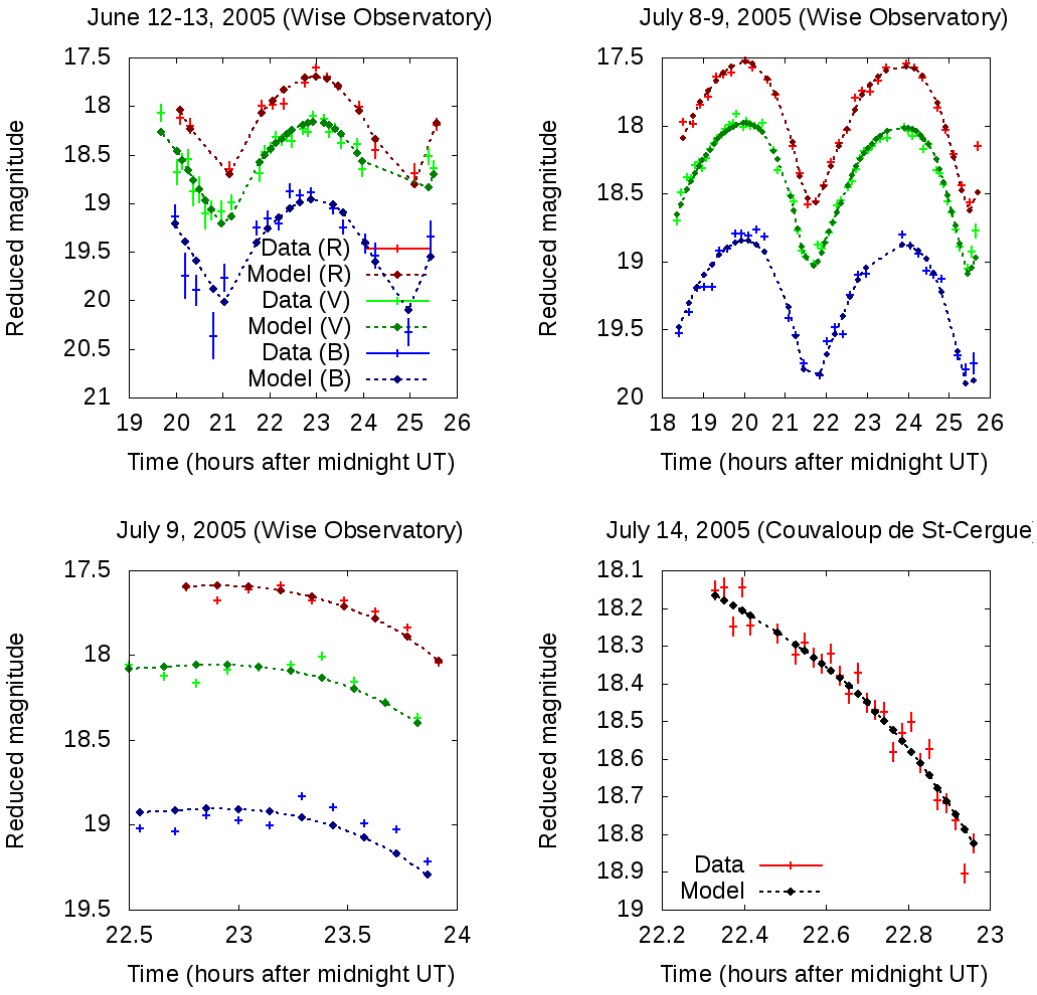

Figure B.4: Lightcurve observations of 1999 JD6, from 2005.

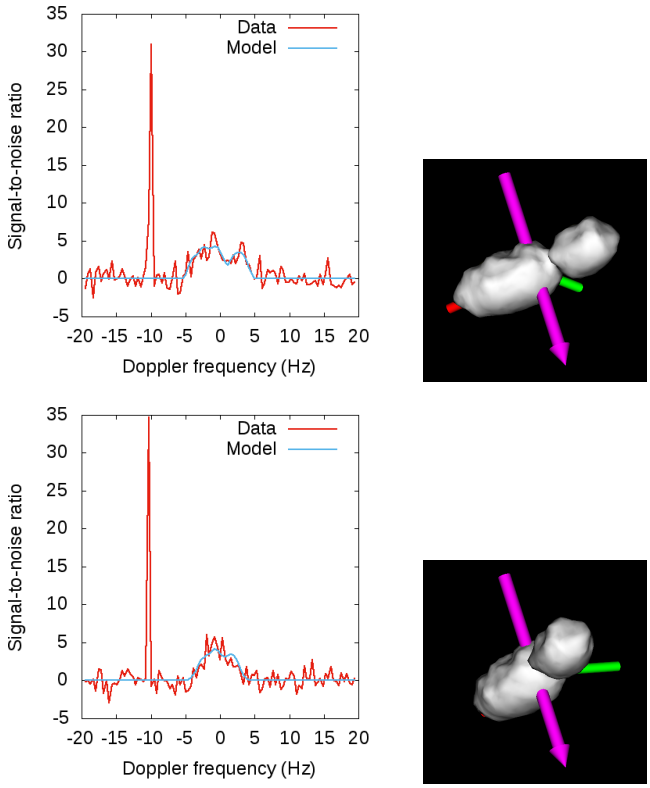

Figure B.5: CW spectra of 1999 JD6 from Arecibo on July 25-26, 2010 (OC polarization only). The left frames show the observations. The spikes near -10 Hz are from harmonics of the power supply. The right frames show plane-of-sky views of the best-fit model at the observation times. In all plane-of-sky views, the sidereal spin vector (the model's shortest principal axis) is shown as a magenta arrow, and the long and intermediate principal axes are shown as red and green shafts, respectively. In the plane-of-sky views, north is upward and east is leftward.

B.1.2 Arecibo observations from July of 2010

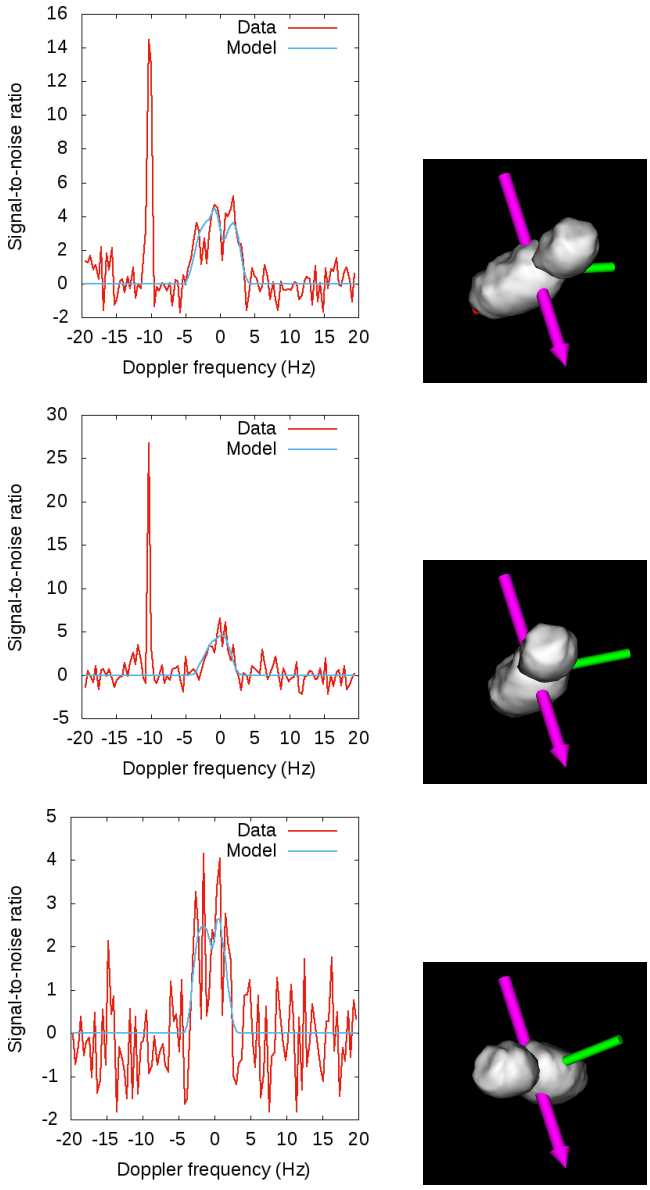

Figure B.6: CW spectra of 1999 JD6 from Arecibo on July 26-28, 2010 (OC polarization only).

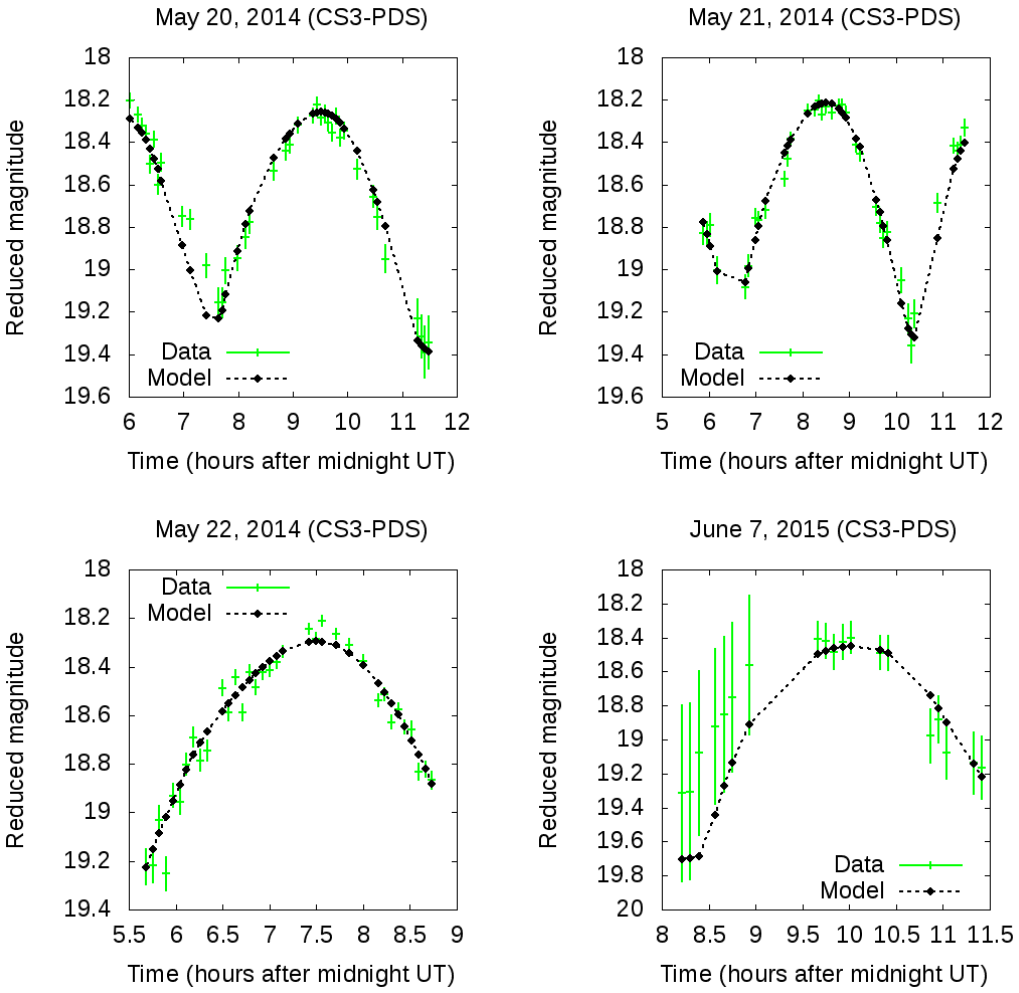

Figure B.7: Lightcurve observations of JD6 from 2014 and 2015.

B.1.3 Lightcurve observations (2014 and 2015)

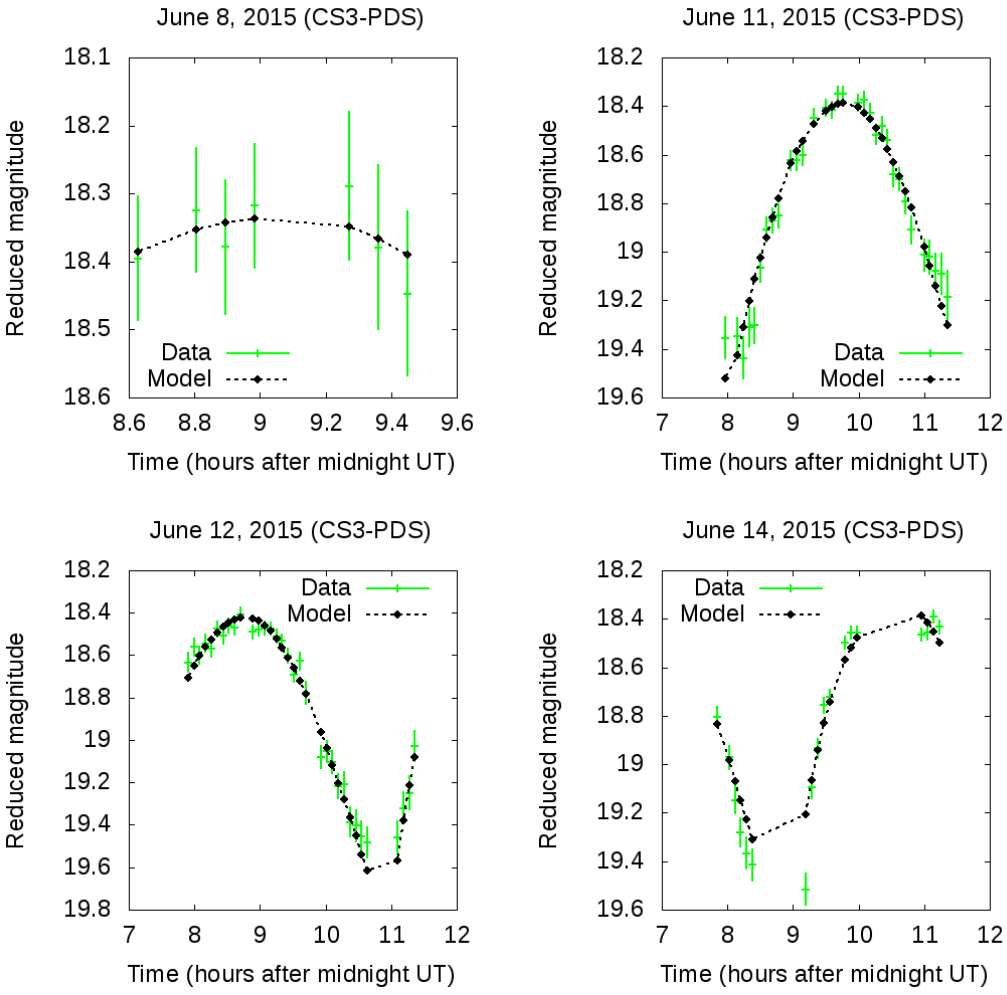

Figure B.8: Lightcurve observations of JD6 from 2015.

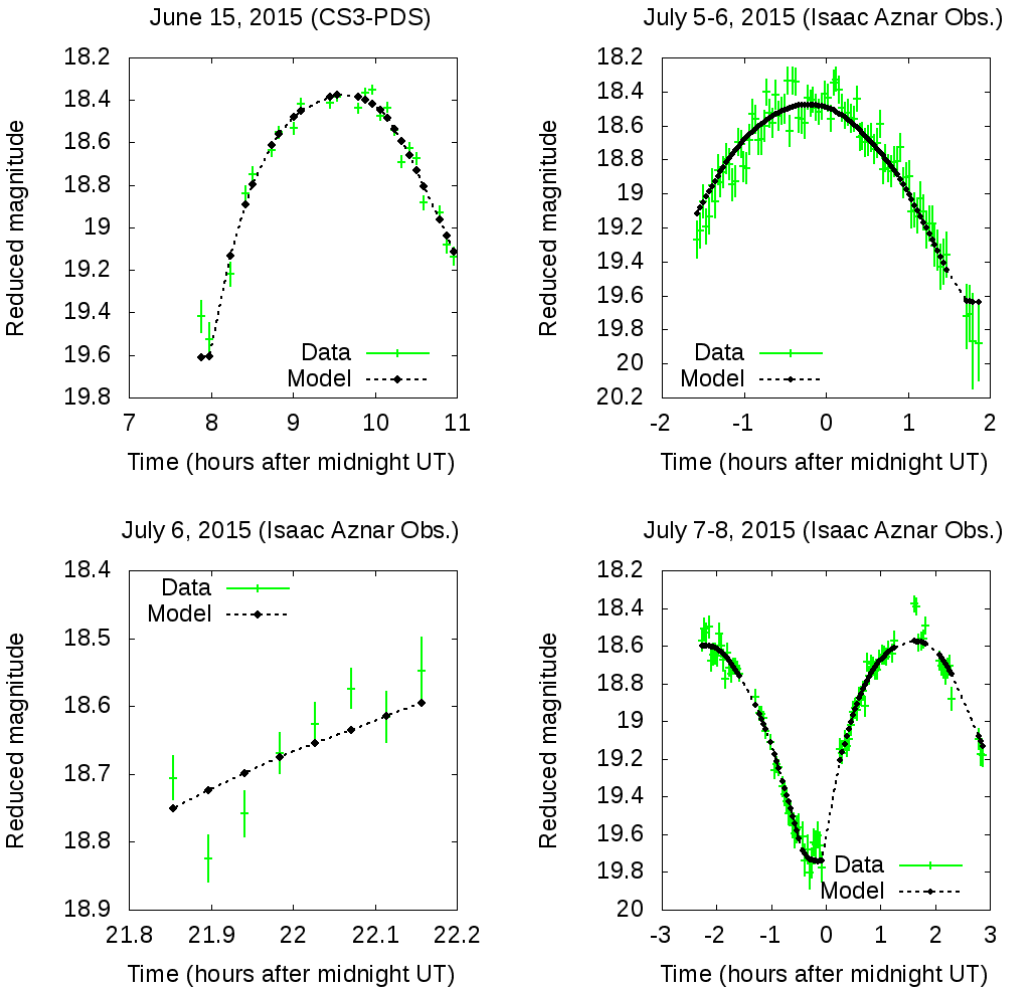

Figure B.9: Additional lightcurve observations of JD6 from 2015.

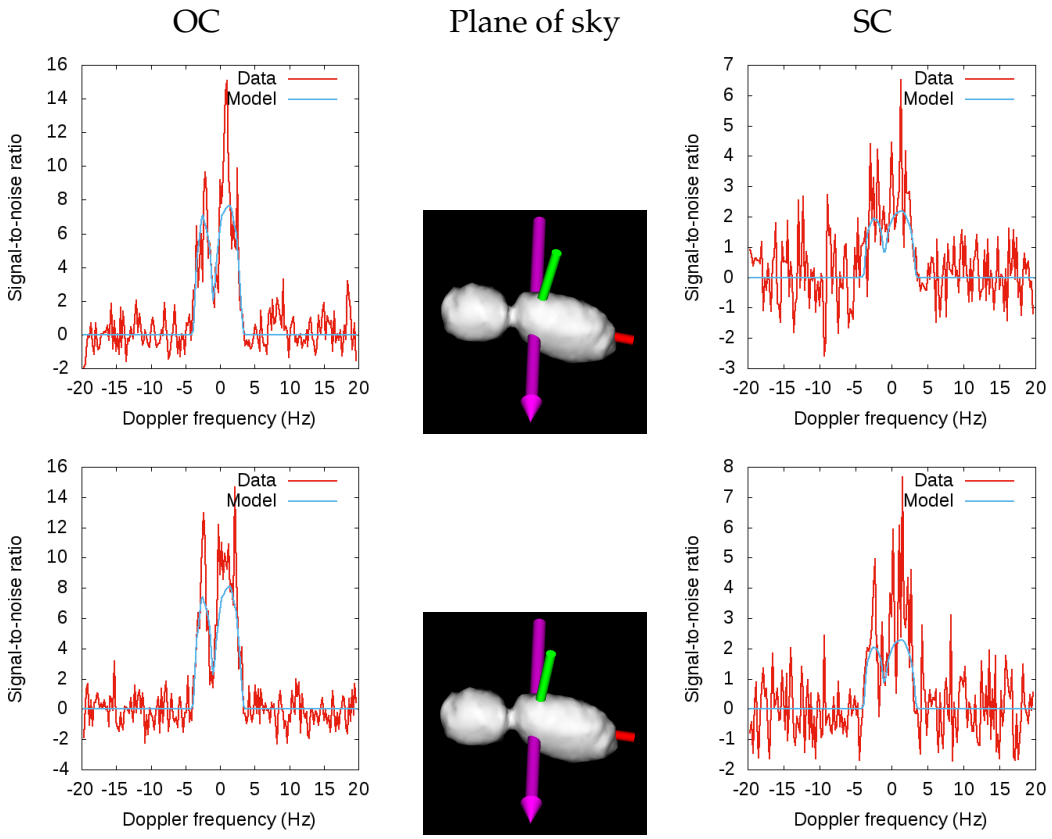

Figure B.10: CW spectra from Arecibo on July 15, 2015 (receive times 05:24 to 05:30 UT; both polarizations). In all subsequent plots of CW spectra, the left frames show the OC observations and the corresponding model spectra. The center frames show plane-of-sky views of the best-fit model at the observation times. The right frames show the SC observations and the corresponding model spectra.

B.1.4 Arecibo observations from July 15, 2015

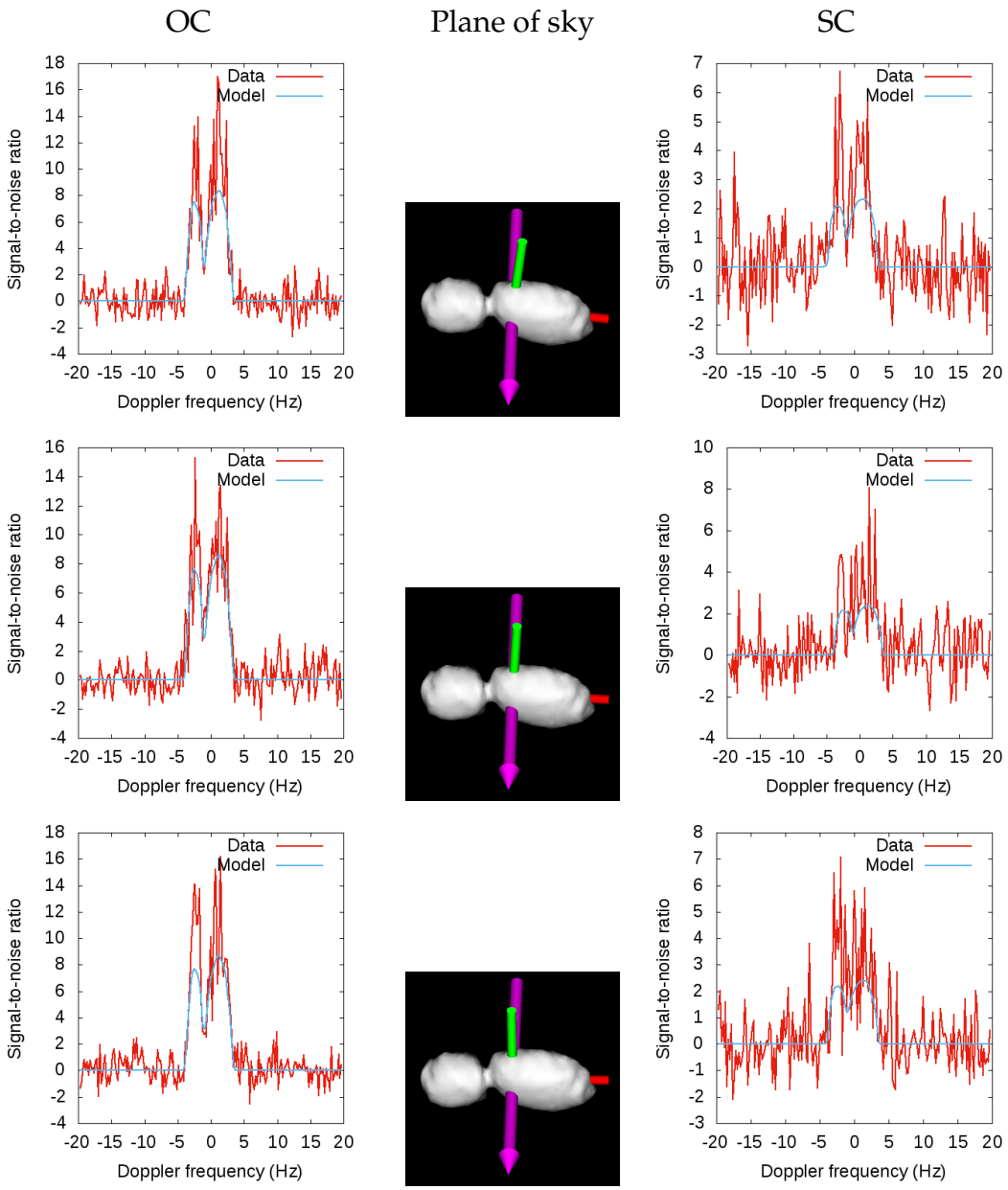

Figure B.11: CW spectra from Arecibo on July 15, 2015 (05:32 to 05:42 UT; both polarizations).

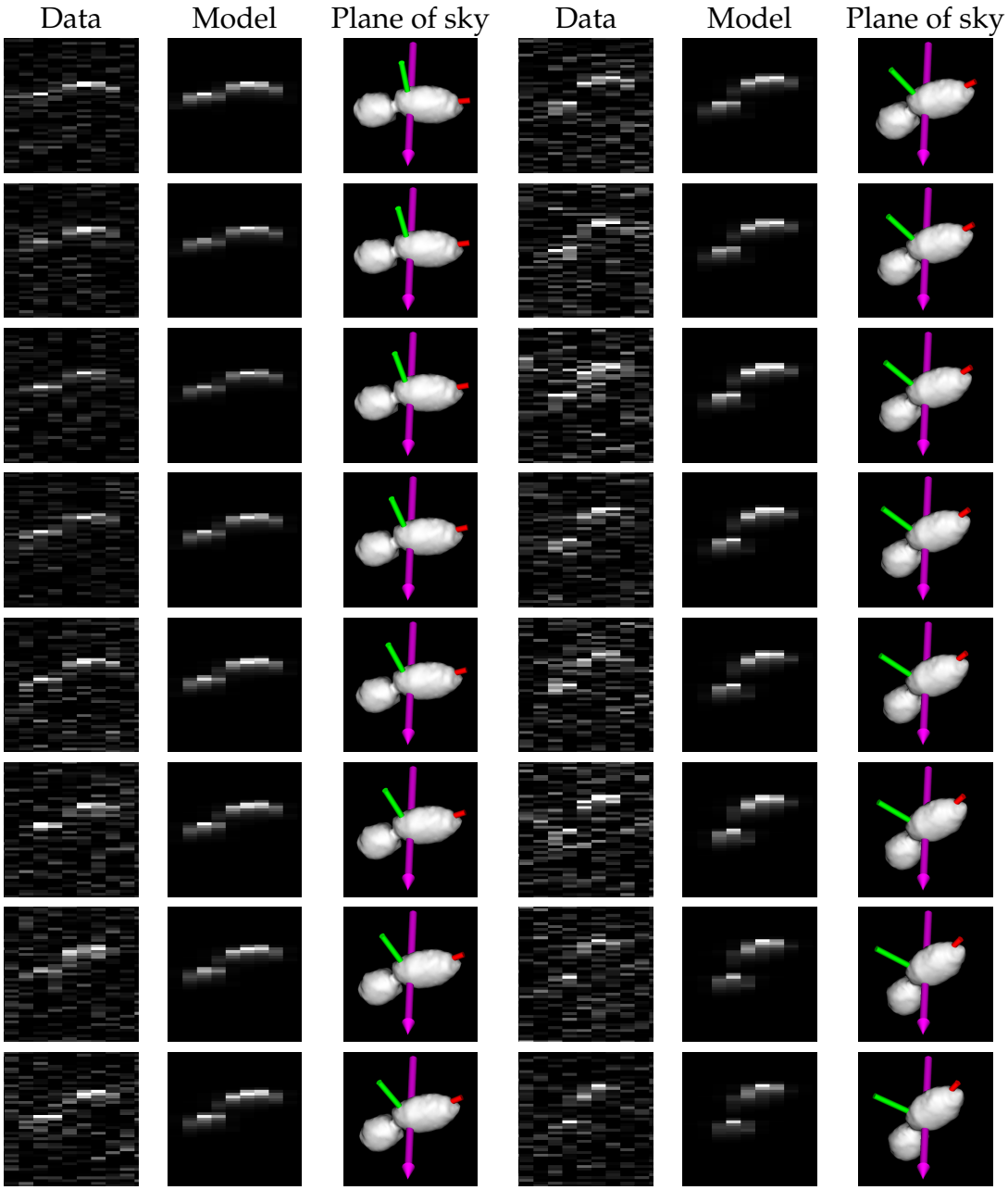

Figure B.12: Arecibo delay-Doppler images from July 15, 2015 (05:51 to 06:56 UT). For all mosaics of delay-Doppler images shown in this appendix, the progression of frames is from the top down, then from left to right. Thus, the last row of the first three columns comes immediately before the first row of the last three columns.

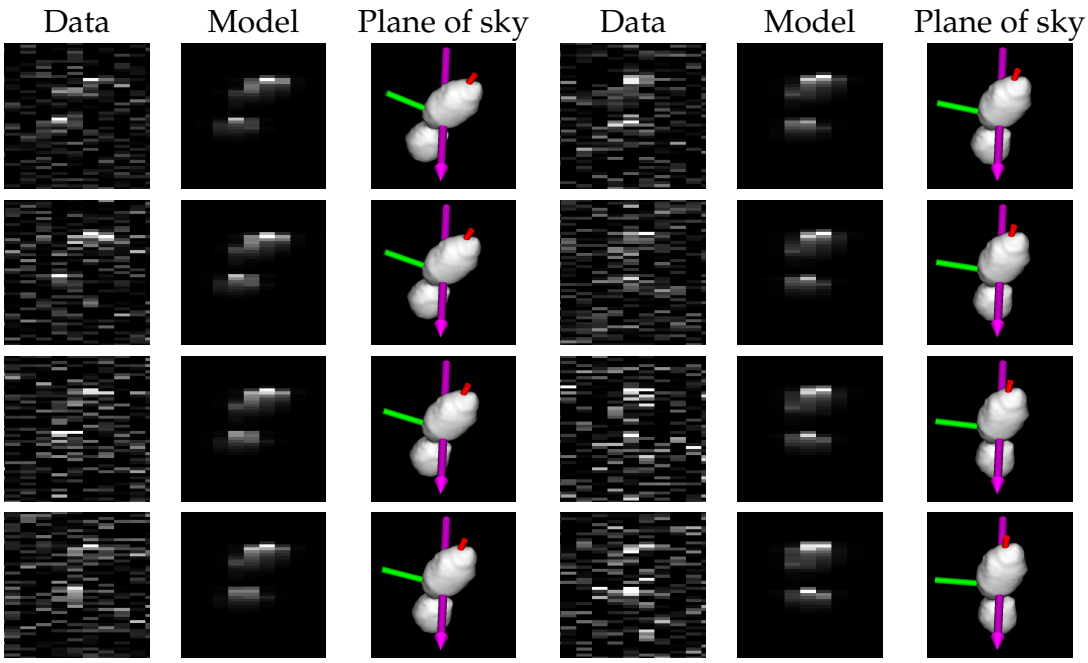

Figure B.13: Arecibo delay-Doppler images from July 15, 2015 (06:58 to 07:29 UT). For each image, the left column shows the radar data, the center column shows the simulated (noise-free) delay-Doppler image derived from the nominal shape model, and the right column shows the simulated plane-of-sky view (as seen from Earth). In the delay-Doppler images, delay is plotted on the vertical axis (increasing from the top down), and Doppler frequency is plotted on the horizontal axis (increasing from left to right). In the plane-of-sky views, the sidereal spin vector (the model's shortest principal axis) is shown as a magenta arrow, and the long and intermediate principal axes are shown as red and green shafts, respectively. In the plane-of-sky views, north is upward and east is leftward. The radar images are stretched so that their spatial scale is the same as that of the plane-of-sky image (square frames with a side length of 3.6 kilometers), but the radar images' vertical axis, range, is perpendicular to the plane of the sky.

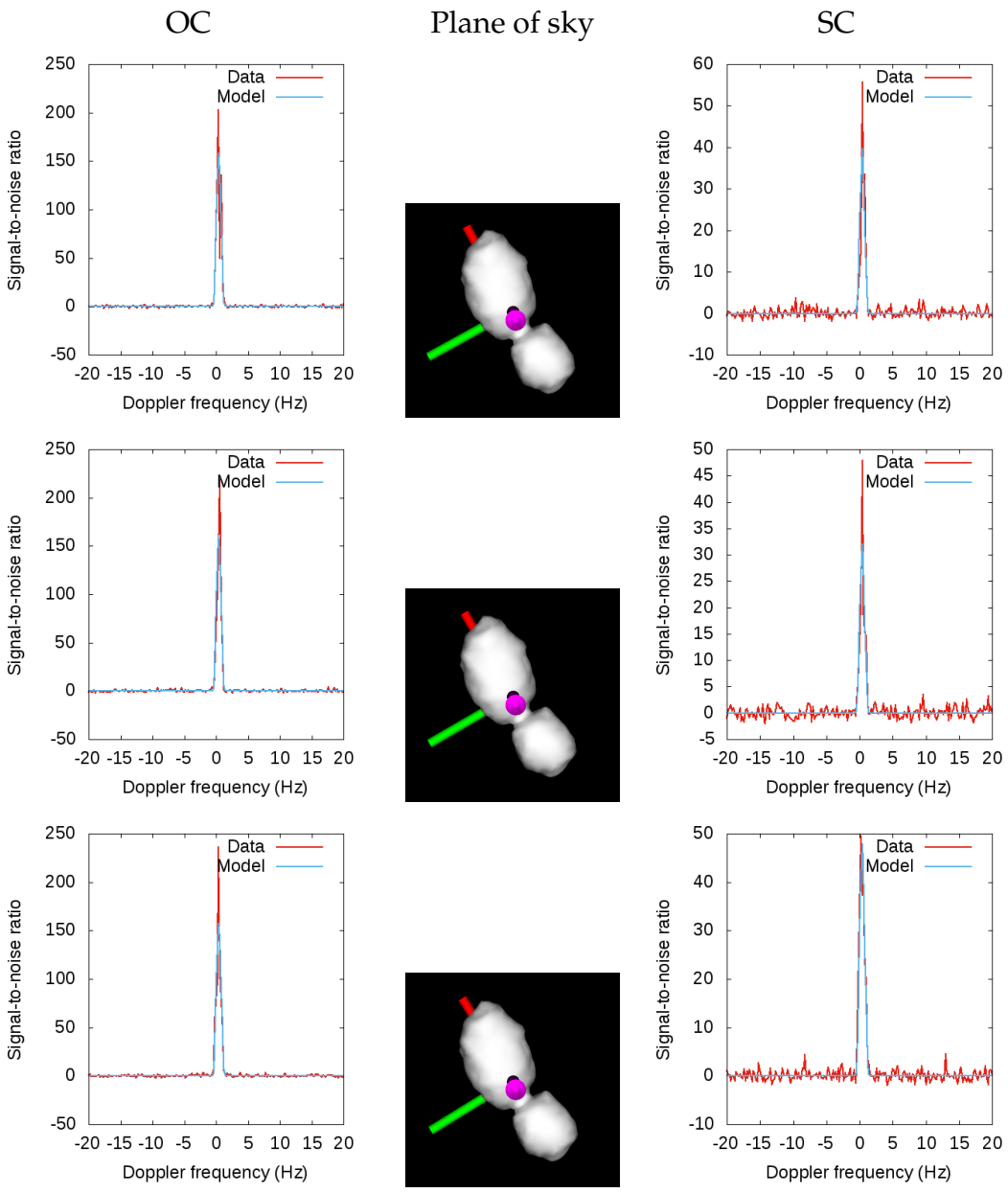

Figure B.14: CW spectra from Goldstone DSS-14 on July 23, 2015 (00:20 to 00:24 UT; both polarizations).

B.1.5 Goldstone observations from July 23, 2015

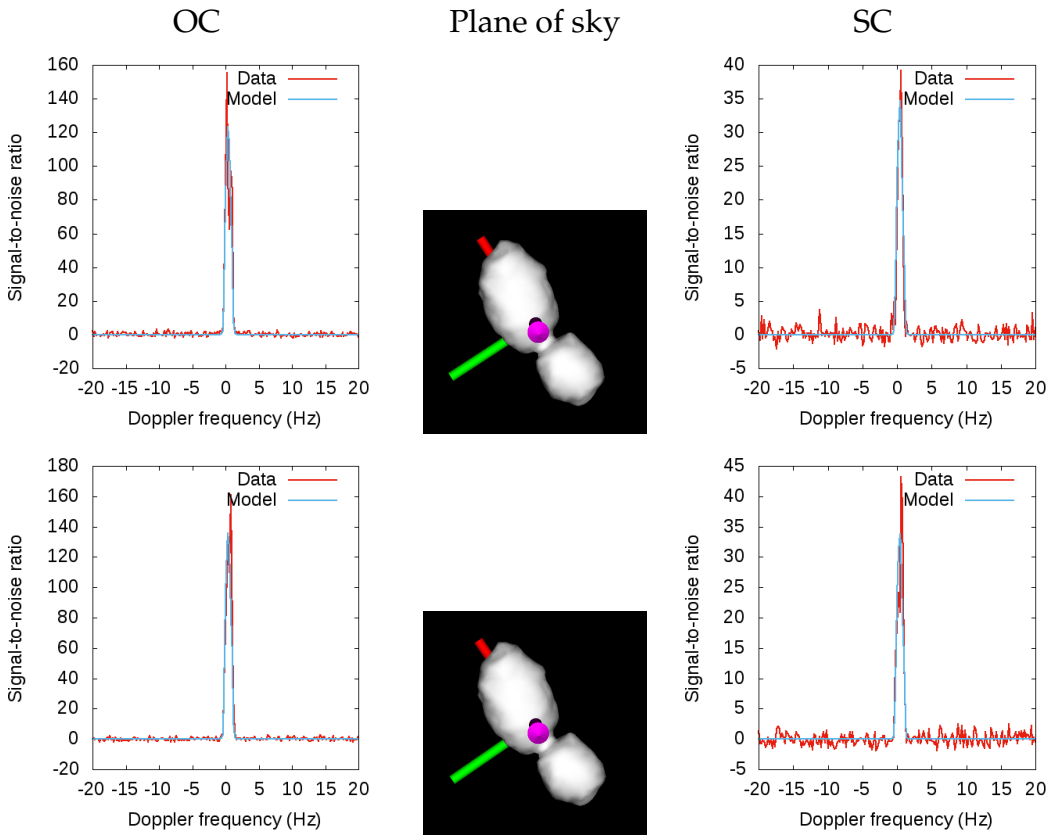

Figure B.15: CW spectra from Goldstone DSS-14 on July 23, 2015 (00:25 to 00:28 UT; both polarizations).

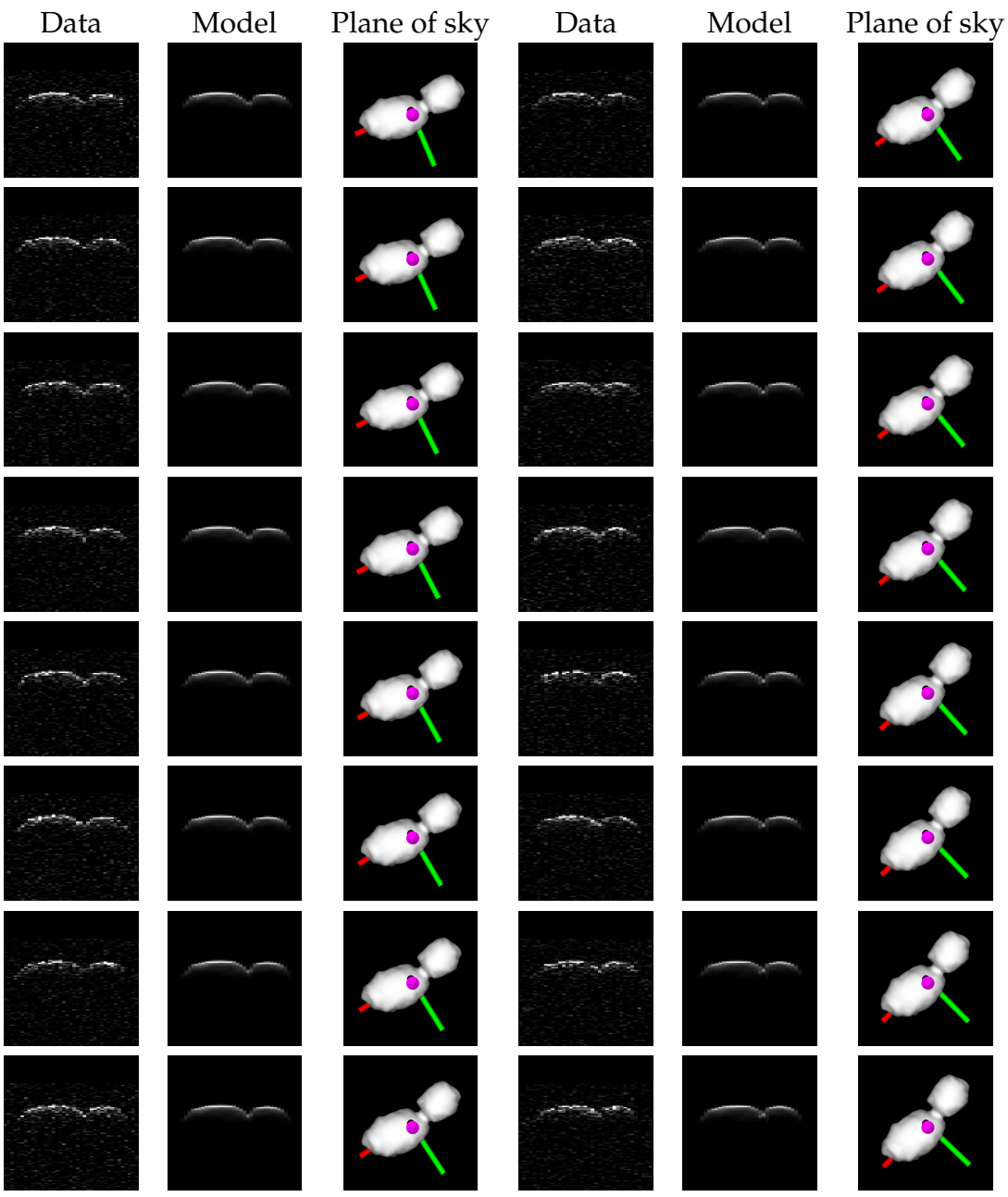

Figure B.16: Goldstone DSS-14 delay-Doppler images from July 23, 2015 (02:08 to 02:38 UT).

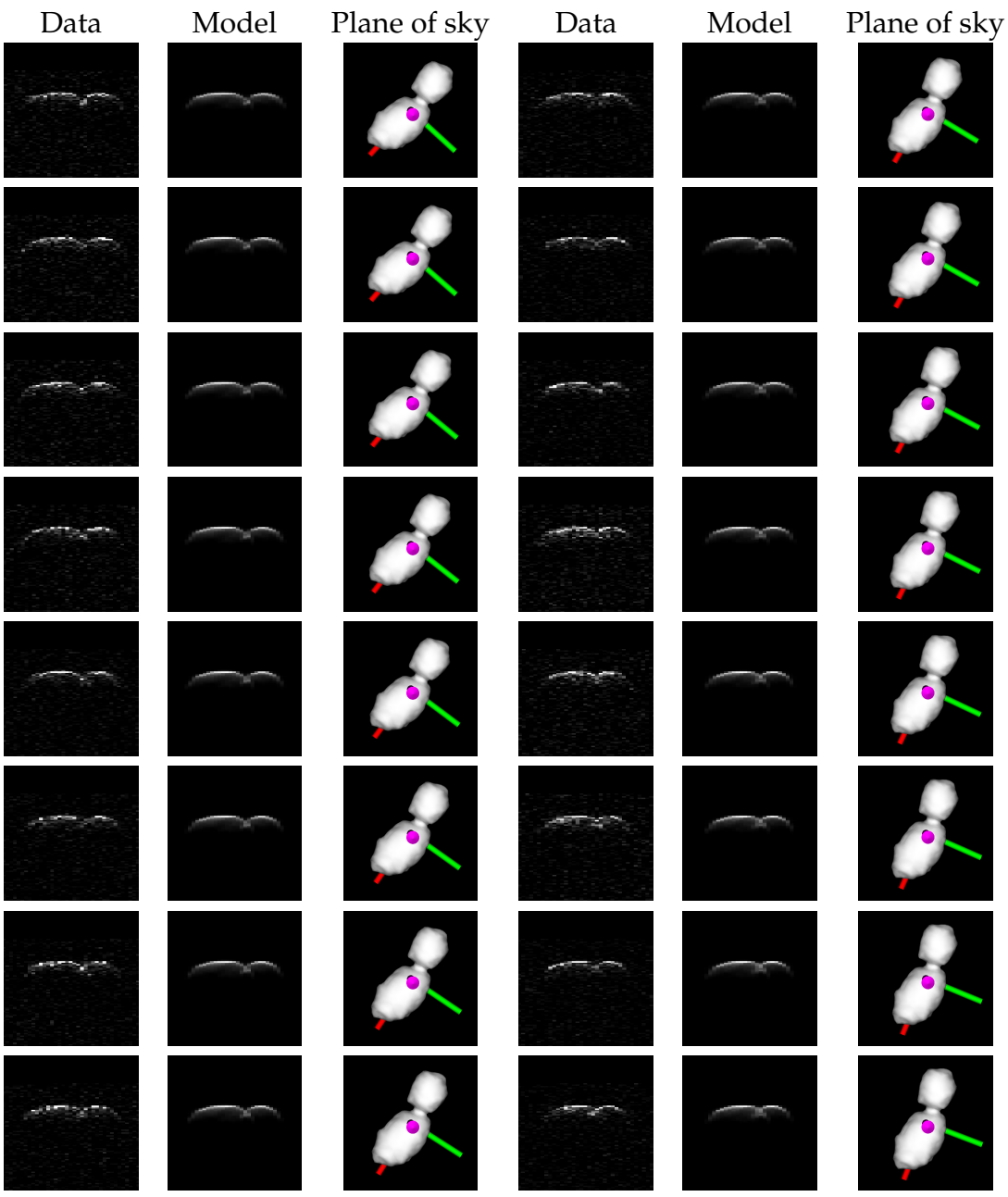

Figure B.17: Goldstone DSS-14 delay-Doppler images from July 23, 2015 (02:39 to 03:08 UT).

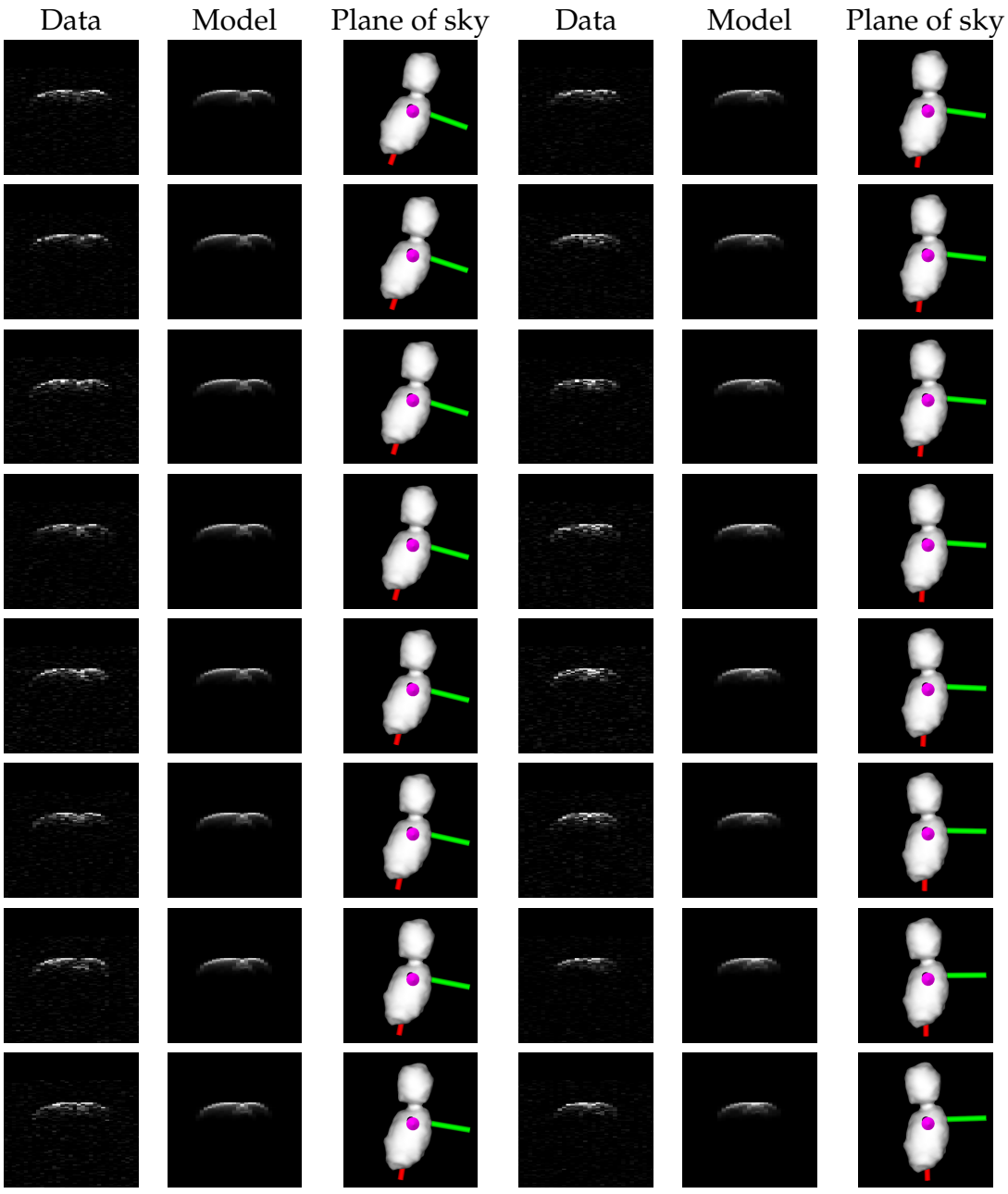

Figure B.18: Goldstone DSS-14 delay-Doppler images from July 23, 2015 (03:09 to 03:37 UT).

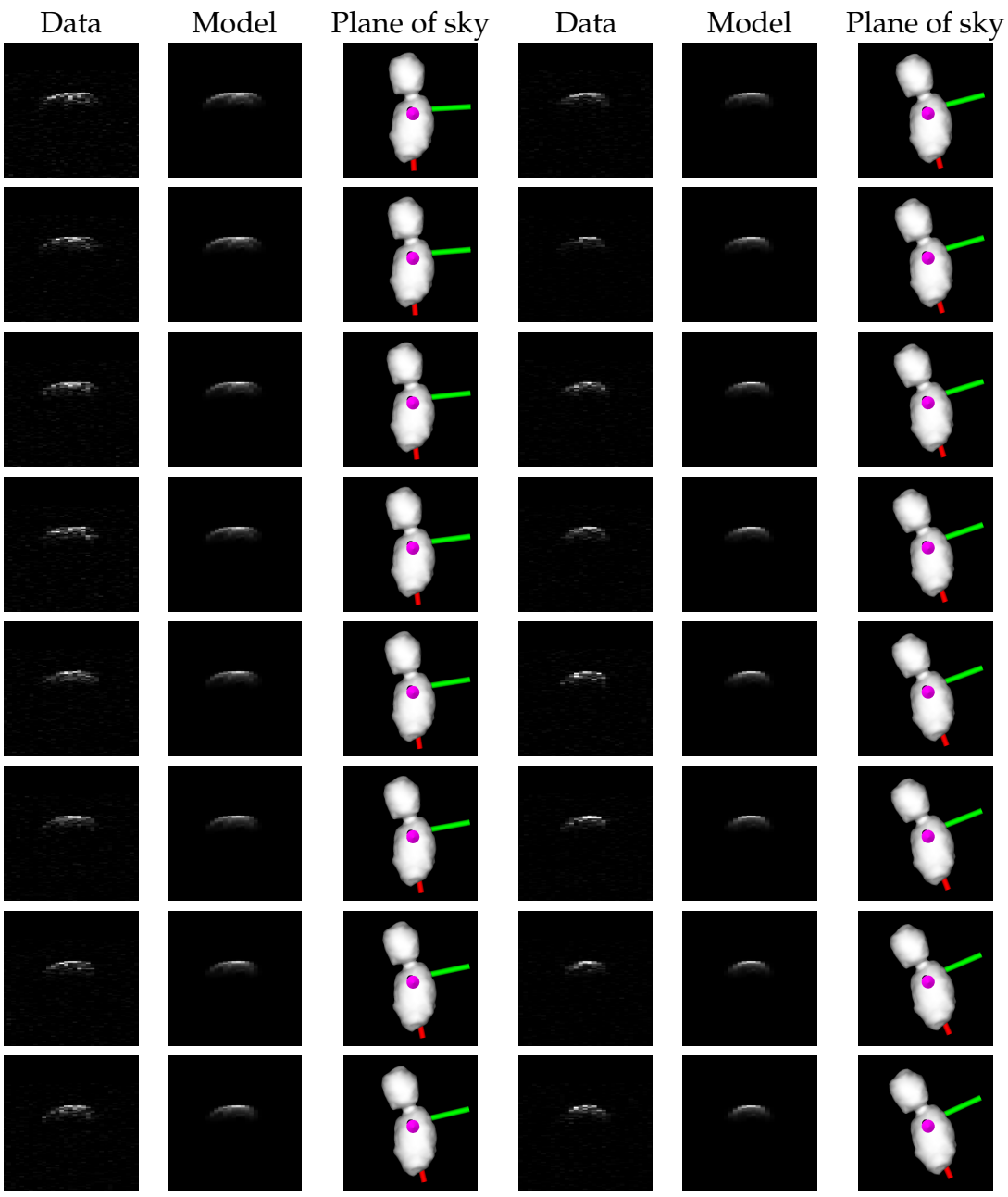

Figure B.19: Goldstone DSS-14 delay-Doppler images from July 23, 2015 (03:38 to 04:06 UT).

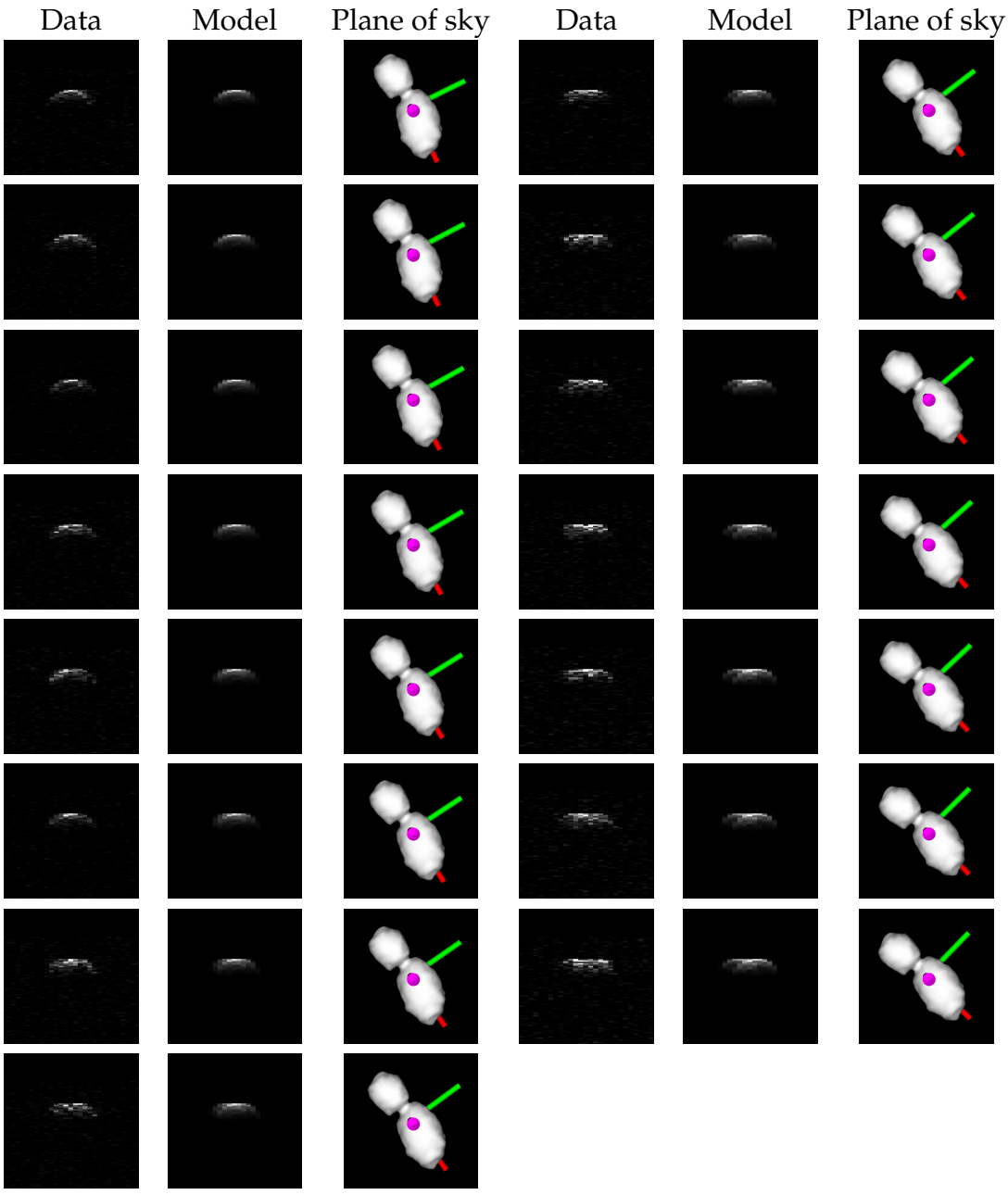

Figure B.20: Goldstone DSS-14 delay-Doppler images from July 23, 2015 (04:07 to 04:34 UT).

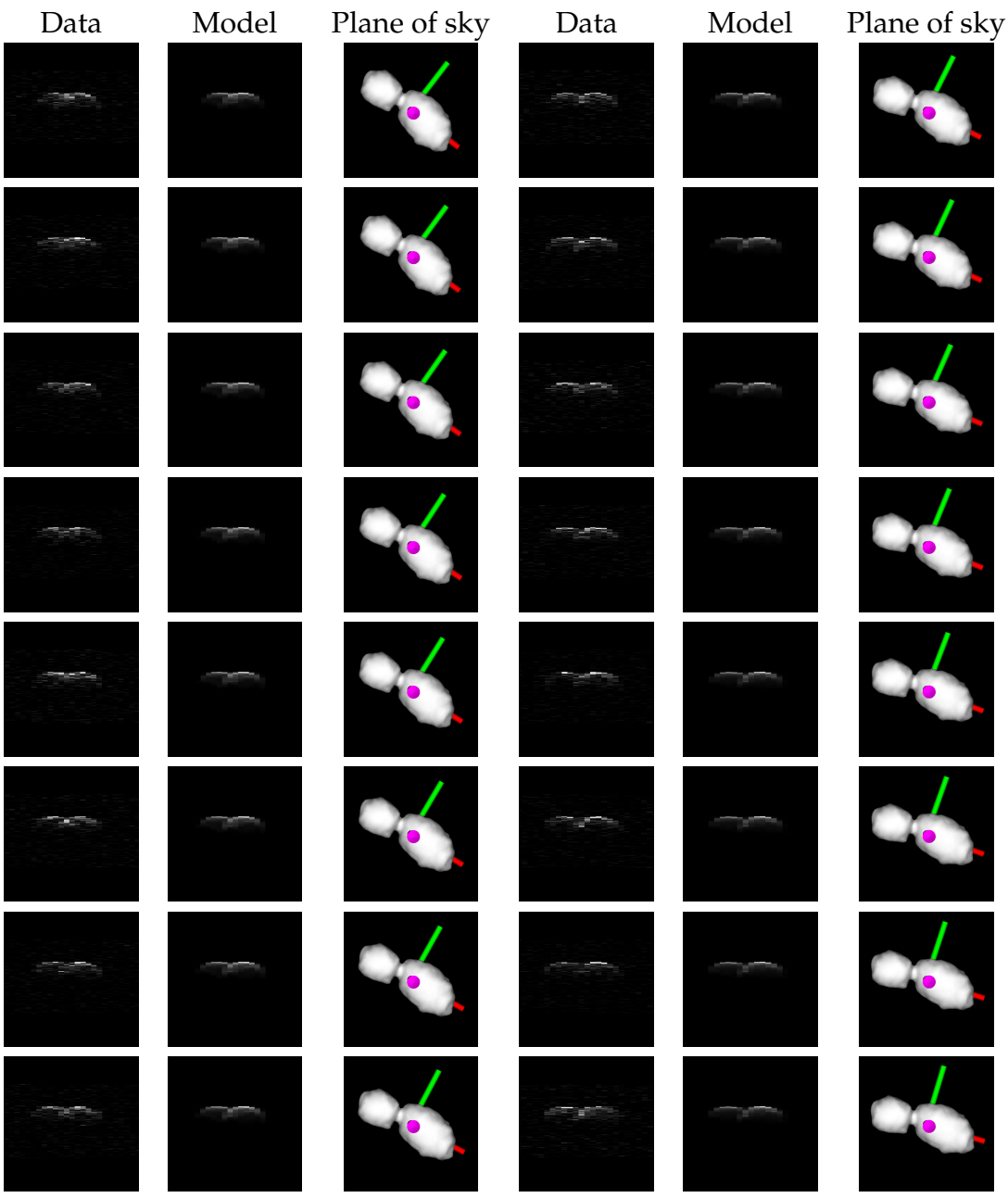

Figure B.21: Goldstone DSS-14 delay-Doppler images from July 23, 2015 (receive times 04:41 to 05:09 UT).

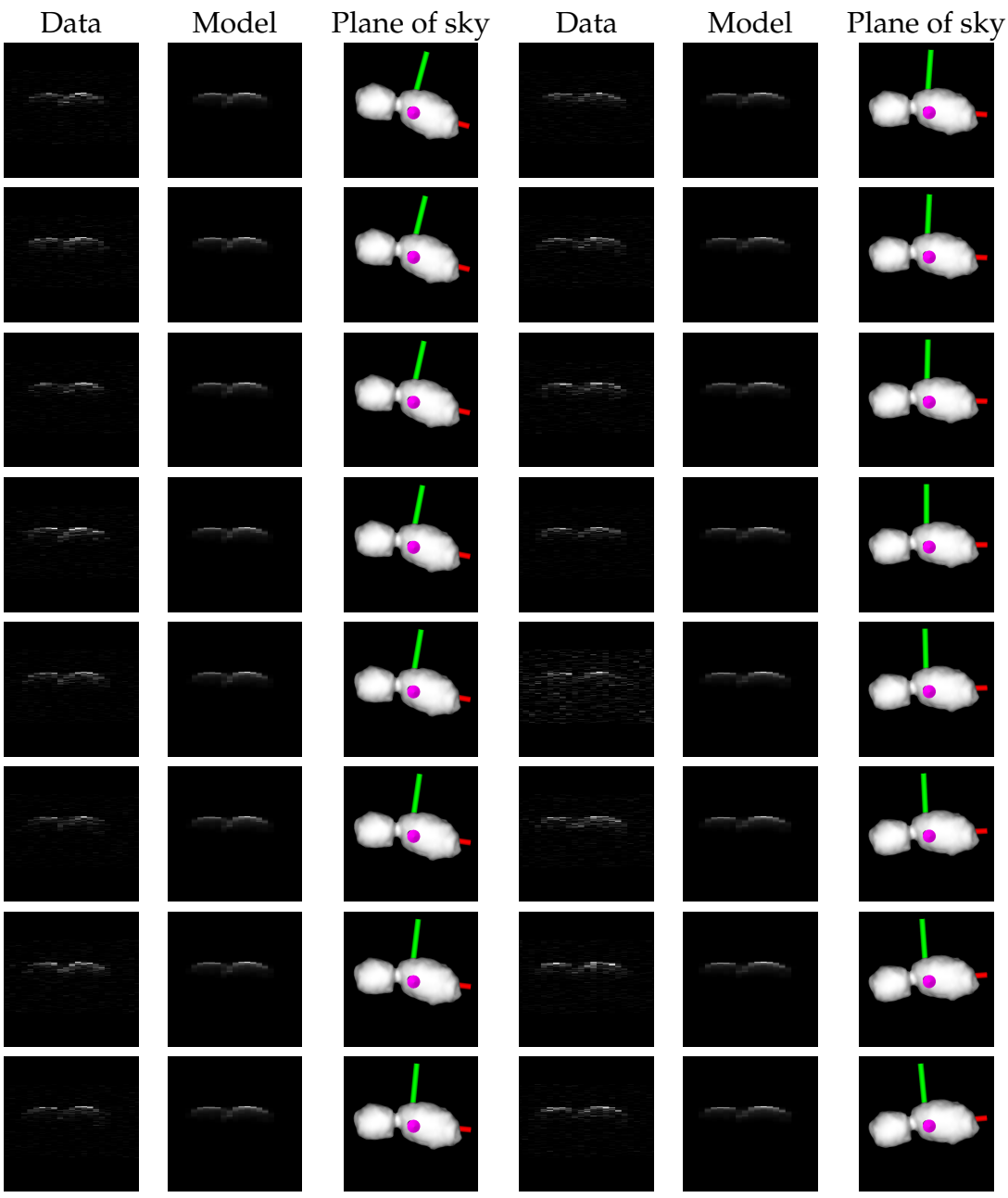

Figure B.22: Goldstone DSS-14 delay-Doppler images from July 23, 2015 (05:10 to 05:38 UT).

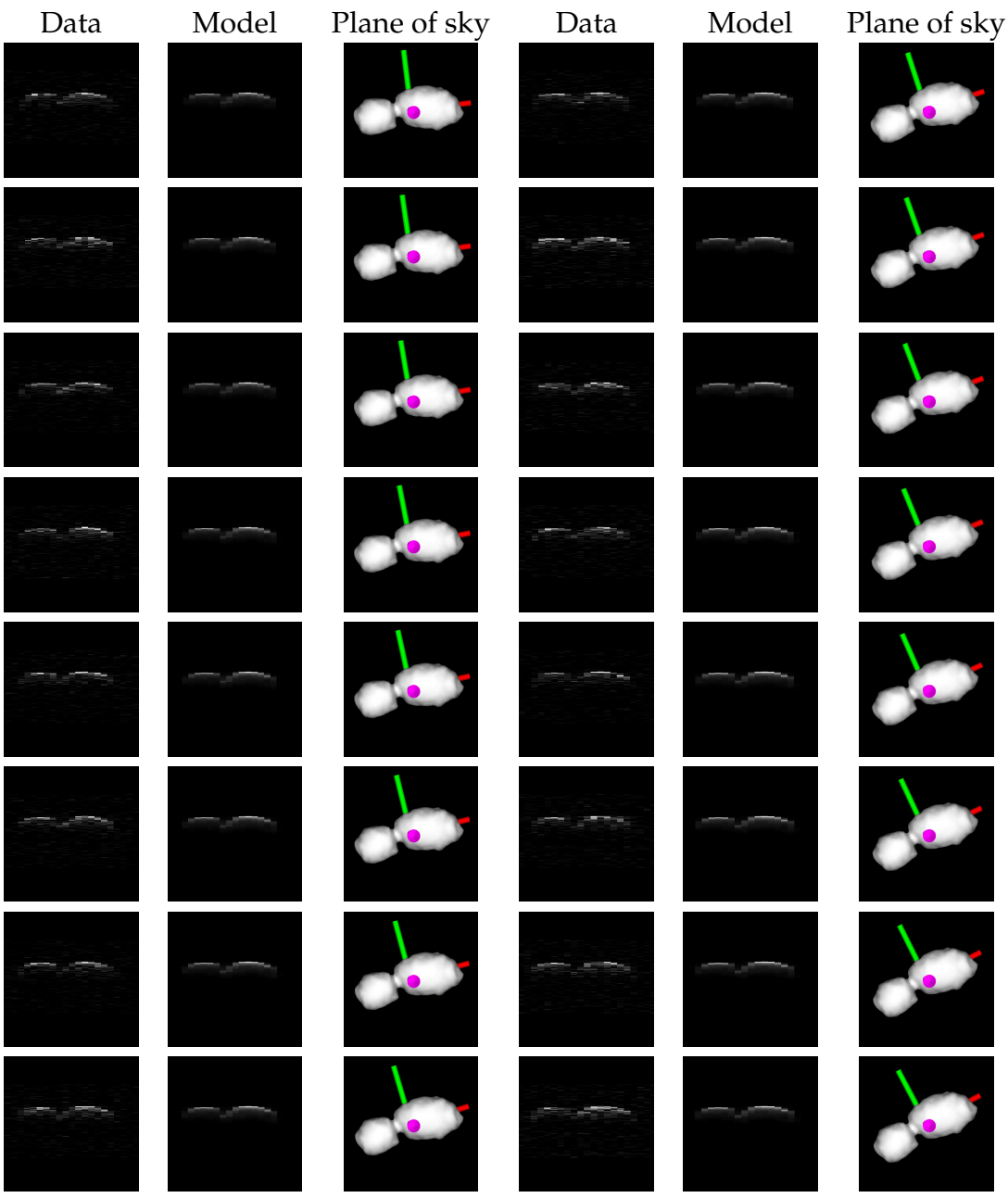

Figure B.23: Goldstone DSS-14 delay-Doppler images from July 23, 2015 (05:39 to 06:07 UT).

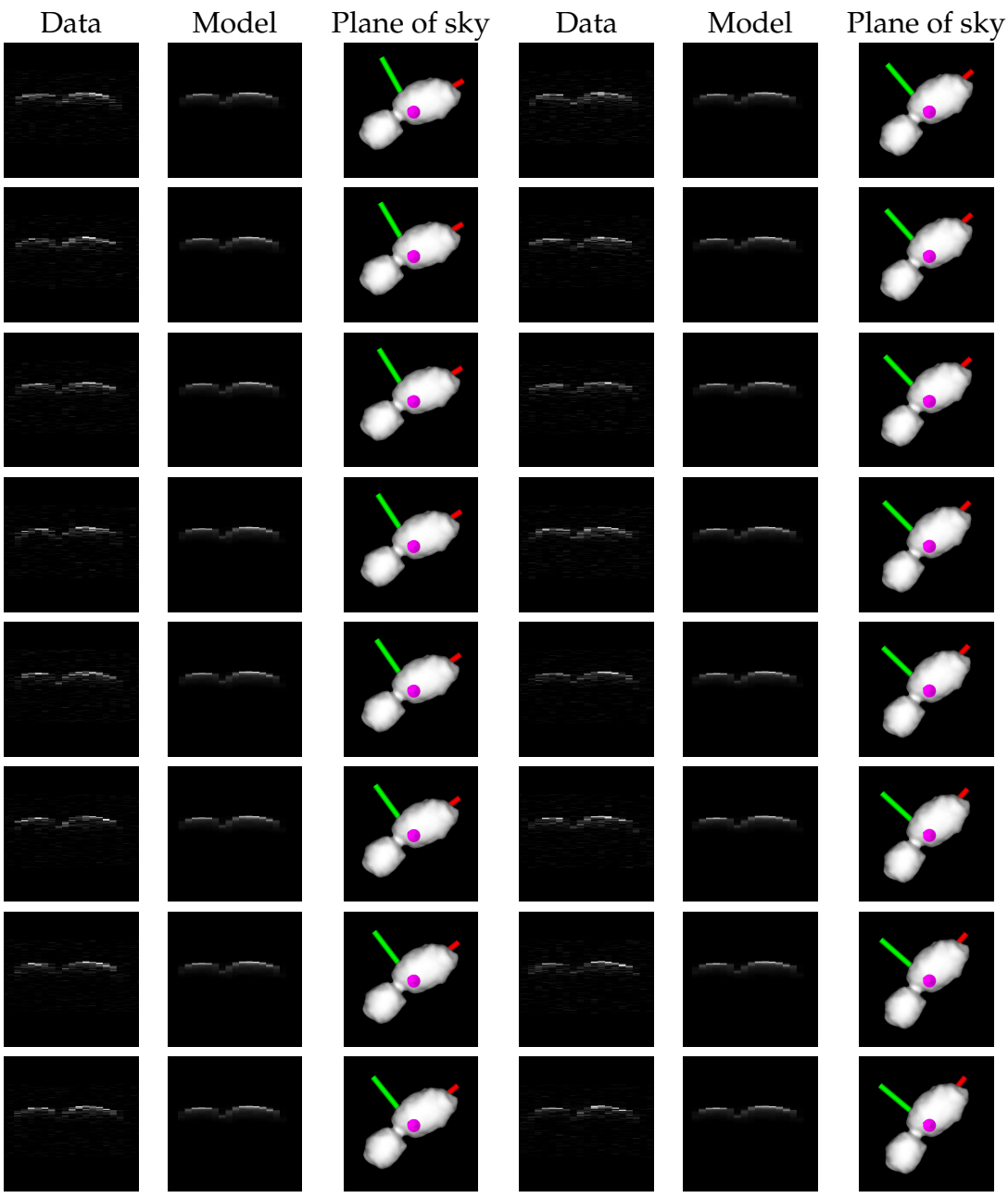

Figure B.24: Goldstone DSS-14 delay-Doppler images from July 23, 2015 (06:08 to 06:35 UT).

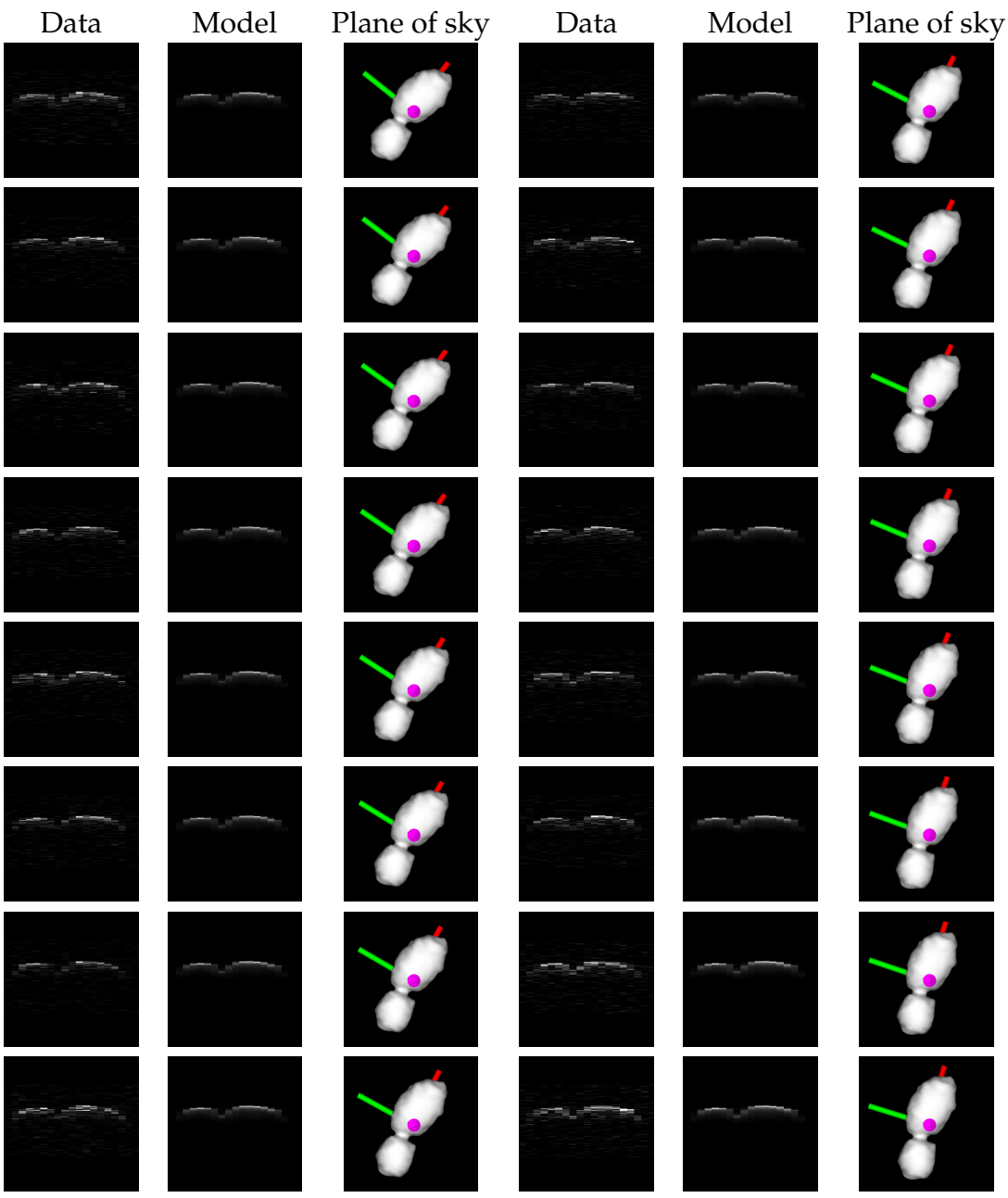

Figure B.25: Goldstone DSS-14 delay-Doppler images from July 23, 2015 (06:36 to 07:04 UT).

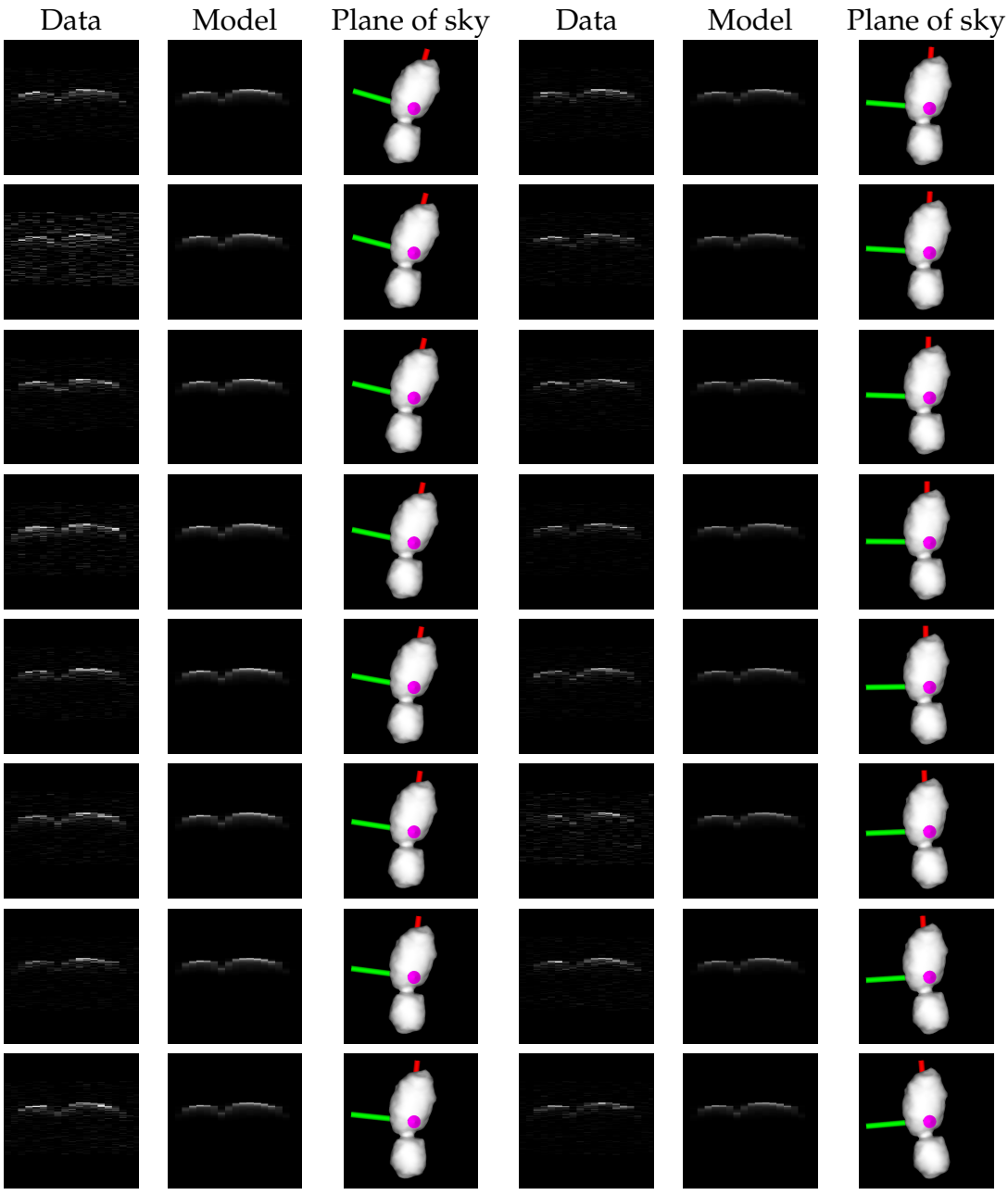

Figure B.26: Goldstone DSS-14 delay-Doppler images from July 23, 2015 (07:05 to 07:33 UT).

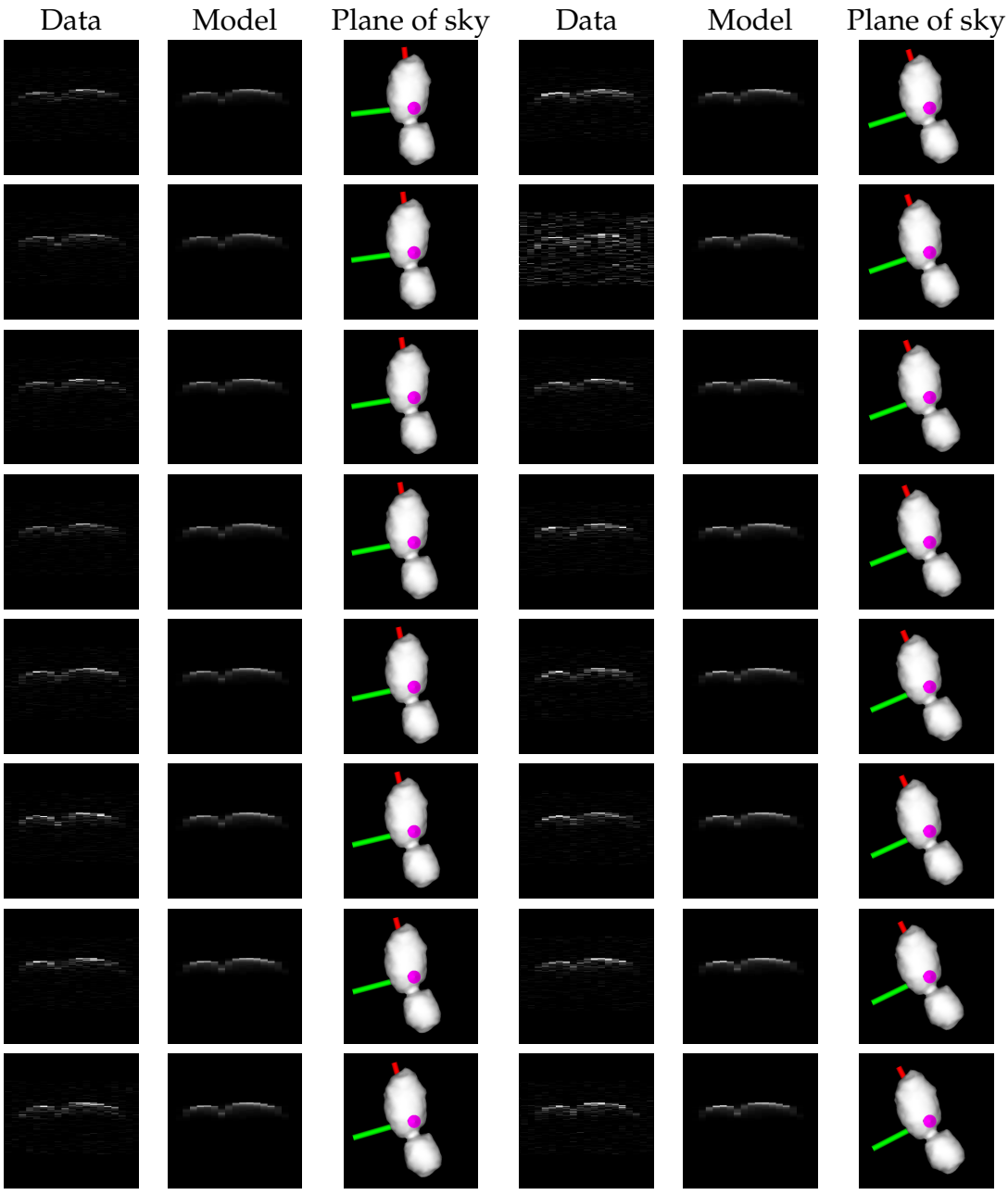

Figure B.27: Goldstone DSS-14 delay-Doppler images from July 23, 2015 (07:34 to 08:02 UT).

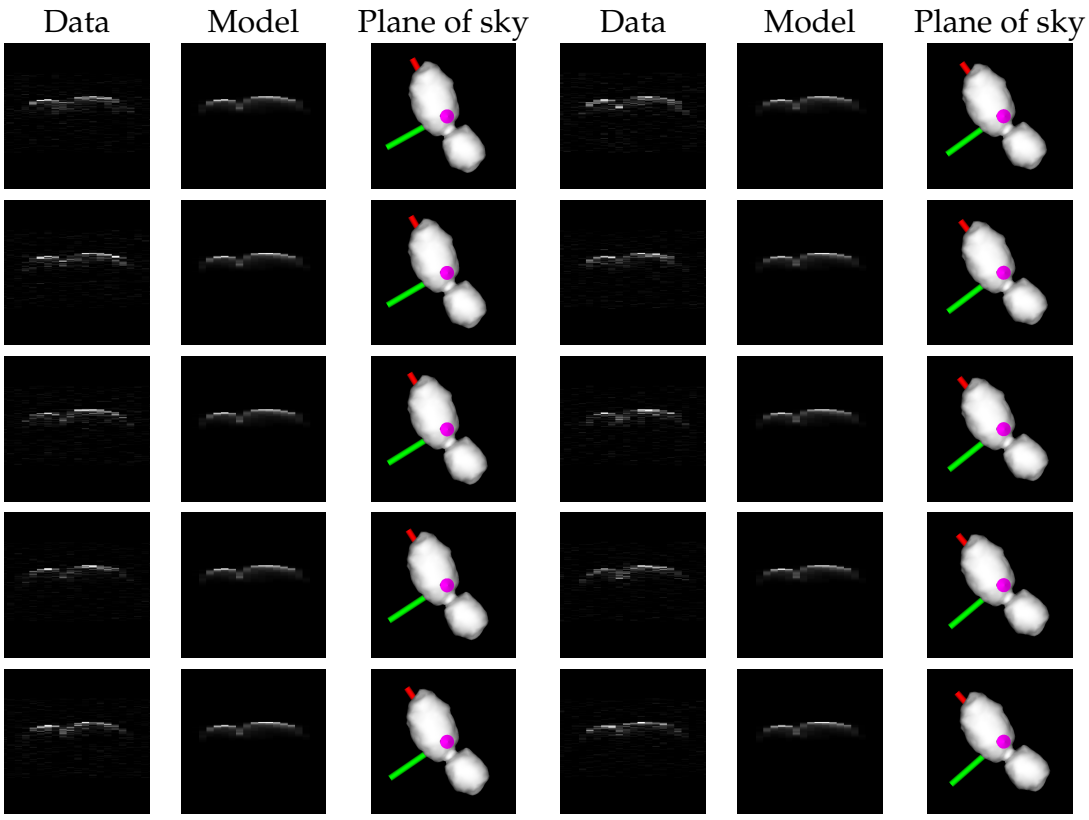

Figure B.28: Goldstone DSS-14 delay-Doppler images from July 23, 2015 (08:03 to 08:20 UT).

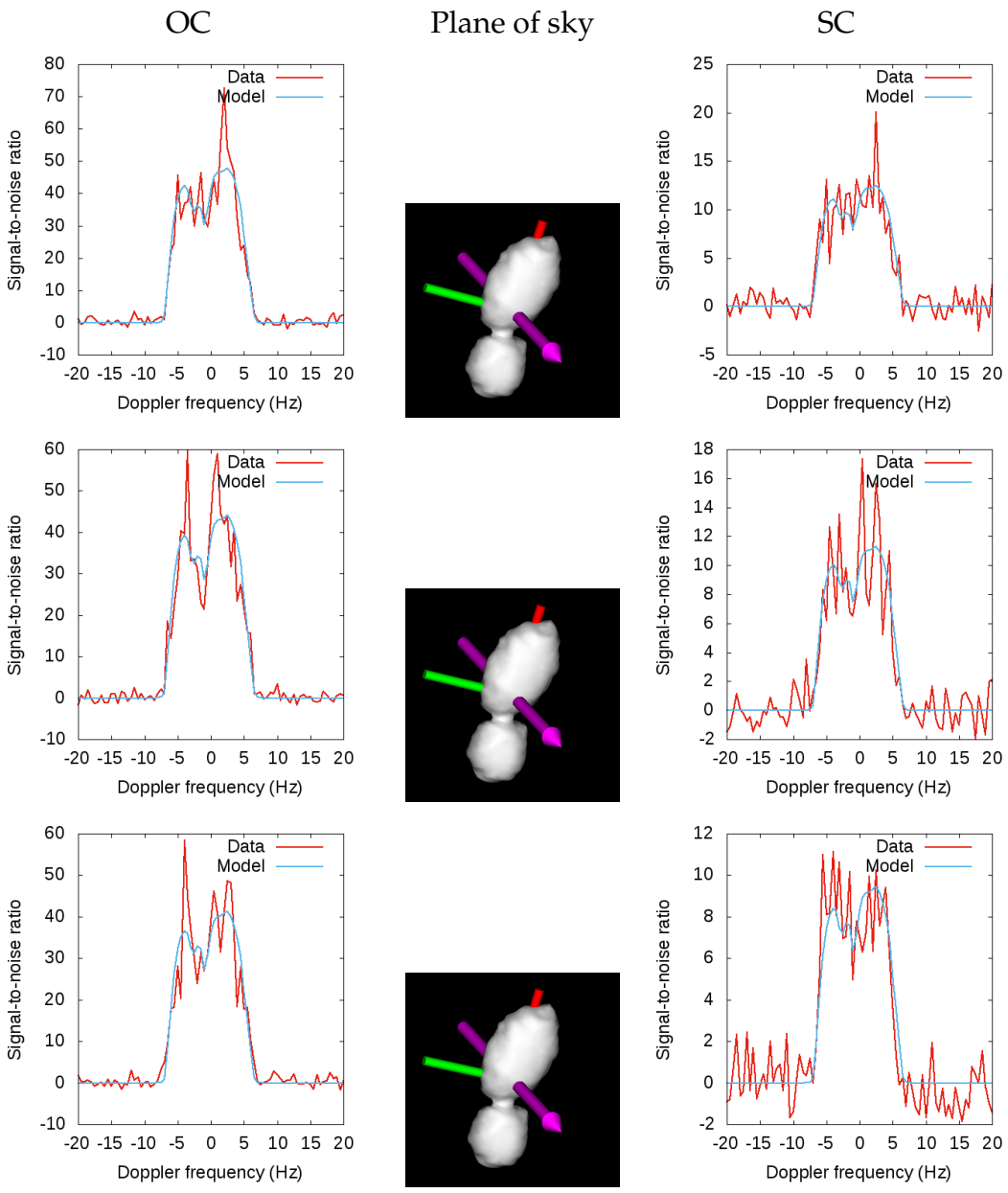

Figure B.29: CW spectra from Goldstone DSS-14 on July 24, 2015 (receive times 23:52 to 23:56 UT; both polarizations).

B.1.6 Goldstone observations from July 24-25, 2015

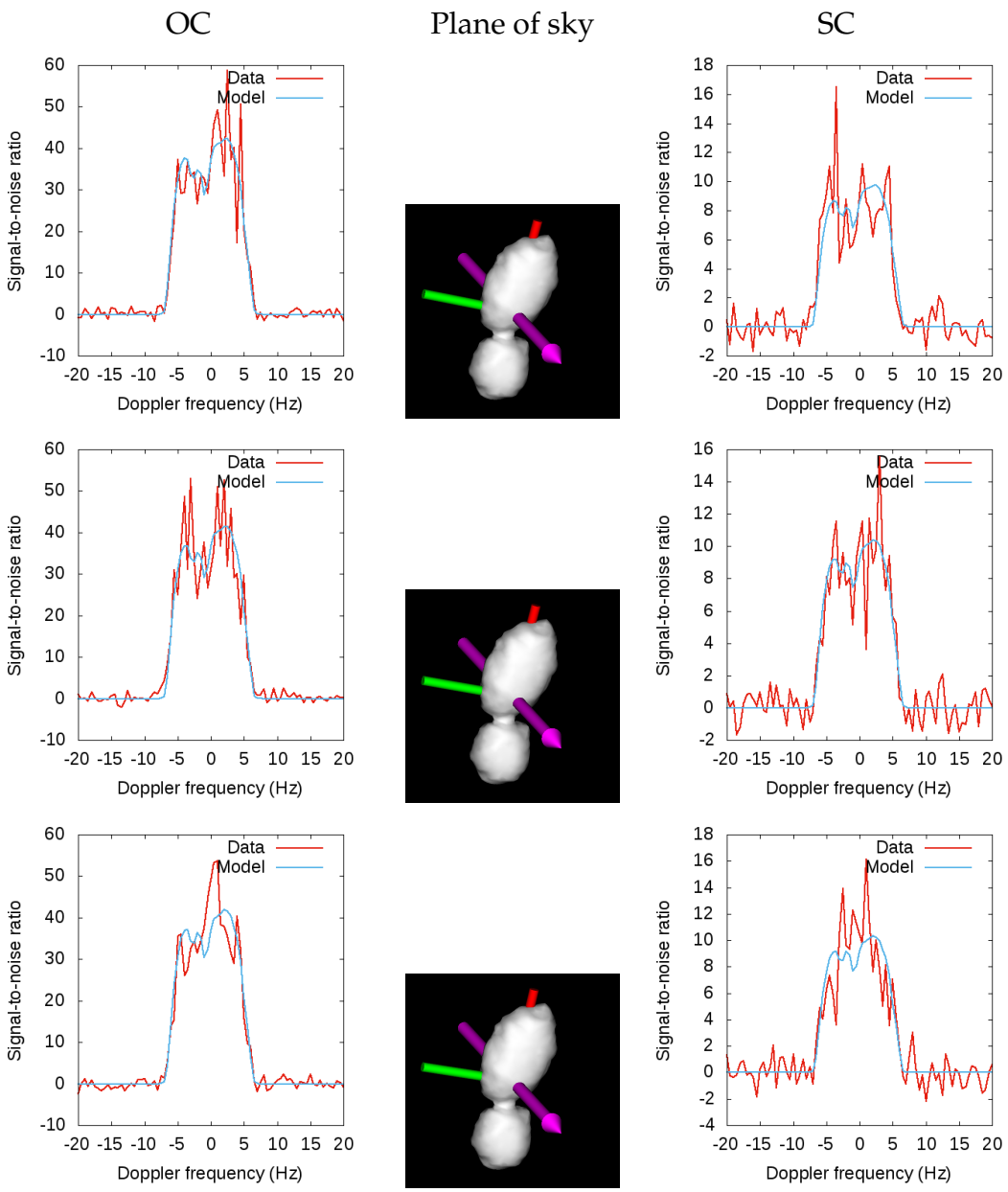

Figure B.30: CW spectra from Goldstone DSS-14 on July 24-25, 2015 (23:57 to 00:01 UT; both polarizations).

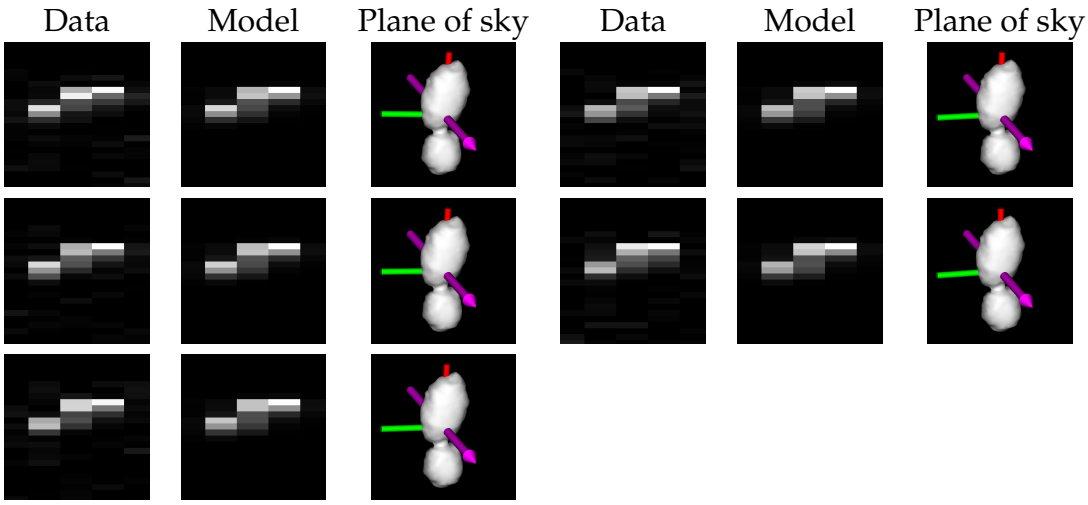

Figure B.31: Goldstone DSS-14 delay-Doppler images from July 25, 2015 (00:11 to 00:18 UT).

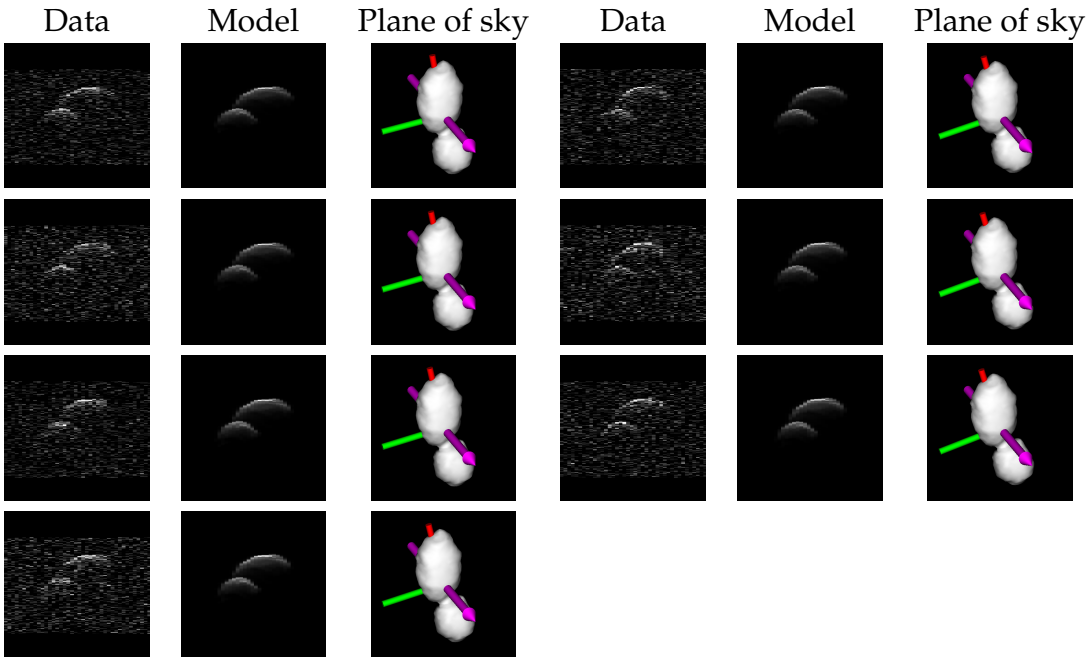

Figure B.32: Goldstone DSS-14 delay-Doppler images from July 25, 2015 (00:33 to 00:43 UT).

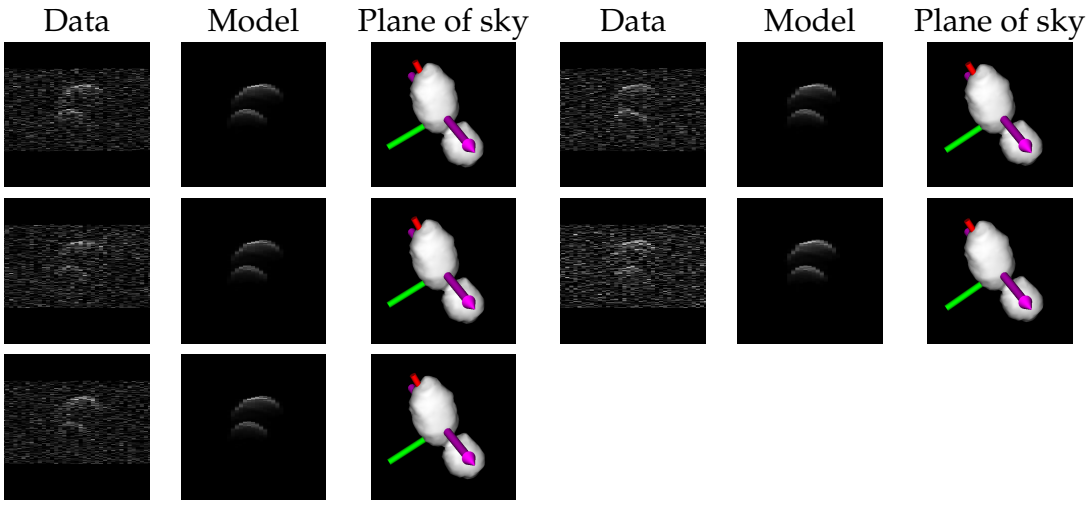

Figure B.33: Goldstone DSS-14 delay-Doppler images from July 25, 2015 (00:56 to 01:03 UT).

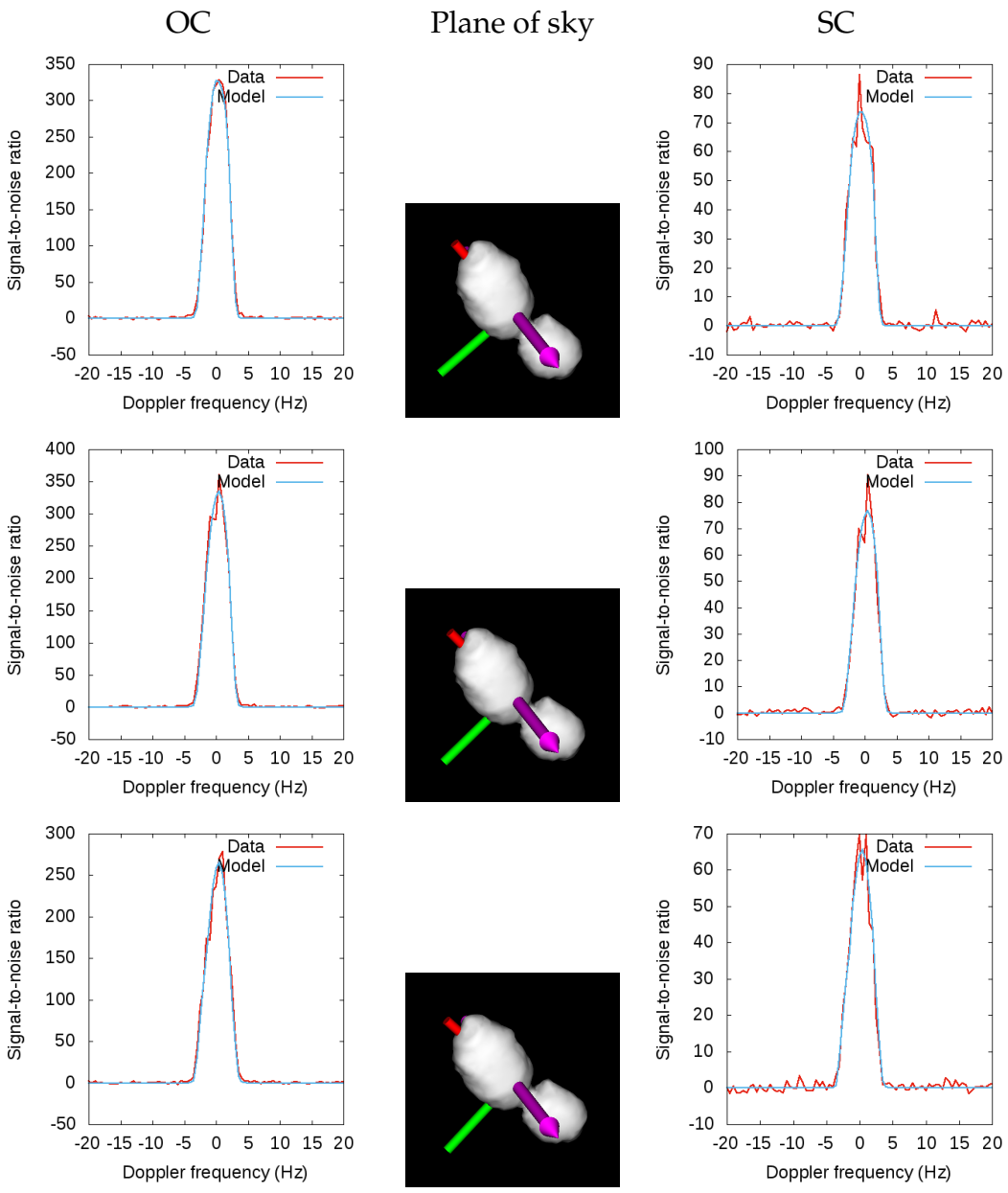

Figure B.34: CW spectra from bistatic observations (Goldstone DSS-14 to Green Bank Telescope) on July 25, 2015 (01:09 to 01:23 UT; both polarizations).

B.1.7 Bistatic observations from July 25, 2015

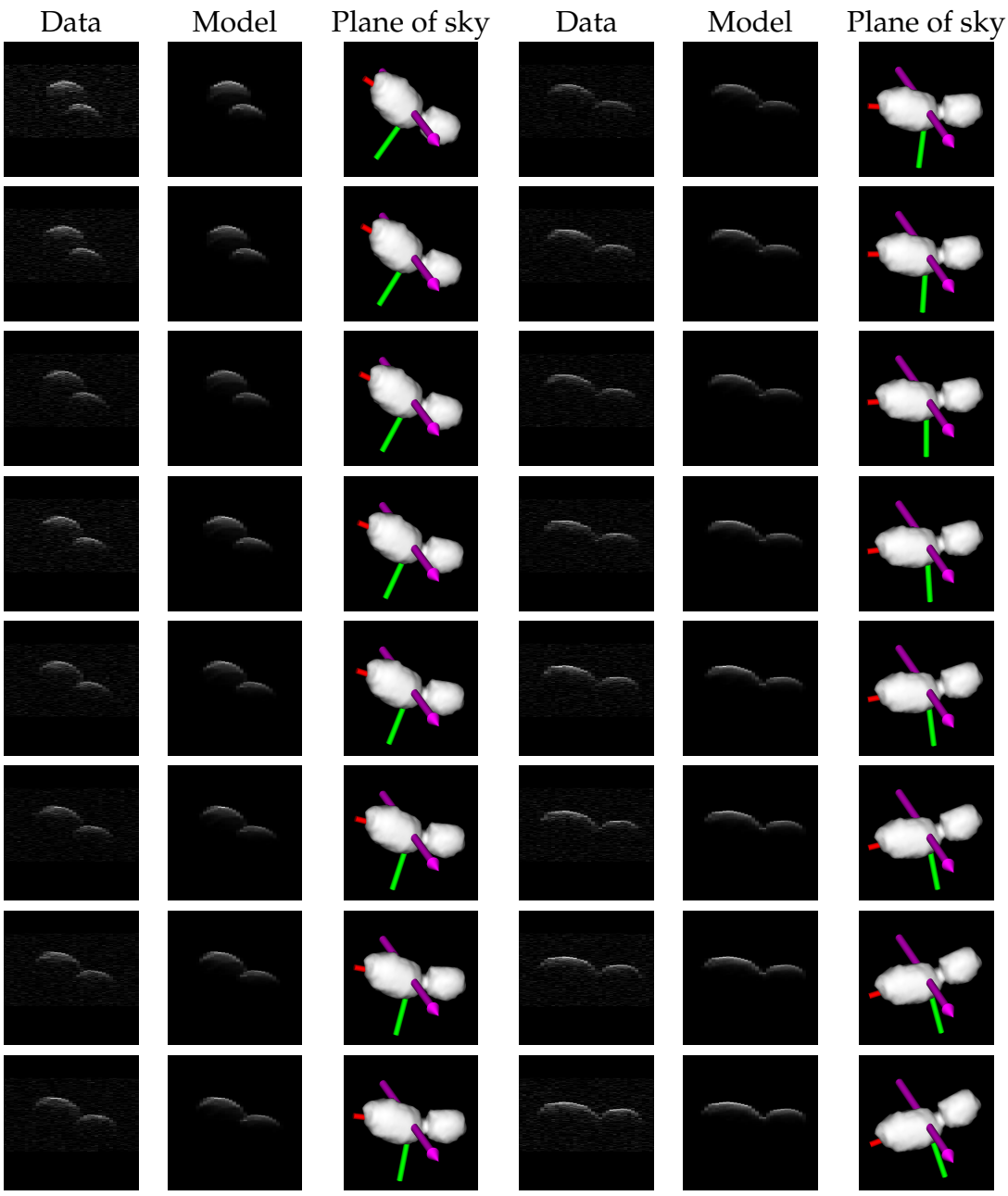

Figure B.35: Delay-Doppler images from bistatic observations (Goldstone DSS-14 to GBT) on July 25, 2015 (01:30 to 02:50 UT).

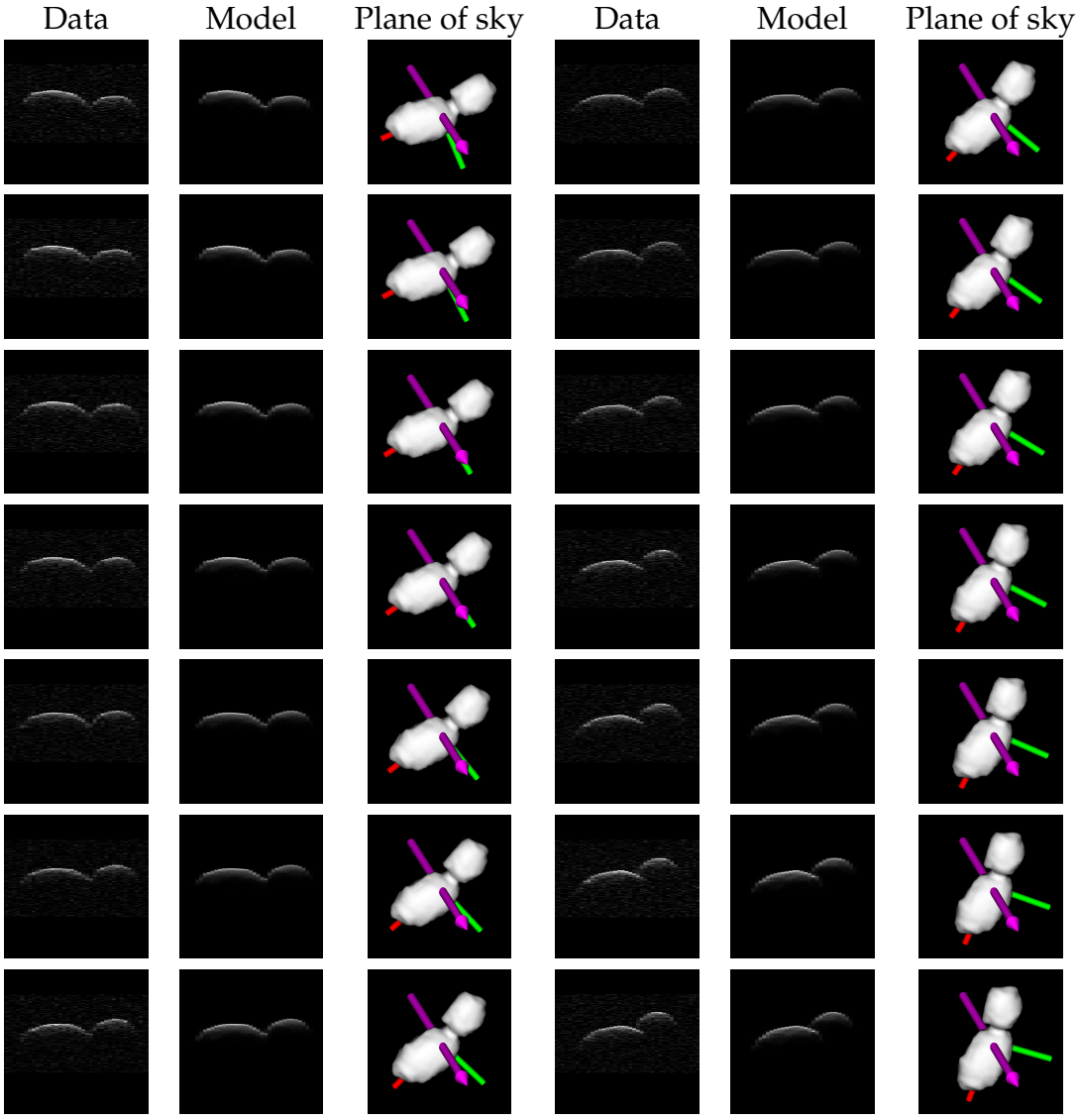

Figure B.36: Delay-Doppler images from bistatic observations (Goldstone DSS-14 to GBT) on July 25, 2015 (02:50 to 04:00 UT).

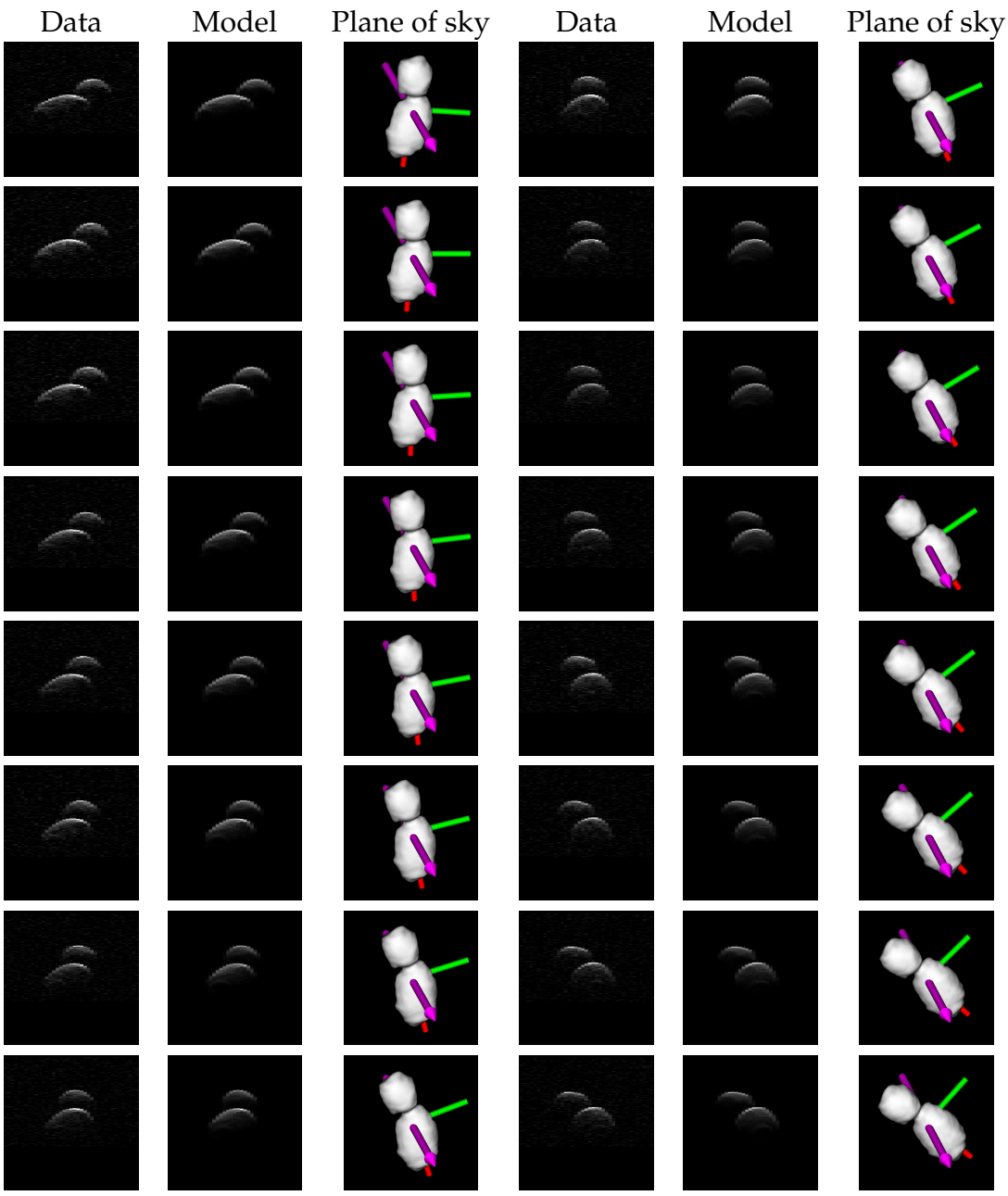

Figure B.37: Delay-Doppler images from bistatic observations (Goldstone DSS-14 to GBT) on July 25, 2015 (04:12 to 05:32 UT).

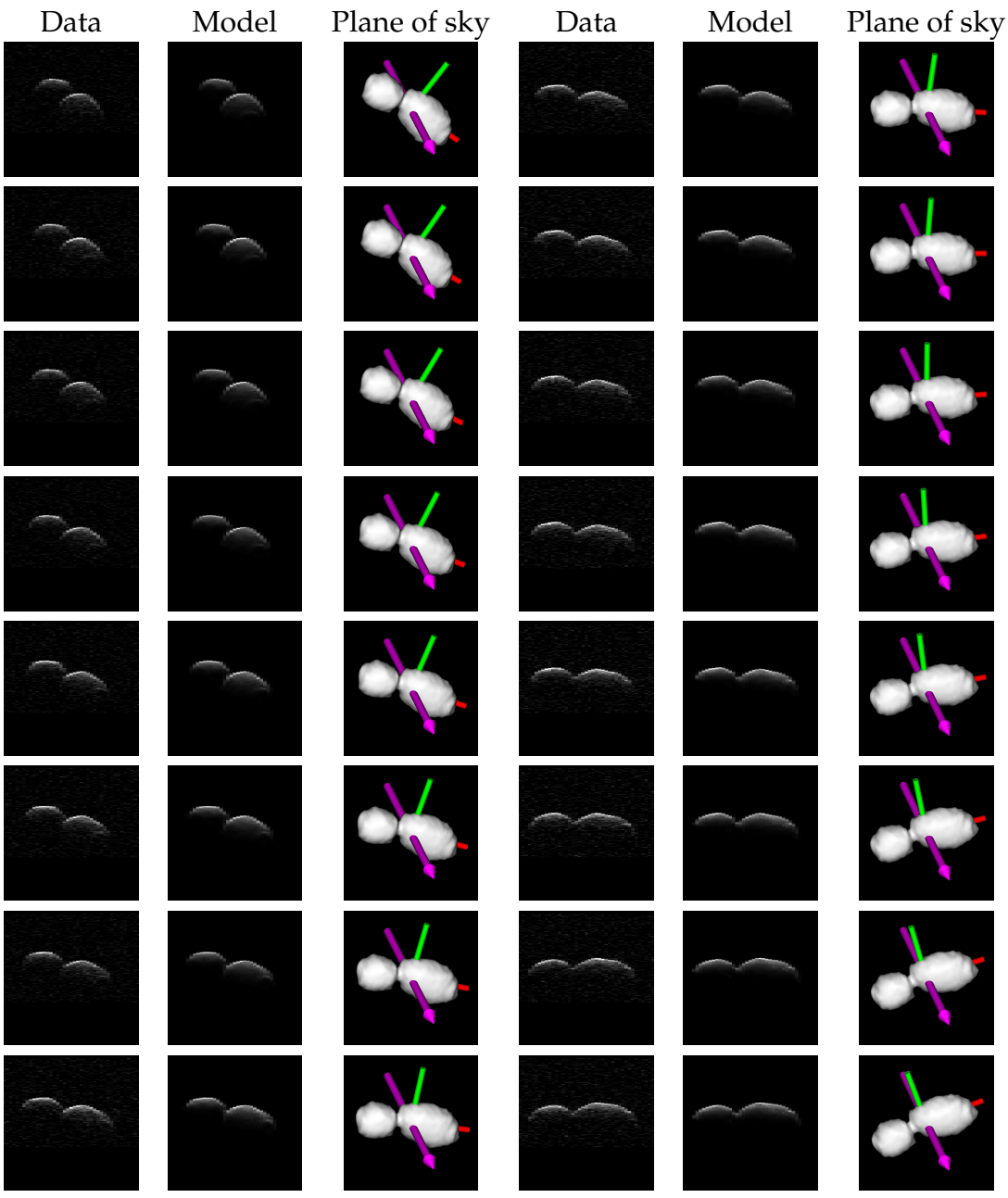

Figure B.38: Delay-Doppler images from bistatic observations (Goldstone DSS-14 to GBT) on July 25, 2015 (05:32 to 06:53 UT).

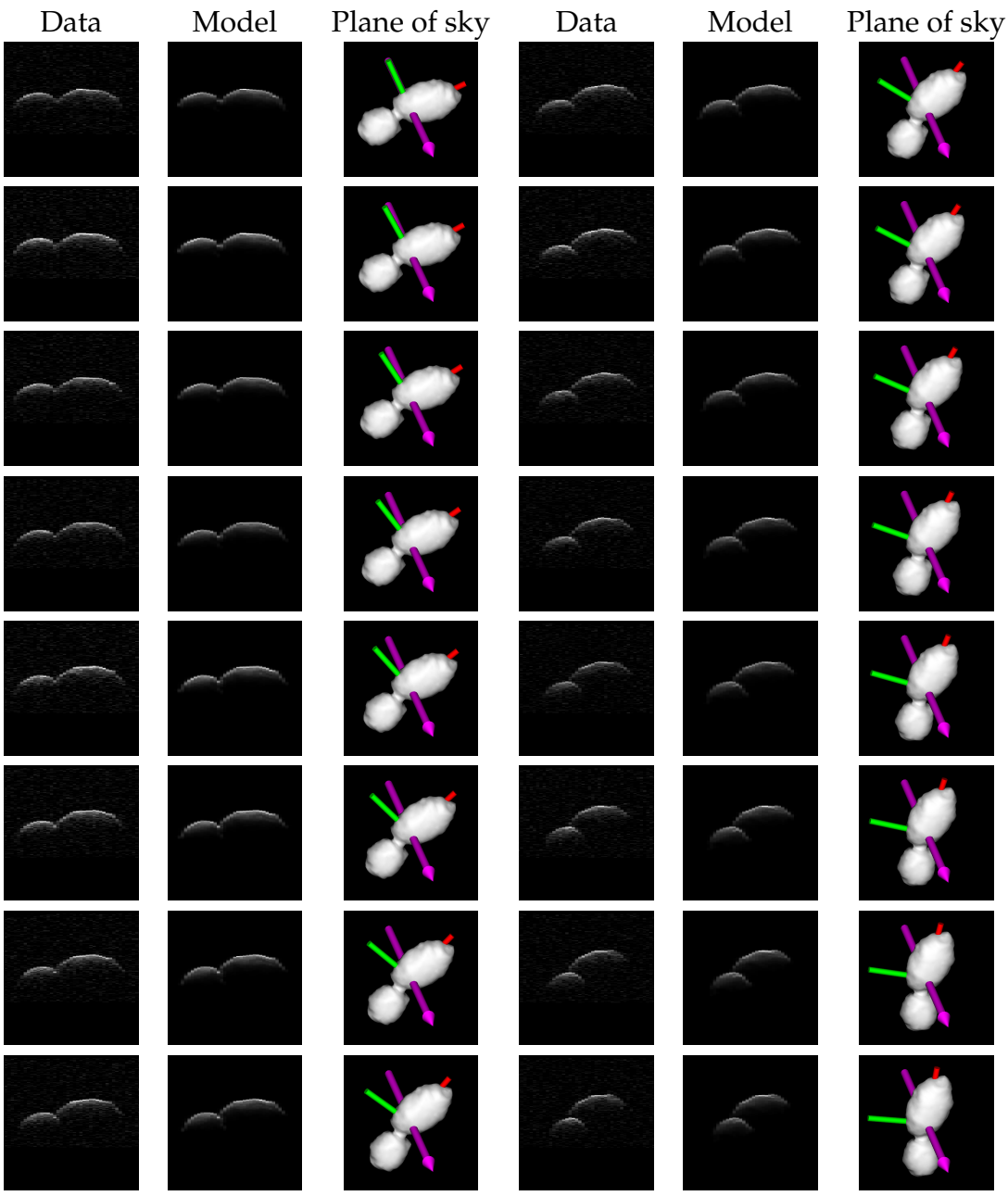

Figure B.39: Delay-Doppler images from bistatic observations (Goldstone DSS-14 to GBT) on July 25, 2015 (06:53 to 08:13 UT).

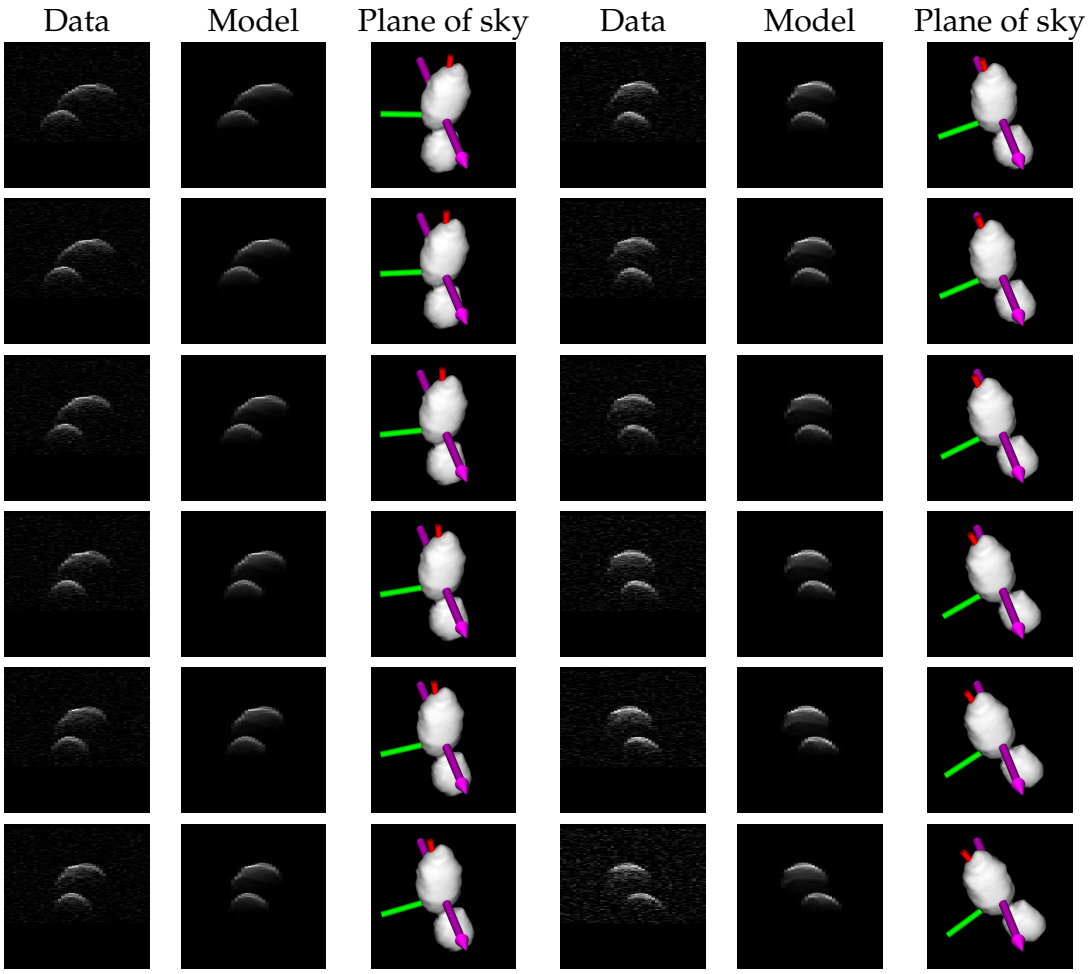

Figure B.40: Delay-Doppler images from bistatic observations (Goldstone DSS-14 to GBT) on July 25, 2015 (08:13 to 09:13 UT).

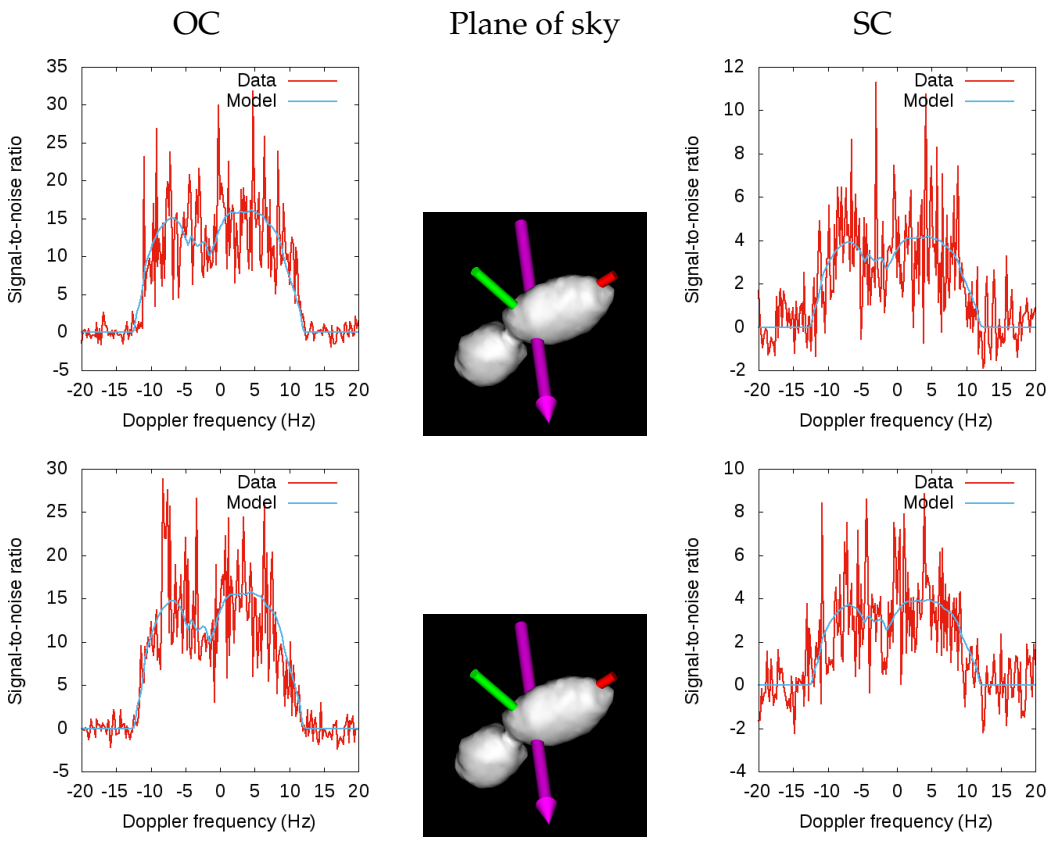

Figure B.41: CW spectra from bistatic observations (Goldstone DSS-14 to Green Bank Telescope) on July 26, 2015 (receive times 14:16 to 14:18 UT; both polarizations).

B.1.8 Bistatic observations from July 26, 2015

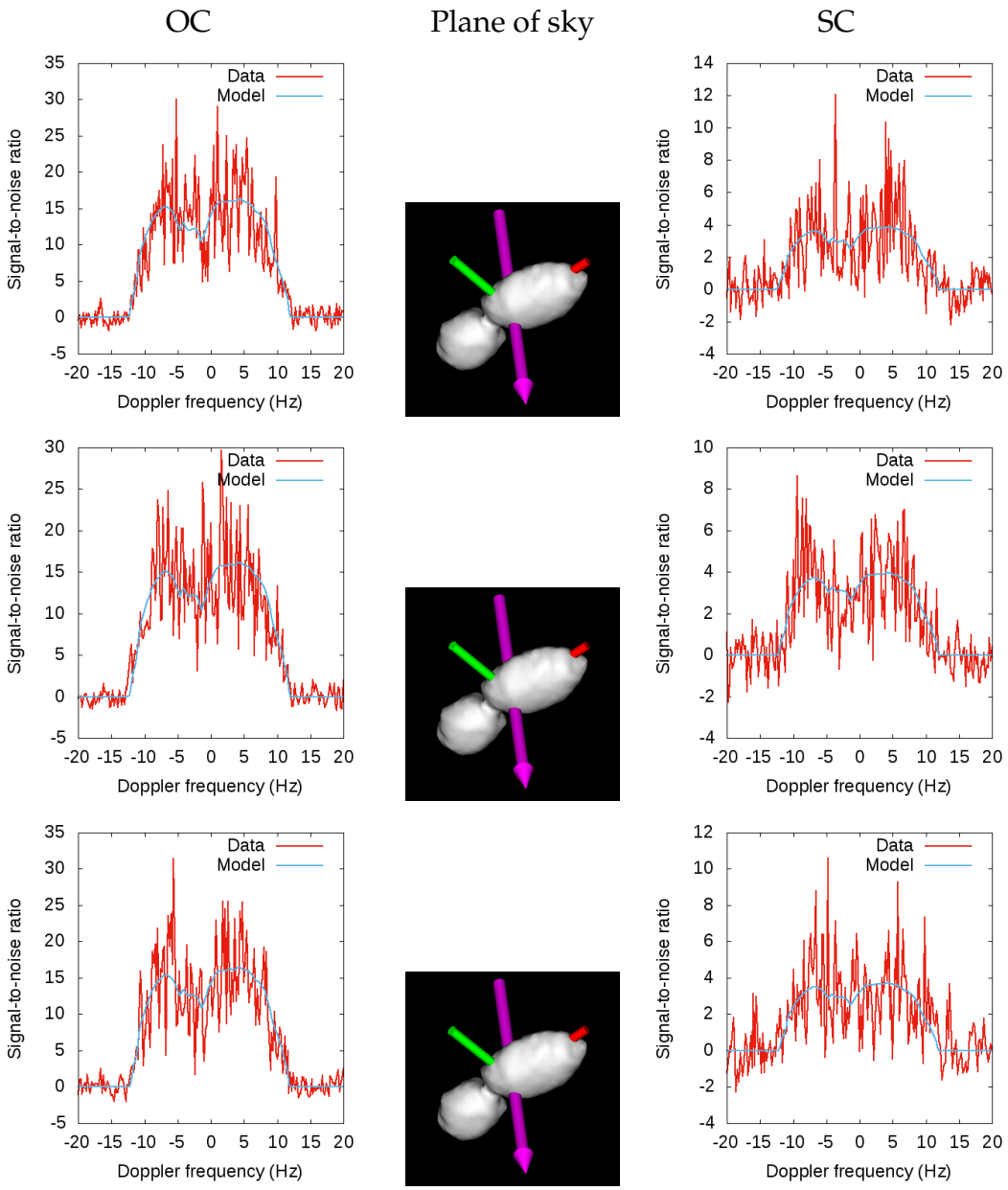

Figure B.42: CW spectra from bistatic observations (Goldstone DSS-14 to GBT) on July 26, 2015 (14:18 to 14:21 UT).

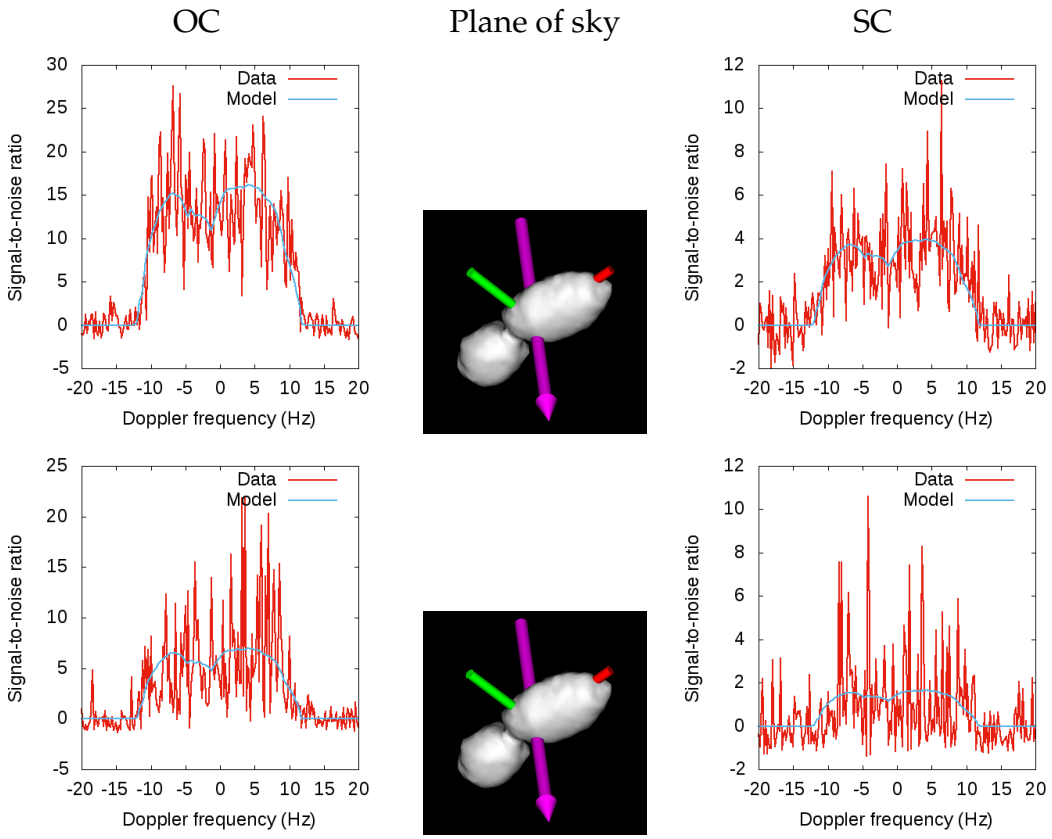

Figure B.43: CW spectra from bistatic observations (Goldstone DSS-14 to GBT) on July 26, 2015 (14:21 to 14:22 UT).

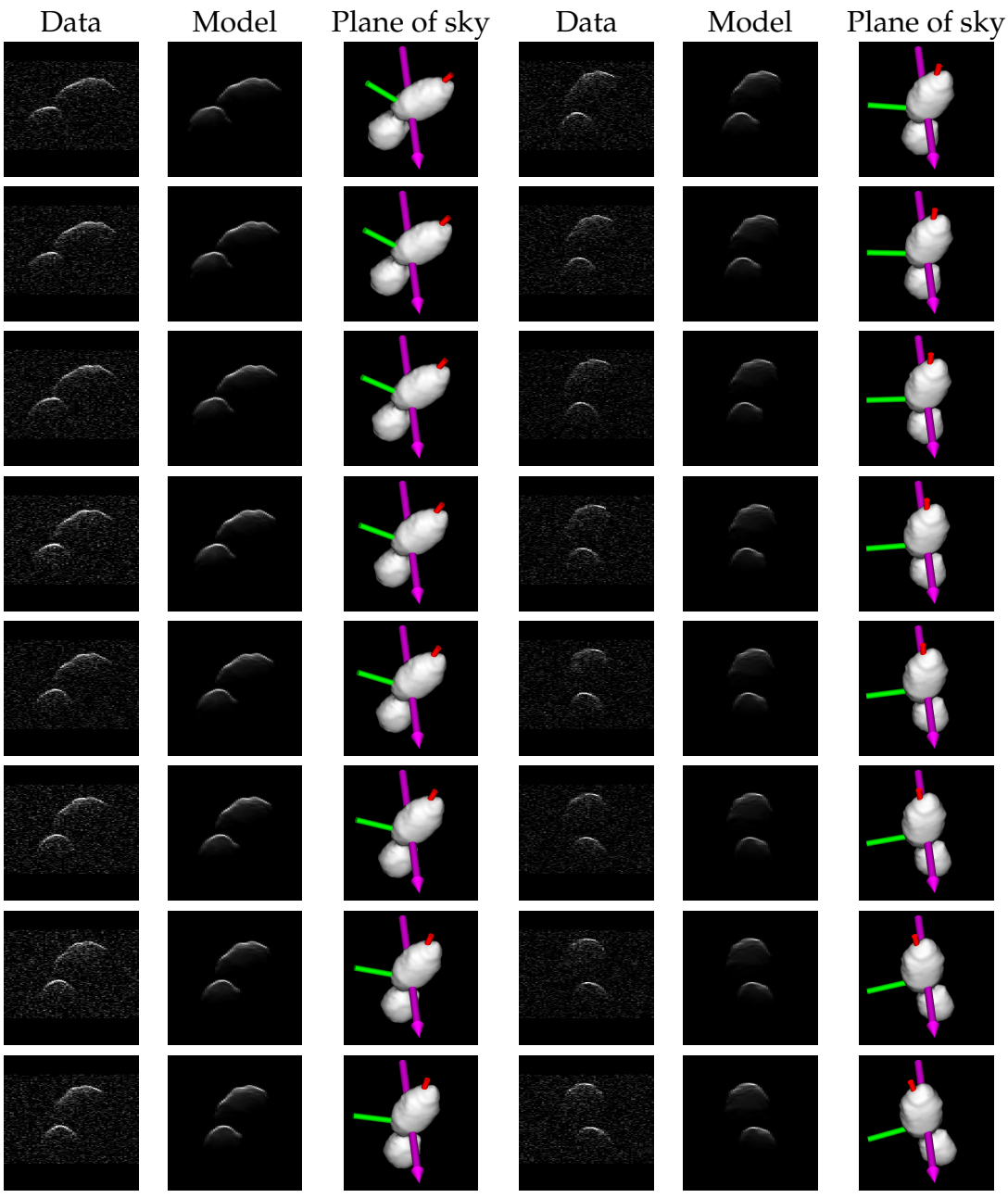

Figure B.44: Delay-Doppler images from bistatic observations (Goldstone DSS-14 to GBT) on July 26, 2015 (14:27 to 15:47 UT).

Figure B.45: Delay-Doppler images from bistatic observations (Goldstone DSS-14 to GBT) on July 26, 2015 (15:47 to 17:07 UT).

Figure B.46: Delay-Doppler images from bistatic observations (Goldstone DSS-14 to GBT) on July 26, 2015 (17:07 to 18:27 UT).

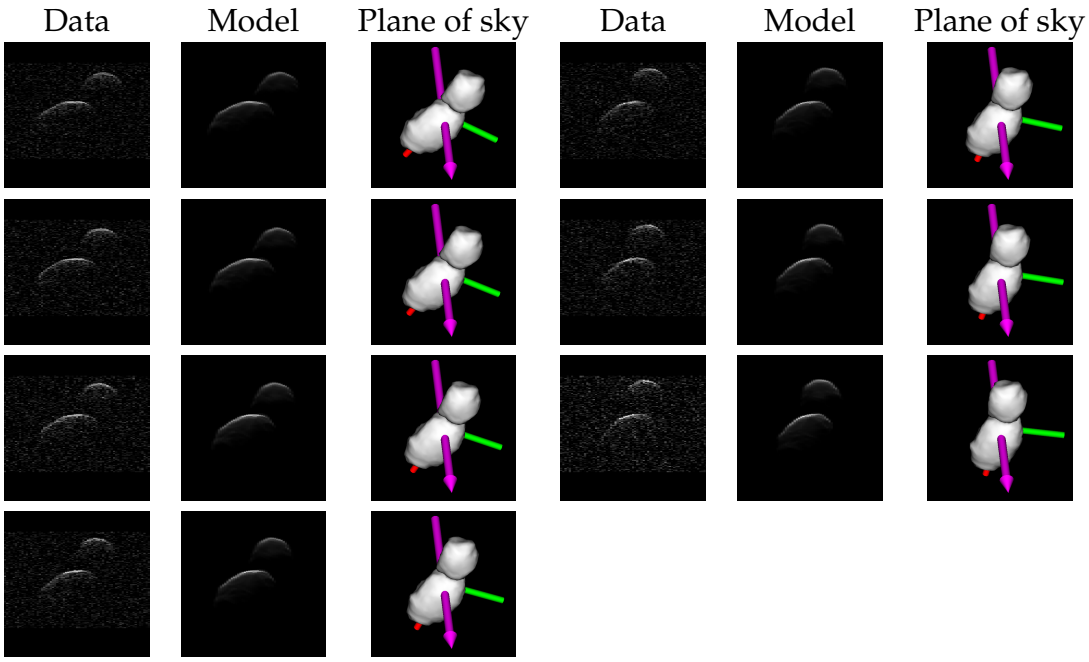

Figure B.47: Delay-Doppler images from bistatic observations (Goldstone DSS-14 to GBT) on July 26, 2015 (18:27 to 19:02 UT).

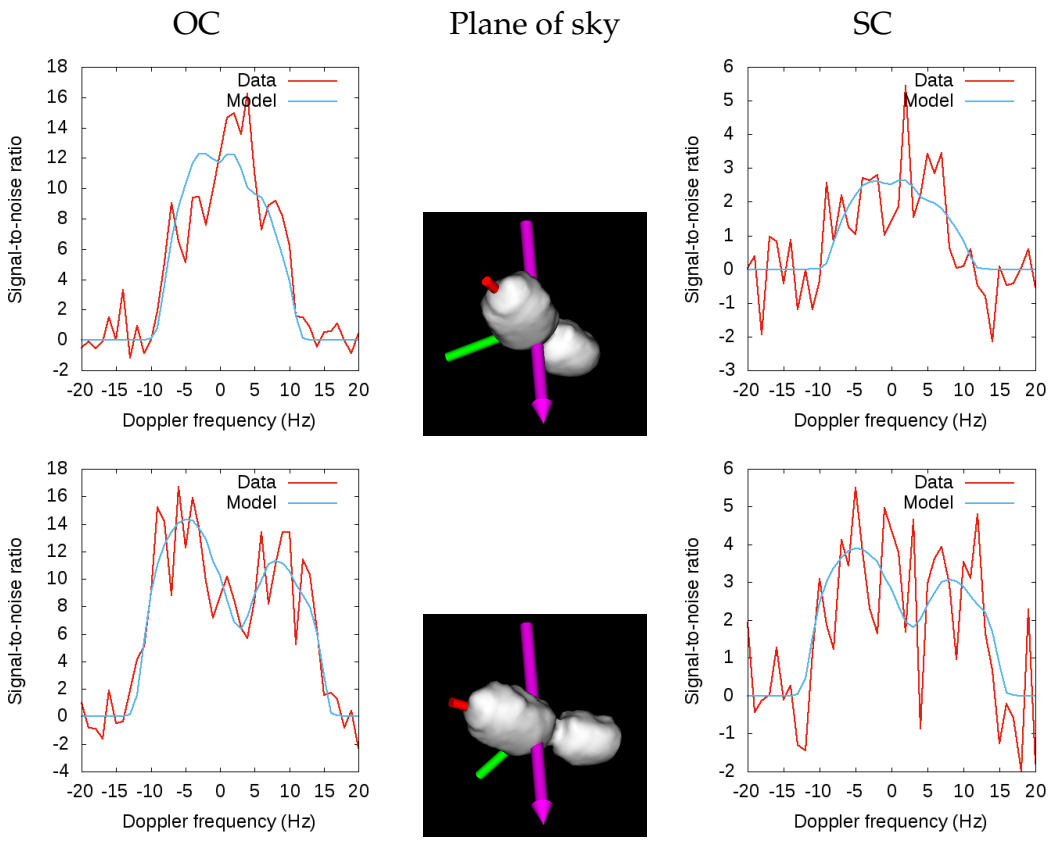

Figure B.48: CW spectra from Goldstone DSS-14 on July 27, 2015 (22:46 to 23:22 UT; both polarizations).

B.1.9 Goldstone observations from July 27-29, 2015

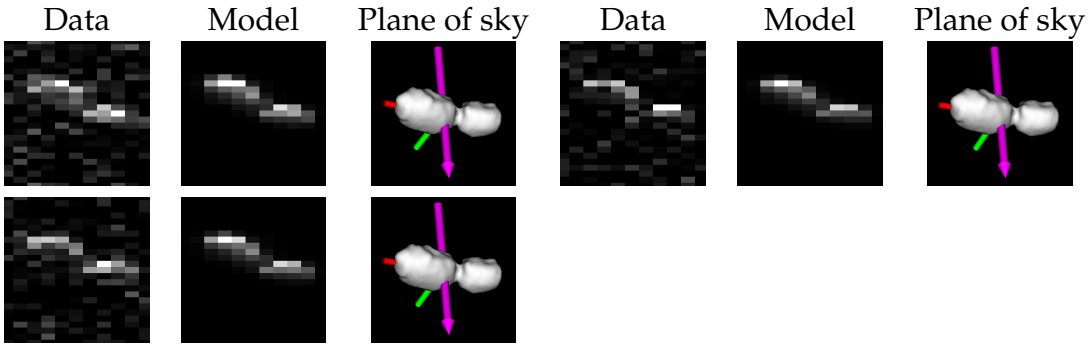

Figure B.49: Goldstone DSS-14 delay-Doppler images from July 27, 2015 (23:33 to 23:38 UT).

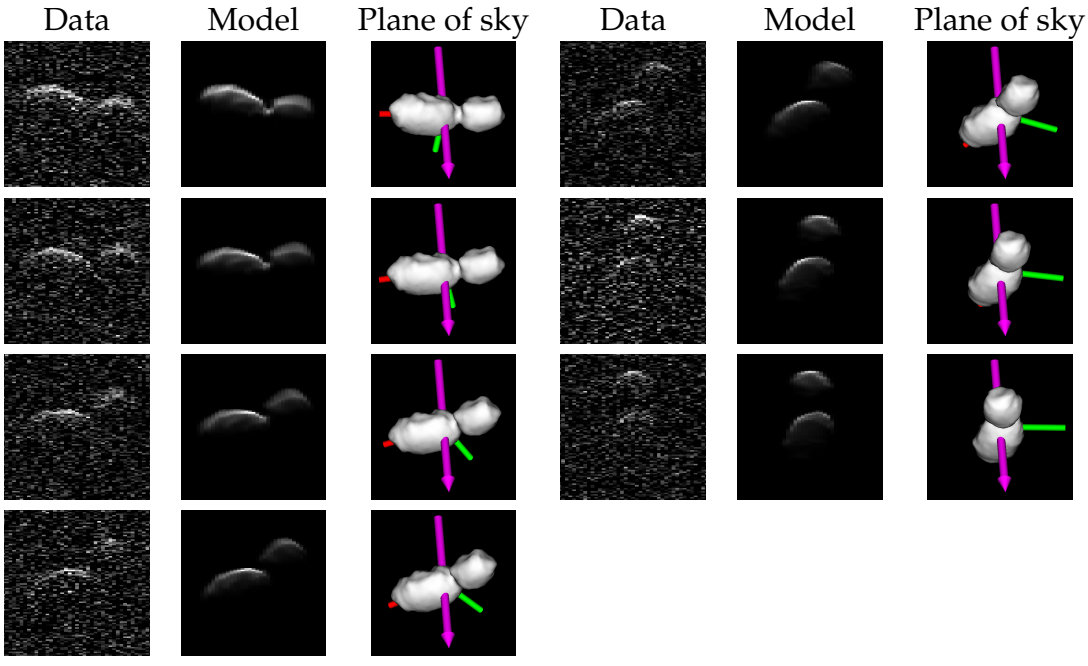

Figure B.50: Sums of the Goldstone DSS-14 delay-Doppler images from July 27-28, 2015 (23:46 to 02:05 UT).

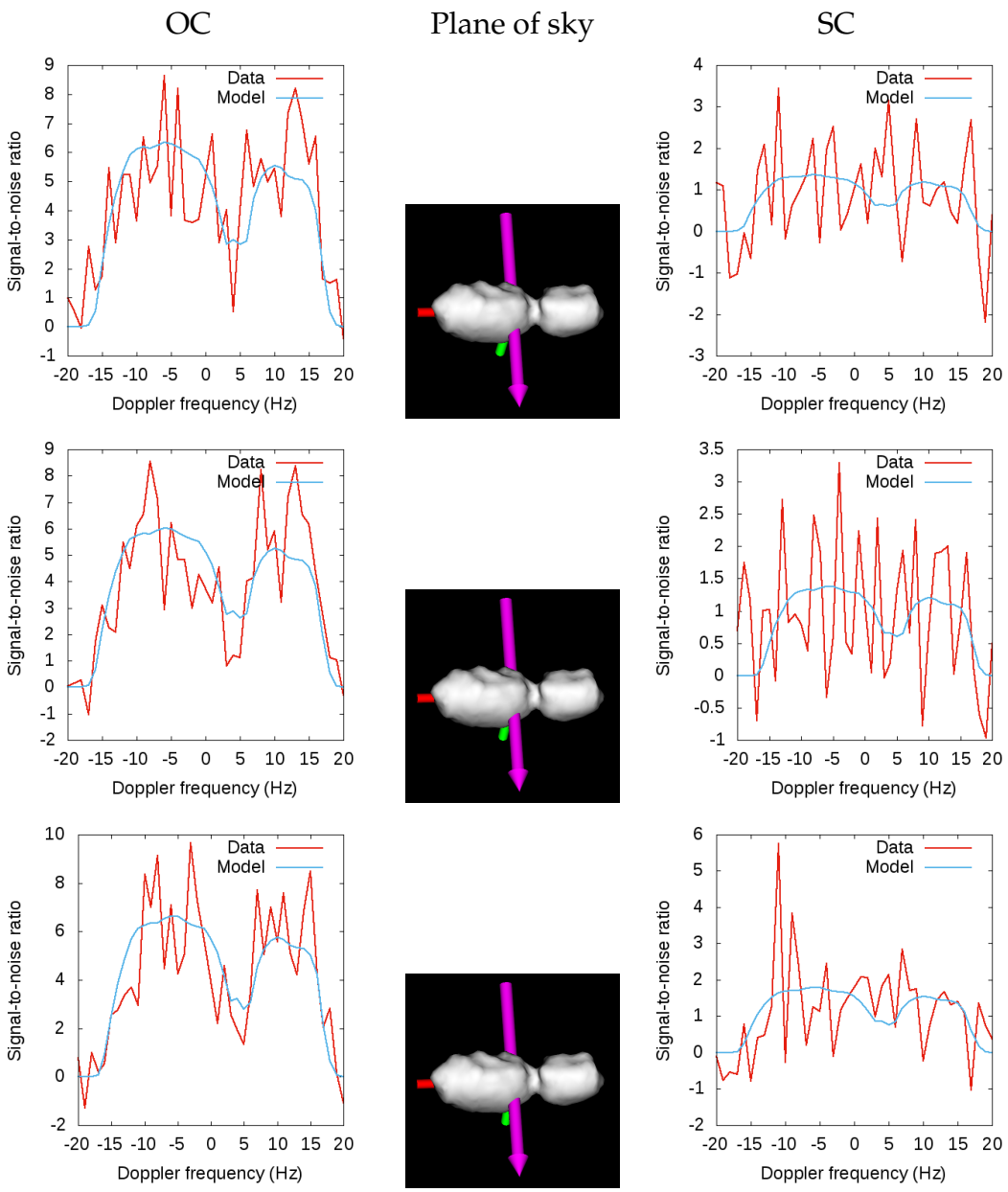

Figure B.51: CW spectra from Goldstone DSS-14 on July 28, 2015 (22:56 to 23:01 UT; both polarizations).

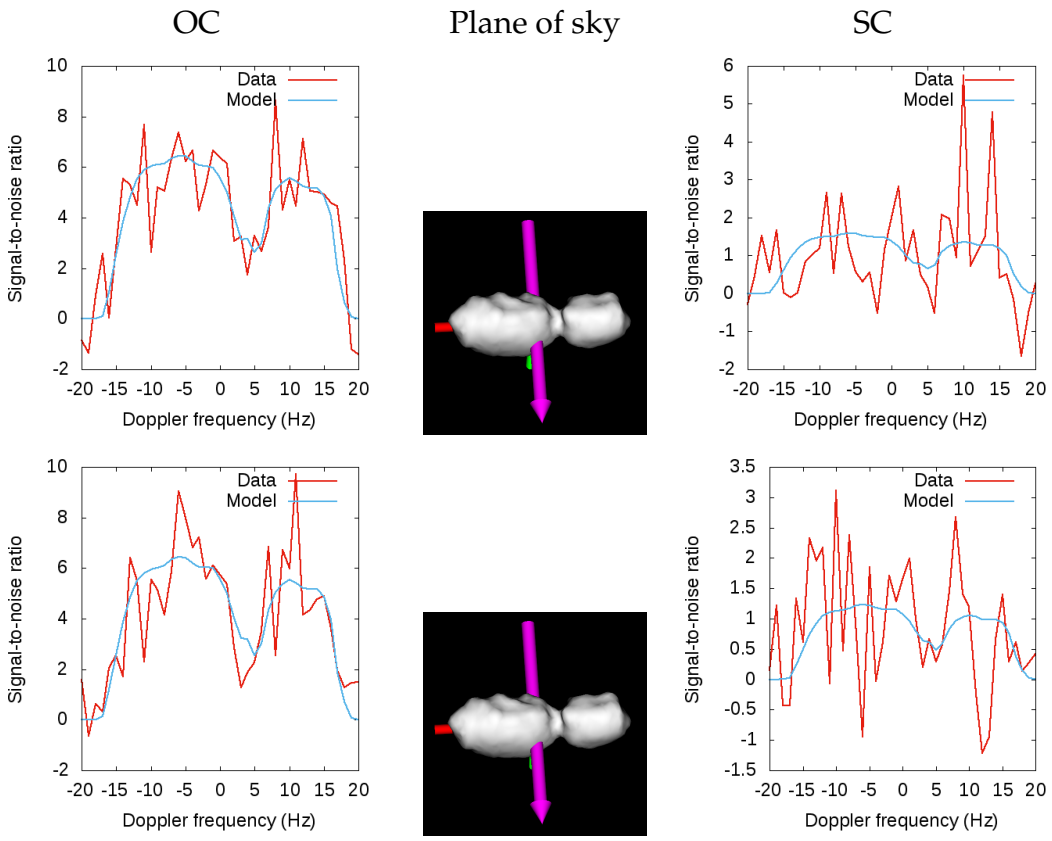

Figure B.52: CW spectra from Goldstone DSS-14 on July 28, 2015 (23:02 to 23:06 UT).

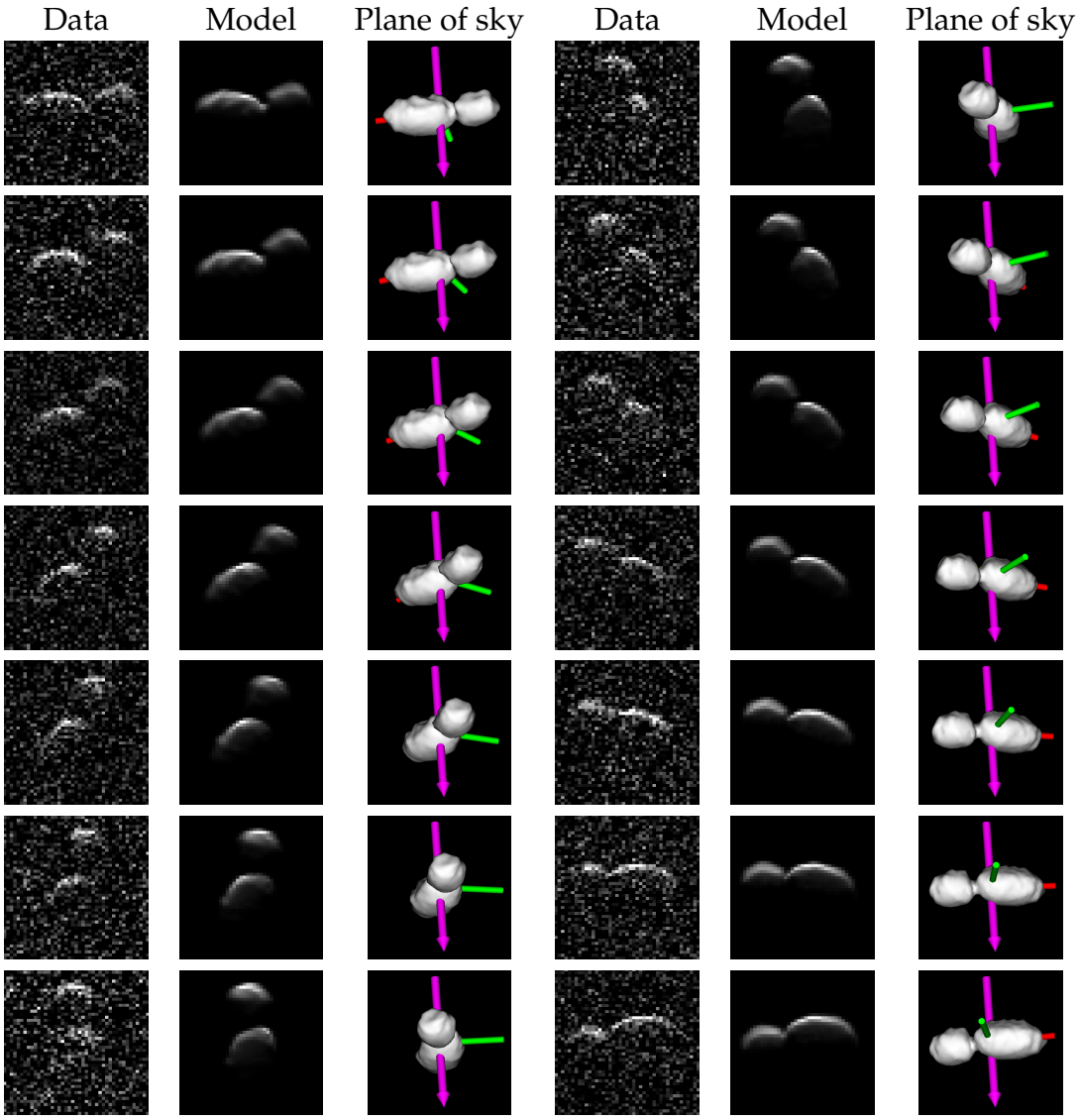

Figure B.53: Sums of the Goldstone DSS-14 delay-Doppler images from July 28-29, 2015 (23:10 to 03:14 UT).

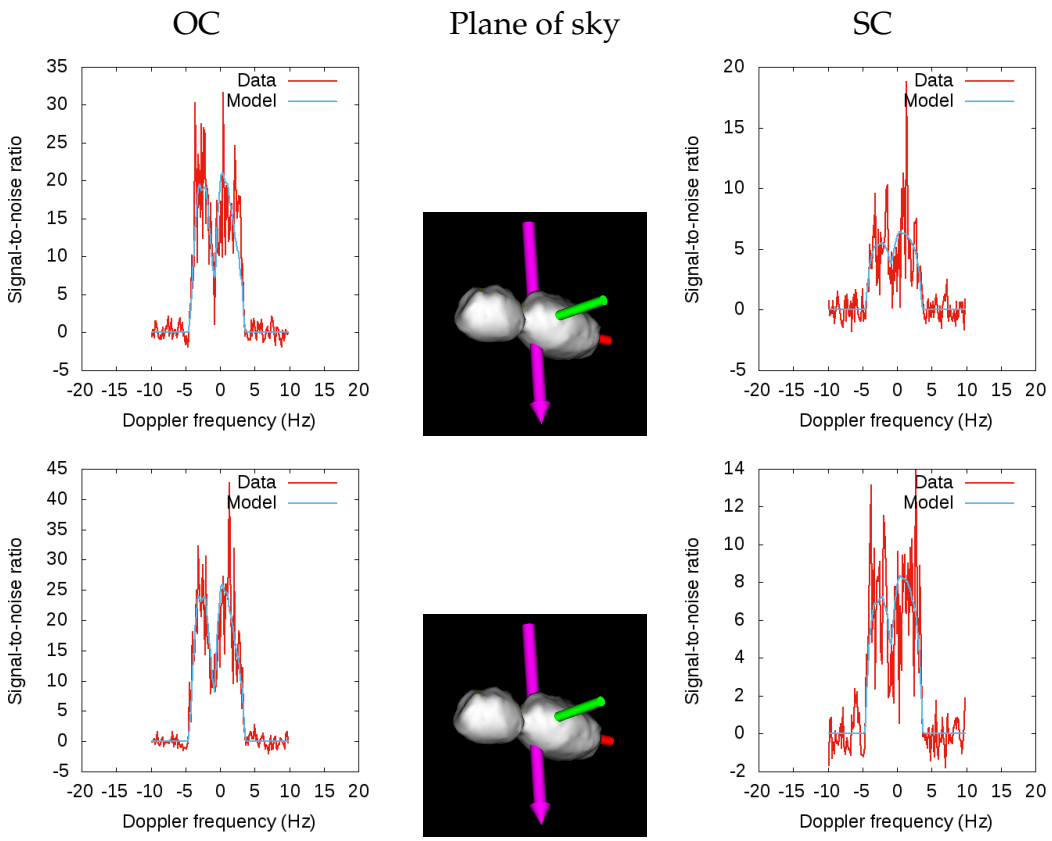

Figure B.54: CW spectra from Arecibo on July 29, 2015 (receive times 17:21 to 17:24 UT; both polarizations).

B.1.10 Arecibo observations from July 29 through August 4, 2015

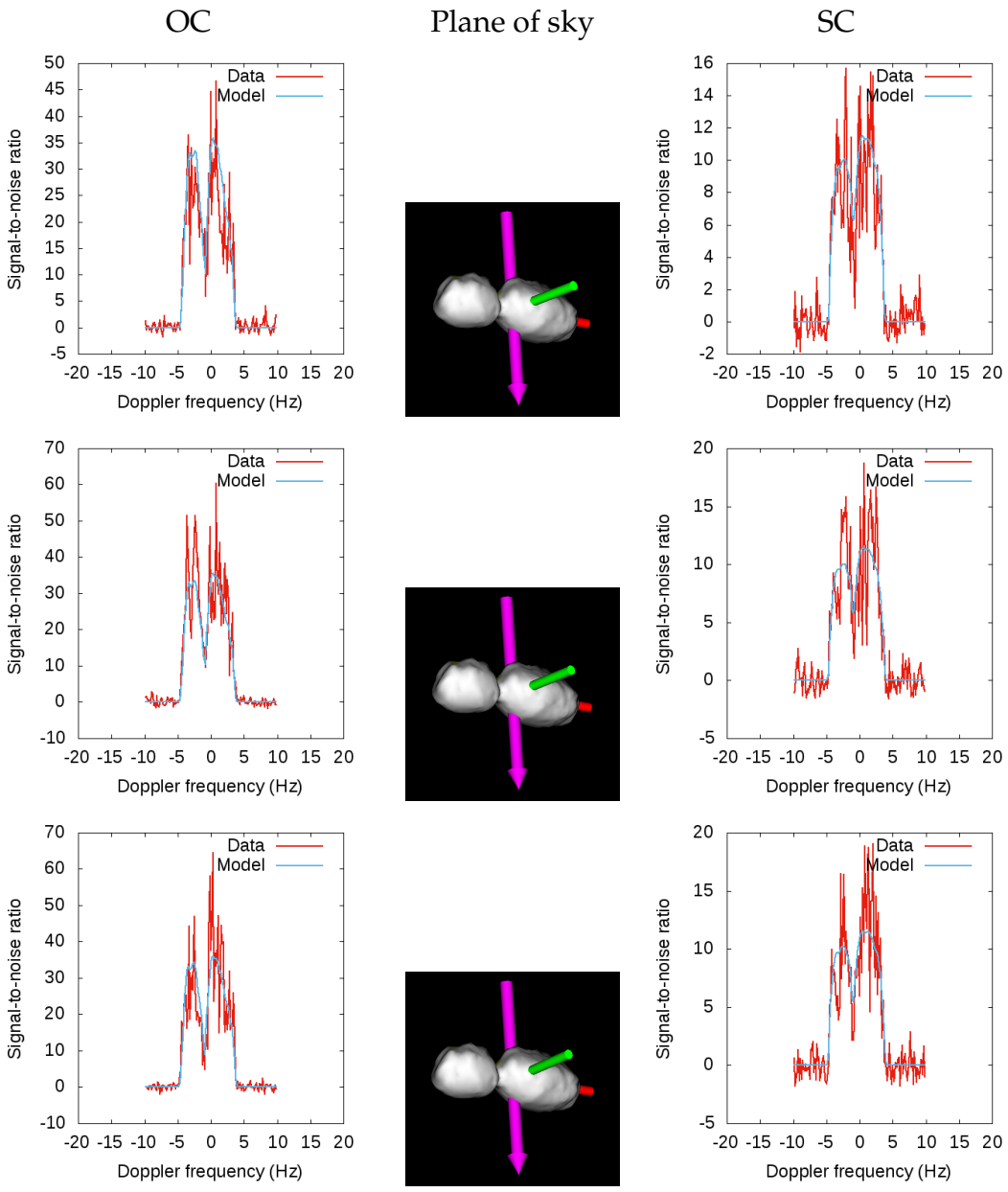

Figure B.55: CW spectra from Arecibo on July 29, 2015 (17:26 to 17:32 UT).

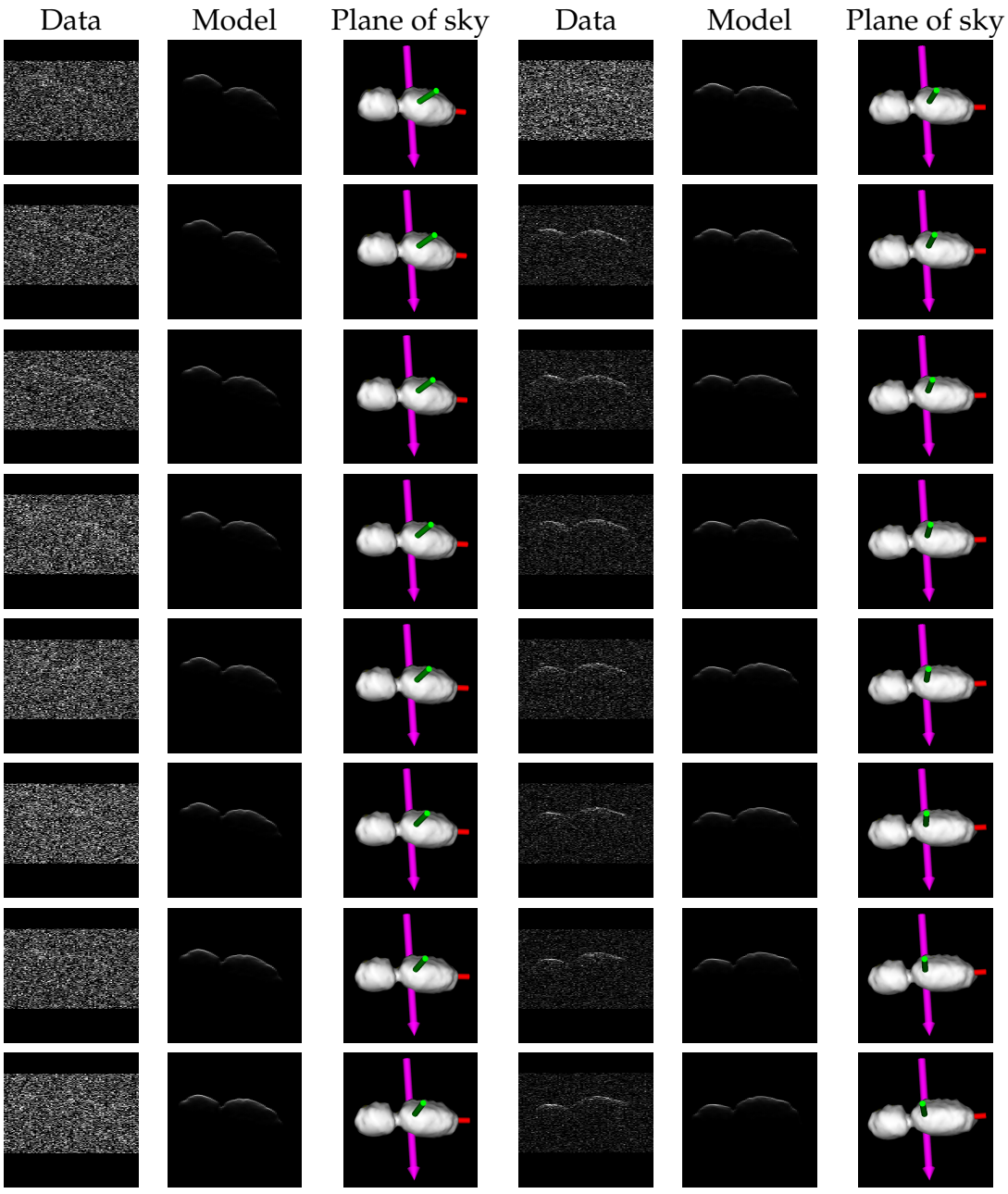

Figure B.56: Arecibo delay-Doppler images from July 29, 2015 (17:43 to 18:21 UT).

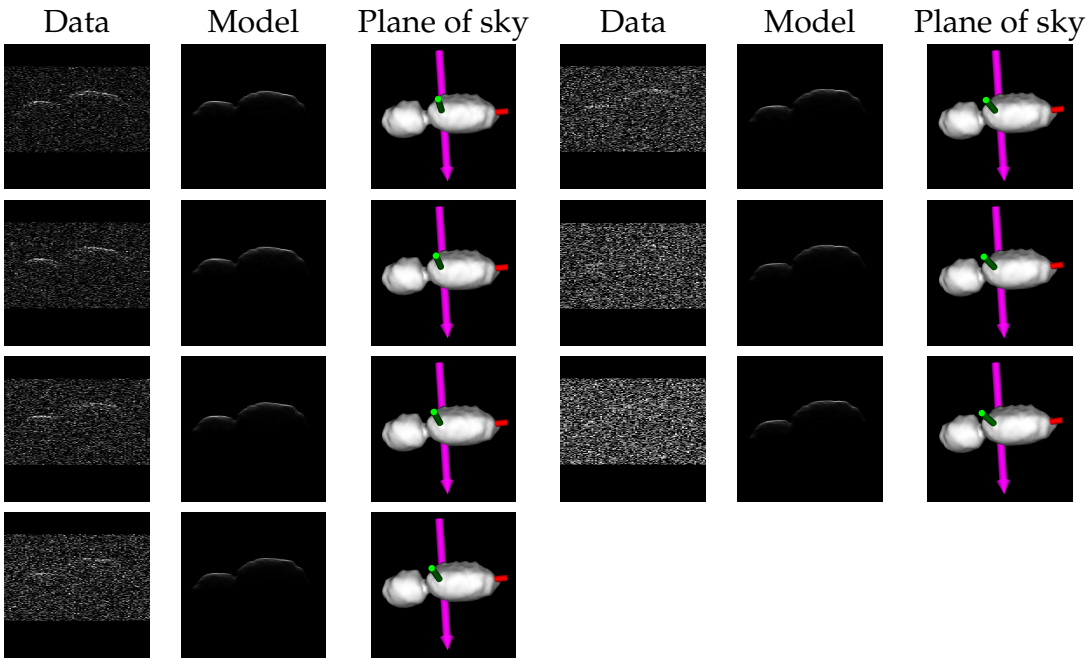

Figure B.57: Arecibo delay-Doppler images from July 29, 2015 (18:22 to 18:38 UT).

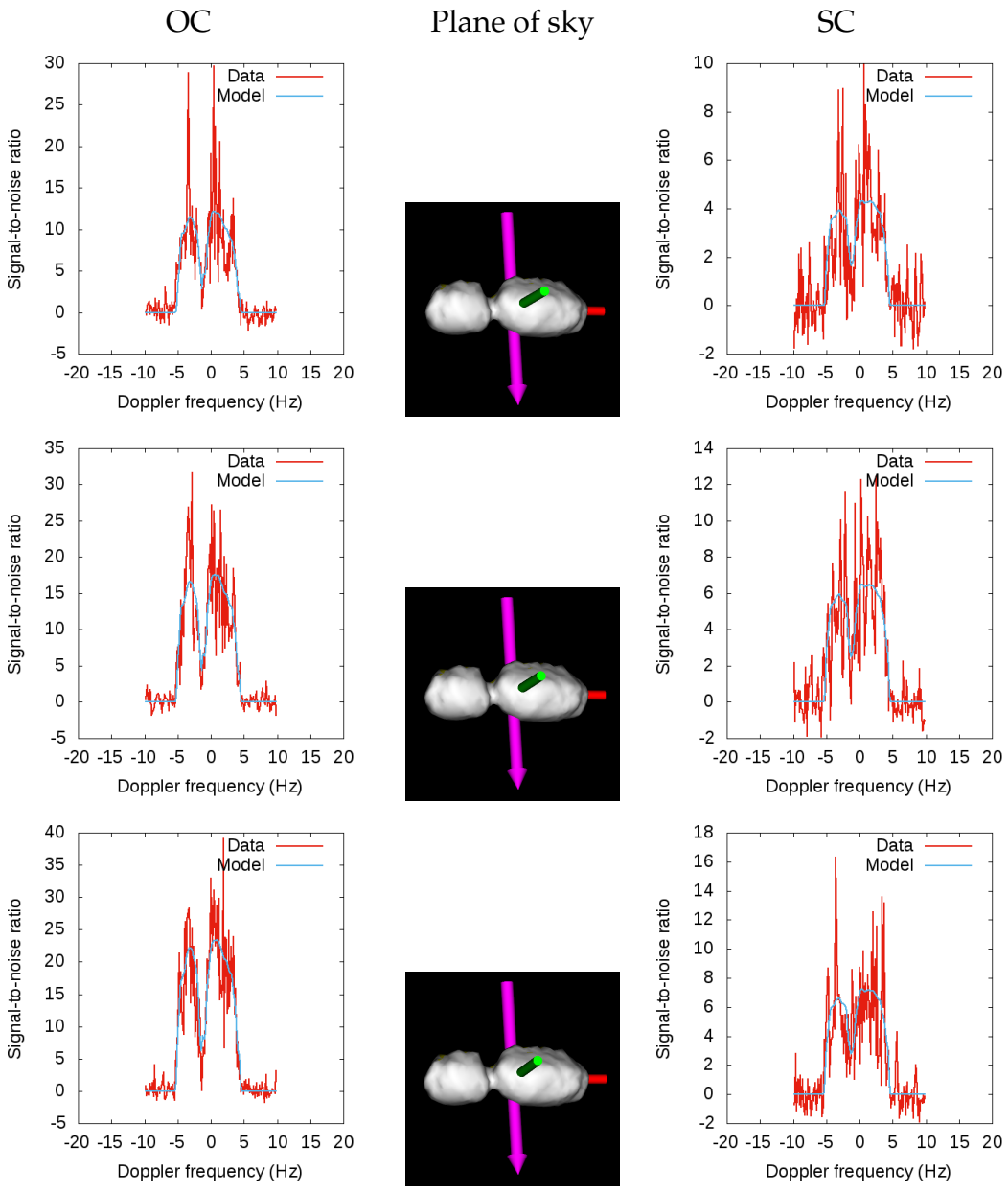

Figure B.58: CW spectra from Arecibo on July 30, 2015 (16:52 to 16:58 UT).

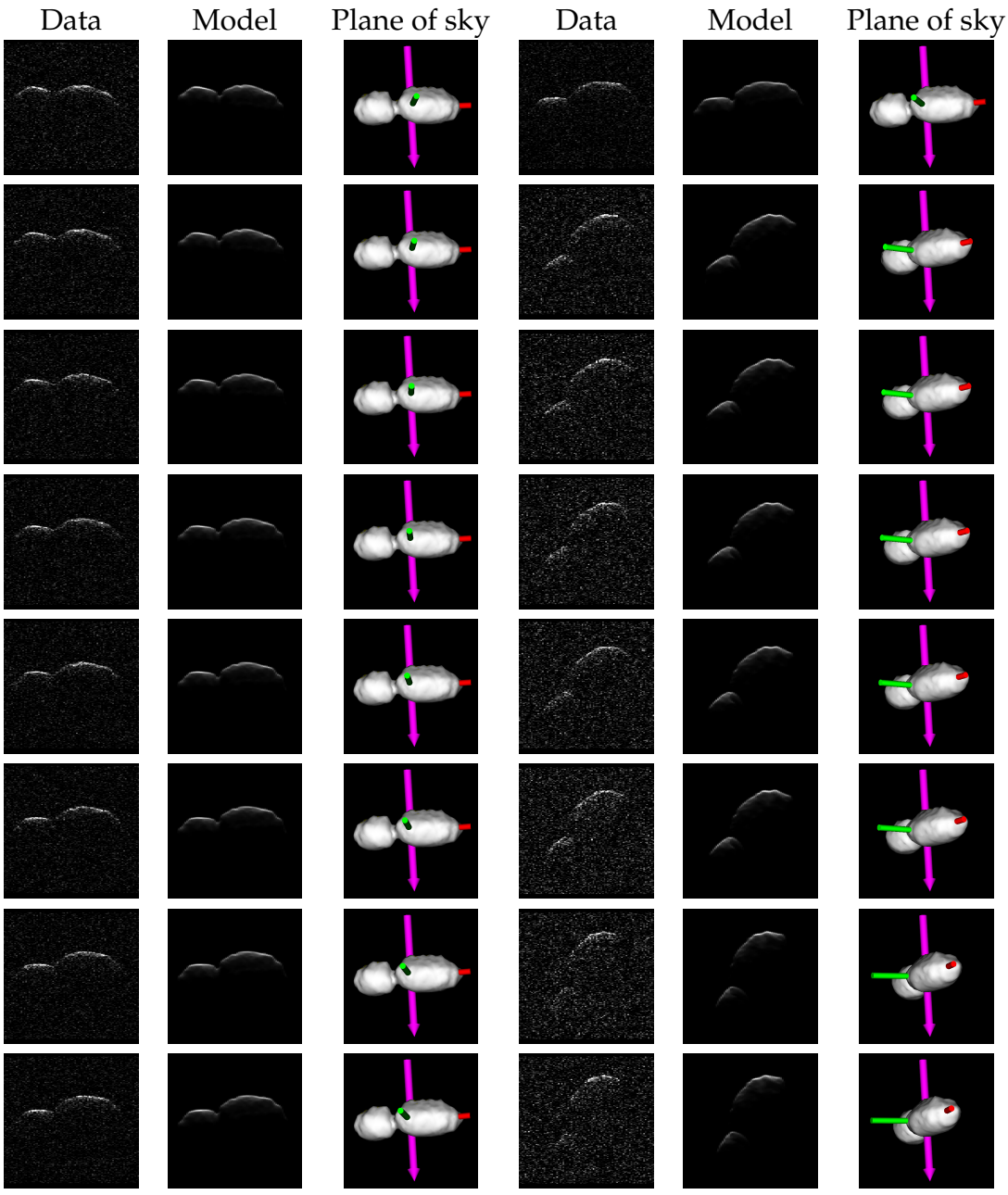

Figure B.59: Arecibo delay-Doppler images from July 30, 2015 (17:10 to 18:41 UT).

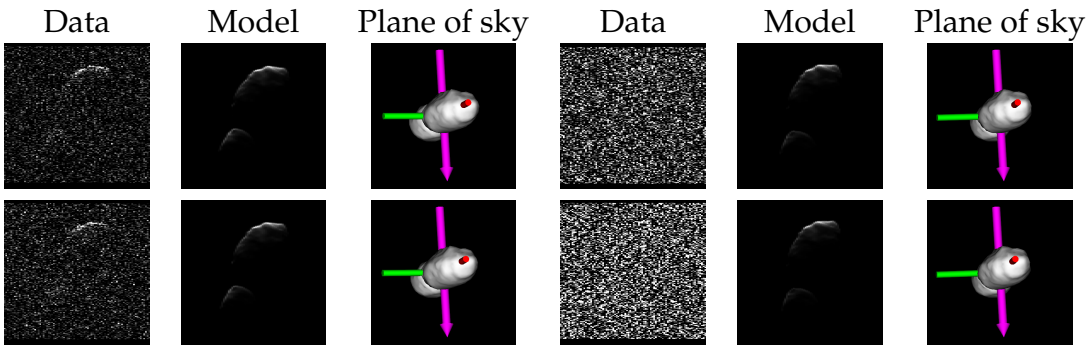

Figure B.60: Arecibo delay-Doppler images from July 30, 2015 (18:43 to 18:55 UT).

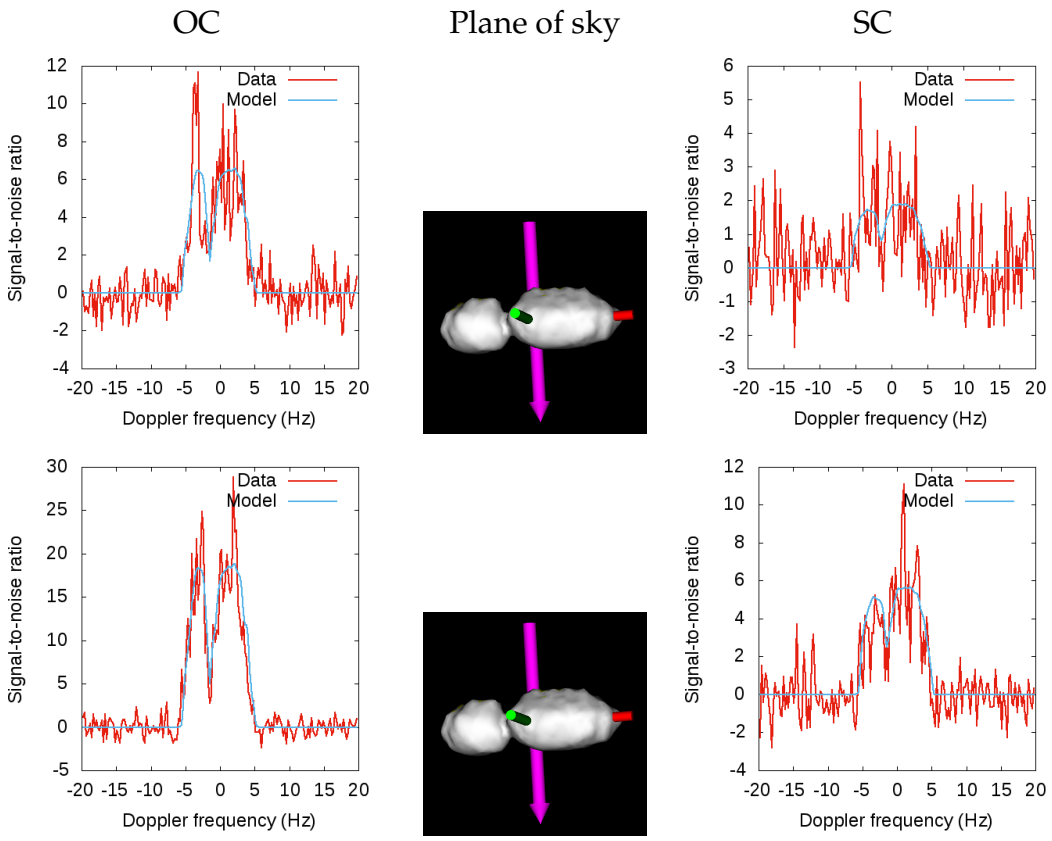

Figure B.61: CW spectra from Arecibo on July 31, 2015 (16:31 to 16:36 UT).

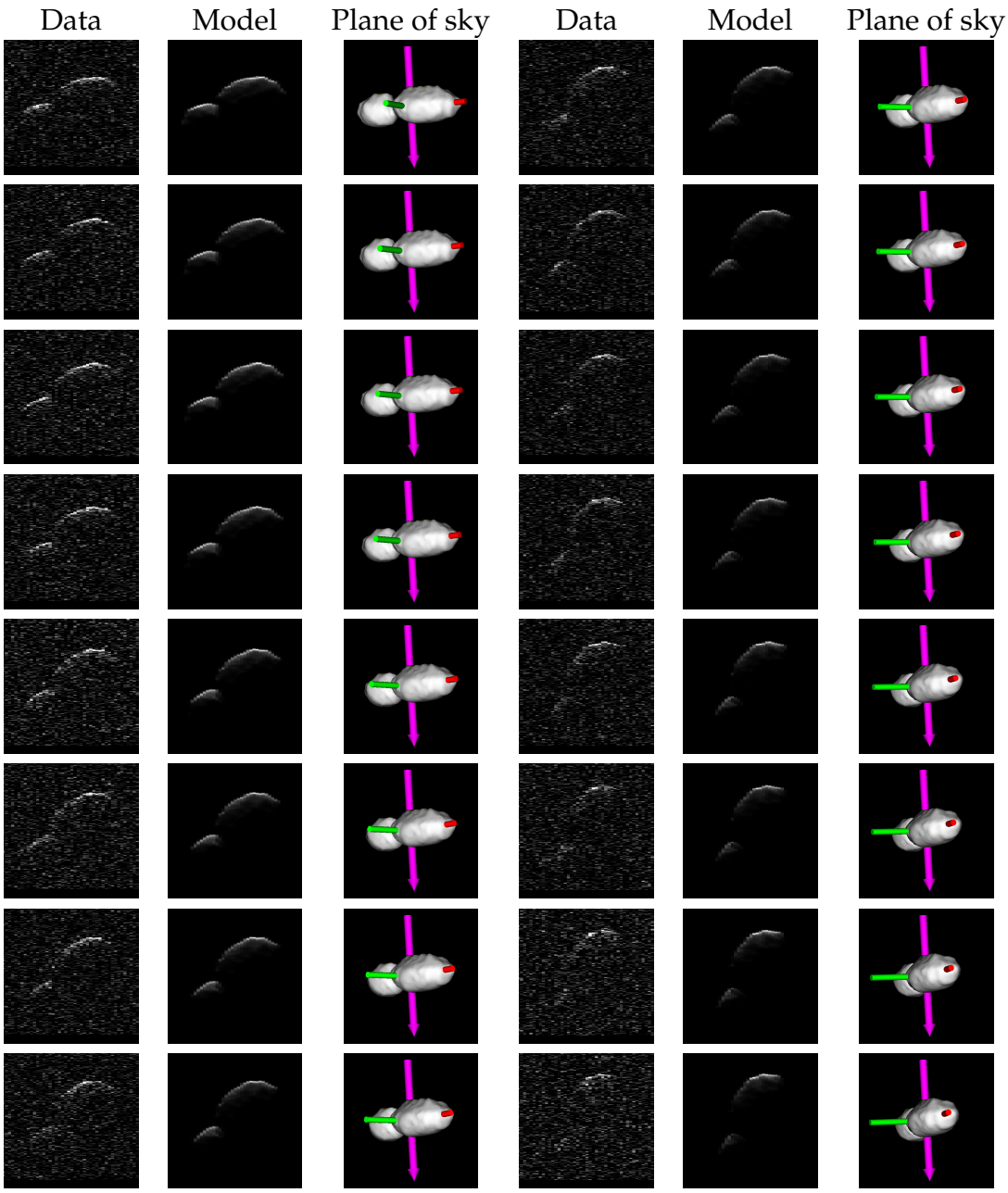

Figure B.62: Arecibo delay-Doppler images from July 31, 2015 (16:48 to 17:46 UT).

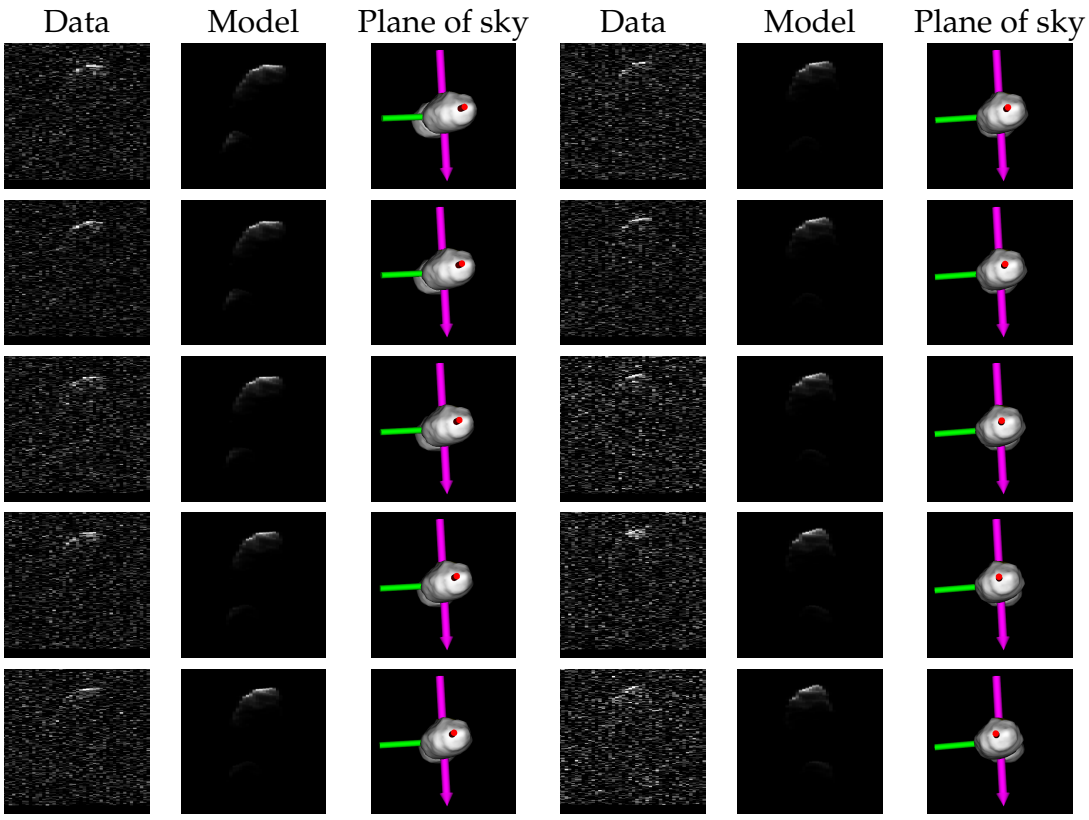

Figure B.63: Arecibo delay-Doppler images from July 31, 2015 (17:47 to 18:18 UT).

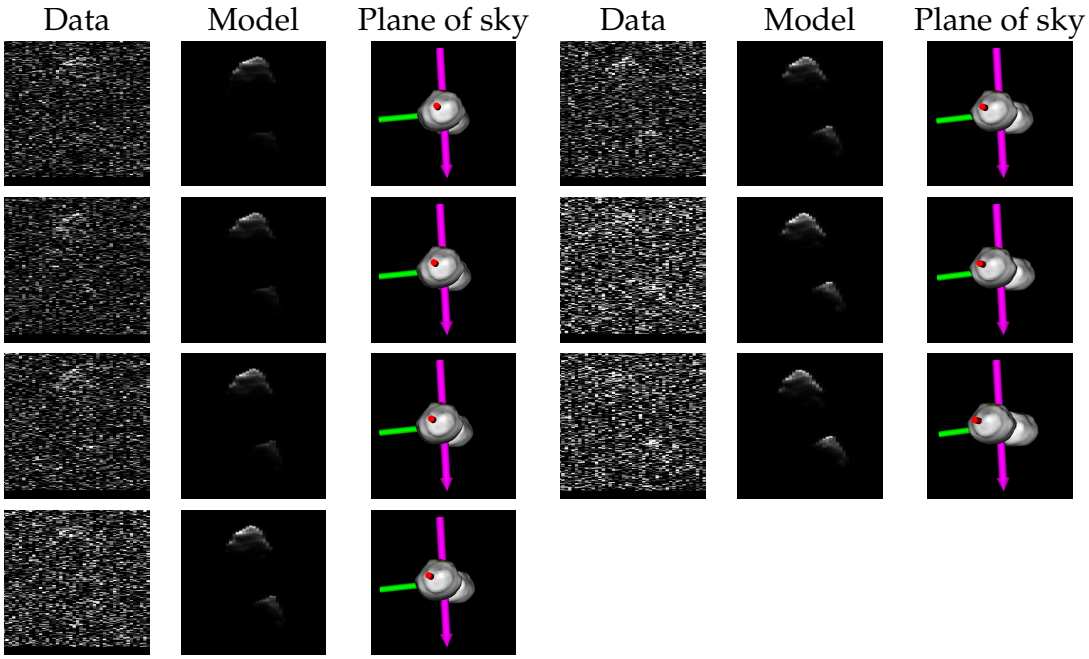

Figure B.64: Arecibo delay-Doppler images from July 31, 2015 (18:19 to 18:42 UT).

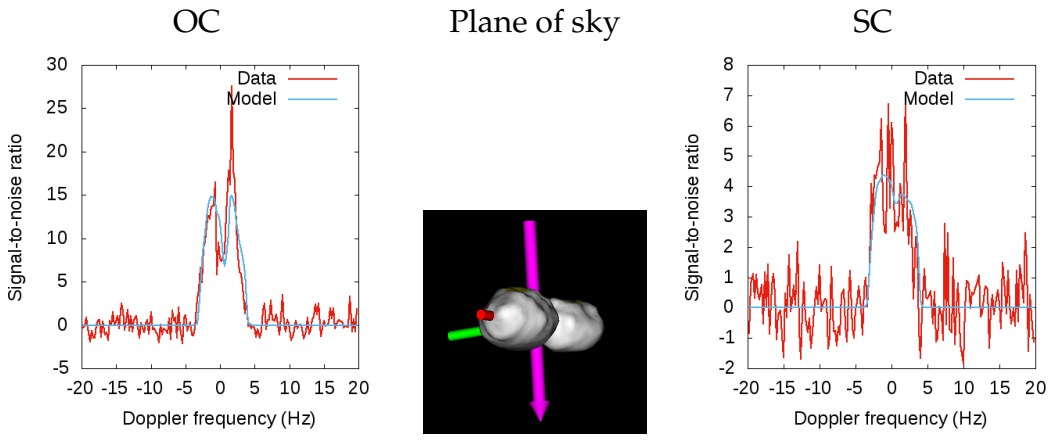

Figure B.65: CW spectra from Arecibo on July 31, 2015 (18:53 to 18:55 UT).

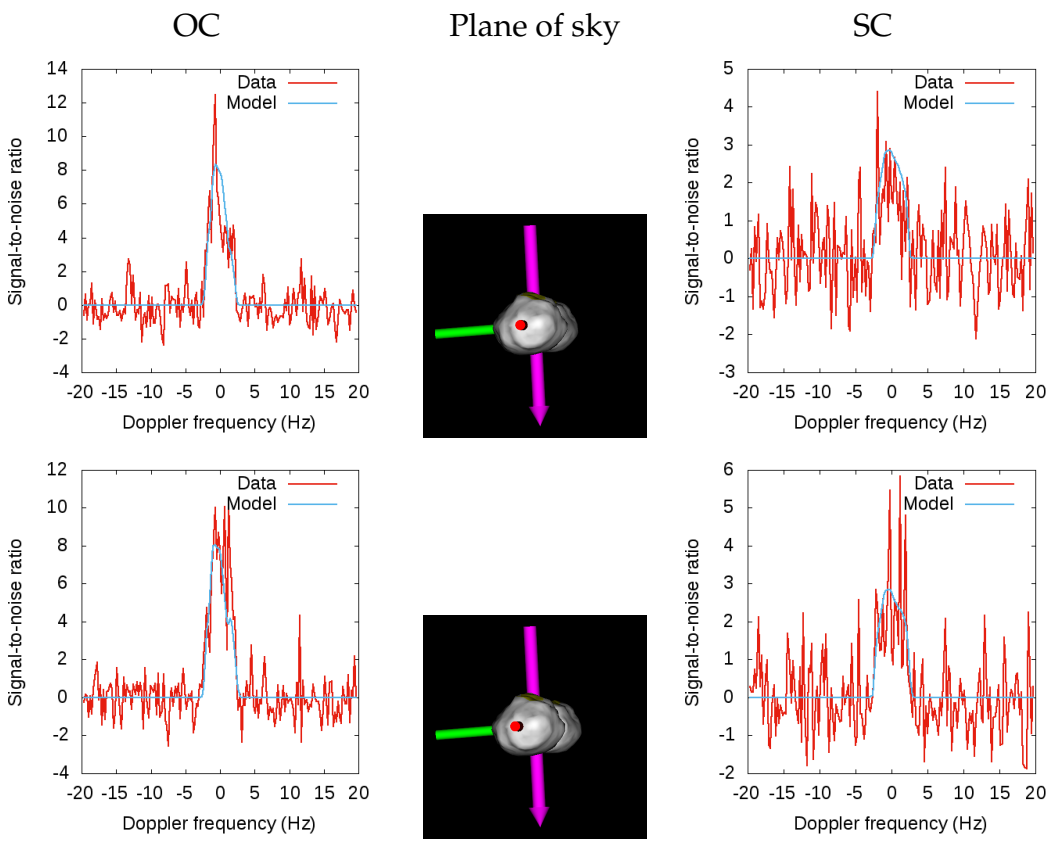

Figure B.66: CW spectra from Arecibo on August 2, 2015 (16:22 to 16:28 UT).

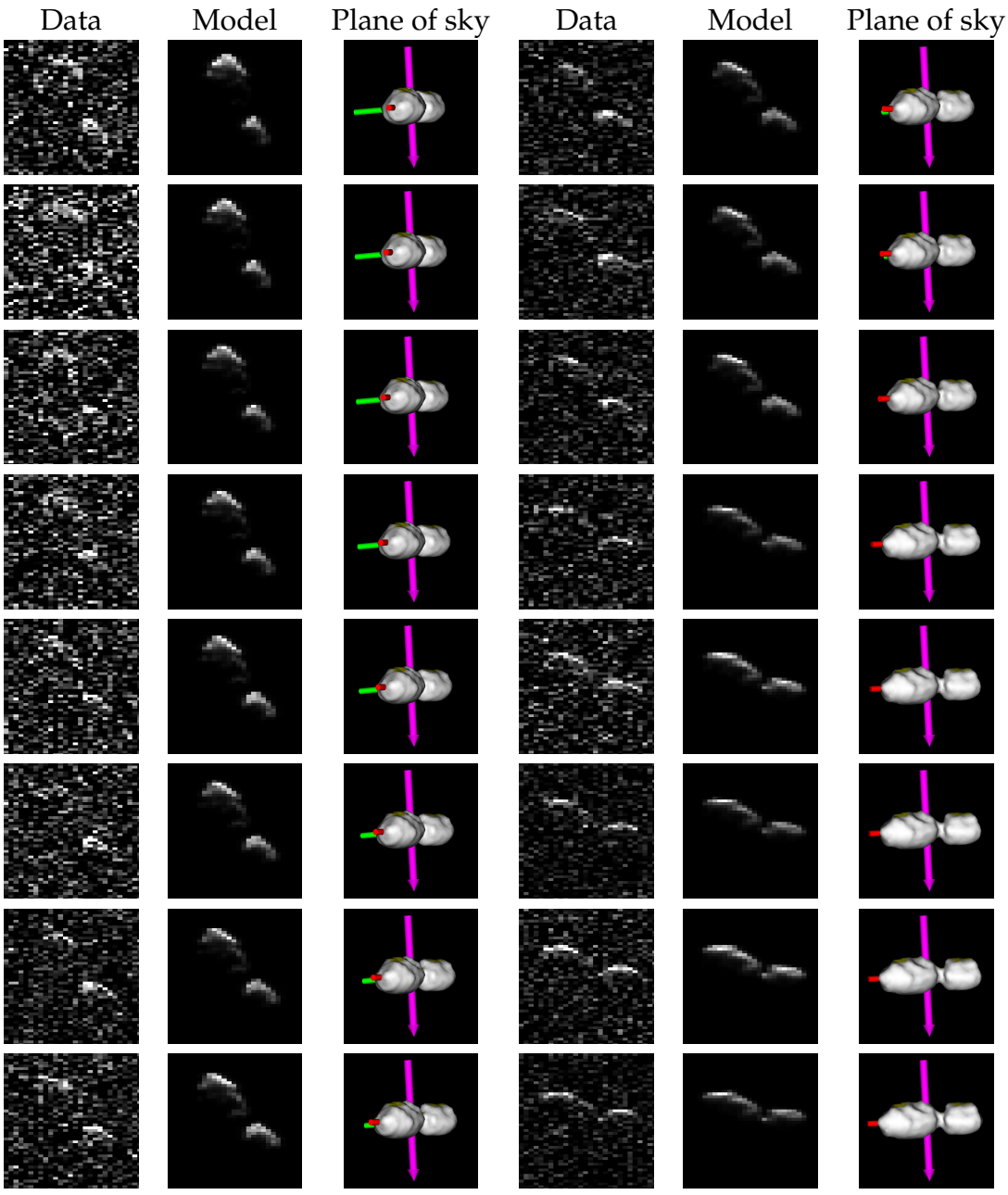

Figure B.67: Arecibo delay-Doppler images from August 2, 2015 (16:39 to 17:51 UT).

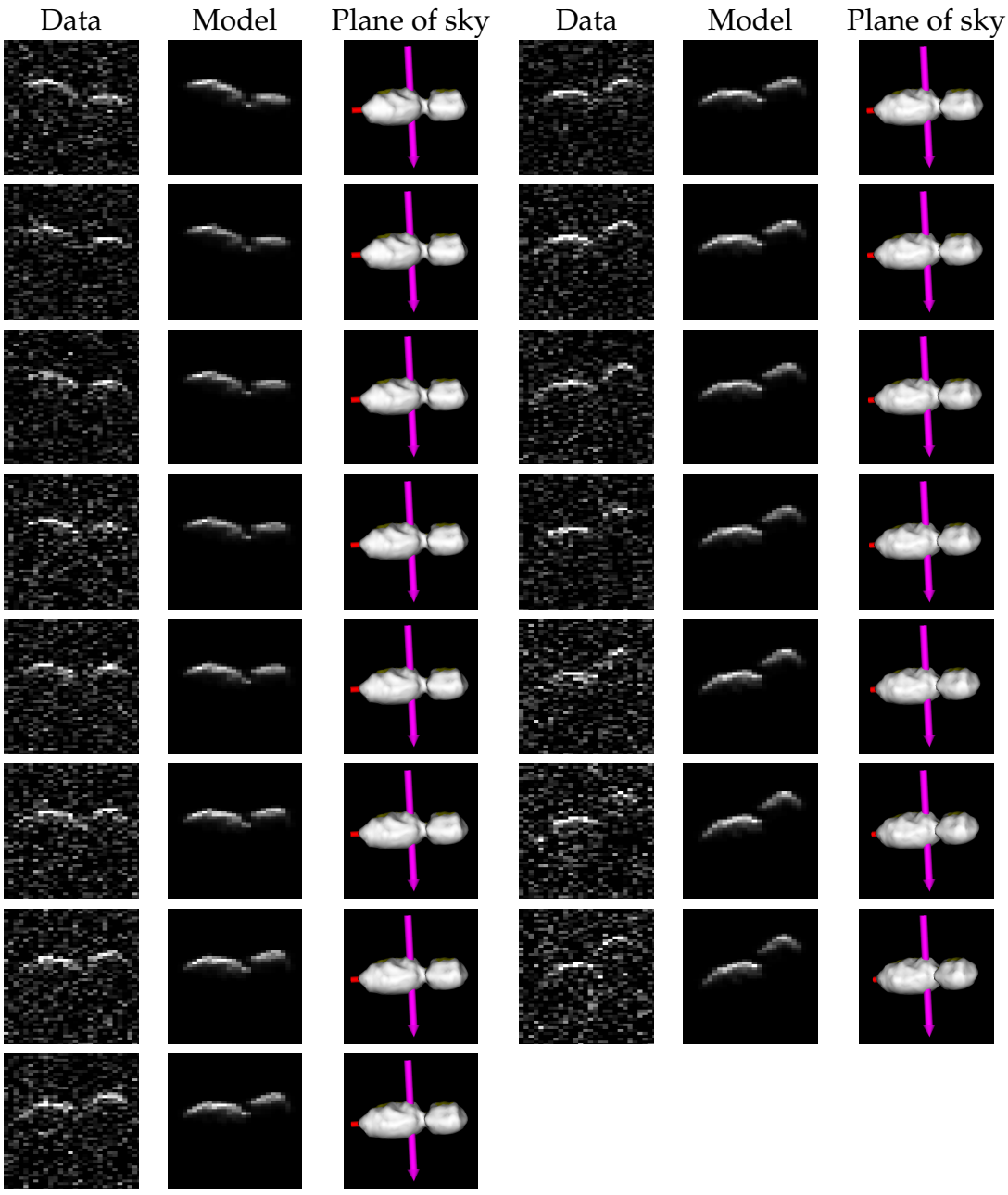

Figure B.68: Arecibo delay-Doppler images from August 2, 2015 (17:53 to 18:47 UT).

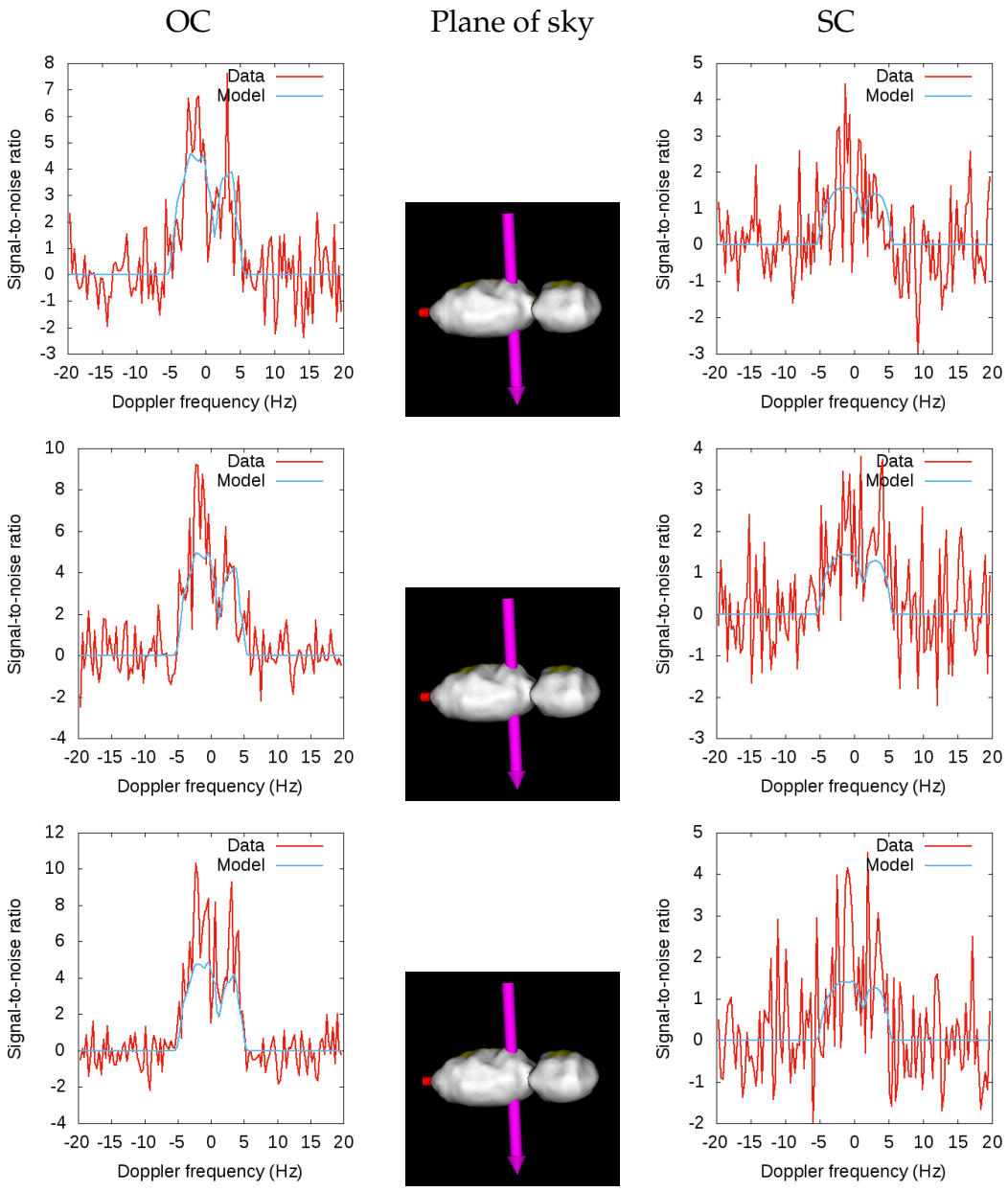

Figure B.69: CW spectra from Arecibo on August 4, 2015 (16:27 to 16:38 UT).

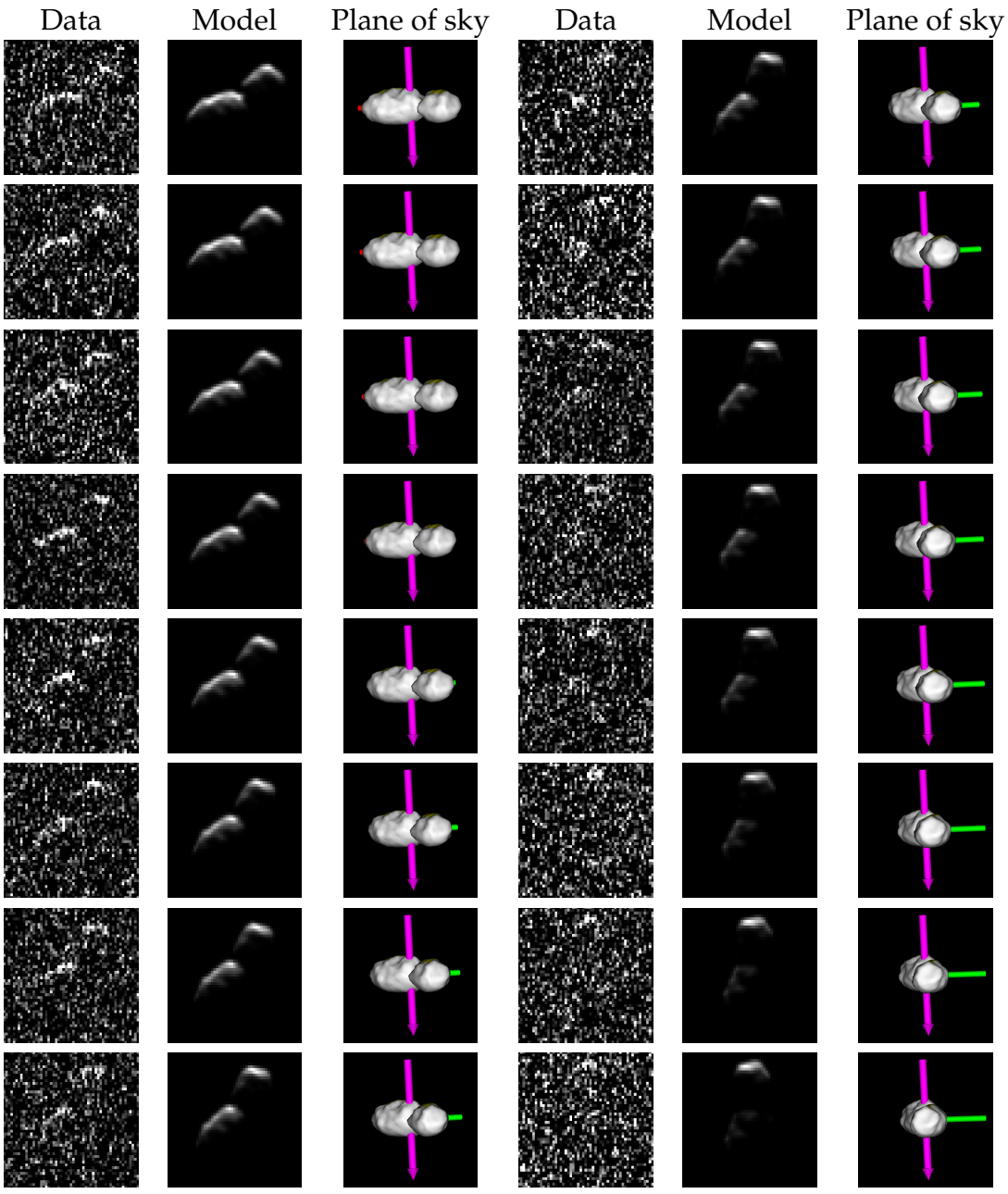

Figure B.70: Arecibo delay-Doppler images from August 4, 2015 (16:47 to 17:56 UT).

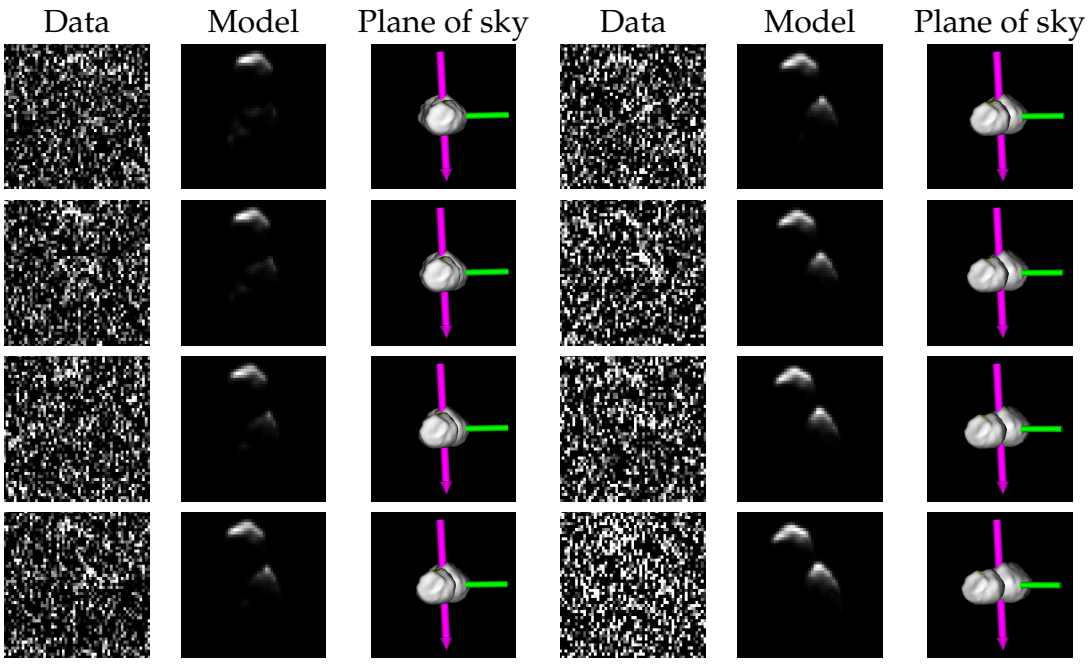

Figure B.71: Arecibo delay-Doppler images from August 4, 2015 (17:59 to 18:32 UT).

BIBLIOGRAPHY

E. M. Alvarez, J. Oey, X. L. Han, O. R. Heffner, A. W. Kidd, B. J. Magnetta, and F. W. Rastede. Period Determination for NEA (162421) 2000 ET70. *Minor Planet Bulletin*, 39:170, July 2012. URL http://adsabs.harvard.edu/abs/2012MPBu...39..170A.

A. Aznar Macías, M. Predatu, O. Vaduvescu, and J. Oey. EURONEAR - First Light Curves and Physical Properties of Near Earth Asteroids. *Romanian Journal of Physics*, 2016. URL http://www.nipne.ro/rjp/accpaps/014-Anzar__F98E87.pdf.

L. A. M. Benner, M. C. Nolan, L. M. Carter, S. J. Ostro, J. D. Giorgini, C. Magri, and J. L. Margot. Radar imaging of near-Earth asteroid 11066 Sigurd. In *AAS/Division for Planetary Sciences Meeting Abstracts #36*, volume 36 of *Bulletin of the American Astronomical Society*, page 1143, December 2004.

L. A. M. Benner, S. J. Ostro, C. Magri, M. C. Nolan, E. S. Howell, J. D. Giorgini, R. F. Jurgens, J.-L. Margot, P. A. Taylor, M. W. Busch, and M. K. Shepard. Near-Earth asteroid surface roughness depends on compositional class. *Icarus*, 198: 294–304, December 2008. doi: 10.1016/j.icarus.2008.06.010.

L. A. M. Benner, M. W. Busch, J. D. Giorgini, P. A. Taylor, and J.-L. Margot. *Radar Observations of Near-Earth and Main-Belt Asteroids*, pages 165–182. 2015. doi: 10.2458/azu_uapress_9780816532131-ch009.

P. R. Bevington and D. K. Robinson. *Data reduction and error analysis for the physical sciences*. 2003. URL http://adsabs.harvard.edu/abs/2003drea.book.....B.

G. J. Black, D. B. Campbell, and P. D. Nicholson. Icy Galilean Satellites: Modeling Radar Reflectivities as a Coherent Backscatter Effect. *Icarus*, 151:167–180, June 2001. doi: 10.1006/icar.2001.6616.

R. H. Brown, D. Morrison, C. M. Telesco, and W. E. Brunk. Calibration of the radiometric asteroid scale using occultation diameters. *Icarus*, 52:188–195, October 1982. doi: 10.1016/0019-1035(82)90178-6.

M. Brozović, L. A. M. Benner, P. A. Taylor, M. C. Nolan, E. S. Howell, C. Magri, D. J. Scheeres, J. D. Giorgini, J. T. Pollock, P. Pravec, A. Galád, J. Fang, J.-L. Margot, M. W. Busch, M. K. Shepard, D. E. Reichart, K. M. Ivarsen, J. B. Haislip, A. P. LaCluyze, J. Jao, M. A. Slade, K. J. Lawrence, and M. D. Hicks. Radar and optical observations and physical modeling of triple near-Earth Asteroid (136617) 1994 CC. *Icarus*, 216:241–256, November 2011. doi: 10.1016/j.icarus.2011.09.002.

M. W. Busch, S. J. Ostro, L. A. M. Benner, M. Brozovic, J. D. Giorgini, J. S. Jao, D. J. Scheeres, C. Magri, M. C. Nolan, E. S. Howell, P. A. Taylor, J.-L. Margot, and W. Brisken. Radar observations and the shape of near-Earth ASTEROID 2008 EV5. *Icarus*, 212:649–660, April 2011. doi: 10.1016/j.icarus.2011.01.013.

D. B. Campbell, J. F. Chandler, S. J. Ostro, G. H. Pettengill, and I. I. Shapiro. Galilean satellites - 1976 radar results. *Icarus*, 34:254–267, May 1978. doi: 10.1016/0019-1035(78)90166-5.

D. B. Campbell, G. J. Black, L. M. Carter, and S. J. Ostro. Radar Evidence for Liquid Surfaces on Titan. *Science*, 302:431–434, October 2003. doi: 10.1126/science.1088969.

D. B. Campbell, B. A. Campbell, L. M. Carter, J.-L. Margot, and N. J. S. Stacy. No

evidence for thick deposits of ice at the lunar south pole. *Nature*, 443:835–837, October 2006. doi: 10.1038/nature05167.

H. Campins, M. S. Kelley, Y. Fernández, J. Licandro, and K. Hargrove. Low Perihelion Near-Earth Asteroids. *Earth Moon and Planets*, 105:159–165, September 2009. doi: 10.1007/s11038-009-9310-2.

M. T. Capria, F. Tosi, M. C. De Sanctis, F. Capaccioni, E. Ammannito, A. Frigeri, F. Zambon, S. Fonte, E. Palomba, D. Turrini, T. N. Titus, S. E. Schröder, M. Toplis, J.-Y. Li, J.-P. Combe, C. A. Raymond, and C. T. Russell. Vesta surface thermal properties map. *Geophysical Research Letters*, 41:1438–1443, March 2014. doi: 10.1002/2013GL059026.

Shane Carr, Roman Garnett, and Cynthia Lo. BASC: applying Bayesian optimization to the search for global minima on potential energy surfaces. In *International Conference on Machine Learning*, pages 898–907, 2016. URL `http://www.jmlr.org/proceedings/papers/v48/carr16.pdf`.

B. E. Clark, J. Veverka, P. Helfenstein, P. C. Thomas, J. F. Bell, A. Harch, M. S. Robinson, S. L. Murchie, L. A. McFadden, and C. R. Chapman. NEAR Photometry of Asteroid 253 Mathilde. *Icarus*, 140:53–65, July 1999. doi: 10.1006/icar.1999.6124.

G. J. Consolmagno, M. W. Schaefer, B. E. Schaefer, D. T. Britt, R. J. Macke, M. C. Nolan, and E. S. Howell. The measurement of meteorite heat capacity at low temperatures using liquid nitrogen vaporization. *Planetary and Space Science*, 87:146–156, October 2013. doi: 10.1016/j.pss.2013.07.009.

J. L. Crowell, E. S. Howell, C. Magri, Y. R. Fernandez, S. E. Marshall, B. D. Warner, and R. J. Vervack. Thermophysical Modeling of NEAs Using SHER-

MAN: 1627 Ivar. In *Lunar and Planetary Science Conference*, volume 47 of *Lunar and Planetary Science Conference*, page 2842, March 2016. URL http://adsabs.harvard.edu/abs/2016LPI....47.2842C.

J. L. Crowell, E. S. Howell, C. Magri, M. C. Nolan, Y. R. Fernández, J. E. Richardson, B. D. Warner, S. E. Marshall, A. Springmann, and R. J. Vervack. Radar and Lightcurve Shape Model of Near-Earth Asteroid (1627) Ivar. *Icarus*, 291: 254–267, July 2017. doi: 10.1016/j.icarus.2016.11.008.

M. C. Cushing, W. D. Vacca, and J. T. Rayner. Spextool: A Spectral Extraction Package for SpeX, a 0.8-5.5 Micron Cross-Dispersed Spectrograph. *Publications of the Astronomical Society of the Pacific*, 116:362–376, April 2004. doi: 10.1086/382907.

M. Delbó, A. dell'Oro, A. W. Harris, S. Mottola, and M. Mueller. Thermal inertia of near-Earth asteroids and implications for the magnitude of the Yarkovsky effect. *Icarus*, 190:236–249, September 2007. doi: 10.1016/j.icarus.2007.03.007.

F. E. DeMeo, R. P. Binzel, S. M. Slivan, and S. J. Bus. An extension of the Bus asteroid taxonomy into the near-infrared. *Icarus*, 202:160–180, July 2009. doi: 10.1016/j.icarus.2009.02.005.

J. P. Emery, A. L. Sprague, F. C. Witteborn, J. E. Colwell, R. W. H. Kozlowski, and D. H. Wooden. Mercury: Thermal Modeling and Mid-infrared (5-12 μm) Observations. *Icarus*, 136:104–123, November 1998. doi: 10.1006/icar.1998.6012.

GPyOpt team. GPyOpt: A bayesian optimization framework in python, 2016. URL http://github.com/SheffieldML/GPyOpt.

B. Hapke. Bidirectional reflectance spectroscopy. III - Correction for macroscopic roughness. *Icarus*, 59:41–59, July 1984. doi: 10.1016/0019-1035(84)90054-X.

A. W. Harris. A Thermal Model for Near-Earth Asteroids. *Icarus*, 131:291–301, February 1998. doi: 10.1006/icar.1997.5865.

A. W. Harris and J. S. V. Lagerros. Asteroids in the Thermal Infrared. *Asteroids III*, pages 205–218, 2002. URL `http://adsabs.harvard.edu/abs/2002aste.conf..205H`.

A. W. Harris, P. Pravec, A. Galád, B. A. Skiff, B. D. Warner, J. Világi, Š. Gajdoš, A. Carbognani, K. Hornoch, P. Kušnirák, W. R. Cooney, J. Gross, D. Terrell, D. Higgins, E. Bowell, and B. W. Koehn. On the maximum amplitude of harmonics of an asteroid lightcurve. *Icarus*, 235:55–59, June 2014. doi: 10.1016/j.icarus.2014.03.004.

J. Hartlap, P. Simon, and P. Schneider. Why your model parameter confidences might be too optimistic. Unbiased estimation of the inverse covariance matrix. *Astronomy and Astrophysics*, 464:399–404, March 2007. doi: 10.1051/0004-6361:20066170.

E. S. Howell, R. J. Vervack, Jr., C. Magri, M. C. Nolan, P. A. Taylor, Y. R. Fernández, M. D. Hicks, J. M. Somers, K. Lawrence, A. S. Rivkin, S. E. Marshall, and J. Crowell. SHERMAN, a shape-based thermophysical model. II: Application to (8567) 1996 HW1. *Icarus*, (in revision), 2017.

R. S. Hudson and S. J. Ostro. Physical Model of Asteroid 1620 Geographos from Radar and Optical Data. *Icarus*, 140:369–378, August 1999. doi: 10.1006/icar.1999.6142.

S. Hudson. Three-dimensional reconstruction of asteroids from radar observations. *Remote Sensing Reviews*, 8(1-3):195–203, 1993. doi: 10.1080/02757259309532195.

J. D. Hunter. Matplotlib: A 2D Graphics Environment. *Computing in Science & Engineering*, 9:90–95, May 2007. doi: 10.1109/MCSE.2007.55.

M. Kaasalainen and J. Torppa. Optimization Methods for Asteroid Lightcurve Inversion. I. Shape Determination. *Icarus*, 153:24–36, September 2001. doi: 10.1006/icar.2001.6673.

A. S. Konopliv, R. S. Park, A. T. Vaughan, B. G. Bills, S. W. Asmar, A. I. Ermakov, N. Rambaux, C. A. Raymond, J. C. Castillo-Rogez, C. T. Russell, D. E. Smith, and M. T. Zuber. The Ceres gravity field, spin pole, rotation period and orbit from the Dawn radiometric tracking and optical data. *Icarus*, 299:411–429, January 2018. doi: 10.1016/j.icarus.2017.08.005.

A. Kryszczyńska, A. La Spina, P. Paolicchi, A. W. Harris, S. Breiter, and P. Pravec. New findings on asteroid spin-vector distributions. *Icarus*, 192:223–237, December 2007. doi: 10.1016/j.icarus.2007.06.008.

A. La Spina, P. Paolicchi, A. Kryszczyńska, and P. Pravec. Retrograde spins of near-Earth asteroids from the Yarkovsky effect. *Nature*, 428:400–401, March 2004. doi: 10.1038/nature02411.

J. S. V. Lagerros. Thermal physics of asteroids. I. Effects of shape, heat conduction and beaming. *Astronomy and Astrophysics*, 310:1011–1020, June 1996. URL `http://adsabs.harvard.edu/abs/1996A%26A...310.1011L`.

J. S. V. Lagerros. Thermal physics of asteroids. IV. Thermal infrared beam-

ing. *Astronomy and Astrophysics*, 332:1123–1132, April 1998. URL http://adsabs.harvard.edu/abs/1998A%26A...332.1123L.

L. A. Lebofsky, G. J. Veeder, M. J. Lebofsky, and D. L. Matson. Visual and radiometric photometry of 1580 Betulia. *Icarus*, 35:336–343, September 1978. doi: 10.1016/0019-1035(78)90086-6.

L. A. Lebofsky, M. V. Sykes, E. F. Tedesco, G. J. Veeder, D. L. Matson, R. H. Brown, J. C. Gradie, M. A. Feierberg, and R. J. Rudy. A refined 'standard' thermal model for asteroids based on observations of 1 Ceres and 2 Pallas. *Icarus*, 68:239–251, November 1986. doi: 10.1016/0019-1035(86)90021-7.

C. Magri, S. J. Ostro, D. J. Scheeres, M. C. Nolan, J. D. Giorgini, L. A. M. Benner, and J.-L. Margot. Radar observations and a physical model of Asteroid 1580 Betulia. *Icarus*, 186:152–177, January 2007. doi: 10.1016/j.icarus.2006.08.004.

C. Magri, E. S. Howell, M. C. Nolan, P. A. Taylor, Y. R. Fernández, M. Mueller, R. J. Vervack, Jr., L. A. M. Benner, J. D. Giorgini, S. J. Ostro, D. J. Scheeres, M. D. Hicks, H. Rhoades, J. M. Somers, N. M. Gaftonyuk, V. V. Kouprianov, Y. N. Krugly, I. E. Molotov, M. W. Busch, J.-L. Margot, V. Benishek, V. Protitch-Benishek, A. Galád, D. Higgins, P. Kušnirák, and D. P. Pray. Radar and photometric observations and shape modeling of contact binary near-Earth Asteroid (8567) 1996 HW1. *Icarus*, 214:210–227, July 2011. doi: 10.1016/j.icarus.2011.02.019.

C. Magri, E. S. Howell, R. J. Vervack, Jr., M. C. Nolan, Y. R. Fernández, S. E. Marshall, and J. L. Crowell. SHERMAN, a shape-based thermophysical model. I. Model description and validation. *Icarus*, (in revision), 2017.

A. Mainzer, T. Grav, J. Bauer, J. Masiero, R. S. McMillan, R. M. Cutri, R. Walker,

E. Wright, P. Eisenhardt, D. J. Tholen, T. Spahr, R. Jedicke, L. Denneau, E. DeBaun, D. Elsbury, T. Gautier, S. Gomillion, E. Hand, W. Mo, J. Watkins, A. Wilkins, G. L. Bryngelson, A. Del Pino Molina, S. Desai, M. Gómez Camus, S. L. Hidalgo, I. Konstantopoulos, J. A. Larsen, C. Maleszewski, M. A. Malkan, J.-C. Mauduit, B. L. Mullan, E. W. Olszewski, J. Pforr, A. Saro, J. V. Scotti, and L. H. Wasserman. NEOWISE Observations of Near-Earth Objects: Preliminary Results. *Astrophysical Journal*, 743:156, December 2011. doi: 10.1088/0004-637X/743/2/156.

A. Mainzer, J. Bauer, T. Grav, J. Masiero, R. M. Cutri, E. Wright, C. R. Nugent, R. Stevenson, E. Clyne, G. Cukrov, and F. Masci. The Population of Tiny Near-Earth Objects Observed by NEOWISE. *Astrophysical Journal*, 784:110, April 2014. doi: 10.1088/0004-637X/784/2/110.

S. E. Marshall, E. S. Howell, C. Magri, R. J. Vervack, D. B. Campbell, Y. R. Fernández, M. C. Nolan, J. L. Crowell, M. D. Hicks, K. J. Lawrence, and P. A. Taylor. Thermal properties and an improved shape model for near-Earth asteroid (162421) 2000 ET70. *Icarus*, 292:22–35, August 2017. doi: 10.1016/j.icarus.2017.03.028.

S. E. Marshall, M. Brozović, L. A. M. Benner, E. S. Howell, D. B. Campbell, R. J. Vervack, C. Magri, J. L. Crowell, Y. R. Fernández, M. W. Busch, J. D. Giorgini, P. A. Taylor, M. C. Nolan, S. P. Naidu, J. S. Jao, C. G. Lee, J. E. Richardson, L. A. Rodriguez-Ford, F. D. Ghigo, A. R. Kobelski, P. Pravec, B. N. L. Sharkey, M. D. Hicks, B. Bozek, A. Aznar, B.-O. Demory, and R. Behrend. Shape modeling of contact binary near-Earth asteroid (85989) 1999 JD6 from radar and lightcurve data. *Icarus*, (in preparation), 2018. URL `http://astro.cornell.edu/~seanm/jd6_shape/`.

D. L. Mitchell, S. J. Ostro, R. S. Hudson, K. D. Rosema, D. B. Campbell, R. Vélez, J. F. Chandler, I. I. Shapiro, J. D. Giorgini, and D. K. Yeomans. Radar Observations of Asteroids 1 Ceres, 2 Pallas, and 4 Vesta. *Icarus*, 124:113–133, November 1996. doi: 10.1006/icar.1996.0193.

D. Morrison. Determination of Radii of Satellites and Asteroids from Radiometry and Photometry. *Icarus*, 19:1–14, May 1973. doi: 10.1016/0019-1035(73)90134-6.

M. Mueller. *Surface Properties of Asteroids from Mid-Infrared Observations and Thermophysical Modeling*. PhD thesis, Freie Universitaet Berlin (Germany), 2007.

S. P. Naidu, J.-L. Margot, M. W. Busch, P. A. Taylor, M. C. Nolan, M. Brozović, L. A. M. Benner, J. D. Giorgini, and C. Magri. Radar imaging and physical characterization of near-Earth Asteroid (162421) 2000 ET70. *Icarus*, 226:323–335, September 2013. doi: 10.1016/j.icarus.2013.05.025.

S. P. Naidu, L. A. M. Benner, J.-L. Margot, M. W. Busch, and P. A. Taylor. Capabilities of Earth-based Radar Facilities for Near-Earth Asteroid Observations. *Astronomical Journal*, 152:99, October 2016. doi: 10.3847/0004-6256/152/4/99.

P. D. Nicholson, R. G. French, D. B. Campbell, J.-L. Margot, M. C. Nolan, G. J. Black, and H. J. Salo. Radar imaging of Saturn's rings. *Icarus*, 177:32–62, September 2005. doi: 10.1016/j.icarus.2005.03.023.

M. C. Nolan, C. Magri, E. S. Howell, L. A. M. Benner, J. D. Giorgini, C. W. Hergenrother, R. S. Hudson, D. S. Lauretta, J.-L. Margot, S. J. Ostro, and D. J. Scheeres. Shape model and surface properties of the OSIRIS-REx target Asteroid (101955) Bennu from radar and lightcurve observations. *Icarus*, 226:629–640, September 2013. doi: 10.1016/j.icarus.2013.05.028.

C. P. Opeil, G. J. Consolmagno, and D. T. Britt. The thermal conductivity of meteorites: New measurements and analysis. *Icarus*, 208:449–454, July 2010. doi: 10.1016/j.icarus.2010.01.021.

C. P. Opeil, G. J. Consolmagno, D. J. Safarik, and D. T. Britt. Stony meteorite thermal properties and their relationship with meteorite chemical and physical states. *Meteoritics and Planetary Science*, 47:319–329, March 2012. doi: 10.1111/j.1945-5100.2012.01331.x.

S. J. Ostro. Planetary radar astronomy. *Reviews of Modern Physics*, 65:1235–1279, October 1993. doi: 10.1103/RevModPhys.65.1235.

S. J. Ostro, R. S. Hudson, L. A. M. Benner, J. D. Giorgini, C. Magri, J.-L. Margot, and M. C. Nolan. Asteroid Radar Astronomy. *Asteroids III*, pages 151–168, 2002. URL `http://adsabs.harvard.edu/abs/2002aste.conf..151O`.

S. J. Ostro, J.-L. Margot, L. A. M. Benner, J. D. Giorgini, D. J. Scheeres, E. G. Fahnestock, S. B. Broschart, J. Bellerose, M. C. Nolan, C. Magri, P. Pravec, P. Scheirich, R. Rose, R. F. Jurgens, E. M. De Jong, and S. Suzuki. Radar Imaging of Binary Near-Earth Asteroid (66391) 1999 KW4. *Science*, 314:1276–1280, November 2006. doi: 10.1126/science.1133622.

Fernando Pérez and Brian E. Granger. IPython: A System for Interactive Scientific Computing. *Computing in Science & Engineering*, 9(3):21–29, 2007. doi: 10.1109/MCSE.2007.53.

D. Polishook and N. Brosch. Photometry of Aten asteroids: More than a handful of binaries. *Icarus*, 194:111–124, March 2008. doi: 10.1016/j.icarus.2007.09.022.

P. Pravec and A. W. Harris. Binary asteroid population. 1. Angular momentum content. *Icarus*, 190:250–259, September 2007. doi: 10.1016/j.icarus.2007.02.023.

C. Raissi, M. Lamee, O. Mosiane, C. Vassallo, M. W. Busch, A. Greenberg, L. A. M. Benner, S. P. Naidu, and N. Duong. New Approaches For Asteroid Spin State and Shape Modeling From Delay-Doppler Radar Images. In *AAS/Division for Planetary Sciences Meeting Abstracts*, volume 48 of *AAS/Division for Planetary Sciences Meeting Abstracts*, page 326.11, October 2016.

J. T. Rayner, D. W. Toomey, P. M. Onaka, A. J. Denault, W. E. Stahlberger, W. D. Vacca, M. C. Cushing, and S. Wang. SpeX: A Medium-Resolution 0.8-5.5 Micron Spectrograph and Imager for the NASA Infrared Telescope Facility. *Publications of the Astronomical Society of the Pacific*, 115:362–382, March 2003. doi: 10.1086/367745.

A. S. Rivkin, R. P. Binzel, J. Sunshine, S. J. Bus, T. H. Burbine, and A. Saxena. Infrared spectroscopic observations of 69230 Hermes (1937 UB): possible unweathered endmember among ordinary chondrite analogs. *Icarus*, 172:408–414, December 2004. doi: 10.1016/j.icarus.2004.07.006.

B. Rozitis and S. F. Green. Physical characterisation of near-Earth asteroid (1620) Geographos. Reconciling radar and thermal-infrared observations. *Astronomy and Astrophysics*, 568:A43, August 2014. doi: 10.1051/0004-6361/201323090.

D. P. Rubincam. Radiative Spin-up and Spin-down of Small Asteroids. *Icarus*, 148:2–11, November 2000. doi: 10.1006/icar.2000.6485.

Jasper Snoek, Hugo Larochelle, and Ryan P. Adams. Practical bayesian opti-

mization of machine learning algorithms. In *Advances in neural information processing systems*, pages 2951–2959, 2012.

T. B. Spahr, G. V. Williams, S. Nakano, and A. Doppler. Minor Planet Circulars Orbit Supplement: 2014 May 14. *Minor Planet Circulars Orbit Supplement*, 292247:294169, May 2014. URL http://www.minorplanetcenter.net/iau/ECS/MPCArchive/2014/MPO_20140514.pdf.

J. R. Spencer, L. A. Lebofsky, and M. V. Sykes. Systematic biases in radiometric diameter determinations. *Icarus*, 78:337–354, April 1989. doi: 10.1016/0019-1035(89)90182-6.

G. M. Szabó, B. Csák, K. Sárneczky, and L. L. Kiss. Photometric observations of 9 Near-Earth Objects. *Astronomy & Astrophysics*, 375:285–292, August 2001. doi: 10.1051/0004-6361:20010813.

P. A. Taylor, E. S. Howell, M. C. Nolan, and A. A. Thane. The Shape and Spin Distributions of Near-Earth Asteroids Observed with the Arecibo Radar System. In *AAS/Division for Planetary Sciences Meeting Abstracts*, volume 44 of *AAS/Division for Planetary Sciences Meeting Abstracts*, page 302.07, October 2012.

D. J. Tholen. *Asteroid taxonomy from cluster analysis of photometry*. PhD thesis, University of Arizona, Tucson, 1984. URL http://adsabs.harvard.edu/abs/1984PhDT.....3T.

D. E. Trilling, M. Mueller, J. L. Hora, A. W. Harris, B. Bhattacharya, W. F. Bottke, S. Chesley, M. Delbo, J. P. Emery, G. Fazio, A. Mainzer, B. Penprase, H. A. Smith, T. B. Spahr, J. A. Stansberry, and C. A. Thomas. ExploreNEOs. I. Description and First Results from the Warm Spitzer Near-

Earth Object Survey. *Astronomical Journal*, 140:770–784, September 2010. doi: 10.1088/0004-6256/140/3/770.

D. E. Trilling, M. Mommert, J. Hora, S. Chesley, J. Emery, G. Fazio, A. Harris, M. Mueller, and H. Smith. NEOSurvey 1: Initial Results from the Warm Spitzer Exploration Science Survey of Near-Earth Object Properties. *Astronomical Journal*, 152:172, December 2016. doi: 10.3847/0004-6256/152/6/172.

S. van der Walt, S. C. Colbert, and G. Varoquaux. The NumPy Array: A Structure for Efficient Numerical Computation. *Computing in Science & Engineering*, 13:22–30, February 2011. doi: 10.1109/MCSE.2011.37.

A. J. Verbiscer and J. Veverka. Interpretation of the IAU two-parameter magnitude system for asteroids in terms of Hapke photometric theory. *Icarus*, 115: 369–373, June 1995. doi: 10.1006/icar.1995.1104.

E. L. Volquardsen, A. S. Rivkin, and S. J. Bus. Composition of hydrated near-Earth object (100085) 1992 UY4. *Icarus*, 187:464–468, April 2007. doi: 10.1016/j.icarus.2006.10.034.

B. D. Warner. Near-Earth Asteroid Lightcurve Analysis at CS3-Palmer Divide Station: 2014 March-June. *Minor Planet Bulletin*, 41:213–224, October 2014.

B. D. Warner. Near-Earth Asteroid Lightcurve Analysis at CS3-Palmer Divide Station: 2015 March-June. *Minor Planet Bulletin*, 42:256–266, October 2015.

B. D. Warner, A. W. Harris, and P. Pravec. The asteroid lightcurve database. *Icarus*, 202:134–146, July 2009. doi: 10.1016/j.icarus.2009.02.003.

B. D. Warner, R. D. Stephens, and A. W. Harris. Save the Lightcurves. *Minor Planet Bulletin*, 38:172–174, July 2011. URL `http://www.minorplanetcenter.net/light_curve2/light_curve.php`.

R. J. Whiteley. ECAS Photometry of NEOs V1.0. *NASA Planetary Data System*, October 2004. URL http://sbn.psi.edu/pds/resource/whiteley.html.

R. J. Whiteley, Jr. *A compositional and dynamical survey of the near-Earth asteroids*. PhD thesis, University of Hawai'i at Manoa, 2001. URL http://adsabs.harvard.edu/abs/2001PhDT.....121W.

Gareth V. Williams. MPEC 1999-J40 : 1999 JD6. *Minor Planet Electronic Circular*, May 1999. URL http://www.minorplanetcenter.org/mpec/J99/J99J40.html.

Gareth V. Williams. MPEC 2000-E54 : 2000 ET70. *Minor Planet Electronic Circular*, March 2000. URL http://www.minorplanetcenter.org/mpec/K00/K00E54.html.